Mean transverse-momentum fluctuations from soft particles produced in pp, p–Pb and Pb–Pb collisions at the LHC

von
Stefan Thomas Heckel
aus Mülheim a.d. Ruhr

Vom Fachbereich Physik der
Johann Wolfgang Goethe-Universität als Dissertation angenommen.

Dekan: Prof. Dr. Michael Lang

Gutachter: Prof. Dr. Harald Appelshäuser

                Prof. Dr. Christoph Blume

Datum der Disputation: 08. Juli 2019

Zusammenfassung

„Außerdem werden wir versuchen, einen kurzen Blick in eine Ära zu werfen, die noch immer von Geheimnissen umhüllt ist: die erste Hundertstelsekunde und das, was ihr voraufging." Dieser Satz stammt von Steven Weinberg aus seinem Buch über „Die ersten drei Minuten", in dem er 1977 den damals aktuellen Stand der Forschung zum Ursprung des Universums beschrieben hat. Zu dieser Zeit konnte man über die erste Hundertstelsekunde nur vage Vermutungen anstellen. Mittlerweile haben wir uns diesen „Geheimnissen" ein Stück weit angenähert. Es wird angenommen, dass in einer sehr frühen Phase bis zu einem Alter von etwa 1–10 Mikrosekunden das Universum aus einem Plasma der elementaren Teilchen der Kernmaterie bestanden hat, dem „Quark-Gluon-Plasma". Dieser Urzustand der Materie kann heutzutage in großen Teilchenbeschleunigern durch die Kollision von schweren Ionen für einen sehr kurzen Zeitraum unter Laborbedingungen erzeugt werden. Der ALICE-Detektor am „Large Hadron Collider" (LHC) am CERN ist zur Vermessung dieses Materiezustandes entwickelt worden. Diese Doktorarbeit befasst sich mit einem Aspekt der Untersuchung dieses Zustandes, der am LHC in Blei–Blei-Kollisionen (Pb–Pb) erzeugt werden kann. Es werden die Fluktuationen des mittleren Transversalimpulses zwischen den einzelnen Kollisions-Ereignissen analysiert und mit entsprechenden Messungen in Proton–Proton-Kollisionen (pp) und Proton–Blei-Kollisionen (p–Pb) verglichen.

Das heutige Verständnis der elementaren Bestandteile des Universums ist im Standardmodell der Teilchenphysik zusammengefasst. Als elementar werden dabei jene Teilchen betrachtet, die sich nicht weiter in kleinere Teilchen aufspalten lassen. Sie werden in die zwei Hauptkategorien der Quarks und der Leptonen eingeteilt, die jeweils aus sechs Teilchen und sechs Antiteilchen bestehen. Zusätzlich enthält das Standardmodell die Austauschteilchen, welche die Wechselwirkungen zwischen den Elementarteilchen vermitteln. Die Austauschteilchen der starken Wechselwirkung, die hier hauptsächlich betracht wird, werden Gluonen genannt. In der uns umgebenden „normalen" Materie kommen nur die beiden leichtesten Quarks vor, das u- und das d-Quark. Sie können jedoch nicht einzeln existieren, sondern sind immer in den Kernbausteinen von Atomen, den Nukleonen, eingeschlossen. Bei den Nukleonen handelt es sich um positiv geladene Protonen (mit einer Quark-Zusammensetzung uud) und elektrisch neutrale Neutronen (udd). Zusammen mit einer Hülle aus negativ geladenen Elektronen bilden sie die Atome.

Am CERN werden Wasserstoff- und Blei-Atome vollständig von ihrer Elektronenhülle befreit und über mehrere Vorbeschleuniger in den LHC eingespeist, wo sie in zwei entgegengesetzt verlaufenden Ringen weiter beschleunigt und schließlich zur Kollision gebracht werden. In diesen Kollisionen können alle bekannten Elementarteilchen erzeugt

werden. Auf Grund der hohen Gesamtenergie der Blei-Kerne können bei ihrem Zusammenstoß für sehr kurze Zeiträume extreme Energiedichten entstehen. Dadurch kann ein Phasenübergang stattfinden von der „normalen" Materie, in der die Quarks in den Nukleonen eingeschlossen sind, zu einem Plasma aus Quarks und Gluonen, innerhalb dessen sich die Elementarteilchen quasi-frei bewegen können. Durch Expansion des Plasmas nimmt die Energiedichte allerdings sehr schnell wieder ab, und es kommt zu einem erneuten Phasenübergang, nach dem alle Quarks wieder in zusammengesetzten Objekten eingeschlossen sein müssen. Diese Objekte werden allgemein als Hadronen bezeichnet und sie umfassen, neben den oben erwähnten Nukleonen, eine Vielzahl an Zuständen, in denen alle Quark-Sorten vorhanden sein können. Die Hadronen und ihre Zerfallsprodukte werden schließlich in Teilchendetektoren, zum Beispiel denen von ALICE, gemessen und sie erlauben Rückschlüsse auf den Zustand, aus dem sie entstanden sind.

Neben ALICE gibt es am LHC mit ATLAS, CMS und LHCb drei weitere große Experimente. ATLAS und CMS sind Mehrzweck-Experimente, mit denen unter anderem das Higgs-Teilchen nachgewiesen worden ist und nach Physik jenseits des Standardmodells gesucht wird. LHCb ist für die Untersuchung von kleinsten Differenzen zwischen Materie und Antimaterie konzipiert. ALICE ist das dedizierte Schwerionen-Experiment am LHC, konstruiert für die gleichzeitige Vermessung und Identifizierung von mehreren tausend Teilchen, die in einer zentralen Pb–Pb-Kollision erzeugt werden können. Die Zentralität ist dabei ein Maß dafür, wie groß der Überlapp der Querschnittsflächen der beiden stoßenden Blei-Kerne ist und eine zentrale Kollision bedeutet einen (nahezu) vollständigen Überlapp, bei dem ein Großteil der Nukleonen beider Kerne an der Kollision teilnimmt.

Der Aufbau von ALICE ist im Wesentlichen in zwei Bereiche unterteilt, das „zentrale Fass" (*central barrel*) und den Myonen-Arm. Der nominelle Interaktionspunkt der beiden LHC-Teilchenstrahlen liegt im Mittelpunkt des *central barrel*, welches aus verschiedenen Detektoren besteht, die von einem großen Solenoid-Magneten umschlossen sind. Die meisten der Detektoren sind symmetrisch in (näherungsweiser) Zylinderform um die Strahlachse angeordnet. Von innen nach außen befinden sich das Innere Spurrekonstruktionssystem (*Inner Tracking System*, ITS), die Spurendriftkammer (*Time Projection Chamber*, TPC), der Übergangsstrahlungsdetektor (*Transition Radiation Detector*, TRD) und der Flugzeitdetektor (*Time-Of-Flight*, TOF). Außerhalb des TOF befinden sich weitere Detektoren, insbesondere verschiedene Kalorimeter, die nicht den kompletten Azimutwinkel abdecken. Zusätzlich sind mehrere kleinere Detektoren nahe am Strahlrohr installiert, die für das Triggern auf Kollisions-Ereignisse und die Klassifikation der Ereignisse, zum Beispiel nach deren Zentralität, benötigt werden. Hierbei sind vor allem die V0-Szintillator-Arrays zu nennen, die für beide vorgenannten Aufgaben genutzt werden. Der Myonen-Arm schließt auf einer Seite an den Solenoid-Magneten an und dient der Messung von Myonen in Vorwärtsrichtung.

Der wichtigste Detektor für die Datenanalyse in der vorliegenden Arbeit ist die TPC. Mit einer Länge entlang der Strahlachse von 5 m, einem inneren Radius in der Transversalebene von 85 cm und einem äußeren Radius von 250 cm umfasst sie ein Volumen von etwa 90 m³, das mit einem Gasgemisch gefüllt ist. Geladene Teilchen, die in den

Kollisionen erzeugt werden, ionisieren die Gasmoleküle auf ihrem Weg durch die TPC. Diese ist in der Mitte durch eine zentrale Elektrode geteilt, zwischen der und den Endkappen ein elektrisches Feld von $100\,\mathrm{kV}$ anliegt. Durch die Ionisationsprozesse frei gewordene Elektronen driften entlang dieses Feldes zu den Endkappen, an denen die Auslesekammern installiert sind, welche den Ort und die Zeit der Ankunft registrieren. Daraus lassen sich die Spuren der Teilchen aus den Kollisionen dreidimensional rekonstruieren. Durch das Magnetfeld von bis zu $0.5\,\mathrm{T}$ werden geladene Teilchen abgelenkt. Ihre Spur, die von den Detektoren wie der TPC gemessen wird, ist deshalb gekrümmt. Aus dieser Krümmung kann der Transversalimpuls der Teilchen bestimmt werden.

Zur Untersuchung der Prozesse, die in den Kollisionen von Protonen und Schwerionen ablaufen, werden zahlreiche verschiedene Messmethoden und Observablen verwendet. Allerdings kann ein erzeugtes Quark-Gluon-Plasma nicht direkt gemessen werden, da seine Energiedichte bereits nach einer Lebensdauer von nur etwa $10^{-23}\,\mathrm{s}$ nicht mehr ausreicht, um diesen Zustand aufrecht zu erhalten, und es zum Phasenübergang zu hadronischer Materie kommt. Die emittierten Teilchen und ihre Zerfallsprodukte lassen jedoch Rückschlüsse auf die vorhergehenden Prozesse und Materiezustände zu. Neben Messgrößen wie den Häufigkeiten der verschiedenen Teilchensorten und ihren Transversalimpuls-Spektren sind das auch Korrelationen zwischen den Teilchen im Orts- oder im Impulsraum. Eine besondere Klasse stellen die Fluktuationen verschiedener Observablen von Ereignis zu Ereignis dar. Die Datenanalyse der vorliegenden Arbeit zählt zu dieser Klasse von Messungen.

Es wird erwartet, dass das in einer Schwerionenkollision erzeugte System ein thermodynamisches Gleichgewicht erreicht, welches durch ein Großkanonisches Ensemble beschrieben werden kann. Dieses ist durch den Druck in Abhängigkeit von der Temperatur, dem Volumen und den chemischen Potentialen der zu erhaltenden Quantenzahlen bestimmt. Die relevanten Quantenzahlen in Schwerionenkollisionen sind die Baryonenzahl, die elektrische Ladung und die Seltsamkeit, die sich aus der Anzahl von s-Quarks und Anti-s-Quarks ergibt. Fluktuationen dieser thermodynamischen Größen werden insbesondere zur Untersuchung des Phasendiagramms stark wechselwirkender Materie verwendet. In dessen typischer Darstellung wird die Temperatur als Funktion des baryo-chemischen Potentials aufgetragen. Für kleine Werte beider Größen liegt hadronische Materie vor, wenn einer der oder beide Werte hinreichend groß werden, kann der Übergang zum Quark-Gluon-Plasma erfolgen. Solche Phasenübergänge sollten deutliche Veränderungen der Fluktuationen thermodynamischer Größen zur Folge haben, insbesondere in der Umgebung des vorhergesagten kritischen Punktes, der am Ende der postulierten Linie des Phasenübergangs erster Ordnung liegen sollte.

In dieser Arbeit werden die Fluktuationen des mittleren Transversalimpulses untersucht, welche in Zusammenhang stehen mit Fluktuationen der Temperatur. Bei den sehr hohen Kollisionsenergien, die am LHC erreicht werden, befindet sich das erzeugte System im Phasendiagramm bei sehr kleinem baryo-chemischem Potential und sehr hoher Temperatur. In diesem Bereich gibt es starke Hinweise darauf, dass kein wirklicher Phasenübergang vorliegt, sondern ein sogenannter *Cross-over*. Hierdurch werden keine starken Veränderungen der Fluktuationen erwartet. Deren Messung kann jedoch Aufschluss über andere Eigenschaften der stattfindenden Prozesse geben. Ins-

besondere lassen die Fluktuations-Messungen Rückschlüsse auf die relevanten Freiheitsgrade im Anfangszustand der Kollisionen zu, also ob eine Kollision als Summe von Nukleon–Nukleon-Stößen beschrieben werden kann, oder ob die partonische Substruktur der Nukleonen, bestehend aus den Quarks und Gluonen, in Betracht gezogen werden muss.

Die Fluktuationen des mittleren Transversalimpulses werden mit dem Zwei-Teilchen-Korrelator der Transversalimpulse der Teilchen bestimmt. Dieser Korrelator ist ein Maß für die nicht-statistischen Fluktuationen; im Falle von rein statistischen Fluktuationen zwischen den Ereignissen verschwindet er also. Ein von Null verschiedenes Resultat bedeutet, dass über die statistischen Fluktuationen hinausgehende dynamische Fluktuationen vorliegen müssen, die sich aus Korrelationen der Teilchen untereinander ergeben. Die Fluktuationen des mittleren Transversalimpulses werden als Funktion der mittleren Teilchenzahldichte gemessen. Die Ergebnisse in den drei untersuchten Kollisionssystemen, also pp-, p–Pb- und Pb–Pb-Kollisionen, werden miteinander verglichen. Daneben werden die inklusiven Fluktuationen in den vollständigen Datensätzen der pp- und p–Pb-Kollisionen bestimmt.

Die Datenanalyse in dieser Arbeit basiert auf ALICE-Daten aus der ersten Laufzeit des LHC aus den Jahren 2010 bis 2013. Die Datenauswertung ist dabei in zwei Teile gegliedert. Im ersten Teil werden die symmetrischen Kollisionssysteme untersucht, also pp- und Pb–Pb-Kollisionen, während der zweite Teil die Analyse der asymmetrischen p–Pb-Kollisionen umfasst. Neben der zeitlichen Reihenfolge der Datennahme liegt der Hauptgrund für diese Differenzierung in der komplexeren Auswertung eines nicht symmetrischen Kollisionssystems. Die symmetrischen Systeme haben den Vorteil, dass bei ihnen das Ruhesystem der Kollisionen mit dem Laborsystem übereinstimmt und somit auch die Akzeptanz der symmetrisch um den Interaktionspunkt aufgebauten Detektoren symmetrisch ist. Mögliche Effekte der unsymmetrischen Akzeptanz müssen bei der Auswertung der p–Pb-Daten berücksichtigt werden.

Eine erste Auswertung der pp- und Pb–Pb-Daten wurde in meiner Masterarbeit vorgenommen [1]. Die dort gewonnenen vorläufigen Ergebnisse wurden in einem Konferenzbericht veröffentlicht [2]. Der erste Teil dieser Doktorarbeit beschäftigt sich mit der finalen Veröffentlichung der pp- und Pb–Pb-Ergebnisse [3,4]. Die dafür im Nachgang der Masterarbeit notwendigen Schritte umfassen unter anderem die Darstellung der Ergebnisse als Funktion der korrigierten Multiplizitätsdichte anstelle der gemessen Teilchenzahl, die Vollendung der Evaluation der systematischen Unsicherheiten sowie eine Erweiterung der Vergleiche mit Monte-Carlo-Simulationen. Zusätzlich werden zahlreiche Effekte hinsichtlich möglicher Einflüsse auf die Messungen studiert. Dazu zählen insbesondere detaillierte Untersuchungen, inwiefern die Bestimmung des mittleren Transversalimpulses von der Position der Kollision im Experiment und der Variation der Akzeptanz der Detektoren mit dem Raumwinkel abhängt. Im Rahmen dieser Studien wird eine stark vereinfachte Simulation selbst entwickelt, mit der entsprechende Effekte separat untersucht werden können. Mit dieser Simulation wird zusätzlich auch die Grundannahme überprüft, dass der Zwei-Teilchen-Korrelator bei rein statistischen Fluktuationen verschwindet.

Im zweiten Teil der Analyse werden neben den Effekten der Akzeptanz in p–Pb-Kollisionen weitere Einflüsse studiert. Ein Beispiel dafür sind Teilchen, welche die zentrale Elektrode der TPC passieren und entweder auf beiden Seiten dieser Elektrode als separate Spuren rekonstruiert werden oder durch die Schnitte auf Qualitätskriterien der einzelnen Teilchenspuren in der Analyse aussortiert werden. In Bezug auf die Akzeptanz wird in den p–Pb-Daten eine Reduktion der Fluktuationen in Vorwärtsrichtung festgestellt. Obwohl es sich um einen relativ kleinen Effekt handelt, wird die Analyse für den Vergleich mit den symmetrischen Kollisionssystemen mit einer eingeschränkten Akzeptanz wiederholt. Für den Vergleich aller drei Systeme muss eine entsprechende Einschränkung auch in den pp-und Pb–Pb-Daten vorgenommen werden, weshalb diese Daten noch einmal ausgewertet werden. Letztendlich werden die Ergebnisse beider Versionen, also mit der vollen und der eingeschränkten Akzeptanz, miteinander verglichen.

Im letzten Kapitel der Arbeit werden die Ergebnisse der Datenanalysen präsentiert. Als Darstellungsform wird der Zwei-Teilchen-Korrelator in Relation zum mittleren Transversalimpuls gesetzt. Es wird die Wurzel aus dem Korrelator geteilt durch den mittleren Transversalimpuls gezeigt. Diese Größe ist dimensionslos und hat den Vorteil, dass sich Anteile der systematischen Unsicherheiten in diesem Verhältnis aufheben. Ein Großteil der Ergebnisse wird als Funktion der mittleren Teilchenzahldichte aufgetragen. Zusätzlich werden die inklusiven Ergebnisse in pp- und p–Pb-Kollisionen gezeigt. Es werden signifikante nicht-statistische Fluktuationen des mittleren Transversalimpulses beobachtet, die in pp-Kollisionen etwa 11–12 % betragen. Vergleiche mit entsprechenden Messungen am ISR bei deutlich niedrigeren Kollisionsenergien ergeben eine Übereinstimmung im Rahmen der Unsicherheiten.

In pp-Kollisionen werden Ergebnisse bei drei verschiedenen Kollisionsenergien miteinander verglichen und es zeigt sich auch als Funktion der Multiplizitätsdichte keine signifikante Energieabhängigkeit bei LHC-Energien. Die Fluktuationen werden mit zunehmender Teilchenzahl kleiner, wobei dieser Verlauf gut mit einem Potenzgesetz beschrieben werden kann. Die Ergebnisse in Pb–Pb-Kollisionen zeigen ein ähnliches Verhalten. Auch hier werden nicht-statistische Fluktuationen gefunden, die mit steigender Teilchenzahldichte abfallen. Im direkten Vergleich von pp- und Pb–Pb-Daten wird eine gute Übereinstimmung im Überlapp-Bereich festgestellt, die so nicht erwartet worden ist. Darüber hinaus entsprechen die Pb–Pb-Ergebnisse bei höheren Multiplizitäten denen einer Extrapolation eines Potenzgesetz-Fits an die pp-Daten. Zu sehr hohen Multiplizitäten zeigen sie jedoch ein verändertes Verhalten und fallen deutlich unter diesen Fit ab. Diese Beobachtung kann mit kollektivem Verhalten in zentralen Pb–Pb-Stößen zusammenhängen. Verschiedene Monte-Carlo-Simulationen werden mit den pp- und Pb–Pb-Ergebnissen verglichen. Während einige dieser Simulationen qualitativ in Übereinstimmung mit den Daten sind, ergeben sich zum Teil dennoch deutliche quantitative Unterschiede.

Pb–Pb-Kollisionen können als Überlagerung von Nukleon–Nukleon-Stößen aufgefasst werden. Eine pp-Kollision entspricht jedoch immer nur einem einzigen Nukleon–Nukleon-Stoß. Betrachtet man also pp-Kollisionen auf der Skala der Nukleonen, so existiert immer nur eine einzige Quelle der Teilchenerzeugung. Dieses Bild ist im

Widerspruch mit den abnehmenden Fluktuationen bei steigender Teilchenzahldichte. Die Übereinstimmung der pp- und Pb–Pb-Daten lässt darauf schließen, dass für die Beschreibung der pp-Daten die Betrachtung auf partonischer Ebene notwendig ist. Dabei kann eine pp-Kollision aus mehreren überlagerten Parton–Parton-Stößen bestehen. Entsprechende Auswirkungen auf die Messungen von Fluktuationen des mittleren Transversalimpulses sind zusammen mit einem Bachelor-Studenten anhand von Monte-Carlo-Simulationen studiert worden [5].

Schließlich werden die Ergebnisse in p–Pb-Kollisionen gezeigt und mit den anderen Kollisionssystemen verglichen. Auch in den p–Pb-Daten werden nicht-statistische Fluktuationen beobachtet, die mit steigender Teilchenzahldichte einem Potenzgesetz folgend kleiner werden. Der Verlauf ist dabei sehr ähnlich dem in pp- und Pb–Pb-Daten. Allerdings wird quantitativ ein kleiner, jedoch signifikanter, Unterschied festgestellt; die p–Pb-Ergebnisse liegen insgesamt etwas niedriger. Dieser Effekt wird durch die Analyse mit einer eingeschränkten Akzeptanz reduziert, aber nicht vollständig aufgehoben.

Trotz dieser kleinen Abweichungen zeigen die Fluktuationen des mittleren Transversalimpulses in allen drei Kollisionssystemen und unabhängig von der Kollisionsenergie ein übereinstimmendes Verhalten. Die Abschwächung der Fluktuationen mit zunehmender Teilchenzahldichte wird durch ein Potenzgesetz beschrieben, dessen Exponent von der Erwartung im Falle einer einfachen Überlagerung von unkorrelierten Quellen der Teilchenproduktion abweicht. Dies deutet darauf hin, dass alle Kollisionssysteme, also insbesondere auch pp-Kollisionen, als ein Zusammenspiel von mehreren Stößen auf partonischer Ebene betrachtet werden müssen. Die in diesen Stößen erzeugten Teilchen sind jedoch nicht voneinander unabhängig, sondern miteinander korreliert. Die im Vergleich zur pp-Extrapolation zusätzliche Reduktion der Fluktuationen hin zu zentralen Pb–Pb-Stößen deutet auf kollektives Verhalten hin, das im Zusammenhang mit der Erzeugung eines Quark-Gluon-Plasmas stehen kann. Es ist aber auch nicht auszuschließen, dass kleine Tropfen dieses Plasmas bei LHC-Energien bereits in den kleinen pp- und p–Pb-Systemen erzeugt werden können und der gemeinsame Verlauf über einen weiten Multiplizitätsbereich dies widerspiegelt.

Contents

Contents

"We will also try to look a little way into an era
that is still clothed in mystery—
the first hundredth of a second, and what went before."

Steven Weinberg, 1977 [6]

1. Introduction

1.1. Strongly interacting matter

1.1.1. From cosmological to macroscopic to femtoscopic scales

Investigating the universe and the properties of its fundamental building blocks is an endeavour which spans over scales with many orders of magnitude. The largest cosmological scale in the universe is the size of the universe itself, whose diameter is estimated to be larger than $9.4 \cdot 10^{10}$ lightyears (ly)[a] or $8.9 \cdot 10^{26}$ m [7]. Within the universe, galaxies represent the areas, in which most of the visible matter is concentrated[b]. Our own galaxy, the milky way, has a diameter of approximatly $100\,000$ ly. Galaxies consist of billions of stars like the sun, which is a typical star with a radius of about $7 \cdot 10^8$ m. The equatorial radius of the earth has with $6.378 \cdot 10^6$ m a size of about one percent of that of the sun [7–9].

All scales mentioned above are orders of magnitude larger than our own human size of the order of 1 m. This size represents a typical macroscopic scale, the scale of objects of our everyday life. In general, sizes of about 10^{-3}–10^3 m are considered macroscopic. All macroscopic objects are composed of atoms, which are many orders of magnitude smaller with a size of about 10^{-10} m. Most of the mass of an atom is concentrated in its dense, positively charged nucleus with a diameter of about 10^{-14} m, which is surrounded by a cloud of negatively charged electrons. In contrast to the nucleus, which itself is build up of nucleons, the electrons are considered to be elementary particles, which cannot be divided further. Electrons are smaller than 10^{-18} m and might be point-like particles [10]. The nucleons, i.e. protons and neutrons, have a size of about 10^{-15} m $= 1$ fm, reaching the femtoscopic scale. They are composed of quarks, which – like electrons – are assumed to be elementary particles [10–14].

Those particles which are assumed to be elementary, are described in the standard model of particle physics. It contains six quarks grouped in three generations of two quarks each, and six leptons, which are grouped in doublets as well. The quarks are identified by their flavour with the six different species: up (u), down (d), strange (s), charm (c), bottom (b) and top (t). The leptons consist of the electron, the muon and the tau and their corresponding neutrinos. Furthermore, the standard model contains the anti-particles of both the quarks and the leptons, which share most of the properties of the corresponding particles but carry the opposite charge. In addition,

---

[a] 1 ly $= 9.461 \cdot 10^{15}$ m [8].
[b] The fraction of visible matter is estimated to be of the order of 4–5% only. The remaining 95–96% are assumed to consist of dark matter and dark energy [7, 9].

the gauge bosons of the four fundamental interactions are included, as well as the Higgs boson, which was recently discovered [15, 16]. An introduction to the standard model of particle physics, the elementary particles and the fundamental forces mediating their interactions can be found in [11] and [12], the latter also covering potential physics beyond the standard model. Recent data on the properties of elementary particles as well as an up-to-date overview of the standard model and related topics can be found in [17].

Despite the much larger number of elementary particles, ordinary matter is composed of only three of them, the up and down quarks building the nucleons, and the electron. The other quarks, the muon and the tau have higher masses and therefore decay into the lighter particles.

Quarks carry colour charge, which is the charge of the strong interaction [10–14]. There are three colour-charge states (red, green and blue) and the corresponding anti-states (anti-colours) carried by anti-quarks. Combining one of the colours with its corresponding anti-colour or combining all three colours (or all three anti-colours) leads to a colourless (white) state. Unlike the electrons, single quarks cannot be observed freely. They are confined in colourless hadrons [10–14]. These can either consist of a quark and an anti-quark, building a meson, or of three quarks (anti-quarks) forming a baryon (anti-baryon). The lightest mesons are the pions and the lightest baryons are the nucleons. The net quark content of the latter consists of three valence quarks (proton: uud, neutron: udd). In addition, a hadron contains quark–anti-quark pairs called sea quarks, as well as gluons, the gauge bosons of the strong interaction. These quark–anti-quark pairs are virtually created and annihilated continuously, and on average their quantum numbers vanish. Hence, together with the gluons they constitute a "sea" of partons around the valence quarks [10, 11]. The gluons also carry colour charge and via exchange of this charge gluons cannot only interact with quarks, but gluons can also interact with gluons. Hence, a nucleon is not a static state of three valence quarks, but a very dynamic object of strongly interacting partons, i.e. quarks and gluons.

1.1.2. Quantum Chromo Dynamics and its phase diagram

The theory of strong interactions is called Quantum Chromo Dynamics (QCD)[c] [10–14]. QCD is a fundamental field theory like Quantum Electro Dynamics (QED), the theory of electromagnetic interactions. Although in general both theories are similar, there are some distinct differences between QCD and QED. In contrast to one electric charge and its corresponding anti-charge, there are three colour charge states and the corresponding anti-states. The gauge bosons mediating the interactions are massless in both theories, but unlike photons, which do not carry electric charge, the gluons

---

[c] Derived from the Greek word "chromos" = colour.

do carry colour charge. Therefore, gluons can interact with each other in contrast to photons[d].

This self-coupling of the gluons is reflected in the QCD Lagrangian, which describes the interactions of quarks and gluons and is defined as [11, 12]

$$\mathcal{L}_{\text{QCD}} = \bar{q}_f \left(i\gamma^\mu D_\mu - m_f \right) q_f - \frac{1}{4} F^i_{\mu\nu} F^{i\mu\nu} . \tag{1.1}$$

The last term describes the gluon-gluon interactions with $F^i_{\mu\nu}$ being the field strength tensors of the gluon fields A^i_μ. The first part contains both the quark-quark and the quark-gluon interactions, although also the quark-quark interactions are mediated by gluons. Equation 1.1 contains the quark fields q_f, the masses of the quarks m_f and

$$D_\mu = \partial_\mu + ig_s \frac{\lambda^i}{2} A^i_\mu . \tag{1.2}$$

Here, g_s denotes the strong coupling constant and the λ^i are the 3×3 Gell-Mann matrices. Within equations 1.1 and 1.2, summation over the flavour index f ($f = 1, 2, ..., 6$) and the gluon index i ($i = 1, 2, ..., 8$) is implied, following the notation from [12].

The interaction strength of the strong interaction is governed by its "running" coupling constant $\alpha_\text{s}(Q^2)$. As the description of a "running" constant implies, the coupling strength is not constant but depending on the momentum transfer Q^2. This is reflected in the definition of the coupling [12]

$$\alpha_\text{s}(Q^2) = \frac{12\pi}{(33 - 2n_f) \cdot \log\left(\frac{Q^2}{\Lambda^2_{\text{QCD}}}\right)} . \tag{1.3}$$

Here, n_f denotes the number of quark flavours[e] and $\Lambda_{\text{QCD}} \approx 200\,\text{MeV}/c$ is the QCD scale parameter [12]. The coupling strength in QCD increases for decreasing Q^2 corresponding to an increasing distance of the strongly interacting objects. Therefore, it is not possible to separate the quarks of a hadron to obtain single free quarks. If the quarks are pulled apart far enough, the energy density in-between becomes high enough to create a new quark–anti-quark pair. Instead of single free quarks, the final state consists of two hadrons, which are again bound objects. Hence, for ordinary matter, the relevant degrees of freedom are of hadronic and not of partonic nature.

However, this hadronic phase is not the only possible state of strongly interacting matter. Decreasing the distance between hadrons corresponding to an increasing Q^2 results in a decreasing $\alpha_\text{s}(Q^2)$. This can lead to a state, where the hadrons overlap, break up and form a deconfined phase of freely moving partons called Quark-Gluon Plasma (QGP) [10, 13, 14, 19, 20]. It can be reached by an extreme compression and/or

---

[d] Although photon–photon interactions – also called light-by-light scattering – are forbidden in classical electrodynamics, they are possible in QED and evidence for this effect has been found by ATLAS [18].

[e] Considering all quark species would imply $n_f = 6$, but the number of quarks participating in the interactions depends on Q^2, leading to an effective number of $n_f = 2$–6 [10, 11].
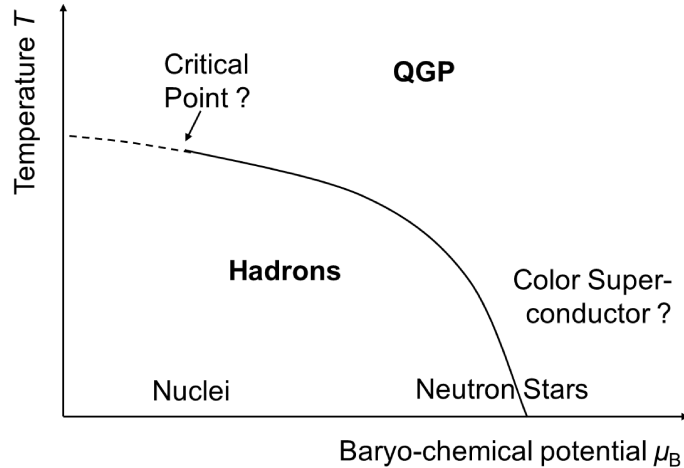
Figure 1.1.: The phase diagram of strongly interacting matter. (Drawn according to [10, 14, 19–22]).

heating of hadronic matter. In the first case, the density of the hadrons has to increase until they overlap. In the second case, the energy of the heating is transferred to the creation of quark–anti-quark pairs (mesons) in between the hadrons, leading to an overlapping of the original hadrons and the created mesons. In contrast to the confinement of partons inside the hadrons in ordinary matter, the hot and dense state of a QGP exhibits a partonic nature called asymptotic freedom [10, 13, 14, 19, 20]. However, the partons are still not able to leave the QGP as free particles. In that sense, they are confined within the QGP, which as a whole is a colourless object.

The possible states of strongly interacting matter are contained in the QCD phase diagram [10, 14, 19–22]. It is shown in figure 1.1 as a schematic view in the two-dimensional plane of temperature (T) and baryo-chemical potential (μ_B). The latter is a measure similar to the pressure arising from the net baryon density, i.e. the number of baryons minus the number of anti-baryons. At low T and low μ_B matter consists of hadrons whereas at high T and/or high μ_B the partonic QGP phase is reached [10, 14, 19–22]. The location and the properties of the phase transition from hadrons to the QGP are still not known precisely. There is strong evidence from lattice QCD calculations, that a crossover phase transition is present at vanishing μ_B and around $T \approx 160 \, \mathrm{MeV}$ [23, 24]. At higher μ_B, a first-order phase transition is assumed. If these assumptions are correct, the first-order transition has to reach a critical endpoint, where the transition to the cross-over region takes place [25, 26]. In addition to the hadronic phase and the QGP, the phase diagram in figure 1.1 contains the predicted region of neutron stars, briefly discussed in the next section, as well as a hypothetical colour-superconductor state [14, 27].

1.1.3. And back again: from femtoscopic to macroscopic to cosmological scales

It is possible to investigate the properties and the phase diagram of strongly interacting matter in the laboratory using ultra-relativistic heavy-ion collisions, which are discussed in more detail in the next section. Within these collisions, a QGP can be created on a femtoscopic scale in space and time, with a QGP volume of the order of 10^3–10^5 fm^3 and a lifetime of about 1–10 fm/c $\approx (0.3$–$3) \cdot 10^{-23}$ s [28].

A QGP may also exist in nature on a macroscopic scale within neutron stars. These are remnants of stars, which have reached the end of their lifetime and where the core has collapsed to a dense object, which does not contain sufficient mass to collaps further to a black hole. Instead, it is stabilised by the neutron degeneracy pressure. Neutron stars typically have a mass of about $1.4 \, M_\odot$[f], concentrated within a radius of 10–15 km [8, 9, 29]. The interior of neutron stars is modelled with a lot of different equations of state using diverse assumptions including some, which require hyper matter (hadrons containing strange quarks) or even a QGP [8, 29]. The potential position of neutron stars in the phase diagram of QCD is also depicted in figure 1.1.

With the first detection of gravitational waves in 2015 [30], a new window for the investigation of the universe has opened. While the first detected event is ascribed to the merging of two black holes, another detection from August 2017 [31] is best described by the merging of two neutron stars. Recently, a number of equations of state have been tested on this single gravitational-wave event [29]. This study shows, that with a high probability at least one of the two neutron stars has to contain hyper matter or a QGP. Future observations of gravitational-wave signals of merging neutron stars may prove the existence of a Quark-Gluon Plasma on macroscopic scales [29].

Finally going back to the cosmological scale, a QGP may have existed in the very early history of the universe [7, 10, 28, 32]. Following the theory, that the universe originates from a big bang [6], where the entire energy content of the universe was contained within a singularity, the rapidly expanding universe would have surpassed a QGP state until about 1–10 μs after the big bang [7, 10, 28, 32]. At this time, the freeze-out of the hot and dense matter would have lead to the formation of the hadrons, constituting the phase transition from the partonic to the hadronic universe.

1.2. Heavy-ion collisions

Strongly interacting matter and its phases can be studied in the laboratory with ultra-relativistic collisions of heavy ions [14, 19, 20, 22]. For this purpose the ions have to be accelerated to almost the speed of light. They are brought into collision either by shooting one beam of ions on a fixed target being at rest or by colliding two beams of ions. The technical aspects of the latter case are summarised in chapter 2 for the Large Hadron Collider (LHC) [33] at CERN and the ALICE experiment [34, 35], which is dedicated to the investigation of heavy-ion collisions at the LHC.

---

[f] The solar mass is $1 \, M_\odot = 1.989 \cdot 10^{30}$ kg [8].
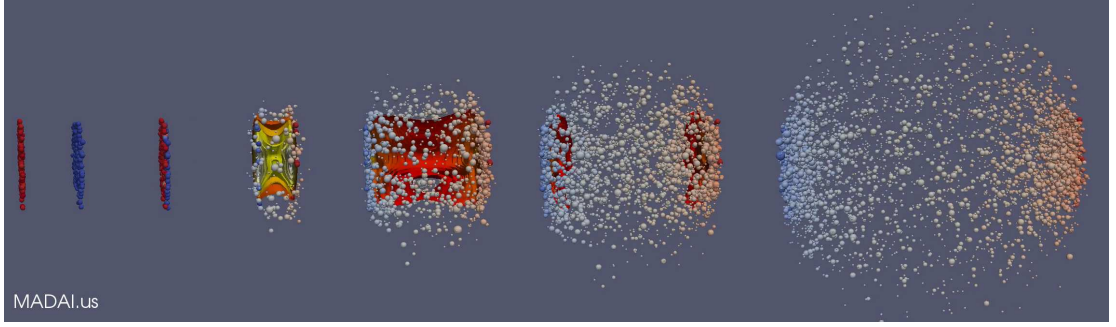
Figure 1.2.: Stages of an ultra-relativistic heavy-ion collision, from UrQMD [36,37].
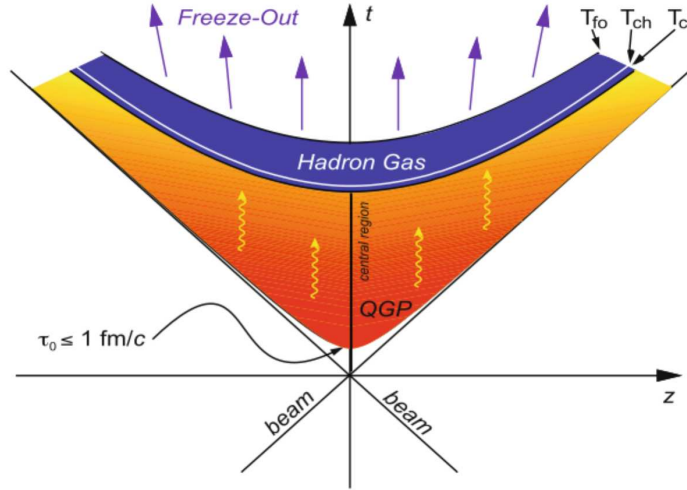
Figure 1.3.: Evolution of an ultra-relativistic heavy-ion collision in time (t) and beam direction (z) [22].

The different stages of an ultra-relativistic heavy-ion collision are illustrated in figure 1.2. In the laboratory frame, the ions are Lorentz contracted and therefore appear as thin discs. In the instant of the collision, the nucleons within the two ions or the partons inside these nucleons undergo initial hard scattering processes which produce a large number of quark–anti-quark pairs of all different flavours, leading to a very high energy density within a small volume. In this way, a hot and dense QGP with partonic degrees of freedom can be created, see also section 1.1.2. This medium is not static but rapidly expanding, accompanied by a fast decrease of the energy density. After a typical lifetime of several fm/c, the energy density is so low that the partonic deconfined matter freezes out and forms hadrons, in which the partons are confined again. These hadrons – together with leptons and photons created during the collision as well – are emitted in all directions and can be measured by particle detectors [14, 19, 20, 22].

Another schematic representation of a heavy-ion collision is shown in figure 1.3. Here, the evolution of the collision is shown in the two-dimensional plane of time (t) and

beam direction (z). The collision takes place at the intersection of the two beams, i.e. $t = z = 0$. The initial hard scatterings are followed by the creation of a QGP, which has a formation time of $\tau_0 \leq 1\,\mathrm{fm}/c$. At the critical temperature T_c the phase transition from a QGP to a hadron gas occurs. Inelastic interactions changing the particle species stop at the chemical freeze-out temperature T_ch. Finally, elastic scatterings cease at the thermal freeze-out T_fo. Afterwards, the momentum distribution of the particles is fixed with the exception of particle decays and interactions of the particles with the detector material [22]. The critical temperature at vanishing baryo-chemical potential ($\mu_\mathrm{B} = 0$) can be calculated in lattice QCD calculations, where a value of $T_\mathrm{c} = (154 \pm 9)\,\mathrm{MeV}$ is obtained [24]. This result is in good agreement with the value for the chemical freeze-out temperature $T_\mathrm{ch} = (156.5 \pm 1.5)\,\mathrm{MeV}$ determined in the statistical hadronisation approach [38]. Hence, the difference of these two temperatures is small and they may even coincide.

1.3. Exploring the Quark-Gluon Plasma

The existence of a deconfined state of quarks and gluons at sufficiently high energy density was postulated in [39, 40]. This hypothetical state of strongly interacting matter was first called a "Quark-Gluon Plasma" in [41]. The experimental search for this QGP using ultra-relativistic heavy-ion collisions[g] started at the Alternating Gradient Synchrotron (AGS) at Brookhaven National Laboratory (BNL), USA, and at the Super Proton Synchrotron (SPS) at CERN, where the discovery of the QGP has been claimed in 2000 [42]. Originally, the QGP was thought of as an ideal gas of quarks and gluons. However, measurements at the Relativistic Heavy Ion Collider (RHIC) at BNL have revealed a behaviour of the QGP as an almost perfect liquid [43, 44]. In 2010, ALICE at the CERN LHC has joined the experimental efforts to investigate the properties of the Quark-Gluon Plasma.

In this section, a selection of important observables for the search for and investigation of the QGP in ultra-relativistic heavy-ion collisions is presented. A comprehensive introduction to "The Physics of the Quark-Gluon Plasma" can be found in the lecture notes [45], among which [21, 22] represent the first two chapters. A view on smaller collision systems follows in section 1.3.2. These contribute to the understanding of strongly interacting matter – not only due to their importance as reference measurements for heavy-ion collisions, but also to investigate the relevant scale of strong interactions at ultra-relativistic energies. In the next section, 1.4, measurements of event-by-event fluctuations are introduced, followed by a more detailed discussion of fluctuations of the mean transverse momentum in section 1.5.

---

[g] Heavy-ion collisions are considered "ultra-relativistic" if the energy density reaches $\epsilon \gtrsim 1\,\mathrm{GeV/fm}^3$ corresponding to a beam energy of $E_\mathrm{beam} \gtrsim 10\,\mathrm{GeV/nucleon}$ [20, 22]. The investigation of heavy-ion collisions at lower collision energies was started before at several reasearch centres around the world [19, 20].

1.3.1. Signatures of a Quark-Gluon Plasma

If a Quark-Gluon Plasma can be created in the collision of two heavy nuclei, it has an extremely short lifetime of the order of several fm/c or about 10^{-23} s. Therefore, it is not possible to study this state of matter using external probes like a beam of particles or photons. Instead, information about this system can only be obtained from the abundances and properties of those particles which are produced during the various stages of its evolution [21, 22] depicted in figure 1.3.

The first stage is the pre-equilibrium stage consisting of the initial collisions of the nucleons within the two nuclei. Here, the hardest processes with the highest possible momentum transfers take place and create the so-called "hard probes". Produced before a QGP can form, the interaction of these hard probes with the QGP medium can be studied and compared to proton–proton (pp) collisions, where no medium is created. Quarkonia are hard probes composed of a heavy quark (c, b) and its corresponding anti-quark ($\bar{c}$, $\bar{b}$). Their abundances in heavy-ion collisions are expected to be suppressed with respect to pp collisions, if a QGP has formed [46]. The ground states of these quarkonia – J/ψ (c$\bar{c}$) and Υ (b$\bar{b}$) – have binding energies much larger than the QCD scale $\Lambda_{\mathrm{QCD}} \approx 200$ MeV [21]. Hence, they have a probability to survive the QGP phase. This probability decreases for the higher quarkonium states because of their lower binding energies. They are dissociated already at lower temperatures within the QGP. Therefore, the analysis of the different quarkonia can serve as a thermometer of the QGP [47].

Other hard probes include dijets originating from a high-momentum quark–anti-quark pair created during the first nucleon–nucleon collisions [48]. These partons fragment into collimated jets of particles, which are oriented back-to-back in the transverse plane. Within vacuum conditions, like in a pp collision, both jets can be measured. If a QGP is formed in a heavy-ion collision, only those jets, which are created close to the surface of the collision zone and directed outwards, can be observed. Jets which have to traverse the medium are suppressed, which is called "jet quenching" [49]. In general, any parton carrying high transverse momentum (p_{T}) looses energy while traversing the QGP, which can be measured as a high-p_{T} particle suppression.

During the entire lifetime of the QGP, electromagnetic probes are created and emitted. These include photons, which are emitted in various processes, as well as dileptons (electron–positron and muon–anti-muon pairs) produced in quark–anti-quark annihilations. As photons and leptons do not interact strongly, they escape the QGP without further modification and can therefore provide information about the QGP properties at the time of their production [50]. However, as they are formed throughout the QGP evolution and also at later stages, the extraction of information about the QGP is challenging.

The phase transition from the deconfined to the confined state goes along with the formation of hadrons. The abundances of the different hadron species are fixed at the chemical freeze-out, when the inelastic interactions among particles cease. The hadron abundances carry information about the freeze-out conditions as well as the state of the matter existing before the freeze-out. For example, the amount of hadrons
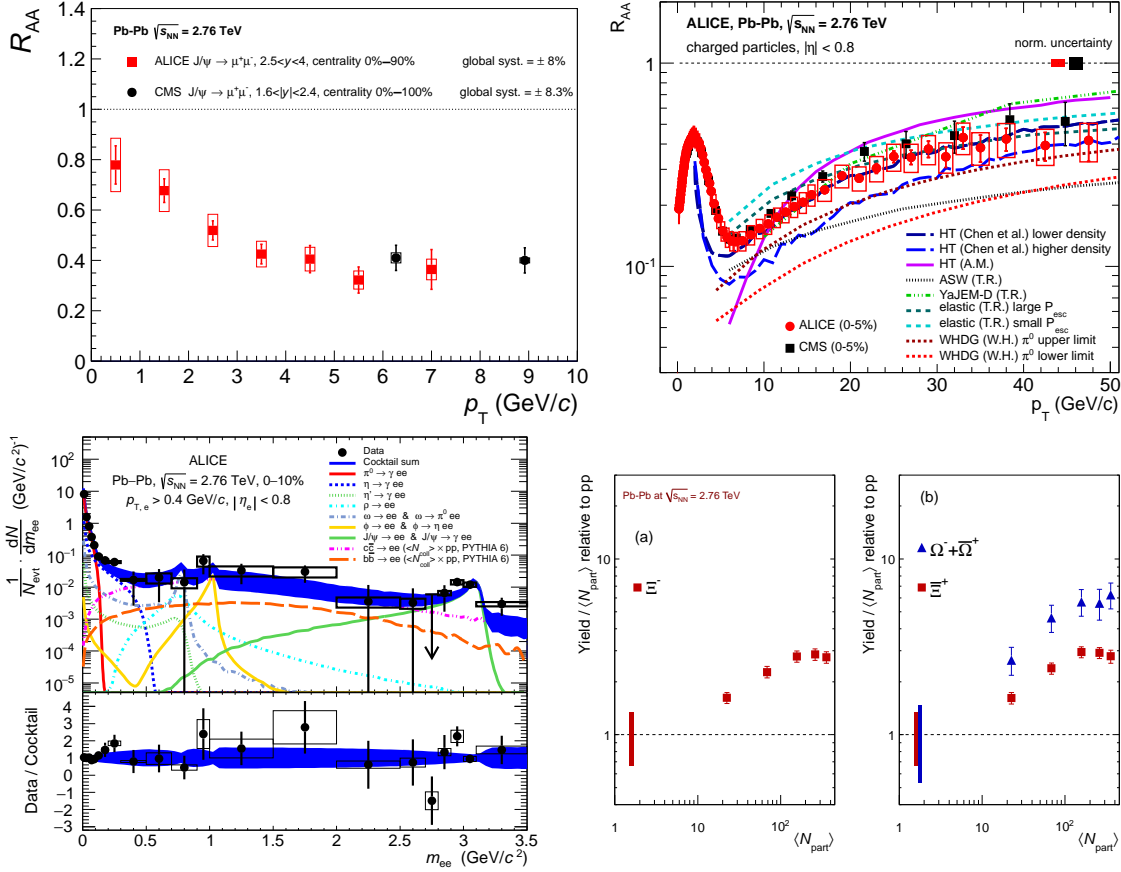
Figure 1.4.: Selection of ALICE results in Pb–Pb collisions at $\sqrt{s_{NN}}$ = 2.76 TeV: R_{AA} as a function of p_T for J/ψ (top left [52]) and charged particles (top right [53]), dielectron yield as a function of m_{ee} (bottom left [54]) and strangeness enhancement versus $\langle N_{part} \rangle$ (bottom right, (a) and (b), [55]).

containing strange quarks is expected to be enhanced within a QGP with respect to pp collisions [51].

All of those observables are studied in heavy-ion collisions at several research centres and experiments, covering a wide range of collision energies. Many results are in agreement with predictions assuming the creation of a deconfined state of strongly interacting matter in the course of the collisions. Although each single measurement may not be considered as a proof of the exsistence of a QGP, its formation in heavy-ion collisions has been established by the variety of observations.

Some examplary results measured by ALICE at the LHC in lead–lead (Pb–Pb) collisions at an energy per nucleon–nucleon collision of $\sqrt{s_{NN}}$ = 2.76 TeV are presented in figure 1.4. In the top panels, the nuclear modification factor R_{AA} comparing the yield in heavy-ion (A–A) collisions with that in pp collisions is shown as a function of p_T for J/ψ (left panel [52]) and charged particles (right panel [53]). In both cases a clear suppression with respect to the pp expectation is observed. The measurement of

charged particles is compared to several theoretical calculations, all of which exhibit qualitatively a behaviour similar to the data. The dielectron yield in Pb–Pb collisions as a function of the invariant mass of the dielectron pair m_{ee} is presented in the bottom left panel [54]. The different contributions to this spectrum are identified and add up to the "Cocktail sum", which is in agreement with the data within the uncertainties. The two figures in the lower right panel demonstrate the enhanced yield of multi-strange particles in Pb–Pb collisions relative to pp as a function of the average number of participating nucleons $\langle N_{\text{part}} \rangle$ [55].

In addition to these observables many more are investigated. The description of all of these measurements would go beyond the scope of this thesis. The lecture notes in [45] provide an introduction to these studies along with an overview of many results. Comprehensive reviews of both theoretical and phenomenological aspects can be found in the books of the "Quark-Gluon Plasma" series. The more recent editions comprise the volumes three [56], four [57] and five [58]. The observations and evaluations of the first years of data taking at RHIC have been summarised by the STAR [43] and PHENIX [44] Collaborations. A comprehensive review of the scientific harvest of the LHC within its first running period (Run 1) can be found in [59], wherein the heavy-ion physics is discussed in chapter [60]. Another review focussing on the results in heavy-ion collisions within LHC Run 1 can be found in [61]. A brief overview of theroretical heavy-ion physics is given in [62] and a recent and detailed review of the status of Lattice QCD calculations can be found in [24].

1.3.2. Small systems: pp and p–A collisions

The same quantities used to investigate the behaviour of strongly interacting matter in heavy-ion collisions are also studied in small collision systems. These include hadron–hadron collisions as well as hadron–nucleus collisions and in these systems, the creation of a Quark-Gluon Plasma is not expected.

However, in recent years, behaviour up to now attributed to the creation of a QGP has also been observed in high-multiplicity pp and p–A collisions. For example, angular correlations resembling those in heavy-ion collisions have been found in p–Pb collisions [63] and strangeness enhancement has been observed in pp collisions [64].

Therefore, discussions are ongoing, whether it might be possible that a Quark-Gluon-Plasma droplet can already be created in the collisions of small systems like pp or p–Pb, or whether the corresponding observations may have a different explanation. In pp collisions, multiple parton–parton collisions could be present. In this case, one pp collision would have to be seen as a superposition of particle-emitting sources, which e.g. may explain azimuthal asymmetries. Recent summaries on possible collectivity in small systems can be found in [65, 66].

Recent measurements at RHIC in p–Au, d–Au and He^3–Au collisions [67] indeed favour the creation of small QGP droplets. However, a final conclusion has not yet been achieved, and this work may add a piece to this puzzle.

1.4. Event-by-event fluctuations

This section provides an overview of event-by-event fluctuations, which are employed to investigate the matter created in heavy-ion collisions. First, the terms "correlations" and "fluctuations" are defined. Afterwards, basic concepts and statistical methods are introduced briefly, followed by descriptions of event-by-event fluctuation observables.

1.4.1. Correlations and fluctuations

Most of the observables discussed in the previous section correspond to the abundances or properties of single particles or spectra of particle species. Measures of correlations and fluctuations always combine properties of several particles or even all particles within one event. Although in general, measurements of correlations and fluctuations are related to each other, they constitute two different groups of observables. Correlations are defined between several particles originating from the same event, e.g. taking into account the correlations of these particles in position or momentum space. Fluctuation measures are typically constructed on complete events and they quantify the differences from one event to the other. In most cases, fluctuation observables are influenced by correlations of particles or they are even built on the measurement of correlations, e.g. between all particle pairs within one event.

An introduction to correlation observables can be found in [68] and [69]. Measurements of correlations in heavy-ion collisions during LHC Run 1 are collected in [60]. Here, only some of the most important correlation measures employed in the study of heavy-ion collisions are listed: correlations of emission angles describing the corresponding azimuthal anisotropies summarised with the term "flow", two-particle number and transverse-momentum correlations revealing the relevant correlation lengths, and Hanbury-Brown–Twiss correlations, measuring the size of the emission region. In addition, observables can be constructed which do not measure the correlations of particles but the correlations of other observables. In this way, correlations of fluctuation measures can be obtained. An example is presented in section 1.4.4.

1.4.2. Basic concepts of fluctuation analyses

A brief introduction to the basic concepts of event-by-event fluctuation analyses in heavy-ion collisions is presented here. The principles of event-by-event fluctuations are discussed in more detail in [70] and a review of hadronic fluctuations and correlations can be found in [71].

The system created in ultra-relativistic heavy-ion collisions is expected to reach a state close to thermal equilibrium [70, 72]. Such a thermal system can be described by the appropriate thermodynamic ensemble. In heavy-ion collisions, typically only a subsystem can be analysed due to the restriction of the measurement to the (pseudo-)rapidity range of the detectors. Therefore, this subsystem is embedded in the heat bath of the overall system and it is able to exchange energy and particles with this bath. Hence in most cases, the grand-canonical ensemble is the appropriate choice [70,

72]. Considering a measurement of rare particles with specific quantum numbers, the conservation of this quantum number within the subsystem has to be taken into account and the canonical ensemble has to be applied.

In the grand-canonical ensemble a system is characterised by the pressure $P(T, V, \vec{\mu})$, which depends on the temperature T, the volume V and the chemical potentials $\vec{\mu}$ of the system. The chemical potentials ensure the conservation of all relevant charges within the full system. In the strongly interacting matter produced in a heavy-ion collision, these charges are the baryon number B, the electric charge Q and the strangeness S [72]. Therefore, the relevant chemical potentials are $\vec{\mu} = (\mu_B, \mu_Q, \mu_S)$.

Event-by-event fluctuations of the temperature and the conserved charges can reveal properties of the strongly interacting matter created in heavy-ion collisions. One of the most important applications is the investigation of the phase transitions described in section 1.1.2 and depicted in figure 1.1. As discussed there, the exact location and properties of these phase transitions are not known. Phase transitions are expected to have a strong influence on fluctuation signals, especially in the vicinity of a possible critical endpoint of a potential first-order phase-transition line [25, 26, 70, 71]. In addition, fluctuations may provide insight into the relevant degrees of freedom within the collisions, i.e. whether the initial state of the collisions is compatible with a nucleonic scattering scenario, or whether the sub-nuclear partonic structure has to be taken into account [73, 74].

Fluctuations are composed of trivial and dynamical fluctuations, the latter containing the relevant information about the properties of the system under study [70, 71]. The trivial fluctuations do not contain information about the system, but they can distort the signals of the dynamical fluctuations and have to be subtracted from the measurement. The finite number of particles created within one collision leads to statistical fluctuations, which are part of the trivial fluctuations. In addition, the volume of the system fluctuates from one event to the other due to the fluctuations of the impact parameter, which cannot be controlled directly in the experiments. Therefore, it is desirable to construct observables, which do not depend on the volume of the system and its fluctuations.

1.4.3. Some fundamental statistics

In this section, the fundamental concepts of the statistics relevant for the analysis of fluctuations are discussed. Consider an event with N particles in the final state and an observable X, which is the sum of the properties x_i of all particles of that event. Then X is defined as

$$X = \sum_{i=1}^{N} x_i \,. \tag{1.4}$$

For example, X could be the number of charged particles N_{ch} with $x_i = 1$ for charged and $x_i = 0$ for neutral particles, or X could be the sum P_{T} of the transverse momenta $p_{\text{T},i}$ of the charged particles with $x_i = p_{\text{T},i}$ for charged and again $x_i = 0$ for neutral particles. The observable X can fluctuate from one event to the next resulting in a

distribution of X for an ensemble of events. This distribution is characterised by its moments [75], which are in general defined as

$$a\text{-th moment of } X : A_a(X) = \frac{1}{n_{\text{ev}}} \sum_{k=1}^{n_{\text{ev}}} X_k^a = \langle X^a \rangle, \tag{1.5}$$

$$b\text{-th central moment of } X : B_b(X) = \frac{1}{n_{\text{ev}}} \sum_{k=1}^{n_{\text{ev}}} (X_k - \langle X \rangle)^b = \langle (X - \langle X \rangle)^b \rangle. \tag{1.6}$$

Here, n_{ev} denotes the number of events within the ensemble. The first moment corresponds to the mean

$$M(X) = \langle X \rangle = \frac{1}{n_{\text{ev}}} \sum_{k=1}^{n_{\text{ev}}} X_k. \tag{1.7}$$

The difference of X in a single event k with respect to the mean of all events is given by

$$\delta X_k = X_k - \langle X \rangle. \tag{1.8}$$

The average value of the δX_k corresponds to the first central moment, which by construction always yields $\langle \delta X_k \rangle = 0$. Hence, it is not useful as an estimate of the spread of the distribution. Instead, the spread is described by the average of the squares of the deviations from the mean [75]. This is the second central moment of the distribution or variance

$$
\begin{aligned}
\sigma^2(X) = \langle \delta X^2 \rangle &= \langle (X - \langle X \rangle)^2 \rangle \\
&= \langle X^2 + \langle X \rangle^2 - 2X\langle X \rangle \rangle \\
&= \langle X^2 \rangle + \langle X \rangle^2 - 2\langle X \rangle^2 \\
&= \langle X^2 \rangle - \langle X \rangle^2.
\end{aligned}
\tag{1.9}
$$

The standard deviation of the distribution is defined as the square root of the variance

$$\sigma(X) = \sqrt{\sigma^2(X)} = \sqrt{\langle X^2 \rangle - \langle X \rangle^2}. \tag{1.10}$$

For a thermal system, which is assumed to be created in a heavy-ion collision, the distribution of a fluctuating observable X is expected to follow a Gaussian distribution [70]. A normal Gaussian distribution is completely described by its two parameters $M(X)$ and $\sigma(X)$ [75]. However, the distribution of X can show deviations from the normal Gaussian form. These deviations are described by the higher moments of a generalised Gaussian distribution, which are the skewness (third central moment) and

1. Introduction

the kurtosis (fourth central moment) [75]. The skewness describing the asymmetry of the distribution is normalised to σ^3, resulting in the dimensionless quantity

$$
\begin{aligned}
S(X) &= \frac{\langle \delta X^3 \rangle}{\sigma^3} = \frac{1}{\sigma^3} \langle (X - \langle X \rangle)^3 \rangle \\
&= \frac{1}{\sigma^3} \langle X^3 - 2X^2 \langle X \rangle + X \langle X \rangle^2 - X^2 \langle X \rangle + 2X \langle X \rangle^2 - \langle X \rangle^3 \rangle \\
&= \frac{1}{\sigma^3} \langle X^3 - 3X^2 \langle X \rangle + 3X \langle X \rangle^2 - \langle X \rangle^3 \rangle \\
&= \frac{1}{\sigma^3} \left(\langle X^3 \rangle - 3 \langle X^2 \rangle \langle X \rangle + 3 \langle X \rangle^3 - \langle X \rangle^3 \right) \\
&= \frac{1}{\sigma^3} \left(\langle X^3 \rangle - 3 \langle X^2 \rangle \langle X \rangle + 2 \langle X \rangle^3 \right) .
\end{aligned}
\tag{1.11}
$$

The skewness of a symmetric distribution is zero. A positive skewness implies a distribution with a larger tail to the right of the mean, a negatively skewed distribution has a larger tail to the left. Like the skewness, the kurtosis is as well defined as a dimensionless quantity, which is zero in case of a normal Gaussian distribution. This is achieved by normalising the fourth central moment to σ^4 and by subtracting 3, yielding

$$
\begin{aligned}
\kappa(X) &= \frac{\langle \delta X^4 \rangle}{\sigma^4} - 3 = \frac{1}{\sigma^4} \langle (X - \langle X \rangle)^4 \rangle - 3 \\
&= \frac{1}{\sigma^4} \left(\langle X^4 \rangle - 4 \langle X^3 \rangle \langle X \rangle + 6 \langle X^2 \rangle \langle X \rangle^2 - 3 \langle X \rangle^4 \right) - 3 .
\end{aligned}
\tag{1.12}
$$

The expansion works along the lines of those of the variance and skewness. A distribution with a higher peak and wider tails than the normal Gaussian exhibits a positive kurtosis, a lower peak and narrower tails lead to a negative kurtosis.

The moments introduced above describe the distribution of a single observable X. Considering a second observable Y, where each event within an event ensemble has the properties (X_k, Y_k), it is possible to obtain information from the correlation of these two quantities. This can be achieved via the covariance [75]

$$
\begin{aligned}
cov(X, Y) &= \frac{1}{n_{\text{ev}}} \sum_{k=1}^{n_{\text{ev}}} (X_k - \langle X \rangle) \cdot (Y_k - \langle Y \rangle) \\
&= \langle (X - \langle X \rangle) \cdot (Y - \langle Y \rangle) \rangle \\
&= \langle XY \rangle - \langle X \rangle \langle Y \rangle .
\end{aligned}
\tag{1.13}
$$

In the case of a correlation of the observables X and Y, i.e. if an X value above average tends to go along with a Y value above average, the covariance is positive. If X and Y are anti-correlated, i.e. X values above average occur more likely with Y values below average, the covariance is negative. For uncorrelated observables the covariance is zero. As an example, the covariance of the mean transverse momentum per event

$\bar{p}_T$ and the number of charged particles N_{ch} is positive, as the event-ensemble $\langle p_T \rangle$ rises with N_{ch}, see e.g. figure 1.7 in section 1.5.1 and [76].

Another measure of the correlation of two observables with the advantage of being dimensionless is the correlation coefficient [75]

$$\rho = \frac{cov(X,Y)}{\sigma_X \sigma_Y} = \frac{\langle XY \rangle - \langle X \rangle \langle Y \rangle}{\sigma_X \sigma_Y} . \qquad (1.14)$$

Like the covariance, ρ is positive for correlated X and Y, negative if they are anti-correlated, and zero in case they are uncorrelated. Due to its definition, ρ can only yield values between -1 and $+1$. At these limits, the observables X and Y are completely correlated $(+1)$ or anti-correlated (-1), which means, that for a given value of X the value of Y is exactly determined.

1.4.4. Fluctuations of conserved charges

Concerning the conserved charges, it is important to distinguish the sum of the charges from the net charge. Taking the electric charge as an example, the sum corresponds to the number of charged particles N_{ch} and the net electric charge Q denotes the difference between positively and negatively charged particles, i.e.

$$N_{ch} = N_+ + N_- \qquad (1.15)$$

$$Q = N_+ - N_- . \qquad (1.16)$$

The fluctuations of these quantities are described by their variances

$$\langle \delta N_{ch}^2 \rangle = \langle \delta N_+^2 \rangle + \langle \delta N_-^2 \rangle + 2\langle \delta N_+ \delta N_- \rangle \qquad (1.17)$$

$$\langle \delta Q^2 \rangle = \langle \delta N_+^2 \rangle + \langle \delta N_-^2 \rangle - 2\langle \delta N_+ \delta N_- \rangle . \qquad (1.18)$$

If no correlations between positive and negative charges would exist, i.e. $\langle \delta N_+ \delta N_- \rangle = 0$, then these two variances would be identical. The charged particle (or multiplicity) fluctuations are enhanced by such correlations while the net-charge fluctuations are reduced. In literature, the fluctuations of the conserved charges of the baryon number B, electric charge Q and strangeness S are typically identified as the fluctuations of the net charges [77, 78]. The mean, variance, skewness and kurtosis of the net charges can be measured in heavy-ion collision experiments, although event samples with large statistics are needed to determine the higher moments. These results are related to the generalised susceptibilities $\chi_q^{(n)}$ [24, 77, 78], which are defined as the n-th derivatives of the thermodynamic pressure with respect to the chemical potential of the conserved charge q

$$\chi_q^{(n)} = \frac{\partial^n \hat{P}}{\partial \hat{\mu}_q^n} . \qquad (1.19)$$

Here, $\hat{P} = P/T^4$ denotes the reduced pressure and $\hat{\mu}_q = \mu_q/T$ the reduced chemical potential with $q = \{B, Q, S\}$ [78]. The first two derivatives are directly related to the mean M_q and the variance σ_q^2 of the distribution of the net charge n_q [77]

$$M_q = \langle n_q \rangle = VT^3 \chi_q^{(1)} \tag{1.20}$$

$$\sigma_q^2 = \langle \delta n_q^2 \rangle = VT^3 \chi_q^{(2)} \, . \tag{1.21}$$

The third and the fourth order susceptibilities can be expressed in terms of central moments of n_q [77]

$$\langle \delta n_q^3 \rangle = VT^3 \chi_q^{(3)} \tag{1.22}$$

$$\langle \delta n_q^4 \rangle - 3 \langle \delta n_q^2 \rangle^2 = VT^3 \chi_q^{(4)} \, , \tag{1.23}$$

which are related to the skewness S_q and kurtosis κ_q

$$S_q = \frac{\langle \delta n_q^3 \rangle}{\sigma_q^3} = VT^3 \frac{\chi_q^{(3)}}{\sigma_q^3} \tag{1.24}$$

$$\kappa_q = \frac{\langle \delta n_q^4 \rangle}{\sigma_q^4} - 3 = VT^3 \frac{\chi_q^{(4)}}{\sigma_q^4} \, . \tag{1.25}$$

Ratios of susceptibilities from the equations above exhibit the advantage that the factor VT^3 including the volume cancels. These ratios depend only on the temperature and the corresponding chemical potential μ_q and they are defined as [24, 77]

$$\frac{\sigma_q^2}{M_q} = \frac{\chi_q^{(2)}}{\chi_q^{(1)}} \, , \qquad \frac{S_q \sigma_q^3}{M_q} = \frac{\chi_q^{(3)}}{\chi_q^{(1)}} \tag{1.26}$$

$$S_q \sigma_q = \frac{\chi_q^{(3)}}{\chi_q^{(2)}} \, , \qquad \kappa_q \sigma_q^2 = \frac{\chi_q^{(4)}}{\chi_q^{(2)}} \, . \tag{1.27}$$

In addition to the susceptibilities of single net charges and their ratios, it is also possible to study correlations between the fluctuations of different net charges corresponding to mixed derivatives of the pressure with respect to the chemical potentials of the net charges $q, r = \{B, Q, S\}$ [77, 78]

$$\chi_{qr}^{(nm)} = \frac{\partial^{n+m} \hat{P}}{\partial \hat{\mu}_q^n \partial \hat{\mu}_r^m} \, . \tag{1.28}$$

The measurements of net-charge fluctuations and their higher moments together with the relations to the susceptibilities, ratios of susceptibilities and correlations of different net charges are employed to extract freeze-out properties of the medium created in high-energy heavy-ion collisions [24, 77, 78]. Assuming that the multiplicities of particles carrying specific quantum numbers are fixed at the chemical freeze-out, the

extracted parameters, i.e. the temperature and the chemical potential, correspond explicitly to this moment of the evolution. Measuring the fluctuations of different net charges can reveal, if these parameters are identical for all particles, indicating a complete equilibration of the system, or if the different particle species freeze out at different temperatures and thus at different times. In the case that the system has been completely equilibrated and, therefore, lost all memory of the previous evolution, the measured moments of the fluctuations should agree with those predicted by a hadron resonance gas model [77].

1.4.5. Fluctuations of ratios

Observables like the number of charged particles N_{ch} or the sum of the transverse momenta of all charged particles P_T within one event are called "extensive quantities" as they scale with the size of the system. The volume of the system created in a heavy-ion collision depends on the impact parameter, which itself fluctuates from event to event. Therefore, fluctuation measurements of extensive quantities are influenced by volume fluctuations which distort the dynamical fluctuations containing the relevant information about the system. In the ratios of susceptibilities of conserved charges defined in the last section the volume dependence cancels. In addition to these specific ratios, the dependence on the volume is removed in the ratios of any two extensive quantities. Such a ratio is called an "intensive quantity" [70].

In order to construct an intensive quantity and determine its fluctuations, consider an event with N final-state particles and two extensive quantities X and Y

$$X = \sum_{i=1}^{N} x_i, \qquad Y = \sum_{i=1}^{N} y_i. \tag{1.29}$$

The ratio of these two quantities yields

$$R_{X,Y} = \frac{X}{Y}. \tag{1.30}$$

The average and the variance of this ratio are defined as [70]

$$\langle R_{X,Y} \rangle = \frac{\langle X \rangle}{\langle Y \rangle} \tag{1.31}$$

$$\langle \delta R_{X,Y}^2 \rangle = \frac{\langle X \rangle^2}{\langle Y \rangle^2} \left(\frac{\langle \delta X \rangle^2}{\langle X \rangle^2} + \frac{\langle \delta Y \rangle^2}{\langle Y \rangle^2} - 2\frac{\langle \delta X \delta Y \rangle}{\langle X \rangle \langle Y \rangle} \right). \tag{1.32}$$

P_T and N_{ch} represent two extensive quantities. Their ratio corresponds to the mean transverse momentum

$$R_{P_T,N_{ch}} = \langle p_T \rangle = \frac{P_T}{N_{ch}}. \tag{1.33}$$

Hence, $\langle p_T \rangle$ constitutes an intensive quantity, which is well suited for the analysis of event-by-event fluctuations. Fluctuations of $\langle p_T \rangle$ are discussed in more detail in section 1.5.

1. Introduction

Another ratio of two extensive quantities, which can be studied in heavy-ion collisions, is that of the numbers of two different particle species N_1 and N_2 [70]

$$R_{1,2} = \frac{N_1}{N_2} .$$ (1.34)

In this case, the variance defined in equation 1.32 is given by

$$\langle \delta R_{1,2}^2 \rangle = \frac{\langle N_1 \rangle^2}{\langle N_2 \rangle^2} \left(\frac{\langle \delta N_1 \rangle^2}{\langle N_1 \rangle^2} + \frac{\langle \delta N_2 \rangle^2}{\langle N_2 \rangle^2} - 2 \frac{\langle \delta N_1 \delta N_2 \rangle}{\langle N_1 \rangle \langle N_2 \rangle} \right) .$$ (1.35)

The last term in this variance describes the correlations between the two particle species. Such correlations emerge for example from hadronic resonance decays. As this term is negative, it reduces the fluctuations of the particle ratio. In the extreme case that all final-state particles of these two species would originate from the decays of neutral resonances, the corresponding fluctuation of the ratio would vanish [70]. Another important aspect determining the size of the particle ratio fluctuations is the relation between the average numbers of the two species $\langle N_1 \rangle$ and $\langle N_2 \rangle$. If the number of one of the species is much larger than the other one, i.e. $\langle N_1 \rangle \gg \langle N_2 \rangle$, then the fluctuation of the other species dominates because of the factors $1/\langle N_x \rangle^2$. In this case the correlations of the two species have to be large to have any significant influence on the fluctuations of the ratio. The largest contribution from the correlation term can be obtained for equally abundant particle species. An example for such a situation is the ratio of positively over negatively charged particles, i.e. $N_1 = N_+$ and $N_2 = N_-$. The number of charged particles N_{ch} and the net charge Q have been discussed already above. For $\langle Q \rangle \ll \langle N_{ch} \rangle$, the mean numbers of both charges get comparable $\langle N_+ \rangle \approx \langle N_- \rangle \approx \langle N_{ch} \rangle/2$ and the average of the ratio goes to $\langle R_{+,-} \rangle \approx 1$. As discussed in [70], in this case equation 1.35 is reduced to

$$\langle \delta R_{+,-}^2 \rangle = \frac{4}{\langle N_{ch} \rangle^2} \left(\langle \delta N_+^2 \rangle + \langle \delta N_-^2 \rangle - 2 \langle \delta N_+ \delta N_- \rangle \right) ,$$ (1.36)

which, using equation 1.18, can be written as

$$\langle \delta R_{+,-}^2 \rangle = 4 \frac{\langle \delta Q^2 \rangle}{\langle N_{ch} \rangle^2} .$$ (1.37)

From this equation a measure of charge fluctuations per entropy can be obtained by multiplying by $\langle N_{ch} \rangle$, because the entropy $\mathcal{S}$ of the system is proportional to N_{ch}, resulting in [70]

$$D \equiv \langle N_{ch} \rangle \langle \delta R_{+,-}^2 \rangle = 4 \frac{\langle \delta Q^2 \rangle}{\langle N_{ch} \rangle} \propto \frac{\langle \delta Q^2 \rangle}{\mathcal{S}} .$$ (1.38)

For a hadron gas, this quantity is expected to yield $D_{HG} \approx 3$ while in the case of a QGP a lower value of $D_{QGP} \approx 1\text{--}1.5$ is predicted [70]. Thus, this quantity represents an observable for the creation of a Quark-Gluon Plasma. Furthermore, it is related to the quantity ν_{dyn}, which is also applied for the investigation of net-charge fluctuations, via [70]

$$D = 4 + \langle N_{ch} \rangle \nu_{dyn} .$$ (1.39)

1.4.6. Existing measurements of event-by-event fluctuations

This introduction of event-by-event fluctuations is concluded with some examplary measurements of the observables discussed in the previous sections. Several analyses of fluctuations of conserved charges have been carried out by the STAR Collaboration [79–82]. Net-charge fluctuations as well as net-proton fluctuations have been studied using Au–Au collision data from the first Beam Energy Scan (BES) program at RHIC with collision energies ranging from $\sqrt{s_{NN}}$ = 7.7 GeV up to $\sqrt{s_{NN}}$ = 200 GeV. The analysis of the moments of the net-charge distribution [81] is performed within the pseudorapidity acceptance of $|\eta| < 0.5$ and the transverse-momentum range of $0.2\,\mathrm{GeV}/c < p_T < 2.0\,\mathrm{GeV}/c$ with the additional requirement of $p_T > 0.4\,\mathrm{GeV}/c$ for protons[h]. In the left panel of figure 1.5, the following products of moments of the net-charge distribution are presented: σ^2/M, $S\sigma$ and $\kappa\sigma^2$. These products correspond to those defined in equations 1.26 and 1.27, which are related to ratios of susceptibilities. All of these quantities are shown for 0–5% most central collisions and for the 70–80% centrality interval corresponding to peripheral collisions. Furthermore, they are compared to predictions from Poisson distributions and from Negative Binomial Distributions (NBD). Within the uncertainties, no non-monotonic behaviour is observed, which would hint to the freeze-out of a QGP close to the predicted critical point.

Products of moments of the net-proton distribution [80] are shown in the right panel of figure 1.5. This analysis has been carried out at midrapidity within $|y| < 0.5$ and $0.4\,\mathrm{GeV}/c < p_T < 0.8\,\mathrm{GeV}/c$. The same centrality intervals as for the net-charge fluctuations are studied and the results for $S\sigma$ are compared to a Skellam distribution. For central collisions, a hint to a potential non-monotonic behaviour around $\sqrt{s_{NN}}$ = 20 GeV is found, although this is not significant given the large uncertainties of the measurements. Within a later analysis of the same quantities extending the p_T range to $0.4\,\mathrm{GeV}/c < p_T < 2.0\,\mathrm{GeV}/c$, the significance of this non-monotonic behaviour in the most central collisions is enhanced [82].

The ALICE Collaboration has measured net-charge fluctuations [85] and net-proton fluctuations [86] in Pb–Pb collisions at a much higher collision energy of $\sqrt{s_{NN}}$ = 2.76 TeV. The net-charge fluctuations show a decreasing trend with an increasing size of the investigated pseudorapidity window and an indication of a saturation slightly above the largest window size of $\Delta\eta$ = 1.6. For this window size, the measure D introduced in equation 1.38 yields $D = 2.3 \pm 0.02\,\mathrm{(stat.)} \pm 0.21\,\mathrm{(syst.)}$, which is in between the predictions for a hadron gas and a QGP and significantly below STAR measurements [79] of the same quantity at lower collision energies, although these have been carried out within a smaller window of $\Delta\eta$ = 1.0. Net-baryon fluctuations have been studied in ALICE using the number of protons and anti-protons as proxies for baryons and anti-baryons [86]. Deviations of the second moment from a Skellam baseline are observed, which are fully covered by the effect of global baryon-number conserva-

---

[h] The removal of low-p_T protons is necessary to suppress spallation protons created in interactions with the beam pipe. The same criterion is applied to anti-protons to be consistent [81].
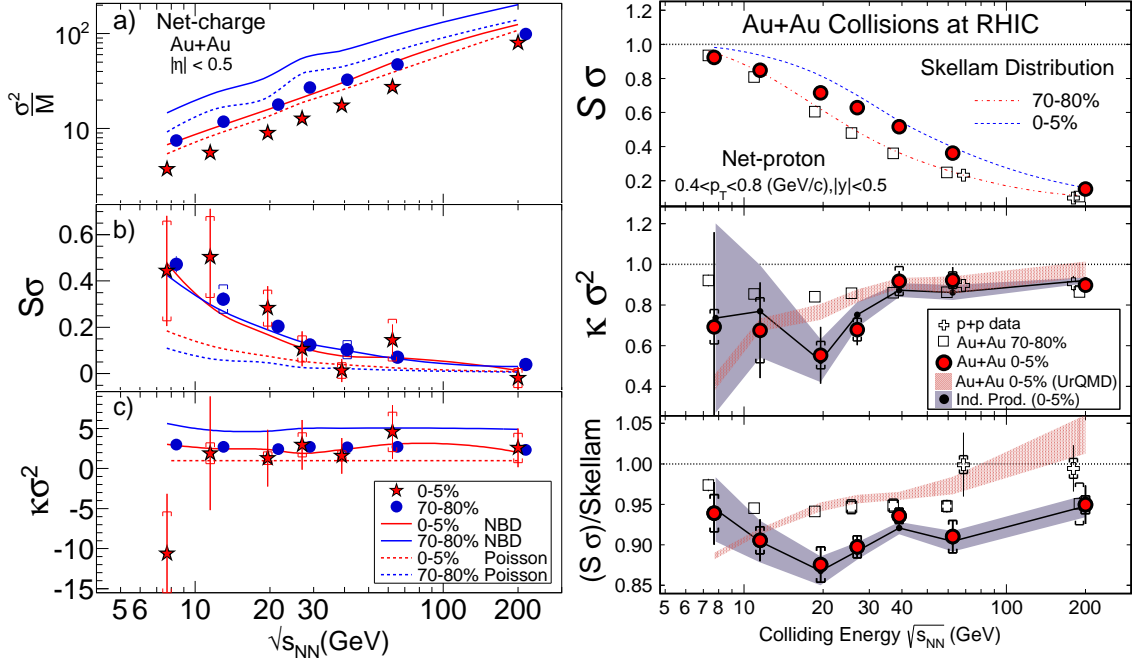
Figure 1.5.: Results for the fluctuations of conserved charges as a function of the collision energy measured with the STAR experiment. Left: Products of moments of the net-charge distribution [81]. Right: Products of moments of the net-proton distribution and comparison to a Skellam expectation [80].

tion. The analysis of higher moments, which may reveal some critical behaviour, is planned [87].

Relative particle-yield fluctuations have been analysed by the ALICE Collaboration in Pb–Pb collisions at $\sqrt{s_{NN}}$ = 2.76 TeV [83]. For the identification of kaons (K), pions (π) and protons (p), the Identity Method[i] is applied. The fluctuations of the particle ratios K/π, p/π, and K/p are studied using the observable ν_{dyn}, which is related to the measure D in equation 1.39. Figure 1.6 shows the results for the 0–5% most central collisions in comparison with STAR measurements from [84] as a function of the collision energy. For all three ratios, the ALICE data consitute a smooth continuation of the trend observed by STAR, but the fluctuations of p/π, and K/p exhibit a sign change from the negative values measured in STAR to positive ones in ALICE, indicating a change in the dynamics of particle production.

---

[i] See the references provided in [83].
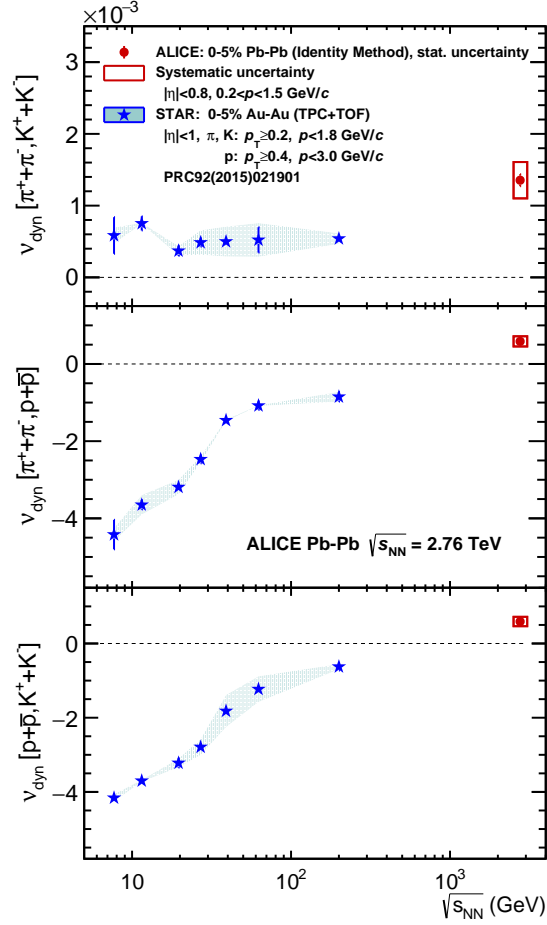
Figure 1.6.: Relative particle yield fluctuations as a function of the collision energy, measured by ALICE [83] and STAR [84].

1.5. Fluctuations of the mean transverse momentum

Event-by-event fluctuations of different quantities are analysed in heavy-ion collisions with the aim to obtain information about the phase diagram of strongly interacting matter and especially about the properties of the phase transition from a hadron gas to a QGP [25, 26, 70, 71, 77, 78, 88, 89]. As introduced above, at low baryo-chemical potential μ_B and high temperature, this phase transition is most likely a crossover [23, 24]. At higher μ_B, a first-order phase transition is expected, which would imply the existence of a second-order critical point at the end of the first order transition line [25, 26]. Another question which can be addressed with event-by-event fluctuation studies is that of the relevant degrees of freedom within the initial collisions of the heavy ions as well as in smaller collision systems [73, 74].

Measurements of fluctuations of the mean transverse momentum $\langle p_\mathrm{T} \rangle$ can contribute to address both of these quests. While they are established in the study of the phase diagram including the search of the critical point [26, 70, 89], their application in the investigation of the relevant degrees of freedom in nuclear and hadronic collisions is a more recent developement [73, 74]. In this work, data from ALICE at the CERN LHC are analysed considering pp, p–Pb and Pb–Pb collisions. The latter are studied at an energy per nucleon–nucleon collision of $\sqrt{s_\mathrm{NN}} = 2.76\,\mathrm{TeV}$ corresponding to an almost vanishing μ_B. In this regime, the relevant degrees of freedom of the initial collisions are investigated. The potential critical point is expected at much higher μ_B corresponding to lower collision energies [24, 25].

The mean transverse momentum constitutes a ratio of two extensive quantities, the sum of the transverse momenta and the number of charged particles, see section 1.4.5 and especially equation 1.33. Hence, $\langle p_\mathrm{T} \rangle$ is an intensive quantity with the advantage, that it does not depend on the volume of the system [70]. Other trivial fluctuations, especially statistical fluctuations, have to be separated from the dynamical ones to obtain meaningful results for the dynamical $\langle p_\mathrm{T} \rangle$ fluctuations. In addition, effects of the measurements, like the efficiency and acceptance of the experiment, have to be taken into account.

1.5.1. Mean transverse momentum

Average quantities like the mean transverse momentum have to be defined carefully. The average of an observable within one event is different from the average over an event sample. In the latter case, the mean of the event averages can be different from the average over all particles within all events. Furthermore, measured quantities are in general not identical to the true values. Detectors have a limited reconstruction efficiency, the measurement can be contaminated by secondary particles not originating from the primary interaction vertex and observables like the transverse momentum are smeared due to the detector resolution. Therefore, the raw measured observables have to be distinguished from their true values. In experimental data, the latter can only be estimated using correction methods often based on Monte Carlo (MC) event generators, where true values correspond to the generated ones and raw values can be obtained by simulating the detector response. In this way, true and raw values can be compared directly in MC simulations. The notations of the different averages used in this work are summarised in table 1.1.

The true average transverse momentum of all primary charged particles generated in event k is definded as

$$\bar{p}_{\mathrm{T},k} = \frac{1}{N_{\mathrm{ch},k}} \sum_{i=1}^{N_{\mathrm{ch},k}} p_{\mathrm{T},i} \, . \tag{1.40}$$

Here, $N_{\mathrm{ch},k}$ denotes the total number of charged particles in event k and the $p_{\mathrm{T},i}$ represent their corresponding transverse momenta. The true average of all event mean transverse momenta $\langle \bar{p}_{\mathrm{T},k} \rangle$ is obtained by calculating the average of the single event

Notation	Meaning
$\langle x \rangle$	True event-sample average
$\bar{x}$	True average in one event
$M(x)$	Raw event-sample average
$M_{\mathrm{EbE}}(x)$	Raw average in one event

Table 1.1.: True quantities correspond to the MC generator level or to fully corrected data values. Raw quantities represent experimental values not corrected for detector effects or full MC simulations including the detector response.

$\bar{p}_{\mathrm{T},k}$, not taking into account that the single events may have different numbers of charged particles. It is defined as

$$\langle \bar{p}_{\mathrm{T},k} \rangle = \frac{1}{n_{\mathrm{ev}}} \sum_{k=1}^{n_{\mathrm{ev}}} \bar{p}_{\mathrm{T},k} \,, \tag{1.41}$$

where n_{ev} denotes the total number of events in the given event sample. In general, the quantity $\langle \bar{p}_{\mathrm{T},k} \rangle$ is not identical to the average of the transverse momenta of all charged particles in all events

$$\langle p_{\mathrm{T}} \rangle = \frac{1}{\sum_{k=1}^{n_{\mathrm{ev}}} N_{\mathrm{ch},k}} \sum_{k=1}^{n_{\mathrm{ev}}} \sum_{i=1}^{N_{\mathrm{ch},k}} p_{\mathrm{T},i} \neq \langle \bar{p}_{\mathrm{T},k} \rangle \,. \tag{1.42}$$

This average transverse momentum can also be calculated for a subset of events, e.g. for an interval m of the charged-particle multiplicity

$$\langle p_{\mathrm{T}} \rangle_m = \frac{1}{\sum_{k=1}^{n_{\mathrm{ev},m}} N_{\mathrm{ch},k}} \sum_{k=1}^{n_{\mathrm{ev},m}} \sum_{i=1}^{N_{\mathrm{ch},k}} p_{\mathrm{T},i} \,. \tag{1.43}$$

In the case of narrow intervals m, where all events within one interval have exactly the same multiplicity $N_{\mathrm{ch},k}$, the two event averages are identical, i.e. $\langle \bar{p}_{\mathrm{T},k} \rangle_m = \langle p_{\mathrm{T}} \rangle_m$. In MC simulations, the true $\langle p_{\mathrm{T}} \rangle_m$ can be obtained from the MC generator level.

As described above, the raw measurement of the mean transverse momentum in an experiment is in general not identical to its true value. In the case of a sufficiently large event sample, the average transverse momentum can be corrected on a statistical basis to obtain the true $\langle p_{\mathrm{T}} \rangle$ for experimental data. ALICE has published $\langle p_{\mathrm{T}} \rangle$ as a function of N_{ch} in the kinematic range $0.15\,\mathrm{GeV}/c < p_{\mathrm{T}} < 10\,\mathrm{GeV}/c$ and $|\eta| < 0.3$ in [76]. These results are presented in figure 1.7 for different collision energies in pp collisions (left panel) and as a comparison of pp, p–Pb and Pb–Pb collisions (right panel).

This approach is not feasible for single events in an event-by-event analysis. Therefore, the raw measured mean value $M_{\mathrm{EbE}}(p_{\mathrm{T}})_k$ of the transverse momenta $p_{\mathrm{T},i}$ of the $N_{\mathrm{acc},k}$ accepted charged particles has to be used as approximation, which for an event k leads to

$$M_{\mathrm{EbE}}(p_{\mathrm{T}})_k = \frac{1}{N_{\mathrm{acc},k}} \sum_{i=1}^{N_{\mathrm{acc},k}} p_{\mathrm{T},i} \,. \tag{1.44}$$
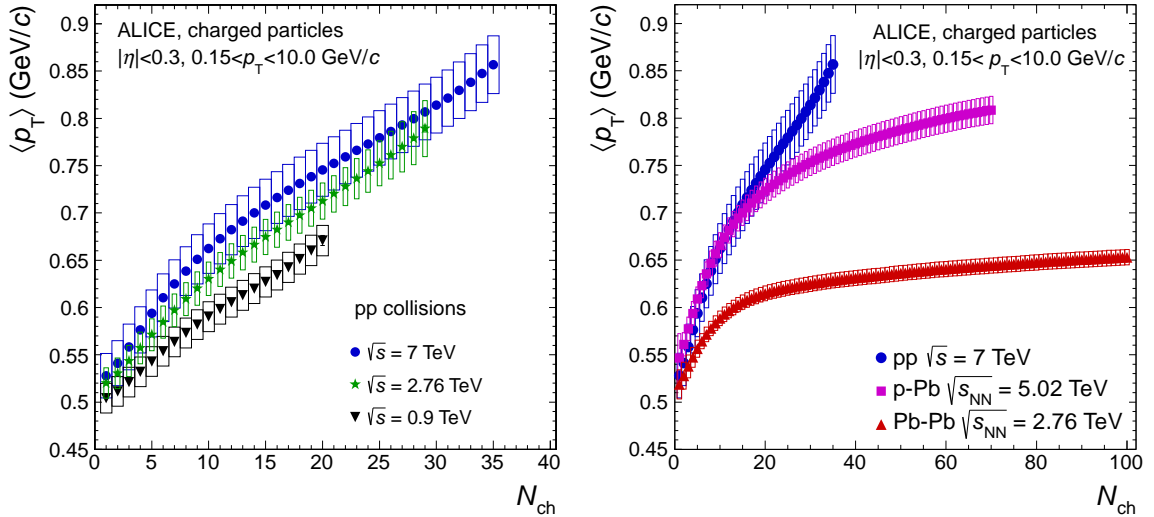
Figure 1.7.: $\langle p_{\mathrm{T}} \rangle$ as a function of N_{ch} measured by ALICE [76]. Left: pp collisions at $\sqrt{s} = 0.9$, 2.76 and 7 TeV. Right: Comparison of pp, p–Pb and Pb–Pb collisions.

In analogy to the true $\langle p_{\mathrm{T}} \rangle_m$, the raw quantity $M(p_{\mathrm{T}})_m$ can be calculated for a given subset of events corresponding for example to an interval of the accepted charged-particle multiplicity N_{acc} and being defined as

$$M(p_{\mathrm{T}})_m = \frac{1}{\sum_{k=1}^{n_{\mathrm{ev},m}} N_{\mathrm{acc},k}} \sum_{k=1}^{n_{\mathrm{ev},m}} \sum_{i=1}^{N_{\mathrm{acc},k}} p_{\mathrm{T},i} = \frac{1}{\sum_{k=1}^{n_{\mathrm{ev},m}} N_{\mathrm{acc},k}} \sum_{k=1}^{n_{\mathrm{ev},m}} N_{\mathrm{acc},k} \cdot M_{\mathrm{EbE}}(p_{\mathrm{T}})_k . \quad (1.45)$$

The relation of $M(p_{\mathrm{T}})_m$ to the single-event $M_{\mathrm{EbE}}(p_{\mathrm{T}})_k$ illustrates that the event-sample average $M(p_{\mathrm{T}})_m$ is identical to the mean of the event averages $M(M_{\mathrm{EbE}}(p_{\mathrm{T}})_k)_m$ for a subset of events with exactly the same number of accepted particles $N_{\mathrm{acc},k}$ and can be different otherwise.

1.5.2. Event-by-event distributions of the mean transverse momentum

As discussed above, the mean transverse momentum fluctuates from one event to the other. The measured distribution of the mean transverse momenta per event $M_{\mathrm{EbE}}(p_{\mathrm{T}})_k$ contains all contributions to these fluctuations, i.e. statistical and volume fluctuations, fluctuations due to the experimental measurements, and the dynamical fluctuations containing the relevant information about the underlying physical processes.

Such an event-by-event distribution of $M_{\mathrm{EbE}}(p_{\mathrm{T}})_k$ has been measured at NA49, a fixed-target experiment at the CERN SPS, in central Pb–Pb collisions at a beam energy of $158 \, \mathrm{AGeV}/c$ corresponding to a centre-of-mass nucleon–nucleon collision energy of $\sqrt{s_{\mathrm{NN}}} = 17.3 \, \mathrm{GeV}$ [90]. The result is obtained at forward rapidity within $4 < y <$
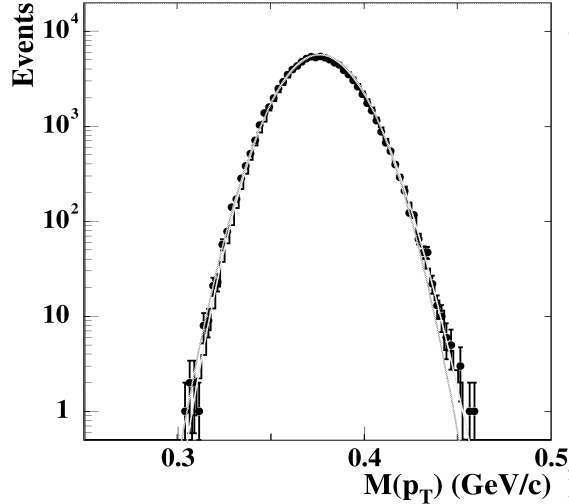
Figure 1.8.: Event-by-event distribution of the raw mean transverse momentum com-
pared to a mixed-event distribution (histogram), a Gaussian (darker
line) and a Gamma distribution (brighter line) [91]. The data points
are measured by NA49 in central Pb–Pb collisions at a beam energy of
$158\,\mathrm{AGeV}/c$ [90].

5.5 and for a transverse-momentum range of $0.005\,\mathrm{GeV}/c < p_\mathrm{T} < 1.5\,\mathrm{GeV}/c$. It is
shown in figure 1.8 together with a mixed-event distribution and some calculations
from [91]. The mixed-event distribution is obtained by randomly combining particles
from different events considering only one particle per real event. In this way, the
non-statistical fluctuations like dynamical fluctuations originating from correlations of
particles or fluctuations of the volume from one event to the other are removed.

In the NA49 measurement, the mean transverse momentum of all charged particles
within the analysed event sample yields $M(p_\mathrm{T}) = (376.75 \pm 0.06)\,\mathrm{MeV}/c$, the uncer-
tainty being statistical only. The standard deviation relative to $M(p_\mathrm{T})$ amounts to
$\sigma(M(p_\mathrm{T}))/M(p_\mathrm{T}) = (4.65 \pm 0.01)\%$ and that of the mixed events yields 4.6% [90].
This comparison indicates, that the mixed-event distribution describes the measured
distribution well, which can also be seen in figure 1.8. Hence, the statistical fluctu-
ations constitute the dominant contribution to the overall fluctuations, leaving only
little room for non-statistical fluctuations. Furthermore, the measured distribution
is in good agreement with a Gaussian (darker line in figure 1.8), except of the tails,
where the Gaussian is slightly narrower than the measurement. The full distribution
including the tails is better described by a Gamma distribution (brighter line), which
has been shown in [91]. There, a standard deviation of $\sigma(M(p_\mathrm{T}))/M(p_\mathrm{T}) = 4.56\%$
is obtained for the case of purely statistical fluctuations, which is close to the value
measured by NA49, but still allows for small non-statistical fluctuations. These are
estimated by NA49 using the observable Φ_{p_T}. Due to its large statistical uncertainty,
the result $\Phi_{p_\mathrm{T}} = (0.6 \pm 1.0)\,\mathrm{MeV}/c$ cannot clarify the existence of dynamical fluctua-
tions [90].

The STAR Collaboration has measured event-by-event distributions of the mean transverse momentum in central Au–Au collisions at $\sqrt{s_{\mathrm{NN}}} = 20, 62, 130$ and $200\,\mathrm{GeV}$ [92]. In contrast to NA49, the acceptance is located around midrapidity within $|\eta| < 1.0$, while the p_{T} range of $0.15\,\mathrm{GeV}/c \leq p_{\mathrm{T}} \leq 2\,\mathrm{GeV}/c$ is comparable. The measured distributions are compared to mixed-event and Gamma distributions. The mixed-event distributions are significantly narrower than the measured ones, indicating the presence of dynamical fluctuations [92]. These have been studied further using the two-particle transverse-momentum correlator discussed in the next section.

1.5.3. Two-particle transverse-momentum correlator

In this work, the event-by-event fluctuations of the mean transverse momentum are quantified using the two-particle transverse-momentum correlator $C = \langle \Delta p_{\mathrm{T},i}, \Delta p_{\mathrm{T},j} \rangle$, which is a measure of the dynamical component of these fluctuations [69, 88, 92, 93]. Within each event, for each particle pair $(i \neq j)$ the product of the momentum differences between the transverse momenta $p_{\mathrm{T},i}$ and $p_{\mathrm{T},j}$ and the inclusive average transverse momentum $\langle p_{\mathrm{T}} \rangle$ of all particles within the event sample is calculated. The sum of these products yields the event quantity

$$c_k = \sum_{i=1}^{N_{\mathrm{ch},k}} \sum_{j=i+1}^{N_{\mathrm{ch},k}} \left(p_{\mathrm{T},i} - \langle p_{\mathrm{T}} \rangle \right) \cdot \left(p_{\mathrm{T},j} - \langle p_{\mathrm{T}} \rangle \right). \tag{1.46}$$

As before, $N_{\mathrm{ch},k}$ is the true number of charged particles in the event k. The number of terms in c_k increases almost quadratically with the multiplicity, but there is no trivial dependence of c_k itself on the multiplicity. In this respect, it is important to note that the product of two momentum differences can be positive or negative and hence, c_k can be positive or negative as well, independent of $N_{\mathrm{ch},k}$. In order to obtain an event-average quantity, c_k is normalised to the number of particle pairs in the event

$$N_{\mathrm{ch},k}^{\mathrm{pairs}} = 0.5 \cdot N_{\mathrm{ch},k} \cdot \left(N_{\mathrm{ch},k} - 1 \right), \tag{1.47}$$

resulting in the two-particle transverse-momentum correlator in one event

$$C_k = \frac{c_k}{N_{\mathrm{ch},k}^{\mathrm{pairs}}} = \frac{1}{N_{\mathrm{ch},k}^{\mathrm{pairs}}} \sum_{i=1}^{N_{\mathrm{ch},k}} \sum_{j=i+1}^{N_{\mathrm{ch},k}} \left(p_{\mathrm{T},i} - \langle p_{\mathrm{T}} \rangle \right) \cdot \left(p_{\mathrm{T},j} - \langle p_{\mathrm{T}} \rangle \right). \tag{1.48}$$

Considering an ensemble of n_{ev} events instead of a single event, the inclusive two-particle transverse-momentum correlator C is obtained by calculating the average of all particle pairs in all events. Note, that this is not identical to the average C_k of all events, as the events may have different multiplicities and hence different $N_{\mathrm{ch},k}^{\mathrm{pairs}}$. In literature, C is often denoted by $\langle \Delta p_{\mathrm{T},i}, \Delta p_{\mathrm{T},j} \rangle$ [69, 92, 93] and it is defined as

$$C = \langle \Delta p_{\mathrm{T},i}, \Delta p_{\mathrm{T},j} \rangle = \frac{1}{\sum_{k=1}^{n_{\mathrm{ev}}} N_{\mathrm{ch},k}^{\mathrm{pairs}}} \sum_{k=1}^{n_{\mathrm{ev}}} \sum_{i=1}^{N_{\mathrm{ch},k}} \sum_{j=i+1}^{N_{\mathrm{ch},k}} \left(p_{\mathrm{T},i} - \langle p_{\mathrm{T}} \rangle \right) \cdot \left(p_{\mathrm{T},j} - \langle p_{\mathrm{T}} \rangle \right)$$

$$= \frac{1}{\sum_{k=1}^{n_{\mathrm{ev}}} N_{\mathrm{ch},k}^{\mathrm{pairs}}} \sum_{k=1}^{n_{\mathrm{ev}}} c_k. \tag{1.49}$$

The structure of C resembles that of the covariance introduced in equation 1.13, although C is not a covariance, as it does not correlate two different quantities, but entities of the same quantity, i.e. the transverse momentum p_T. However, due to its structure, the two-particle correlator does share some general properties of the covariance.

The contribution of a single particle pair $(p_{T,i}, p_{T,j})$ to the two-particle correlator C_k of the corresponding event is positive, if both $p_{T,i}$ and $p_{T,j}$ are below or above $\langle p_T \rangle$, and it is negative, if one of the transverse momenta is below and the other one above the average. In the case of completely uncorrelated transverse momenta, the positive and negative contributions to the C_k of the events tend to cancel and the correlator C of the event ensemble goes to zero. Note, that due to the limited number of particles per event, the single-event correlators C_k have still non-zero values, which reflect the statistical event-by-event fluctuations of the mean transverse momentum $\bar{p}_T$. If the transverse momenta in one event yield in a correlated way values above or below the event-ensemble $\langle p_T \rangle$, then also the $\bar{p}_T$ in this event is higher or lower than the sample $\langle p_T \rangle$ with this deviation being larger than expected from a purely statistical fluctuation. In this case, most of the particle pairs add a positive contribution to C_k. If p_T correlations are present in many (or even all) of the events within the event sample, then the inclusive correlator C has to be positive, like the covariance, which is positive in case of correlations of the two observables under consideration.

In the opposite case of an anit-correlation of two observables the covariance gets negative. The absolute value of the negative covariance is increasing for a larger degree of anti-correlation. This situation is different for the two-particle correlator. In an event with a lot of anti-correlated particle pairs, i.e. pairs with one p_T above and one p_T below $\langle p_T \rangle$ yielding a negative contribution to C_k, there exist also particle pairs with both p_T being above or below $\langle p_T \rangle$ adding a positive contribution to C_k. The C_k of the event can be negative, but a complete anti-correlation leading to large negative values cannot be reached[j].

In conclusion, for an ensemble of events, the two-particle correlator C goes to zero in case of purely statistical fluctuations of the mean transverse momentum $\bar{p}_T$ from one event to the other and gets positive in case of correlated transverse momenta leading to dynamical fluctuations of $\bar{p}_T$ beyond the statistical ones. Anti-correlations in p_T reduce the fluctuations of $\bar{p}_T$ and C can become negative, but the negative magnitude is restricted. The behaviour of vanishing C for uncorrelated transverse momenta is confirmed with some simple simulations, which are described in section 3.9.

Both the numerator and the denominator of the two-particle transverse momentum correlator C are proportional to the square of the particle detection efficiency and hence, C is robust against efficiency losses. However, this is only valid in case of a p_T-independent detection efficiency. As in ALICE the efficiency does depend on p_T, the cancellation of efficiencies does not hold entirely. The correlator C contains products of

---

[j] There is an exception, which is the case of exactly two particles, one with p_T above and one with p_T below $\langle p_T \rangle$. However, in this case only one term is present in the calculation of C_k, which also restricts its magnitude.

transverse momenta and hence depends on the squares of the p_{T}-dependent efficiency. Taking the square root of C, this dependence gets comparable to that on the mean transverse momentum $\langle p_{\mathrm{T}} \rangle$. Therefore, the quantity $\sqrt{C}/\langle p_{\mathrm{T}} \rangle$ is introduced, which further reduces the dependence on the detection efficiency also in the p_{T}-dependent case. $\sqrt{C}/\langle p_{\mathrm{T}} \rangle$ yields the dynamical mean transverse-momentum fluctuations relative to $\langle p_{\mathrm{T}} \rangle$.

Although $\sqrt{C}/\langle p_{\mathrm{T}} \rangle$ is a robust quantity, it is not fully independent of detector effects. The detection efficiency may vary from event to event and also other effects like secondary contamination and p_{T} resolution play an important role. Therefore, $\sqrt{C}/\langle p_{\mathrm{T}} \rangle$ cannot be measured in the experiment directly. It has to be approximated by the corresponding raw quantity, where the true $\langle p_{\mathrm{T}} \rangle$ is replaced by the measured $M(p_{\mathrm{T}})$, the true $N_{\mathrm{ch},k}$ in event k is substituted by the raw $N_{\mathrm{acc},k}$ and the true $N_{\mathrm{ch},k}^{\mathrm{pairs}}$ by $N_{\mathrm{acc},k}^{\mathrm{pairs}}$. The latter is calculated by exchanging $N_{\mathrm{ch},k}$ with $N_{\mathrm{acc},k}$ in equation 1.47. In conclusion, the measured two-particle correlator is defined for a single event

$$C_k = \frac{1}{N_{\mathrm{acc},k}^{\mathrm{pairs}}} \sum_{i=1}^{N_{\mathrm{acc},k}} \sum_{j=i+1}^{N_{\mathrm{acc},k}} (p_{\mathrm{T},i} - M(p_{\mathrm{T}})) \cdot (p_{\mathrm{T},j} - M(p_{\mathrm{T}})) \tag{1.50}$$

and for an event ensemble

$$C = \frac{1}{\sum_{k=1}^{n_{\mathrm{ev}}} N_{\mathrm{acc},k}^{\mathrm{pairs}}} \sum_{k=1}^{n_{\mathrm{ev}}} \sum_{i=1}^{N_{\mathrm{acc},k}} \sum_{j=i+1}^{N_{\mathrm{acc},k}} (p_{\mathrm{T},i} - M(p_{\mathrm{T}})) \cdot (p_{\mathrm{T},j} - M(p_{\mathrm{T}})). \tag{1.51}$$

The observable C is defined for a complete event sample, where also $M(p_{\mathrm{T}})$ is determined from all tracks of all events in that sample. Such an event sample can be separated into subsamples, e.g. by dividing the events in multiplicity classes. These subsamples are denoted by the subscript m. In these cases, also $M(p_{\mathrm{T}})_m$ is calculated separately for each subsample, leading to

$$C_m = \frac{1}{\sum_{k=1}^{n_{\mathrm{ev},m}} N_{\mathrm{acc},k}^{\mathrm{pairs}}} \sum_{k=1}^{n_{\mathrm{ev},m}} \sum_{i=1}^{N_{\mathrm{acc},k}} \sum_{j=i+1}^{N_{\mathrm{acc},k}} (p_{\mathrm{T},i} - M(p_{\mathrm{T}})_m) \cdot (p_{\mathrm{T},j} - M(p_{\mathrm{T}})_m). \tag{1.52}$$

Finally, the square root of this version of the two-particle transverse-momentum correlator is divided by the measured $M(p_{\mathrm{T}})_m$. The result is the quantity $\sqrt{C_m}/M(p_{\mathrm{T}})_m$, which yields the measured dynamical mean transverse-momentum fluctuations relative to the measured mean transverse momentum. $\sqrt{C_m}/M(p_{\mathrm{T}})_m$ as a function of the average charged-particle multiplicity density $\langle \mathrm{d}N_{\mathrm{ch}}/\mathrm{d}\eta \rangle$ is the main observable analysed in this work.

1.5.4. Measurements of transverse-momentum fluctuations

Mean p_{T} fluctuations have first been measured at ISR [94] in pp, pα and $\alpha\alpha$ collisions. For this study, a different method as described above has been employed. Within this method [94], the dispersion

$$D(\bar{p}_{\mathrm{T}}) = \left(\langle \bar{p}_{\mathrm{T}}^2 \rangle - \langle \bar{p}_{\mathrm{T}} \rangle^2 \right)^{1/2} \tag{1.53}$$

is calculated. It is assumed, that the statistical contribution to the square of the dispersion $D^2(\bar{p}_T)$ is decreasing with $1/n$, where n denotes the number of produced particles. Assuming that the non-statistical contribution is independent of the multiplicity, the squared dispersion normalised to $\langle \bar{p}_T \rangle$ can be written in the form

$$\left[D_n(\bar{p}_T)/\langle \bar{p}_T \rangle \right]^2 = A + B/n \,. \tag{1.54}$$

Within this approach, the size of the non-statistical fluctuations can be obtained in the limit of $n \to \infty$, yielding [94]

$$R = \sqrt{A} = \left[D(\bar{p}_T)/\langle \bar{p}_T \rangle \right]_{n \to \infty} \,. \tag{1.55}$$

First results in heavy-ion collisions were obtained by NA49 at the CERN SPS [90] and later in [95, 96]. As well at the SPS, the CERES Collaboration has measured $\langle p_T \rangle$ fluctuations in Pb–Au collisions and at several collision energies [93, 97–99]. At RHIC, both PHENIX [100, 101] and STAR [92, 102, 103] have measured $\langle p_T \rangle$ fluctuations. The NA61/SHINE experiment is still taking data at the SPS and measures fluctuations in multiple collision systems [104–106]. Mean p_T fluctuations in proton–antiproton collisions have been measured by CDF [107]. Some of these studies employ different observables to quanitfy the mean p_T fluctuations, for example Φ_{p_T} (see section 1.5.2). Definitions of these quantities and their relations among each other can be found in [108].

The measurements in this work are compared to several of the results obtained by other experiments in chapter 5. In addition to the work presented within this thesis and in [1–5], ALICE has published further analyses employing the two-particle transverse-momentum differential correlations in [109, 110].

2. The experiment: ALICE

This work is based on data measured with ALICE (A Large Ion Collider Experiment) [34, 35] located at the Large Hadron Collider (LHC) [33] at CERN. Following a short introduction of CERN, the LHC and the full accelerator chain, the main part of this chapter describes the ALICE detector systems with a focus on the detectors required for the present analysis and a special emphasis on the Time Projection Chamber (TPC) [111]. Finally, the data taking and reconstruction procedures [112] are outlined.

2.1. CERN and the Large Hadron Collider

The European Organization of Nuclear Research is a huge scientific research centre located at the Franco-Swiss border near Geneva. Originally it has been called "Conseil Européen pour la Recherche Nucléaire" (European Council for Nuclear Research), where the acronym CERN is derived from [113]. The central part of CERN consists of a large accelerator complex [33, 114, 115], which is sketched in figure 2.1. First, the particles are emitted by ion sources and initially accelerated by a LINear ACcelerator (LINAC). Protons are obtained by removing the electron from hydrogen atoms. They are accelerated in LINAC 2 up to an energy per proton of $50\,\mathrm{MeV}$ and further up to $1.4\,\mathrm{GeV}$ in a first small circular accelerator, the Proton Synchrotron Booster (PSB, "BOOSTER" in figure 2.1). In the lead (Pb) ion source, a highly purified lead sample is heated up to $800\,°\mathrm{C}$. In this way, a vapour of lead atoms is generated, which is ionised by an electron current, leading to a variety of lead-ion charge states with a maximum around Pb^{29+}. With the help of a charge separator these ions are selected and accelerated in LINAC 3 to an energy per nucleon of $4.2\,\mathrm{MeV}/u$. Next, a carbon foil is used to strip additional electrons from the lead ions. The resulting Pb^{54+} is accelerated in the Low Energy Ion Ring (LEIR) up to $72\,\mathrm{MeV}/u$.

Afterwards, both protons and heavier ions are accelerated in the Proton Synchrotron (PS), reaching $25\,\mathrm{GeV}$ in the case of protons and $5.9\,\mathrm{GeV}/u$ in the case of Pb^{54+}. The latter is send through a second foil to remove all remaining electrons and obtain fully stripped Pb^{82+}. Via the transfer line TT2, the particle beams are carried to the Super Proton Synchrotron (SPS), which accelerates protons up to $450\,\mathrm{GeV}$ and lead ions up to $177\,\mathrm{GeV}/u$. From the SPS, the beams are injected into both LHC rings via the transfer lines TI2 and TI8.

With a circumference of about $27\,\mathrm{km}$, the LHC currently is the largest particle accelerator on earth. The highest energies reached up to now are $6.5\,\mathrm{TeV}$ per beam for protons and $2.56\,\mathrm{TeV}/u$ for lead ions [115]. Hence, the maximum centre-of-mass en-
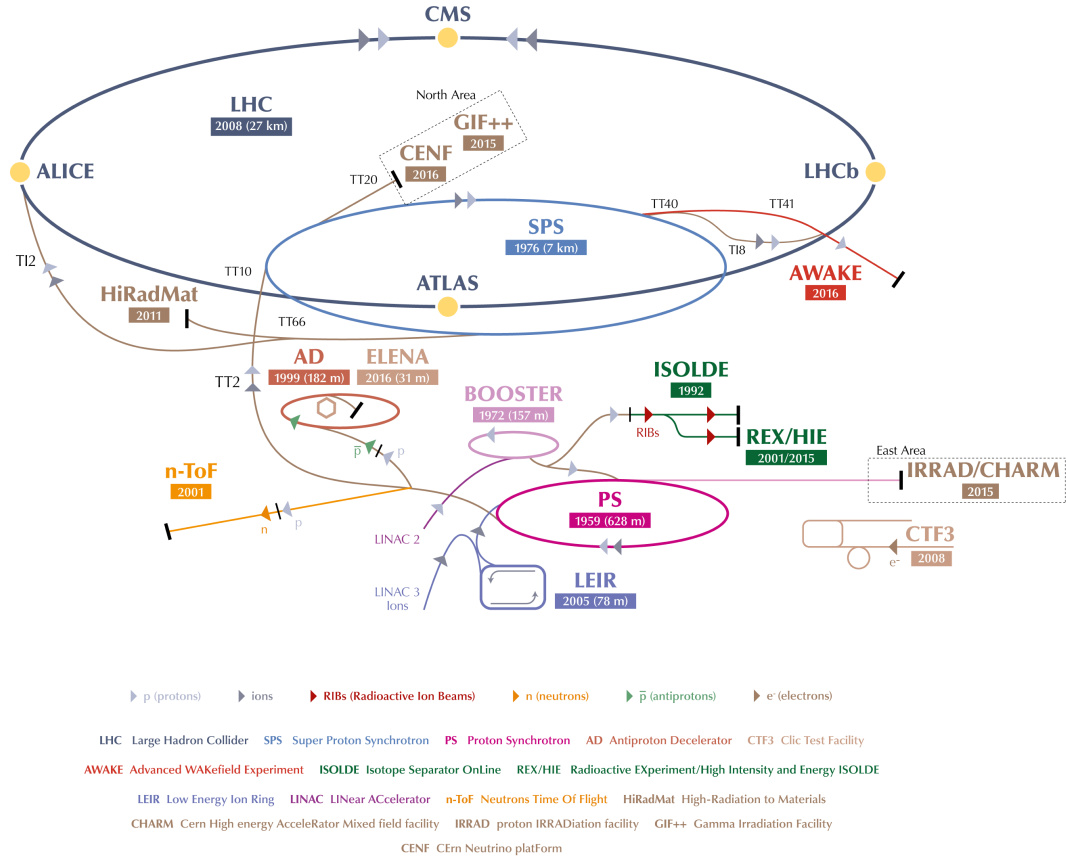
Figure 2.1.: CERN accelerator complex [114].

ergy achieved so far in proton–proton (pp) collisions is $\sqrt{s}$ = 13 TeV and the maximum energy per nucleon-nucleon collision achieved in Pb–Pb collisions is $\sqrt{s_{NN}}$ = 5.02 TeV. Lead consists of 82 protons and – for the nuclide used here – 126 neutrons, resulting in 208 nucleons in total. If all nucleons in both colliding lead ions participate in the collision, a total amount of energy of $208 \cdot 5.02$ TeV = 1044 TeV is released in a single Pb–Pb collision. The maximum energy reachable with the LHC is slightly higher than the one achieved so far. The design values correspond to $\sqrt{s}$ = 14 TeV in pp and $\sqrt{s_{NN}}$ = 5.52 TeV in Pb–Pb collisions, the latter corresponding to a maximum centre-of-mass energy in one Pb–Pb collision of 1148 TeV [33].

The LHC has been built in the tunnel constructed for the former Large Electron-Positron (LEP) collider [33]. This tunnel has a length of 26 659 m and is located between 45 m and 170 m underground. As the LHC is a particle-particle collider (and not a particle-antiparticle collider like LEP), two rings are needed to circulate two counter-rotating beams. With an internal diameter of only 3.7 m, the space inside the tunnel is limited, which would have severely complicated the installation of two separate accelerator rings. Therefore, a twin-bore magnet design has been implemented,

where both rings are located within the same tube. The main drawback of this solution is the magnetic coupling of the two rings, which is especially important in the case of asymmetric collision systems like p–Pb, where the energy of the two beams cannot be adjusted such that the centre-of-mass system is at rest in the laboratory frame.

The main components of the LHC are the 1232 dipole magnets needed to keep the particle beams on a circulating orbit [33,115]. Each of these superconducting magnets is 15 m long and has a peak magnetic flux density of 8.33 T. The magnets are operated at a very low temperature of 1.9 K and inside the beam pipes, an ultrahigh vacuum of 10^{-13} atm is reached. Under these conditions, up to 2808 bunches of particles with a bunch spacing of 25 ns can be circulated in each of the two rings.

An important measure to quantify the intensity of the beams is the instantaneous luminosity $\mathcal{L}$, which is defined as [17]

$$\mathcal{L} = \frac{N_1 N_2 f_{\text{coll}}}{4\pi\sigma_x\sigma_y} \ . \tag{2.1}$$

Here, N_1 and N_2 denote the number of particles per bunch in beam 1 and beam 2, f_{coll} is the frequency of the collisions and σ_x and σ_y describe the effective beam widths in the transverse (i.e. x and y) directions. The nominal value of $N_1 = N_2 = 1.15 \cdot 10^{11}$ protons per bunch (ppb) results in a design peak luminosity of $1.0 \cdot 10^{34}$ cm^{-2} s^{-1}. In the Pb–Pb running mode, the nominal peak luminosity corresponds to $1.0 \cdot 10^{27}$ cm^{-2} s^{-1} [33].

In the pp campaign of 2016, the nominal peak luminosity was reached for the first time and later exceeded by about 40%, reaching a maximum of $1.4 \cdot 10^{34}$ cm^{-2} s^{-1} [116]. The beam parameters in these LHC fills were 2220 bunches per LHC ring with 25 ns bunch spacing and $1.1 \cdot 10^{11}$ ppb. In Pb–Pb collisions, the highest luminosity to date was reached in the last fill of the 2015 Pb–Pb run with $3.6 \cdot 10^{27}$ cm^{-2} s^{-1}, which is a factor of 3.6 higher than the design value [117]. Note, that the luminosity in ALICE was levelled at the design luminosity in this running period. Originally, the LHC had not been designed to deliver p–Pb collisions in addition to the symmetric systems. To accommodate the great interest in these kind of collisions, reviewed in detail in [118], p–Pb collisions were integrated in the LHC programme. A pilot run in 2012 proved the feasibility and delivered first collisions to the experiments [119], followed by a first dedicated running period in early 2013 [120]. Within the second p–Pb collision run in 2016, a peak luminosity of $8.9 \cdot 10^{29}$ cm^{-2} s^{-1} was reached [121], which is about a factor of 6 higher than the value of $1.5 \cdot 10^{29}$ cm^{-2} s^{-1} estimated in [118]. With xenon (Xe), a different heavy ion than lead was tested in a short pilot run of Xe–Xe collisions in 2017 [122].

Following the original LEP design with eight arcs interspersed with eight straight sections, also the LHC is divided into eight sections, each of which is equipped with its own access shafts. Four of these access points are located above huge caverns housing the large experiments built around the four interaction points, where the collisions of the particle beams take place. ALICE [35] is one of these four major experiments. It is located at the access point 2 of the LHC, close to one of the beam injectors from the SPS (transfer line TI2). An overview of ALICE is provided in

section 2.2. The other large experiments are ATLAS [123] at point 1, CMS [124] at point 5, and LHCb [125] located at point 8 near the second beam injector (TI8). Both ATLAS and CMS are multi-purpose detector systems covering a wide range of physics topics including the successful search for [15,16] and precise measurement of the Higgs boson [126,127] as well as the search for physics beyond the Standard Model [128,129]. The aim of LHCb is to study particles containing heavy quarks in order to investigate the tiny asymmetry between matter and antimatter observed in our universe [130]. The experimental lineup of the LHC is complemented by three smaller experiments, namely LHCf [131] (close to ATLAS), TOTEM [132] (near CMS) and MoEDAL [133] (within the LHCb cavern).

At CERN, experiments are not only performed at the highest energies achieved by the LHC. In addition, most of the machines described above as pre-accelerators for the LHC have their own physics programmes in dedicated experimental areas, some of them are also shown in figure 2.1. These experiments cover a wide range of collision energies and physics topics including detailed studies of antimatter, the structure of hadrons, potential connections between cosmic rays and cloud formation and many more [134].

2.2. Overview of the ALICE setup

Among the four large LHC experiments, ALICE is specifically designed to study the collisions of heavy ions [34,35]. Given the extreme temperatures and energy densities reached in these collisions, it is expected, that a deconfined state of quarks and qluons, the so-called Quark-Gluon Plasma, is created (see section 1.1.2). The main goal of ALICE is to investigate this state and the physics of strongly interacting matter. In addition to heavy-ion collisions, ALICE also records data on pp and proton–nucleus (typically p–Pb) collisions. These serve as important reference measurements for the heavy-ion physics, but also to study the relevant degrees of freedom of strongly interacting matter at ultra-relativistic energies. Here, the strengths of ALICE – also with respect to the other LHC experiments – are its excellent Particle IDentification (PID) capabilities and the possiblity to measure charged particles down to low transverse momenta (p_T) of about $150 \, \text{MeV}/c$ [112].

A schematic layout of the ALICE detector systems is presented in figure 2.2. The overall size of the apparatus is $16 \cdot 16 \cdot 26 \, \text{m}^3$ with the long axis pointing along the beam direction [35, 112]. In total, ALICE weighs approximately $10\,000 \, \text{t}$, whereof the largest fraction of about $7\,800 \, \text{t}$ is contained in a huge solenoid magnet. The overall setup of ALICE and its 17 detector systems[a] is subdivided into three main parts: the central barrel, the forward detectors and the muon spectrometer. All detector systems of the central barrel are completely embedded in the solenoid, covering the

---

[a] Here, the situation in the first years of data taking (LHC Run 1) and the method of counting as in [112] is used, i.e. counting the ITS systems (SPD, SDD, SSD) separately, but the ZDC (ZDC:ZN, ZDC:ZP, ZDC:ZEM) as one system. Before the start of LHC Run 2, two additional systems (AD, DCal) have been installed, increasing the number to 19 detector systems.
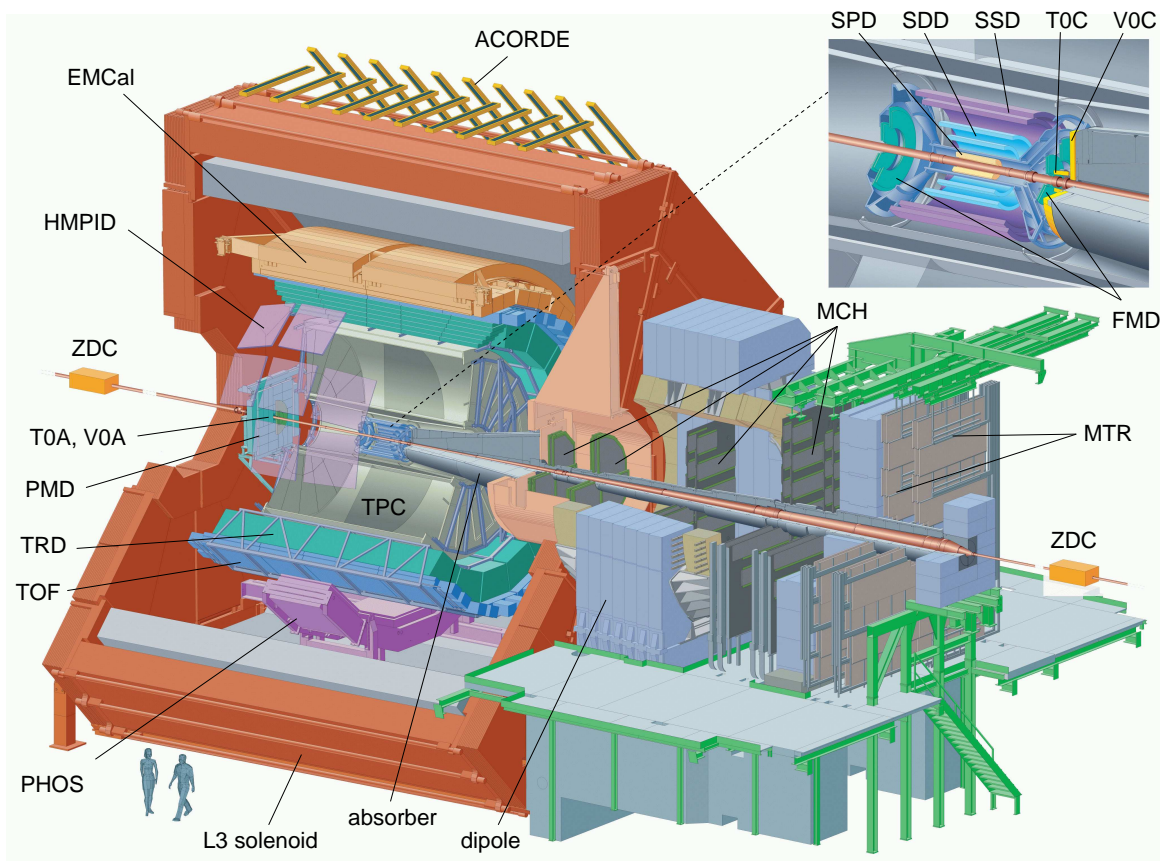
Figure 2.2.: Schematic overview of the ALICE setup [112]. This layout corresponds to the original plan for the experimental setup as described in [35]. Some of the detector systems were not completed at the beginning of data taking and new detectors have been added later, see text for details.

kinematic range around midrapidity. The forward detectors are located close to the beam pipe both inside and outside the solenoid. The muon spectrometer is placed on one side along the beam outside of the solenoid. It contains a separate dipole magnet. All detector systems are described in more detail in section 2.3 with a focus on those, which are most important for this work, namely the Inner Tracking System (section 2.3.1), the Time Projection Chamber (section 2.3.2), and the V0 scintillator arrays (section 2.3.3)[b].

The large solenoid magnet was originally constructed for the L3 experiment [135] at LEP and is therefore still called the "L3" magnet. It is a room-temperature magnet with an octagonal structure [35]. The aluminium coil is surrounded by a steel flux return yoke, which can be easily identified in figure 2.2 as the red-painted structure. The yoke is closed at the end caps by large doors. On the side, where the muon

---

[b] For the V0 detectors, the alternative notation "VZERO" is used in many ALICE publications, to avoid an ambiguity with the V^0 decay of a neutral particle into two charged particles. As this aspect is not important for this work, the original notation is used as for example in [35, 112].

spectrometer is installed next to the solenoid, the doors have to stay closed. On the other side, the doors can be opened in longer shutdown periods, simplifying the maintenance of the central-barrel detector systems and permitting the installation of additional detector modules. The nominal flux density of the L3 solenoid magnet is 0.5 T at an operating current of 30 kA. The smaller dipole magnet is part of the muon spectrometer and located only about 10 cm away from the solenoid. Its nominal magnetic flux density of about 0.67 T is reached at an operating current of 6 kA, leading to a field integral between the interaction point and the muon filter at the end of the muon spectrometer of about 3 Tm.

The coordinate system used in ALICE is an orthogonal Cartesian system with the origin defined as the nominal interaction point in the centre of ALICE [112]. The z axis is defined along the direction of LHC Beam 2, going towards the access point 1 with the ATLAS experiment. Hence, the positive direction along z is named the "A side". The negative direction along z is analogously called the "C side", as it is pointing towards point 5 with the CMS experiment. The x and y axes span the plane transverse to the beam direction, with the x axis pointing towards the centre of the LHC and the y axis pointing upwards. The muon spectrometer is located at the C side of the experiment.

Currently, more than 1800 members from 177 institutes in 41 countries around the world are involved in the ALICE Collaboration [136].

2.3. ALICE detector systems

The ALICE detector systems are classified into three categories: the central barrel, the forward detectors and the muon spectrometer [35, 112]. The central-barrel detectors cover the kinematic region around midrapidity, most of them spanning a total range of about two units of rapidity. The innermost system is the Inner Tracking System (ITS), consisting of three subsystems with two layers each, which are described in more detail in section 2.3.1. All of these detector layers, as well as the surrounding Time Projection Chamber (TPC, section 2.3.2), Transition Radiation Detector (TRD)[c] and Time-Of-Flight (TOF) detector, cover the full azimuthal angle. Outside of the TOF, two calorimeters are installed – the ElectroMagnetic Calorimeter (EMCal) and the PHOton Spectrometer (PHOS) – as well as the High Momentum Particle Identification Detector (HMPID). During the Long Shutdown 1 (LS1) of the LHC, the calorimeters have been complemented by the Dijet Calorimeter (DCal). All central-barrel detectors follow the same 18-fold segmentation in azimuth, with the exception of the ITS. Hence, one sector of the TPC, TRD, TOF or the calorimeters covers 20° in azimuth.

The forward detector systems consist of smaller detectors located close to the beam pipe covering kinematic ranges of large pseudorapidities. Most of them are installed inside the L3 magnet, with the exception of the Zero Degree Calorimeters (ZDC). The

---

[c] At the beginning of data taking in 2009, seven out of 18 TRD supermodules were installed. The other supermodules have been installed successively during LHC shutdown times. The TRD has been completed in 2014 during the Long Shutdown 1 of the LHC [137].
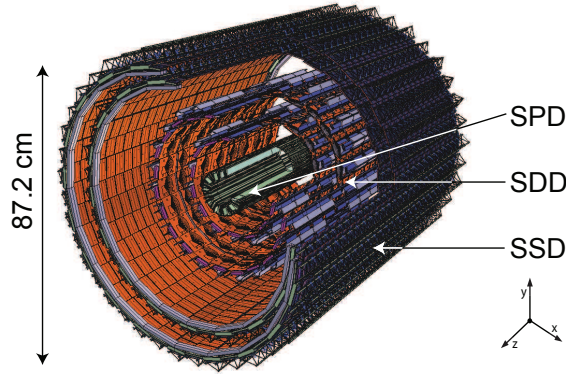
Figure 2.3.: Layout of the ALICE Inner Tracking System [138].

other forward detectors include the V0 scintillator arrays (section 2.3.3) and the T0 Cherenkov detectors. They are complemented by the Forward Multiplicity Detector (FMD), the Photon Multiplicity Detector (PMD) and the ALICE Diffractive (AD) detector, which has been installed during LS1 outside of the L3 magnet.

In addition to the dipol magnet, two absorbers, five tracking stations of Muon CHambers (MCH) and two further stations of Muon TRiggers (MTR) constitute the muon spectrometer. A special detector system, which does not belong to any of the three categories defined above, is the ALICE COsmic Ray DEtector (ACORDE) installed on top of the L3 magnet.

2.3.1. Inner Tracking System (ITS)

The Inner Tracking System (ITS) [35, 138] is the detector system of ALICE located closest to the interaction point. One of its main purposes is to determine the primary interaction vertex of the collisions as well as the secondary vertices originating from particle decays. Together with the TPC, the ITS is one of the main detectors used for charged-particle tracking. In addition, the four outer layers of the ITS are capable to identify particles via their specific energy loss dE/dx.

The layout of the six ITS layers is presented in figure 2.3. Three different techniques are used, each installed in two neighbouring layers. Starting from the inner side, the first two layers consist of Silicon Pixel Detectors (SPD), the innermost layer at a distance of only 3.9 cm from the nominal centre of the particle beams. The next two layers are equipped with Silicon Drift Detectors (SDD) and the outer layers with Silicon Strip Detectors (SSD). The outermost layer has a radial distance of 43 cm to the nominal beam position and an overall length of almost 1 m. All layers are built symmetrically around midrapidity, covering at least a pseudorapidity range of $|\eta| < 0.9$. Detector types, positions, acceptances and spatial resolutions of the single layers are summarised in table 2.1. All layers cover the full azimuthal angle.

Layer	Type	r (cm)	$|z|$ (cm)	$|\eta|$	Res. $\varphi \times z$ (μm^2)
1	pixel	3.9	14.1	2.0	12×100
2	pixel	7.6	14.1	1.4	12×100
3	drift	15.0	22.2	0.9	35×25
4	drift	23.9	29.7	0.9	35×25
5	strip	38.0	43.1	0.97	20×830
6	strip	43.0	48.9	0.97	20×830

Table 2.1.: Main characteristics of the six ITS detector layers. r denotes the radial distance from the nominal beam position, $|z|$ the length in both directions from the nominal interaction point and the last column shows the resolution in $r\varphi$ and z directions. The values are taken from [35, 138].
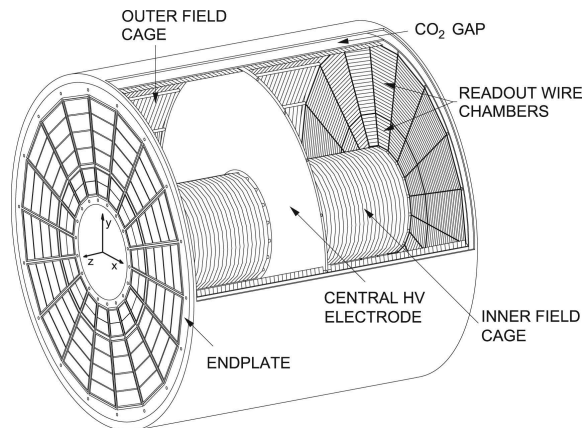

Figure 2.4.: Layout of the ALICE Time Projection Chamber [111].

2.3.2. Time Projection Chamber (TPC)

ALICE is the dedicated heavy-ion experiment at the LHC and it has been anticipated, that a central Pb–Pb collision at LHC energies would produce up to 8 000 charged particles[d] per unit of rapidity around midrapidity [34, 35]. The Time Projection Chamber (TPC) [111] is a gaseous detector, which has been specifically designed to simultaneously measure such a large number of particles. It is the main tracking detector of the ALICE central barrel with a pseudorapidity acceptance of about $|\eta| < 0.9$ and almost full acceptance in azimuth[e]. The measurement of the trajectories of the charged particles and their curvature in the magnetic field of the L3 solenoid enables the determination of the particle momenta. Furthermore, the TPC is the most important PID detector of ALICE. Together with the ITS, it is also used to determine the primary interaction vertex.

---

[d] With $\mathrm{d}N_{\mathrm{ch}}/\mathrm{d}\eta \approx 1600$ in 0–5% most central Pb–Pb collisions [139], the measured value is significantly smaller than the original predictions.

[e] The full acceptance in azimuth is only slightly reduced by the dead zones at the boundaries of the readout chambers.

A schematic view of the main components of the TPC is shown in figure 2.4. It has a cylindrical shape with the central axis of the cylinder coinciding with the beam axis. The active volume of the TPC has a length of 5 m along the beam direction, an inner radius of 85 cm and an outer radius of 247 cm, resulting in a total gas volume of about 90 m³. This active volume is subdivided into two halves by the Central Electrode (CE) at the position of the nominal interaction point. A high voltage of −100 kV is applied to the CE, leading to a drift field of 400 V/cm between the CE and the two endplates. Both the inner and the outer cylinder of the active volume are equipped with a field cage consisting of 165 strips on each side of the CE. These strips are connected with a resistor chain to create a highly uniform electrostatic field throughout the complete active volume.

Both the inner and the outer field cages are surrounded by containment vessels on the sides opposite to the active volume. These vessels are filled with CO_2 and serve as an electric and thermal insulation. In addition, a sophisticated system of heat screens and cooling circuits facilitates to keep the whole active volume in thermal uniformity on the level of 0.1 K, which is required for the stability of the drift velocity within the TPC gas.

Charged particles traversing the TPC ionise the gas molecules within the active volume. The freed electrons are accelerated by the drift field towards the endplates. Due to multiple scattering processes within the TPC gas, their drift velocity is nearly constant. The endplates are equipped with readout chambers, which measure the two-dimensional position of the arriving electrons as well as their arrival times. Together with a precise determination of the drift velocity, the third spatial dimension along the beam direction can be reconstructed.

The drift velocity is measured with the help of a laser system. Straight laser tracks traverse the active volume of the TPC perpendicular to the beam direction at well-defined positions. They ionise the gas molecules like charged particles and therefore can be measured by the readout chambers. As the time, when they are fired, is known precisely, the velocity of the drifting electrons can be obtained from the difference to the arrival times at the readout chambers.

Readout chambers

The endplates of the TPC are subdivided into 18 sectors. Each sector is further split into two readout chambers with trapezoidal geometries, the Inner ReadOut Chamber (IROC) covering the radial range 85 cm $\lesssim r \lesssim$ 132 cm and the Outer ReadOut Chamber (OROC) covering 135 cm $\lesssim r \lesssim$ 247 cm [35, 111]. As readout technique, Multi-Wire Proportional Chambers (MWPCs) with cathode pad readout are employed. A cross section through one of the readout chambers is presented in figure 2.5. In this view, the pad plane is located at the bottom, which corresponds to the transverse plane of the endplates and the side opposite to the active volume in the real TPC. The electrons from the drift region are accelerated towards anode wires located above the pad plane. These anode wires are followed by a cathode wire plane and a gating
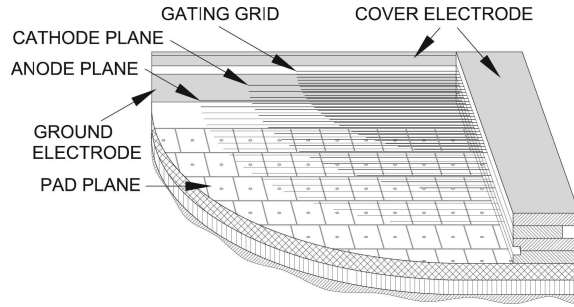
Figure 2.5.: Cross section through a readout chamber of the TPC, with the pad plane, the three wire planes and the cover electrode [111].

ROC	Pad	Radial range (mm)	Pad rows	Pad size $\varphi \times r$ (mm²)	Total pads
IROC	short	$848 < r < 1321$	63	4×7.5	5504
OROC	medium	$1346 < r < 1986$	64	6×10	5952
OROC	long	$1986 < r < 2466$	32	6×15	4032
Full TPC		$848 < r < 2466$	159	$-$	557 568

Table 2.2.: Parameters of the readout chambers (ROCs) of the TPC and their different pad geometries as well as for the full TPC. The values are taken from [35, 111].

grid. The latter is opened, when a collision event has been triggered[f] and is closed again after the full drift time of about $100\,\mu$s, i.e. when the drift electrons with the longest drift path, produced around the CE, have arrived at the anode wires. On top of the readout-chamber frames, cover electrodes at the potential of the field cage in that position help to keep the electrostatic field uniform in the vicinity of the readout chambers.

Three different sizes of readout pads are used in the pad planes of the readout chambers. The sizes increase with the radial distance from the interaction point and are optimised to keep the maximum occupancies low[g]. The smallest pads with $4 \times 7.5\,$mm² are installed in the IROCs, while the OROCs consist of two areas with medium and with large pads. Details about the pad geometries are listed in table 2.2. In total, the TPC readout consists of almost 560 000 pads.

Readout and front-end electronics

Drift electrons arriving at the readout chambers are strongly accelerated near the anode wires, generating an electron avalanche. The corresponding mirror charge mea-

---

[f] For details on the triggering see section 2.4.

[g] The occupancy is defined as the ratio of the pads with signal to all pads. The maximum occupancies were originally estimated with the assumption of $dN_{ch}/d\eta \approx 8\,000$ to be about 40% for the innermost and 15% for the outermost pad row [35].

sured by the readout pads produces a fast rising signal with a long undershooting tail, which originates from the remaining positive ions drifting towards the active volume [35, 111]. As these ions are much heavier than electrons, their drift velocity is much slower and hence their mirror charge is measured on the pad plane for a significantly longer time. The ions are absorbed by the cathode wires or by the gating grid, which is closed after the maximum electron drift time of about $100\,\mu$s. This time is short enough such that no ions from the amplification at the anode wires reach the gating grid in its open state.

Each of the readout pads corresponds to one readout channel, consisting of a charge sensitive amplifier/shaper, an Analogue-to-Digital Converter (ADC) and a digital processor. The latter executes several tasks, e.g. baseline suppression and ion tail cancellation. One ALICE TPC ReadOut (ALTRO) chip integrates the ADC and the digital processor of 16 single channels together with a multi-event buffer memory. Eight ALTRO chips are implemented on one Front-End Card (FEC), hence one FEC contains the readout electronics for 128 channels. Up to 25 FECs are controlled by one Readout Control Unit (RCU) corresponding to one readout partition. Each sector of the TPC contains six partitions, two for the IROC and four for the OROC. Together with further equipment, the front-end electronics (i.e. the FECs and RCU boards) are not installed directly on the readout chambers, but on the service support wheels. These are located on both sides of the TPC next to the endplates with the readout chambers, but mechanically and thermally separated.

Gas mixture

A typical gas mixture for gaseous detectors consists of a noble gas as main component and an additional quencher gas, which is needed to mitigate secondary ionisation processes. The molecules of the noble gas are ionised by the traversing charged particles. At the beginning of data taking in 2009, a ternary mixture was used in the ALICE TPC, with neon (Ne) as main component, CO_2 as quencher and the addition of nitrogen (N_2), which was intended to provide a more stable operation and better control of the gas mixture. The proportion of mixture was (90/10/5) for $Ne/CO_2/N_2$ corresponding to 85.7% of Ne, 9.5% of CO_2 and 4.8% of N_2 [111]. The operation with this mixture was not as stable as anticipated and the nitrogen was identified as a possible reason. Therefore, the nitrogen was removed and the mixture changed to Ne/CO_2 (90/10) with no significant change of the behaviour. During LS1, the noble gas component was changed to argon (Ar) with the advantage of a more robust operation of the TPC readout chambers [140]. Due to significant space-charge distortions – much larger with Ar because of its higher primary ionisation and slower ion mobility – the mixture was switched back to Ne/CO_2 in early 2017.

Clusters and particle trajectories

The readout pads are installed in rows perpendicular to the radial direction in the centre of the readout chambers. The ionisation electrons originating from a charged

particle traversing the TPC gas typically produce a signal on a few neighbouring pads in each pad row. This information is used to reconstruct one cluster per pad row, where the position in $r\varphi$ direction corresponds to the weighted average of the charges on the readout pads. Each sector of the TPC has 159 pad rows (see table 2.2) and therefore each particle trajectory can produce up to 159 TPC clusters [112]. This number can be lowered, e.g. due to the crossing of the track through chamber boundaries with small dead regions, due to inactive readout pads or because the charge deposited in a pad row is below the noise cancellation threshold. Typical values of the number of TPC clusters per track are around 130 with a large spread and also depending on the overall data taking conditions.

The clusters of the TPC are the main ingredient for the reconstruction of charged-particle tracks in the central barrel of ALICE. These trajectories are curved due to the magnetic field of the solenoid, which is used to determine the particle momenta with the help of the relation [17]

$$p \cdot \cos\lambda = 0.3 \cdot z \cdot B \cdot \rho \,. \tag{2.2}$$

Here, p denotes the particle momentum, λ is the angle of the trajectory to the plane perpendicular to the magnetic field, z the charge of the particle, B the magnetic flux density and ρ the radius of curvature. More details about the tracking can be found in section 2.4.3.

Particle identification in the TPC

Charged particles are idendified in the TPC via their specific energy loss dE/dx measured as a function of the particle momentum [111, 112]. For each cluster – i.e. in each pad row – the charge deposited on the readout pads is measured. The total charge of one cluster is proportional to the energy loss of the particle on its path above this pad row. As the particle track typically is inclined within and with respect to the readout plane, the path length has to be calculated correspondingly. In this way, up to 159 separate measurements of the charge are performed for each particle track. Clusters in the vicinity of chamber boundaries are discarded, because part of the charge may be lost in the dead region between the chambers. From the remaining clusters, a truncated mean is calculated, where the 40% highest-charge values are removed to obtain a more robust result for the dE/dx [111, 112].

The energy loss of charged particles within a medium was first derived by Bethe [141]. Later, it was modified with contributions by Bloch [142] and therefore is called the "Bethe-Bloch parametrisation", which has the form [143]

$$\frac{dE}{dx} = \frac{4\pi N e^4}{m_e c^2} \frac{z^2}{\beta^2} \left(\ln\left(\frac{2m_e c^2 \beta^2 \gamma^2}{I}\right) - \beta^2 - \frac{\delta(\beta)}{2} \right) \,. \tag{2.3}$$

Here, m_e and e are the mass and charge of the electron, N is the number density of electrons in the medium, z and β denote the charge and velocity of the projectile and I is the mean excitation energy of the medium. $\delta(\beta)$ is a material-dependent correction term.
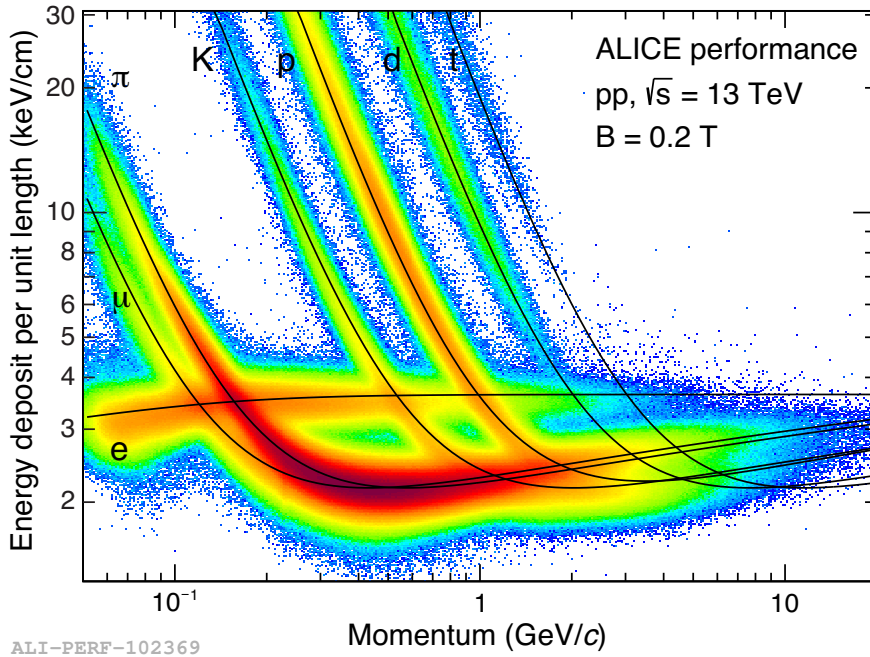
Figure 2.6.: Specific energy loss as a function of the particle momentum in the TPC for pp collisions at $\sqrt{s} = 13\,\text{TeV}$ [17, 140]. In this specific example, a lower magnetic field of $B = 0.2\,\text{T}$ (compared to the nominal field of $B = 0.5\,\text{T}$) leads to a lower momentum threshold, where a better separation of particle species with similar masses is obtained.

Figure 2.6 shows the dE/dx as a function of the particle momentum for pp collisions at $\sqrt{s} = 13\,\text{TeV}$. The energy loss distributions follow Bethe-Bloch parametrisations, which are visualised as lines for all particle species, separatly. In a different representation of dE/dx as a function of the velocity $\beta\gamma$, all species follow the same Bethe-Bloch curve. Using the momentum instead of the velocity splits these curves due to the different masses of the particle species. It is possible to identify the charged particles on a track-by-track basis for low momenta up to about $1\,\text{GeV}/c$ with the exception of a few regions, where the distributions of the different species are crossing. At higher momenta, the identification is performed on a statistical basis using multi-Gausian fits [112].

In the data sample used in figure 2.6, a lower magnetic field of $B = 0.2\,\text{T}$ as compared to the nominal field of $B = 0.5\,\text{T}$ enables the measurement down to even lower momenta, where also a separation of the pions (π) and muons (μ) can be observed. Usually, the nominal field is employed, which expands the charged-particle tracking capabilities to significantly higher momenta.
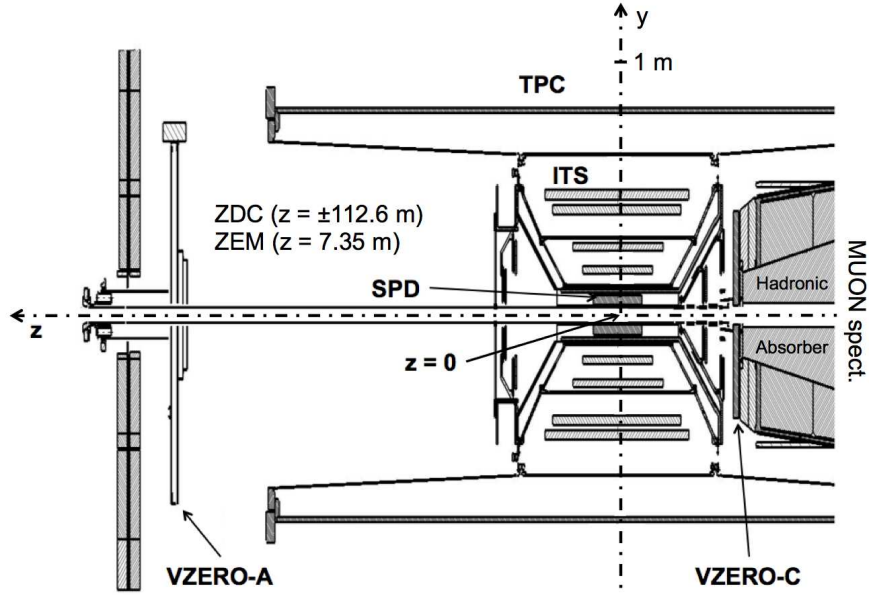
Figure 2.7.: Cross section along the beam direction of the inner part of ALICE indicating the positions of the two V0 (VZERO) detector arrays [144]. The ITS layers and the inner wall of the TPC are shown as well as a part of the hadronic absorber on the C side in front of the muon spectrometer. The nominal interaction point in ALICE is denoted by "$z = 0$".

2.3.3. V0 scintillator arrays

For triggering and the determination of basic event properties, the V0 scintillator arrays [35, 144] constitute one of the most important detector systems in ALICE. They provide minimum-bias and centrality triggers and measure the charged-particle multiplicity, which is used to determine the event centrality in Pb–Pb collisions. In addition, they help to distinguish beam-beam from beam-gas interactions, the latter being rejected for physics analyses. With the measurement of the azimuthal distribution of charged particles, the event plane can be determined. Finally, the luminosity of the LHC beams can be measured.

The V0 detector system is composed of two independent arrays of scintillator counters installed on both sides of the nominal interaction point of ALICE inside the L3 solenoid. Their position along the beam (z) direction is not symmetric, as can be seen in figure 2.7. V0A is located on the A side at $z = 329\,\text{cm}$, V0C is installed directly in front of the hadronic absorber needed for the muon spectrometer on the C side, with $z = -87\,\text{cm}$ much closer to the nominal interaction point ($z = 0$). Placed close to the beam pipe, both arrays cover forward ranges of pseudorapidity with $2.8 < \eta < 5.1$ and $-3.7 < \eta < -1.7$ for V0A and V0C, respectively. Each of the arrays consists of four rings, which are subdivided into eight sections of 45° in azimuth resulting in 32 channels per array.

2.3.4. Further detector systems

The ALICE detector systems which are most important for the present work (ITS, TPC and V0) are described in the sections above. Here, the remaining detectors are depicted briefly, grouped into central-barrel detectors, forward detectors, the muon spectrometer and ACORDE. They are described in detail in [35] and the references therein. The performance of the ALICE detector systems during LHC Run 1 is discussed in [112].

Central-barrel detectors

Surrounding the TPC, the **Transition Radiation Detector (TRD)** is used to separate electrons from hadrons and to improve the charged-particle tracking. It is composed of 18 supermodules, each consisting of six layers of Xe-CO_2-filled MWPCs in radial direction, which are separated in five stacks in z direction. The pseudorapidity range of the TRD extends to $|\eta| < 0.84$.

The **Time-Of-Flight (TOF)** detector is the outermost detector in the central barrel, which covers the full azimuthal angle. With the same 18-fold segmentation as the TPC and the TRD, it covers $|\eta| < 0.9$ in pseudorapidity. Its main purpose is the identification of charged hadrons at intermediate momenta. It consits of Multigap Resistive Plate Chambers, which are used to measure the arrival time of charged particles with a resolution of about 80 ps.

Outside of the TOF, several detectors are installed, which do not span the full azimuthal angle. The **PHOton Spectrometer (PHOS)** is made of dense scintillating $PbWO_4$ crystals providing a high granularity and high energy resolution. Its main task is the measurement of direct photons as well as photons from neutral meson decays. It is located at the bottom of the central-barrel part of ALICE and only covers a small acceptance of $|\eta| < 0.12$ in pseudorapidity and $220° < \varphi < 320°$ in azimuth.

Opposite of the PHOS and with a similar acceptance in azimuth ($80° < \varphi < 187°$) the **ElectroMagnetic Calorimeter (EMCal)** spans a much larger range in pseudorapidity of $|\eta| < 0.7$, but has a lower granularity and energy resolution. The EMCal is a Pb-scintillator calorimeter mainly built to detect particle jets. During LS1, it was complemented by additional modules surrounding PHOS, which are called **Dijet Calorimeter (DCal)** [140], as they enable the measurement of back-to-back dijets together with the EMCal. The DCal has an acceptance of $0.22 < |\eta| < 0.7$ and $260° < \varphi < 320°$ as well as $|\eta| < 0.7$ and $320° < \varphi < 327°$.

The **High Momentum Particle Identification Detector (HMPID)** is a ring-imaging Cherenkov detector made of a liquid C_6F_{14} radiator and a CsI photocathode. It is used to identify charged hadrons at intermediate momenta and covers an acceptance of $|\eta| < 0.6$ and $1° < \varphi < 59°$.

2. The experiment: ALICE

Forward detectors

Measuring the interaction time of the collisions and hence generating a start time (T0) for the TOF is the main purpose of the **T0 detector**. It is the fastest detector in ALICE and provides the first trigger signal. The T0 consits of two arrays of Cherenkov counters (T0A and T0C) installed close to the beam pipe on both sides of the interaction point. T0A is located at $z = 375$ cm and covers $4.61 < \eta < 4.92$, T0C is installed at $z = -72.7$ cm with a coverage of $-3.28 < \eta < -2.97$. A time resolution of 20–25 ps in Pb–Pb and about 40 ps in pp collisions is achieved with the T0. Furthermore, the longitudinal (z) position of the collisions can be inferred from the time difference between the signals in T0A and T0C.

Three types of **Zero Degree Calorimeters (ZDC)** are installed in ALICE. All of them are located close to the beam pipe and outside of the L3 magnet. In heavy-ion collisions, they are used to detect the spectator nucleons, which do not take part in the interactions. This provides an estimate of the centrality of the collisions. Two sets of detectors are placed inside the LHC tunnel on both sides of the nominal interaction point at a distance of $|z| = 112.5$ m[h]. Both are equipped with tungsten-quartz calorimeters to measure neutrons (ZN) and with brass-quartz calorimeters for the measurement of protons (ZP). The third type is an electromagnetic lead-quartz calorimeter (ZEM) installed on the A side at $z = 7.25$ m next to the doors of the L3 magnet. The ZEM is needed to resolve the ambiguity between the most central and the most peripheral events, both inducing small signals in the ZNs and ZPs. The different calorimeters span pseudorapidity ranges of $|\eta| > 8.8$ (ZN), $6.5 < |\eta| < 7.5$ (ZP) and $4.8 < \eta < 5.7$ (ZEM).

The **Forward Multiplicity Detector (FMD)** is employed to measure the charged-particle multiplicity over a wide range of pseudorapidity. It is segmented into three rings of silicon strip detectors installed at different positions along the beam line ($z = -70$ cm, 80 cm and 320 cm). The overall coverage is $-3.4 < \eta < -1.7$ and $1.7 < \eta < 5.0$.

Photons can be measured in the forward direction on the A side by the **Photon Multiplicity Detector (PMD)**. It is constructed of lead converter plates followed by gas proportional counters. The PMD is installed at $z = 364$ cm and covers $2.3 < \eta < 3.7$.

During LS1, the **ALICE Diffractive (AD) detector** has been installed, which provides triggers on diffractive events [140]. Two double layers of scintillation counters placed at $z = 17.0$ m and $z = -19.5$ m span a pseudorapidity range of $4.8 < \eta < 6.3$ and $-7.0 < \eta < -4.9$. They are able to detect charged particles with transverse momenta down to $p_{\mathrm{T}} \approx 20$ MeV/c.

---

[h] Originally, the ZDCs had been installed at $|z| = 116$ m. They were moved slightly closer to ALICE, first to $|z| = 114$ m and later, during the 2011–2012 winter shutdown, to their final position of $|z| = 112.5$ m [112].

Muon spectrometer

The muon spectrometer located at the C side of the experiment is designed to measure muons with a high purity, especially those originating from heavy-quark decays. It consists of two absorbers, five tracking stations called **Muon CHambers (MCH)**, two trigger stations called **Muon TRiggers (MTR)** and the dipole magnet described in section 2.2. Both MCH and MTR stations include two detector layers, each, resulting in total in ten tracking and four trigger layers. The first hadronic absorber of about 10 nuclear interaction lengths (λ_{int}) is installed inside the L3 solenoid and spans the range $-503\,\mathrm{cm} < z < -90\,\mathrm{cm}$. In negative z direction, it is followed by two MCH stations inside the solenoid, one in the dipole magnet and two further stations outside of the magnets. Following another absorber of about $7\,\lambda_{int}$, the two MTR stations at $z = -16.1\,\mathrm{m}$ and $z = -17.1\,\mathrm{m}$ conclude the muon spectrometer, which covers $-4 < \eta < -2.5$ in pseudorapidity and the full azimuthal angle.

ACORDE

Placed on top of the L3 magnet, the **ALICE COsmic Ray DEtector (ACORDE)** triggers on cosmic muons, which are not absorbed by the rock forming the ALICE cavern. These high-energetic muons produce straight trajectories in the ALICE detectors. Hence, they are used to measure the spatial alignment of the different detector systems and for detector calibration purposes. Furthermore, ACORDE is employed to trigger on high-multiplicity events of cosmic muons, which are used for astrophysical studies [145].

2.4. Data taking and reconstruction

In the first two LHC running periods, ALICE has taken data in all collision systems and at all collision energies provided by the LHC. During LHC Run 1 (2009–2013), these involved pp collisions at $\sqrt{s}$ = 0.9, 2.36, 2.76, 7 and 8 TeV, p–Pb collisions at $\sqrt{s_{NN}}$ = 5.02 TeV and Pb–Pb collisions at $\sqrt{s_{NN}}$ = 2.76 TeV [112]. LHC Run 2 has started in 2015 and will proceed until the end of 2018. New record collision energies have been reached with $\sqrt{s}$ = 13 TeV in pp, $\sqrt{s_{NN}}$ = 8.16 TeV in p–Pb and $\sqrt{s_{NN}}$ = 5.02 TeV in Pb–Pb collisions, accompanied by reference measurements at $\sqrt{s_{NN}}$ = 5.02 TeV in the small (pp and p–Pb) collision systems [116, 117, 121]. In 2017, a pilot run of Xe–Xe collisions at $\sqrt{s_{NN}}$ = 5.44 TeV has been carried out [122]. In this work, data from the first LHC running period are analysed. Therefore, the following sections are focussed on the data taking conditions and data reconstruction in LHC Run 1, which is described in more detail in [112].

2.4.1. Beam conditions

Among the four large LHC experiments, ALICE is specifically designed to measure and identify a large number of particles at the same time [34,35]. ATLAS and CMS set

their focus on the accumulation of high statistics to investigate rare probes [123, 124]. The LHC has been designed to deliver large integrated luminosities, which cannot be recorded by ALICE. Therefore, the luminosity in ALICE is reduced by adjusting several beam parameters [112].

The LHC beams are running in two parallel beam pipes within the LHC magnets. To bring them into collision at the interaction points, they have to be slightly deflected leading to a crossing angle between the two beams. This angle is adjusted in ALICE as one of the measures to reduce the luminosity. In addition, the number of interacting bunches is reduced in ALICE and the beams are less focussed at the ALICE interaction point. In the case of very high beam intensities, a special collision scheme is applied in ALICE, where the main bunches of one beam are collided with "satellite" bunches of the other beam. These satellite bunches are separated from the main bunches and contain typically about 0.1% of their intensity [112].

With these adjustments, the maximum interaction rate in ALICE was around $700\,\mathrm{kHz}$ in pp collisions. The average number of interactions per bunch crossing (μ) depends on the interaction rate and was in the range $0.05 < \mu < 0.3$. In the p–Pb running period in early 2013, the luminosity was reduced only slightly in ALICE, leading to a maximum interaction rate of $200\,\mathrm{kHz}$ and $\mu \approx 0.06$. The Pb–Pb campaigns in 2010 and 2011 did not exceed the data taking limits of ALICE with a maximum interaction rate of about $200\,\mathrm{Hz}$ and $3\,\mathrm{kHz}$, respectively. Hence, no reduction of the luminosity was applied. The average number of hadronic interactions per bunch crossing in Pb–Pb collisions was about $10^{-5} < \mu < 10^{-4}$ in 2010 and $10^{-4} < \mu < 10^{-3}$ in 2011 [112].

2.4.2. Trigger

The data taking in ALICE is based on trigger signals in several fast detectors. The Central Trigger Processor (CTP) collects the trigger information from these detectors, takes the trigger decision and distributes it to all detector systems. In the case of a positive CTP decision, the data from all detectors is sent to the Data AcQuisition (DAQ), where the event is built and finally stored [112].

Different trigger conditions can be applied in the CTP. A trigger class can connect different trigger decisions. The most basic class of trigger configurations used by ALICE are the minimum-bias (MB) triggers. Their aim is to record all hadronic interaction events between particles of the two LHC beams and to reject all other events, hence generating a data sample with the smallest possible bias from the trigger decisions themselves. The main contribution to the background events originates from interactions of particles of one beam with gas molecules inside the beam pipe. In the standard running mode, where the main bunches from both beams are brought into collision at the ALICE interaction point, also interactions from one main and one satellite bunch are considered as background, as they occur outside of the time window defined for the main–main interactions. The latter contribution is only relevant in Pb–Pb collisions.

This work is based entirely on MB triggered data samples. Two different MB trigger conditions have been used in ALICE in LHC Run 1, the MBor and MBand triggers.

The MBor condition requires at least one hit in the SPD and in one of the V0 arrays, i.e. V0A or V0C. It has a high efficiency for hadronic interactions and is used in low-luminosity running periods like the pp data samples used in this work. The MBand trigger is defined as a coincidence of hits in both V0 detectors, i.e. V0A and V0C. In running conditions with high luminosity and hence high background levels, the MBand condition has the advantage of a higher purity than the MBor trigger. It is applied in the p–Pb and Pb–Pb periods analysed in this work.

Other trigger conditions used by ALICE include central (0–10%) and semi-central (0–50%) triggers in Pb–Pb collisions, high-multiplicity triggers in pp collisions and triggers on rare probes. Examples for the latter are the requirement of a mimimum energy deposit in a spatial window in one of the calorimeters or the measurement of at least one electron in the TRD above a transverse-momentum threshold.

2.4.3. Event and track reconstruction

The first step of the event and track reconstruction is the clusterisation, which is performed separately for each detector [112]. In this step, the measured raw data is converted into clusters representing positions in space and time as well as signal amplitudes for some of the detectors. The next step is a first estimate of the interaction vertices based on the clusters in the SPD. Afterwards, the tracking of charged particles is performed in the central barrel followed by the final determination of the vertices. The charged-particle tracking and the reconstruction of the vertices is described in detail in [112] and summarised below.

Preliminary estimate of the interaction vertices

The clusters of the two SPD layers – i.e. the two innermost layers of the ITS – are used to build short tracklets. These SPD tracklets are extrapolated to the nominal beam positions. The point in space, where most of the tracklets converge, is determined. This serves as the first estimate of an interaction vertex. By definition, it has the largest number of tracklets assigned and hence it is called the primary interaction vertex of this event. In an iterative procedure, further vertices are searched for, which may originate from additional interactions in the same or a nearby bunch crossing. The occurence of several interactions recorded in one event is called "pile-up".

Charged-particle tracking

Following the preliminary determination of the primary interaction vertex, the next step is the reconstruction of charged-particle tracks in the central barrel. The track finding is a three-stage procedure, starting at the outer radius of the TPC and going first inwards, then outwards and finally inwards again [146]. In all three stages, a Kalman-filter technique [147] is applied.

At first, track seeds are built with the outer TPC clusters. These seeds are propagated inwards, checking each pad row for the closest cluster within a search window. In
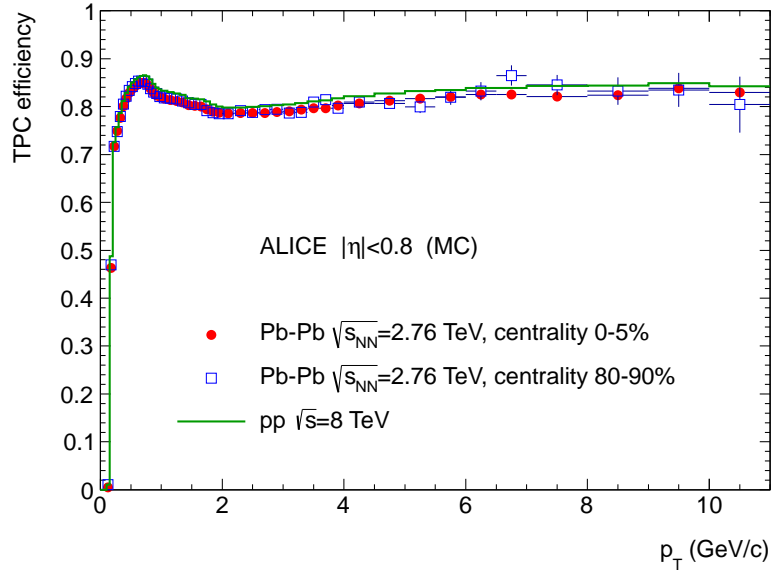
Figure 2.8.: Track finding efficiency for primary charged particles in the TPC as a function of the transverse momentum (p_T) [112]. Results are obtained from Monte Carlo (MC) simulations in pp collisions at $\sqrt{s}$ = 8 TeV and Pb–Pb collisions at $\sqrt{s_{NN}}$ = 2.76 TeV.

this way, up to 159 clusters can be assigned to one TPC track, although typically this number is smaller (see section 2.3.2). Figure 2.8 shows the TPC track finding efficiency for primary charged particles[i] as a function of the transverse momentum obtained from Monte Carlo (MC) simulations. The result for pp collisions is compared to 0–5% central and 80–90% peripheral Pb–Pb collisions, illustrating that the TPC tracking efficiency is almost independent of the occupancy in the TPC.

Tracks found in this first iteration within the TPC are stored as "TPC-standalone" tracks. The track reconstruction continues with the extrapolation of the TPC-stand-alone tracks to the outermost layer of the ITS, where all clusters within a search window are used as seeds for separate track hypotheses. These seeds are propagated through all six ITS layers and in this way, several ITS track candidates are obtained for each TPC track. The candidate with the highest track quality is added to the TPC track to construct a global track containing clusters from both the TPC and the ITS. Subsequently, the ITS clusters, which are not attached to global tracks, are used to build additional ITS standalone tracks not including any information from the TPC. The next step is the outward propagation of the tracks. Again using a Kalman filter, the clusters found in the first inward tracking stage are refitted and the track parameters are updated. When the outer radius of the TPC is reached, the tracks are propagated to the TRD, the TOF, the calorimeters and the HMPID, but without

---

[i] The ALICE definition of primary charged particles is described in [148].

further updates of the track kinematics[j]. Finally the third tracking stage is performed, refitting the tracks again inwards from the outer radius of the TPC to the innermost layer of the ITS. Finally, the kinematic track parameters of the global TPC-ITS tracks are stored in the event.

Final determination of the vertices

Following the charged-particle tracking in the central barrel, the primary interaction vertex is determined from global TPC-ITS tracks [112]. For each track, its point of closest approach to the nominal beam line is identified. Those points far away from the others are removed. From the remaining points, the average position is calculated. In a second step, the tracks are weighted corresponding to their distance to the preliminary vertex position. The final position of the primary interaction vertex is obtained from a fit using the weighted global tracks. In events with a low number of tracks, the nominal beam position is used as an additional constraint in the vertex fit. This procedure results in a higher precision of the primary vertex than the preliminary estimate using only SPD tracklets.

Afterwards, the algorithm searches for additional interaction vertices in the same event, which are determined in the same way as the primary vertex, discarding all tracks already assigned to a vertex. When no further interaction vertices are found, secondary vertices are determined, which do not originate from interactions of beam particles, but from particle decays and conversions of photons in the detector material. A detailed description of the determination of secondary vertices can be found in [112].

2.4.4. Centrality determination

In this work, the results are typically presented as a function of the charged-particle multiplicity density $\mathrm{d}N_{\mathrm{ch}}/\mathrm{d}\eta$. In heavy-ion collisions, events are also characterised by the collision geometry related to the impact parameter b, which is defined as the distance of the centres of the colliding nuclei in the plane perpendicular to the beams [112, 149]. As the quantity b cannot be measured directly in the experiment, it is substituted by the percentage of the total hadronic interaction cross section, which is denoted as "centrality" in the following. In this representation, the most central collisions with an impact parameter close to $b = 0$ correspond to the smallest values of the centrality.

In ALICE, the centrality is determined in two different ways, either by the charged-particle multiplicity measured in one of the detector systems or by the energy deposited in the ZDCs (see section 2.3.4) [112, 149]. The standard method is called "V0 amplitude", which is defined as the sum of the amplitudes measured in the V0A and V0C arrays. Figure 2.9 shows the distribution of events as a function of the V0 amplitude in Pb–Pb collisions at $\sqrt{s_{\mathrm{NN}}} = 2.76$ TeV. The measured distribution is fitted with a

---

[j] During data taking in LHC Run 2, the TRD has been added to the charged-particle tracking in the central barrel. It is needed to correct the space-point distortions observed in the TPC and furthermore improves the transverse-momentum resolution [137].
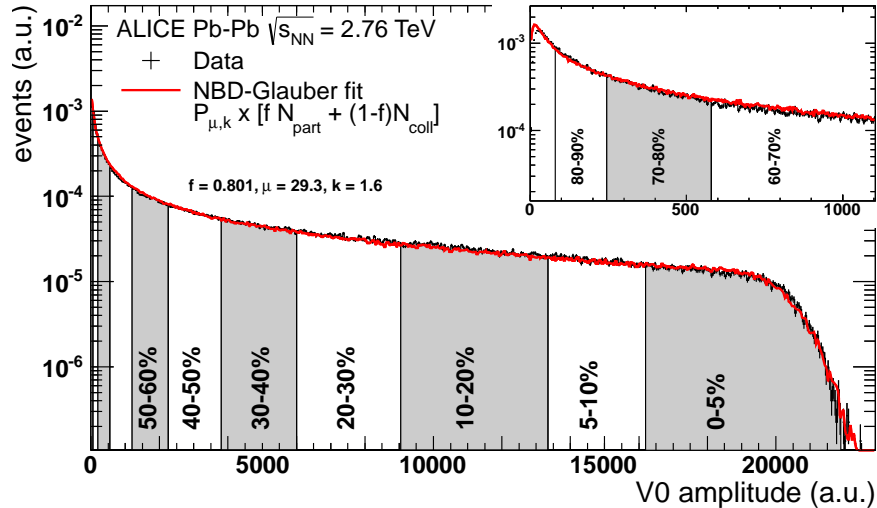
Figure 2.9.: Distribution of events as a function of the V0 amplitude (V0A+V0C) [112]. The red line corresponds to a Glauber-model fit. The inset highlights the peripheral region.

Glauber Monte Carlo model [150], which describes a heavy-ion collision in a purely geometrical way. The Monte Carlo simulation is performed event by event and the geometrical quantities are calculated as statistical averages. The initial distributions of the nucleons in the two nuclei correspond to the nuclear density profile. The nucleons are assumed to move on straight lines and they encounter nucleon-nucleon collisions corresponding to the inelastic nucleon-nucleon cross section. The number of nucleons participating in the collisions (N_{part}) and the number of binary nucleon-nucleon collisions (N_{coll}) define the number of particle sources (N_{sources}) corresponding to a two-component model

$$N_{\mathrm{sources}} = f N_{\mathrm{part}} + (1 - f) N_{\mathrm{coll}}. \tag{2.4}$$

In this relation, the parameter f describes the contribution of soft processes, which is proportional to N_{part}, while $(1 - f)$ is the contribution of hard processes proportional to N_{coll}. For each source, the particle production follows a negative binomial distribution (NBD) $P_{\mu,k}$. The fit parameters for f, μ and k can be found in figure 2.9. The Glauber-model fit is performed in the high-multiplicity part of the V0-amplitude distribution corresponding to central collisions and extrapolated to the peripheral part. The integral of this fit provides an estimate of the total number of hadronic interaction events, which is used to identify the point, where 90% of the hadronic cross section are reached. In the region of 90–100% centrality, the measured event sample contains a significant amount of non-hadronic interactions. The events in the 0–90% centrality range are subdivided into centrality classes, which are indicated in figure 2.9.

The same procedure is also performed using the charged-particle multiplicities measured in only one of the V0 arrays (V0A or V0C), the SPD or the TPC. The resolutions of the centrality obtained with the different methods are presented in figure 2.10 including the different approach using the energy deposited in the ZDCs. The V0 ampli-
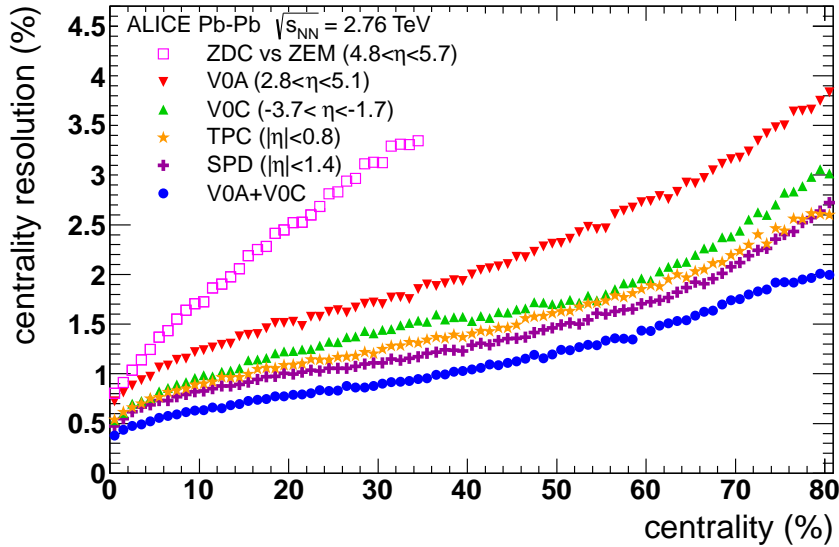
Figure 2.10.: Resolution of the centrality estimators used in ALICE [112]. The V0 amplitude (V0A+V0C) shows the best centrality resolution.

tude (V0A+V0C) provides the best centrality resolution and is therefore the standard method in ALICE analyses. A detailed description of the centrality determination in ALICE can be found in [149].

2.4.5. Data structure

In ALICE, the structure of the data taking is organised in years, periods and runs. Periods usually represent long time intervals with the same global conditions. Reasons to switch a period include for example a change of the collision system or collision energy, an alteration of the magnetic field settings or a change of the LHC conditions like the number of bunches. Periods are subdivided into runs, which correspond to shorter time intervals of typically a few hours with stable running conditions. A change in the configuration of the ALICE detector systems participating in the data taking requires the start of a new run. Other reasons causing the stop of a run include variations of parameters such as environmental conditions, issues with detector systems and the dump of the LHC beams.

A period is always labelled with the prefix "LHC" followed by two numerics representing the year of the data taking (e.g. "10" for the year 2010) and one letter. For example, in 2010 the Pb–Pb data taking consisted of only one period, denoted by "LHC10h". The runs are consecutively numbered throughout the entire ALICE data taking and as such constitute unique identifiers for a certain data interval.

The raw data measured by the detectors is reconstructed using the AliRoot software framework [35,151,152], which builds on the C++ based ROOT framework [153,154]. A data set can be reconstructed several times, e.g. to profit from developments within

the reconstruction software. Each reconstruction is called a "pass" and the passes are enumerated (pass1, pass2, etc.). The reconstructed data is stored in Event Summary Data (ESD) objects. ESD objects contain all information about the events including the vertices, tracks and additional information on the detector level. The ESD objects are further processed to obtain Analysis Object Data (AOD) files. These include only those information necessary for physics analysis leading to a significantly smaller file size than the corresponding ESD objects. Together with a different internal structure, the processing time for an analysis is faster when performed on AOD files. However, some analyses require information, which is only stored in the ESD objects. In general, physics analyses can be performed using the ESD or the AOD format.

3. Analysis of symmetric systems: pp and Pb–Pb

The analysis of event-by-event fluctuations of the mean transverse momentum of charged particles measured with ALICE is divided into two parts, which are described in this and the following chapter. The first analysis is focussed on symmetric collision systems using pp and Pb–Pb collisions. It has been started in my Master's thesis [1], where preliminary results have been obtained and presented in [2]. This chapter is devoted to the continuation of this study including a detailed evaluation of the systematic uncertainties and additional comparisons to Monte Carlo (MC) event generators. The final results have been published in [3, 4].

In the case of symmetric collisions, the centre-of-mass system and the laboratory system are in coincidence, which facilitates the analysis. Hence, the study of the asymmetric p–Pb collision system contains additional challenges like a careful choice of the pseudorapidity range of the measurement. For a comparison, also the pp and Pb–Pb systems have to be re-analysed. This new analysis of all three collision systems is described in detail in chapter 4.

3.1. Data sets

This analysis is based on pp and Pb–Pb collisions measured with ALICE during the first LHC data taking phase (LHC Run 1) [112]. In pp collisions, the collision-energy dependence is investigated with data measured in 2010 at $\sqrt{s}$ = 0.9 and 7 TeV and in 2011 at $\sqrt{s}$ = 2.76 TeV. Pb–Pb collisions are analysed at a collision energy of $\sqrt{s_{NN}}$ = 2.76 TeV taken in 2010. All data sets used in this analysis are summarized in table 3.1. The number of events per data set corresponds to the number of events after the physics selection procedure has been applied, but before any other selection criteria on the event or track level are considered.

System	$\sqrt{s_{NN}}$	Year	Events
pp	0.9 TeV	2010	6.9 M
pp	2.76 TeV	2011	66.0 M
pp	7.0 TeV	2010	289.6 M
Pb–Pb	2.76 TeV	2010	19.4 M

Table 3.1.: ALICE data sets used in this analysis. The number of events is quoted after the physics selection and before any other selection criteria.

3.1.1. Selection of data periods and runs

The general structure of the ALICE data and reconstruction scheme is described in section 2.4.5. Most of the data sets used in this analysis consist of one period of data taking with the exception of the pp collision data set at $\sqrt{s}$ = 7 TeV measured in 2010, which includes several periods. For all of these data sets, each period is subdivided in typically several tens of and up to more than one hundred runs. The data taking conditions may change from one run to the next and therefore it has to be verified for each run that it is usable for physics analyses. All data-taking periods considered in this work and all runs included in the analysis are listed in Appendix A.

3.1.2. Monte Carlo simulations

In addition to the experimental data measured by ALICE, results from several Monte Carlo (MC) event generators are analysed. For each ALICE data set, some MC simulations are provided within the ALICE Collaboration, including the modelling of the detector response with GEANT3 [155]. These MC simulations are called "full simulations", as they contain the full chain of event generation and propagation of the particles through the detector. MC simulations without detector response are referred to as "generator level". In the full simulations, the generated events and particles can be compared directly to those expected to be measured within the experiment. Effects like the finite detection efficiency, contamination of the measured track sample with secondary particles and the detector resolution, e.g. of the transverse momentum p_T, can be studied. In pp collisions, the MC event generator PYTHIA6 [156] with the Perugia-0 tune [157] is used for this purpose for all three collision energies analysed. In the case of Pb–Pb collisions HIJING [158] is applied as event generator.

MC simulations represent important tools for the analysis of detector effects, but they can also help to study effects with a physical origin. Different MC event generators implement different approaches to simulate the initial state of the collisions and their time evolution. Furthermore, it is possible to enable or disable effects and study explicitly their influence on measurable quantities. Such investigations are performed in pp collisions at $\sqrt{s}$ = 7 TeV using several tunes of the PYTHIA6 event generator and one version each of PYTHIA8 [159] and PHOJET [160]. In the case of PYTHIA6, the default versions of the Perugia-0 and Perugia-11 tunes [157] are analysed and compared to a modified tune of Perugia-11, in which the color reconnection mechanism, usually activated in PYTHIA, is disabled (NOCR tune). In Pb–Pb collisions, two versions of AMPT [161] are studied in addition to HIJING. Besides the default AMPT version, another one with the string melting mechanism switched on is considered. All MC simulations used in this analysis are listed in table 3.2, summarising information like the collision system and energy, the analysed tunes and the available number of events. Some of the MC simulations are only available at the generator level, i.e. without the propagation of the particle trajectories through a detector simulation. An approach to use a simple efficiency filter for the generator-level MC productions has been tested for some of the available full simulations. This approach is described in section 3.8. As

it only slightly reduces the differences to the full simulations, it is not applied for the comparison to experimental data. Instead, the differences between generator-level and full simulations are included in the systematic data uncertainties. These differences are found to be small, for details see section 3.7. Finally, results of all MC simulations are presented at the generator level. In this way, the event generators are directly comparable among each other and can be compared to the experimental data within the uncertainties.

Sys.	$\sqrt{s_{\mathrm{NN}}}$	Generator	Version	Tune	Type	Events
pp	0.9 TeV	PYTHIA6	6.421	Perugia-0	full	6.6 M
pp	2.76 TeV	PYTHIA6	6.421	Perugia-0	full	3.4 M
pp	7.0 TeV	PHOJET	1.12	–	full	74.5 M
pp	7.0 TeV	PYTHIA6	6.421	Perugia-0	full	131.3 M
pp	7.0 TeV	PYTHIA6	6.425	Perugia-11 default	gen	74.2 M
pp	7.0 TeV	PYTHIA6	6.425	Perugia-11 NOCR	gen	72.2 M
pp	7.0 TeV	PYTHIA8	8.150	4C	gen	168.4 M
Pb–Pb	2.76 TeV	HIJING	1.36	no jet quenching	full	1.7 M
Pb–Pb	2.76 TeV	AMPT	1.25	default	gen	892 k
Pb–Pb	2.76 TeV	AMPT	2.25	string melting	full	823 k

Table 3.2.: Overview of Monte Carlo generators and tunes used in this analysis. The type is differentiated in full simulations including detector response (full) and those, where only the generator level is available (gen). The number of events corresponds to the events after physics selection and before any other selection criteria for full simulations and to the number of input events for the generator level, in case of PYTHIA8 with the additional requirement of $N_{\mathrm{ch}} > 0$ within the kinematic acceptance.

3.2. Event selection

Mainly, hadronic interactions between particles of the two circulating beams are of interest for physics analyses. Other types of events including background events and those originating from cosmic particles have to be rejected within the event selection. In general, events are recorded following a trigger decision, see section 2.4.2. In ALICE, typically several triggers are running in parallel and for each event the corresponding trigger is stored. During the analysis, the events with the relevant trigger class are selected.

In addition, only those events are selected, where a primary vertex is reconstructed. This vertex has to be close to the nominal interaction point in the centre of ALICE, as otherwise the acceptance of the subdetectors would be shifted. Furthermore, it is possible that several hadronic interactions of beam particles are recorded as one event. These pile-up events are identified and removed from the analysed event sample to avoid an influence of the additional tracks on the physics results.

3.2.1. Physics selection procedure

The physics selection procedure is the first step of the event selection. Within this procedure events are selected corresponding to the requested trigger class. In addition, several conditions are applied to reject background and to reduce the amount of pile-up events. In the present work, minimum-bias (MB) triggers are selected for all analysed data sets. For details about the MB trigger requirements see section 2.4.2.

The largest source of background is machine-induced background, which originates from interactions of beam particles with material in the machine. Inelastic interactions with residual gas molecules within the beam pipe contribute to this type of background as the most important component [112]. The machine-induced background is rejected using the signal arrival times in the two V0 arrays. In the case of pp collisions, the correlation of single clusters and tracklets in the SPD is employed as an additional constraint. The correlation of the signal arrival times in the neutron ZDCs is used in Pb–Pb collisions to reject events from collisions of one main and one satellite bunch. The background rejection is described in more detail in [112].

The criteria employed in the physics selection for the purpose of background rejection also reduce pile-up from different bunch crossings. For example, these pile-up events produce similar signal arrival-time differences in the V0 arrays or in the ZDCs. Pile-up originating from the same bunch crossing has to be rejected in the analysis, which is described in section 3.2.3.

3.2.2. The primary vertex

For each event, one primary interaction vertex is determined. Further pile-up vertices and secondary vertices can be contained in the event, the latter originating from particle decays or interactions with detector material. The reconstruction of the primary vertex is described in section 2.4.3. In an event sample, the primary vertices are distributed around the nominal interaction point in the centre of the experiment. While the distribution in the plane transverse to the beam direction is narrow, it is expanded about multiple tens of centimetres along the beam direction.

Different estimators of the primary vertex

Multiple approaches are employed for the reconstruction of the vertices. A preliminary estimate is performed at the beginning of the event and track reconstruction procedure using only SPD tracklets. The final vertices are determined at the end of the reconstruction using global TPC-ITS tracks. As an alternative, the primary vertex is estimated from TPC-standalone tracks, taking no information from the ITS into account. For the majority of events, the primary vertex position of all three approaches agrees within much less than 1 cm in all three spatial directions.

The precision in the determination of the primary vertex is limited by the finite resolution of the particle trajectories and by the number of particles contributing to the vertex reconstruction. A higher number of particles leads to a better estimate of the

vertex position. In events with a low number of particles, it is possible that not all of the estimators are able to find at least one interaction vertex.

In this analysis, the primary vertex from the global TPC-ITS tracks is used as default. If this vertex is not determined successfully for an event, the vertex using SPD-tracklets is taken as an alternative. In the case that also this vertex is not available, the vertex from TPC-standalone tracks is used. If no primary vertex can be found, the event is rejected.

Selection criteria on the primary vertex

The requirement of a successfully reconstructed primary interaction vertex is implemented via the necessity to have at least one track contributing to the primary-vertex determination. In addition, the maximum allowed distance of the reconstructed primary vertex from the nominal interaction point along the beam (z) direction is set to 10 cm. The reason for this selection is the shift in the geometrical acceptance for the charged-particle tracks in the subdetectors with the z position of the vertex. At the exact position of the nominal interaction point (i.e. $z = 0$), the geometrical acceptance of the central-barrel detectors is symmetric in pseudorapidity. With increasing distance from the nominal centre, the acceptance increases on one side of the experiment and decreases on the other side. The maximum z-vertex distance of 10 cm ensures a uniform tracking acceptance both in the ITS and in the TPC within a pseudorapidity interval of $|\eta| < 0.8$.

As described above, three different approaches are available for the determination of the primary vertex. The vertex from global TPC-ITS tracks is usually dominated by the contribution from the SPD, which is the subdetector closest to the nominal beam positions. Therefore, the global and the SPD-tracklets vertices are typically in good agreement. The estimate of the primary vertex using TPC-standalone tracks can differ from the other two approaches because of the much larger distance of the inner TPC space points from the interaction region and hence the worse resolution towards the vertex. However, the acceptance of the TPC is much more uniform in the azimuthal (φ) direction. Hence, it is possible that the TPC-standalone algorithm determines a primary vertex, which is not found by the other estimators. Furthermore, several collisions can be recorded together as one event and the different vertex estimators may identify different interactions as the primary vertex. One possibility to remove such events is a cut on the difference of the z positions of the primary vertex determined by the different approaches. In this analysis, a cut on the absolute difference of at maximum 10 cm of the primary vertex estimated from TPC-standalone tracks and the one determined from global tracks is applied.

All of the selection criteria concerning the primary vertex used in this analysis are varied to study their influence on the final results. This influence is found to be small and in some cases negligible. Details about the corresponding determination of the systematic uncertainties can be found in section 3.7.

3.2.3. Pile-up rejection

Pile-up events contain several hadronic interactions, which can originate from the same or nearby bunch crossings. The average number of collisions within one bunch crossing (μ) is less than one in ALICE and depending significantly on the collision system and the beam conditions (see also section 2.4.1). Nevertheless, several interactions can occur in one bunch crossing, especially in case of high interaction rates and large values of μ. In addition, collisions from nearby bunch crossings can be recorded in the same event, because the time gap between two bunches is smaller than the detector read-out time.

In principle, it is possible to use events containing several collisions in physics analyses. However, the particle tracks originating from these additional interactions can distort the results, especially if at least one pile-up vertex is located close to the primary interaction vertex. This can lead to a larger number of tracks assigned to the primary vertex. Correlation analyses as in the present work can be sensitive to such effects, as the tracks from the different collisions are completely uncorrelated and may reduce any correlation signal significantly.

In the Pb–Pb collision data set recorded in 2010 and used in this analysis, no significant contribution from pile-up is expected due to a low interaction rate and $10^{-5} < \mu < 10^{-4}$ [112]. With higher interaction rates and $\mu \approx 0.05$, the pp collision data sets analysed in this work have some contribution from pile-up events, although it is small compared to later data taking periods.

The physics selection procedure reduces pile-up from different bunch crossings via time differences of the signals in the V0 arrays and in the ZDCs, see section 3.2.1. In pp collisions, an additional pile-up rejection is implemented, which is used to reject pile-up from the same bunch crossing. It is based on the vertices found by the vertex estimator using SPD tracklets. An event is rejected, if in addition to the primary vertex at least one pile-up vertex fulfilling several conditions is found. These conditions include a minimum number of three tracklets originating from the vertex with the second most tracks in the event. Another parameter, the minimal distance of the second collision vertex to the primary vertex, is set to 0.8 cm. With this parameter, it is ensured, that no events are rejected, which contain only one real collision being reconstructed as two interaction vertices. Pile-up events are also reduced using the difference in the z position of the primary vertex determined from global TPC-ITS tracks and from TPC-standalone tracks as described in section 3.2.2.

3.2.4. Summary of the event selection

The event selection criteria explained in detail in the last sections are summarised in table 3.3. Most of the criteria are identical for the different collision systems and energies. However, some details of the physics selection and the definition of the MB trigger conditions differ as described in sections 3.2.1 and 2.4.2, respectively. In the present analysis, the SPD pile-up rejection is only used in pp collisions, as the Pb–Pb data set does not contain any significant contribution from pile-up events.

Event selection criterion	Value
Physics selection procedure	active
Trigger condition	minimum bias
Number of vertex contributors	≥ 1
Vertex-z distance from nominal interaction point	$\leq 10\,\mathrm{cm}$
Vertex-z difference (TPC–global)	$\leq 10\,\mathrm{cm}$
SPD pile-up rejection (pp): 2nd vertex multiplicity	≥ 3
SPD pile-up rejection (pp): distance of vertices	$> 0.8\,\mathrm{cm}$

Table 3.3.: Summary of the event selection criteria applied in this analysis. The SPD pile-up rejection is only used in pp collisions.

3.3. Track selection

The reconstruction of events and charged-particle trajectories is described in section 2.4.3. The main tracking detectors of the ALICE central barrel are the TPC and the ITS, which can be combined to obtain global tracks or used separately for alternative tracking schemes. These schemes differ in the efficiency and acceptance to measure charged particles as well as the contamination by secondary particles and the transverse-momentum resolution. Track selection criteria are applied in the analysis to select primary charged particles originating from the primary interaction vertex and to reduce the contribution from false trajectories not belonging to a physical particle, low-quality tracks and secondary particles.

3.3.1. Charged-particle tracking detectors and schemes

The ITS provides a very good spatial resolution close to the collision vertex and is able to discriminate the tracks even in the high track density of a central Pb–Pb collision [35]. If a track contains a hit in at least one of the SPD layers, it can be excluded that it originates from a secondary vertex outside the SPD, e.g. due to a particle decay or an interaction with the material of the outer ITS layers or the TPC. Some detector parts, in particular of the ITS and especially of the SPD, have been inactive during the data-taking periods used in this work [112]. Therefore, the acceptance of the ITS is not uniform in azimuth.

The TPC provides a very uniform acceptance in azimuth with only a small residual modulation due to its sector boundaries. With the large track length up to the outer radius of the TPC of about 2.5 m and the high number of up to 159 space points per track, the TPC has excellent tracking capabilities and a very good transverse-momentum resolution [111]. However, the rejection of secondary particles is not as good as in the ITS, owing to the large distance to the collision vertex and the material of the ITS within the TPC inner radius of about 0.85 m.
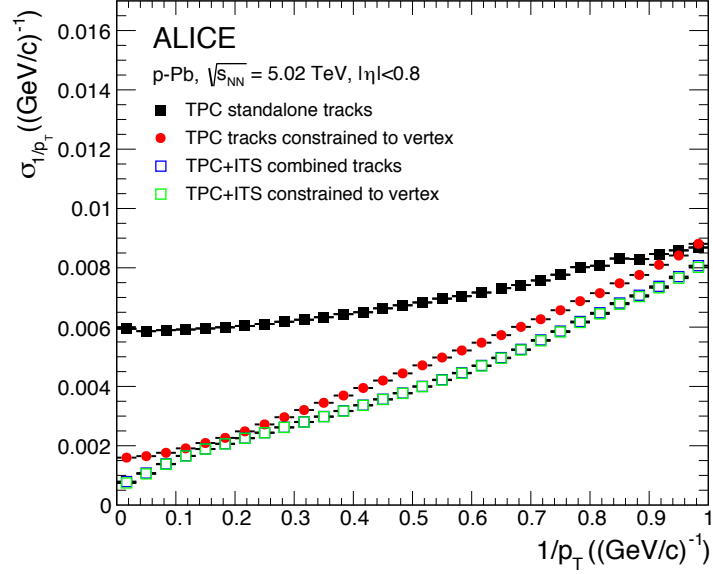
Figure 3.1.: Resolution of $1/p_T$ for several tracking schemes [112]. While the resolution of TPC-standalone tracks is improved by the constraint to the vertex, it does not change in the case of global TPC-ITS tracks, where the open coloured squares overlap exactly.

In figure 3.1 the $1/p_T$ resolution σ_{1/p_T} is presented for several tracking schemes in p–Pb collisions at $\sqrt{s_{NN}} = 5.02$ TeV. It is related to the p_T resolution σ_{p_T} via [112]

$$\frac{\sigma_{p_T}}{p_T} = p_T \cdot \sigma_{1/p_T} \,. \tag{3.1}$$

Global tracks, which are reconstructed using combined information from the TPC and the ITS, constitute the default charged-particle tracking scheme for the ALICE central barrel. This scheme provides a very good p_T resolution, which does not change if the tracks are constrained to the primary vertex, as shown in figure 3.1. In addition, the secondary contamination is low, especially if at least one hit in the SPD is required in the analysis. However, the acceptance is not unifrom in azimuth due to the inactive parts of the ITS. The p_T resolution of the TPC-standalone tracks is comparable to that of the global TPC-ITS tracks at low p_T around 1 GeV/c, but it is worse at higher p_T. Adding a constraint to the primary vertex improves the p_T resolution of the TPC-standalone tracks significantly, reaching similar values than the global TPC-ITS tracks up to $p_T \approx 10$ GeV/c.

In this analysis, a third option of a hybrid tracking scheme can be applied. At first, global TPC-ITS tracks are considered with strict selection criteria including at least one hit in the SPD. If a global track is rejected by these conditions, the corresponding TPC-standalone track constrained to the primary vertex is analysed. In this way, the secondary contamination is kept low – although not as low as in the global tracking scheme – and the azimuthal acceptance is almost uniform – although not as uniform as in the TPC-standalone case.

In the present work, TPC-standalone tracks without constraint to the primary vertex are used as default. The main reason for this choice is the uniform azimuthal acceptance. The analysis is performed within a p_T range of $0.15\,\text{GeV}/c < p_T < 2\,\text{GeV}/c$. At $p_T = 2\,\text{GeV}/c$ corresponding to $1/p_T = 0.5\,(\text{GeV}/c)^{-1}$, the relative p_T resolution σ_{p_T}/p_T is still very good with about 1.4%. The hybrid tracking scheme is applied to check the influence of the p_T resolution and of the secondary contamination. The results of the two tracking schemes are in good agreement, but some small discrepancies are observed and included in the systematic uncertainties, see section 3.7.

3.3.2. Track selection criteria

The aim of this analysis is to study the soft particles produced in the collisions and hence an upper p_T cut of $2\,\text{GeV}/c$ is chosen. The lower p_T cut of $0.15\,\text{GeV}/c$ is necessary due to the decreasing reconstruction efficiency of the TPC at low p_T. Furthermore, the range of $0.15\,\text{GeV}/c < p_T < 2\,\text{GeV}/c$ is identical to a measurement of event-by-event mean p_T fluctuations performed by the STAR experiment [92], which is important for a direct comparison. The pseudorapidity range of $|\eta| < 0.8$ is chosen to ensure a uniform tracking efficiency within this range. In the STAR measurement, the pseudorapidity acceptance is of a similar magnitude, but with $|\eta| < 1.0$ slightly larger.

Secondary particles not originating from the primary vertex, false trajectories built from fake hits in the detectors or wrong combinations of hits to trajectories, and tracks with a poor quality of the momentum fit are significantly reduced by several track selection criteria. Both in the TPC-standalone and in the hybrid analysis, a minimum number of at least 70 out of the maximum of 159 space points in the TPC is required for each track. The quality of the trajectories within the TPC is ensured with a maximum χ^2 of the momentum fit of 4.0 per cluster in the TPC. In the first iteration of the hybrid scheme using global TPC-ITS tracks, at least one hit within the first two ITS layers (i.e. the SPD) is needed. Successful refits both of the TPC and the ITS are as well only required in the case of global TPC-ITS tracks in the hybrid analysis. Tracks originating from reconstructed secondary weak-decay topologies (*kinks*) are rejected for both tracking schemes. Also the selection criteria on the maximum distance of closest approach (DCA) of the trajectory extrapolated to the primary vertex are identical in the two analyses. Along the beam (z) direction, the DCA has to be less than $3.2\,\text{cm}$, in the transverse (xy) plane it is restricted to $2.4\,\text{cm}$. In addition, a two-dimensional DCA requirement is enabled corresponding to an ellipse in the plane of DCA_z and DCA_{xy}. Both DCA parameters are normalised to their maximum allowed values ($3.2\,\text{cm}$ and $2.4\,\text{cm}$) and added in quadrature. If the resulting total relative DCA exceeds one, the track is located outside of the ellipse and it is rejected. This criterion further reduces the amount of secondary particles.

Global TPC-ITS tracks, which are rejected by the strict quality criteria in the first step of the hybrid analysis, are re-analysed on a TPC-standalone basis and are accepted, if their extrapolation is in agreement with the primary vertex calculated from SPD tracklets.

Track selection criterion	TPC only	Hybrid
Pseudorapidity acceptance	$\|\eta\| < 0.8$	
Transverse-momentum acceptance	$0.15\,\mathrm{GeV}/c < p_\mathrm{T} < 2\,\mathrm{GeV}/c$	
Number of TPC clusters	≥ 70	≥ 70
Number of ITS hits	–	≥ 1 (SPD)*
TPC χ^2/d.o.f.	≤ 4.0	≤ 4.0
TPC refit	no	yes*
ITS refit	no	yes*
Reject kink daughters	yes	yes
DCA to vertex (xy)	$\leq 2.4\,\mathrm{cm}$	$\leq 2.4\,\mathrm{cm}$
DCA to vertex (z)	$\leq 3.2\,\mathrm{cm}$	$\leq 3.2\,\mathrm{cm}$
DCA to vertex 2D	yes	yes

Table 3.4.: Track selection criteria for the TPC-standalone and the hybrid tracking scenario. *In the hybrid scenario, for global TPC-ITS tracks at least one hit in the SPD is required as well as the TPC and ITS refits. If a track does not fulfill these conditions, the corresponding TPC-standalone track constrained to the SPD vertex is analysed without these requirements.

All of the selection criteria applied on the track level are summarised in table 3.4 for both tracking schemes. The influence of these selection criteria on the final results is studied by variations of the cut values. For most of the criteria, this influence is small or even negligible. Remaining differences are included in the systematic uncertainties, which are described in section 3.7.

3.4. Mean transverse momentum

The calculation of the mean transverse momentum is the first step in the analysis of its fluctuations. The true average transverse momentum $\langle p_\mathrm{T} \rangle$ of primary charged particles produced in the collisions within a defined kinematic range has to be distinguished from the raw mean transverse momentum $M(p_\mathrm{T})$ of those charged particles, which have been measured and accepted by the criteria discussed in the last sections. An introduction to the various averages of p_T considering true and raw values as well as averages in single events and in event ensembles is presented in section 1.5.1.

3.4.1. Mean transverse momentum in pp collisions

In this analysis, intervals in the accepted charged-particle multiplicity of $\Delta N_\mathrm{acc} = 1$ are used for the calculation of $M(p_\mathrm{T})_m$ in pp collisions. Therefore, all events in each interval m have the same number of N_acc tracks and according to equation 1.45 the average transverse momentum for the interval m can be written as

$$M(p_\mathrm{T})_m = M(M_\mathrm{EbE}(p_\mathrm{T})_k)_m = \frac{1}{n_\mathrm{ev,m}} \sum_{k=1}^{n_\mathrm{ev,m}} M_\mathrm{EbE}(p_\mathrm{T})_k \,. \tag{3.2}$$
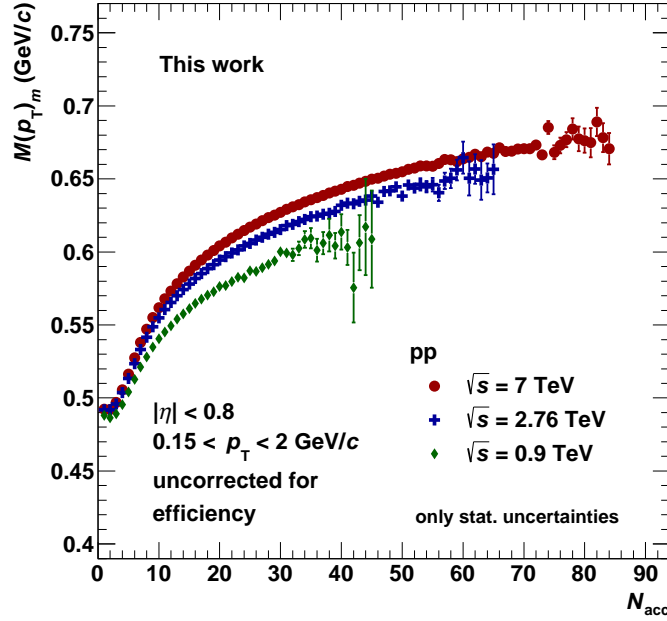
Figure 3.2.: Raw $M(p_T)_m$ as a function of N_{acc} measured in pp collisions at $\sqrt{s} = 0.9$, 2.76 and 7 TeV.

The raw measured $M(p_T)_m$ as a function of the accepted charged-particle multiplicity N_{acc} is presented in figure 3.2 for pp collisions at $\sqrt{s} = 0.9$, 2.76 and 7 TeV in the kinematic acceptance of $|\eta| < 0.8$ and $0.15\,\text{GeV}/c < p_T < 2\,\text{GeV}/c$. For all three energies, $M(p_T)_m$ increases with the multiplicity, exhibiting a steeper increase at low than at high multiplicities. $M(p_T)_m$ also rises with the collision energy, although this dependence is much less pronounced than that on multiplicity. The inclusive raw $M(p_T)$ averages measured for the full event samples are listed in table 3.5. These inclusive values also reflect the moderate increase of $M(p_T)$ with the collision energy.

$\sqrt{s}$	$M(p_T)$
0.9 TeV	526.3 MeV/c
2.76 TeV	555.2 MeV/c
7.0 TeV	574.1 MeV/c

Table 3.5.: Inclusive raw $M(p_T)$ measured in pp collisions at different collision energies.

Several MC simulations are performed for pp collisions at $\sqrt{s} = 7\,\text{TeV}$ using three tunes of PYTHIA6 and one version each of PYTHIA8 and PHOJET. At first, the results for the true mean transverse momentum $\langle p_T \rangle_m$ as a function of the average charged-particle multiplicity density $\langle dN_{ch}/d\eta \rangle$ are compared among the different MC event generators. This comparison is shown in figure 3.3 for the kinematic acceptance
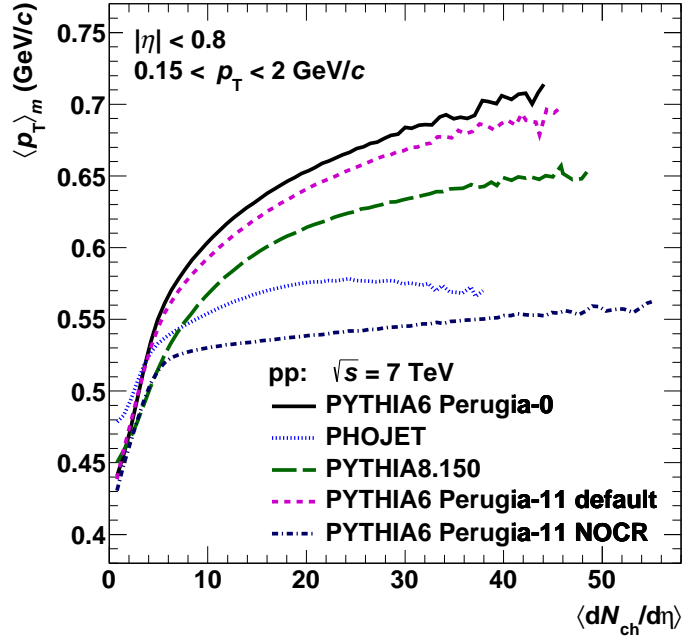
Figure 3.3.: Results for the true average transverse momentum $\langle p_{\mathrm{T}} \rangle_m$ as a function of $\langle \mathrm{d}N_{\mathrm{ch}}/\mathrm{d}\eta \rangle$ in pp collisions at $\sqrt{s} = 7\,\mathrm{TeV}$ from different MC event generators [3].

of $|\eta| < 0.8$ and $0.15\,\mathrm{GeV}/c < p_{\mathrm{T}} < 2\,\mathrm{GeV}/c$. The event generators yield not only quantitatively, but also qualitatively different results. The default versions of PYTHIA6 (tunes Perugia-0 and Perugia-11) and PYTHIA8 (version 8.150, tune 4C) show an increasing $\langle p_{\mathrm{T}} \rangle_m$ with multiplicity, similar to the behaviour observed in data. However, the PYTHIA6 Perugia-11 NOCR tune, where the colour reconnection mechanism is switched off, and PHOJET exhibit an almost flat behaviour with multiplicity except of a steep rise at low multiplicities similar to the other generators.

The simulations using PYTHIA6 Perugia-0 and PHOJET are available including a full simulation of the ALICE detector response using GEANT3. The results obtained from these full simulations are comparable to the raw measured data in terms of detection efficiency of primary particles, secondary contamination and momentum smearing. In these cases, the raw $M(p_{\mathrm{T}})_m$ can be calculated as a function of N_{acc} and compared directly to the experimental data. The simulations with PYTHIA6 Perugia-11 tunes and with PYTHIA8 have been performed explicitly for this analysis and are available only on the generator level. To facilitate a similar comparison with data, an efficiency filter has been developed and applied to these simulations, which is described in detail in section 3.8. Note, that this filter is not able to reproduce the behaviour of a full detector simulation concerning the event-by-event mean p_{T} fluctuations, but the inclusive p_{T} spectra and, hence, $M(p_{\mathrm{T}})_m$ are reasonably well described.

The raw $M(p_{\mathrm{T}})_m$ is calculated for all MC simulations in pp collisions at $\sqrt{s} = 7\,\mathrm{TeV}$, either from full simulations, or using the efficiency filter. The ratio of $M(p_{\mathrm{T}})_m$ as a
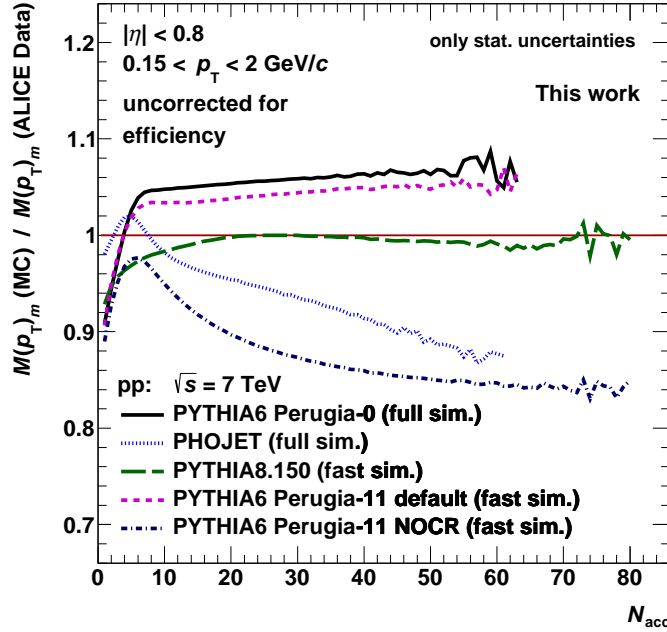
Figure 3.4.: Ratio of $M(p_T)_m$ from MC event generators to the measured ALICE data as a function of N_{acc} in pp collisions at $\sqrt{s}$ = 7 TeV.

function of N_{acc} from MC to ALICE data is presented in figure 3.4. Except of the low multiplicity part with $N_{acc} \lesssim 10$, PYTHIA8 describes the data best showing only small deviations up to 2%. Both default tunes of PYTHIA6 (Perugia-0 and Perugia-11) describe the data trend as well, but exeed the data by about 4–6% for $N_{acc} \gtrsim 5$. PHOJET as well as PYTHIA6 Perugia-11 with the NOCR tune show reasonable agreement with the data only at small multiplicities, but fail to describe the increase with multiplicity.

3.4.2. Mean transverse momentum in Pb–Pb collisions

As in pp collisions, $M(p_T)_m$ increases as a funtion of N_{acc} also in Pb–Pb collisions at $\sqrt{s_{NN}}$ = 2.76 TeV, shown in figure 3.5 together with the pp results, also for $\Delta N_{acc} = 1$ and in the same kinematic acceptance of $|\eta| < 0.8$ and $0.15\,\text{GeV}/c < p_T < 2\,\text{GeV}/c$. At the lowest multiplicities, values around $M(p_T)_m \approx 500\,\text{MeV}/c$ are comparable to those in pp collisions, but the increase with multiplicity is not as steep as in pp and furthermore shows a weak structure of changing slopes up to multiplicities around $N_{acc} \approx 1000$, where almost a saturation of $M(p_T)_m$ is observed. Note, that the raw quantity $M(p_T)_m$ is not corrected for efficiency losses or other detector effects, as described above. Therefore, no definite physics conclusion can be drawn from these observations, neither from the very good agreement of $M(p_T)_m$ in pp and Pb–Pb at very low multiplicities, nor from the subtle details of the trend in Pb–Pb collisions, which may originate from detector effects rather than from the underlying physics.
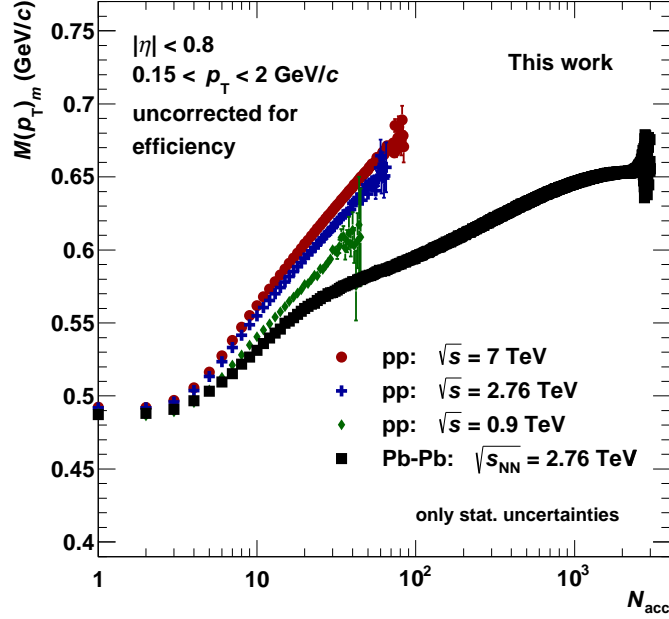
3. Analysis of symmetric systems: pp and Pb–Pb

Figure 3.5.: Comparison of $M(p_\mathrm{T})_m$ as a function of N_acc in pp collisions at $\sqrt{s} = 0.9$, 2.76 and 7 TeV with Pb–Pb collisions at $\sqrt{s_\mathrm{NN}} = 2.76$ TeV.

A fully corrected analysis of $\langle p_\mathrm{T} \rangle_m$ as a function of N_ch has been published by ALICE for all collisions systems including p–Pb collisions in [76], but only up to a multiplicity of $N_\mathrm{ch} = 100^\mathrm{a}$. Within the experimental uncertainties, consistent results at low multiplicities are observed in all three collision systems as well as a clear separation of the trends at higher multiplicities, similar to the observations in the raw $M(p_\mathrm{T})_m$ in the present work. The weak structure in Pb–Pb seen in this analysis in the raw $M(p_\mathrm{T})_m$ occurs in a multiplicity region not covered by the published results.

In figure 3.6, $M(p_\mathrm{T})_m$ is presented as a function of N_acc in Pb–Pb collisions for different interval widths. As in pp, the default calculation of $M(p_\mathrm{T})_m$ is performed in intervals of N_acc with $\Delta N_\mathrm{acc} = 1$. Intervals with $\Delta N_\mathrm{acc} = 100$ are shown for comparison. Furthermore, $M(p_\mathrm{T})_m$ is determined in 5% intervals of the collision centrality and presented as a function of the average number of accepted tracks $\langle N_\mathrm{acc} \rangle$, which is calculated for each interval. The results for $M(p_\mathrm{T})_m$ of all three approaches agree well, which shows that $M(p_\mathrm{T})_m$ as a function of multiplicity does not depend on the interval width.

The large statistics of the data sets used in this work both in pp and in Pb–Pb collisions allow to use narrow intervals for the determination of $M(p_\mathrm{T})_m$, taking $\Delta N_\mathrm{acc} = 1$ for the full multiplicity range in pp collisions and for Pb–Pb collisions up to $N_\mathrm{acc} = 1000$. Above, larger intervals are applied with $\Delta N_\mathrm{acc} = 100$ or 5% in centrality. In this multiplicity region, $M(p_\mathrm{T})_m$ is almost saturated around 650 MeV/c and using the larger

---

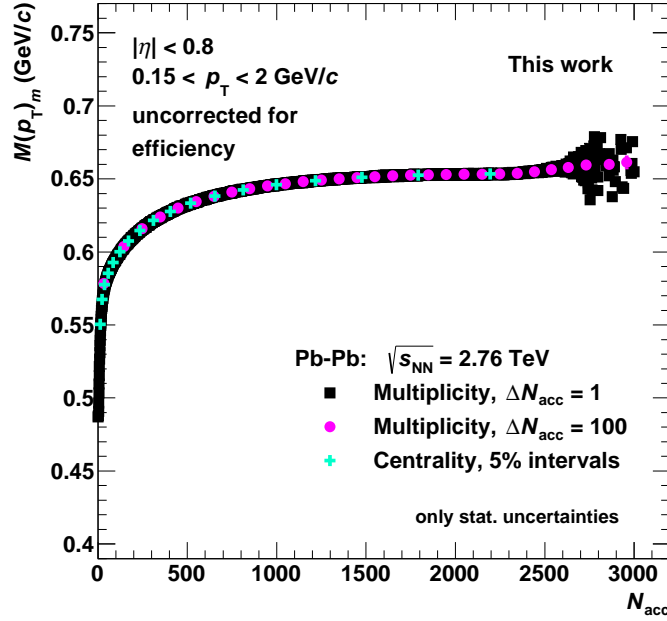$^\mathrm{a}$ Note, that here N_ch is calculated within $|\eta| < 0.3$.

Figure 3.6.: $M(p_T)_m$ as a function of N_{acc} in Pb–Pb collisions at $\sqrt{s_{NN}}$ = 2.76 TeV for two different interval widths in N_{acc} and for 5% centrality intervals.
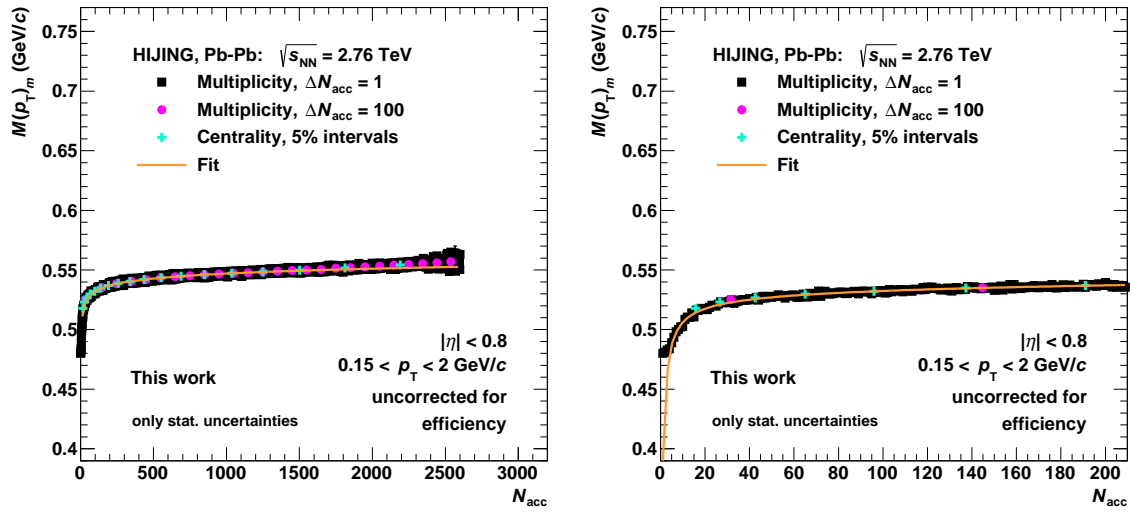

Figure 3.7.: Left: $M(p_T)_m$ as a function of N_{acc} as in figure 3.6, but for the HIJING MC simulation. Also shown is a fit to $M(p_T)_m$, see text for details. Right: The same, but zoomed in on the low multiplicity region.

intervals has the advantage of reducing statistical fluctuations without introducing any significant bias on the results for the mean transverse-momentum fluctuations.
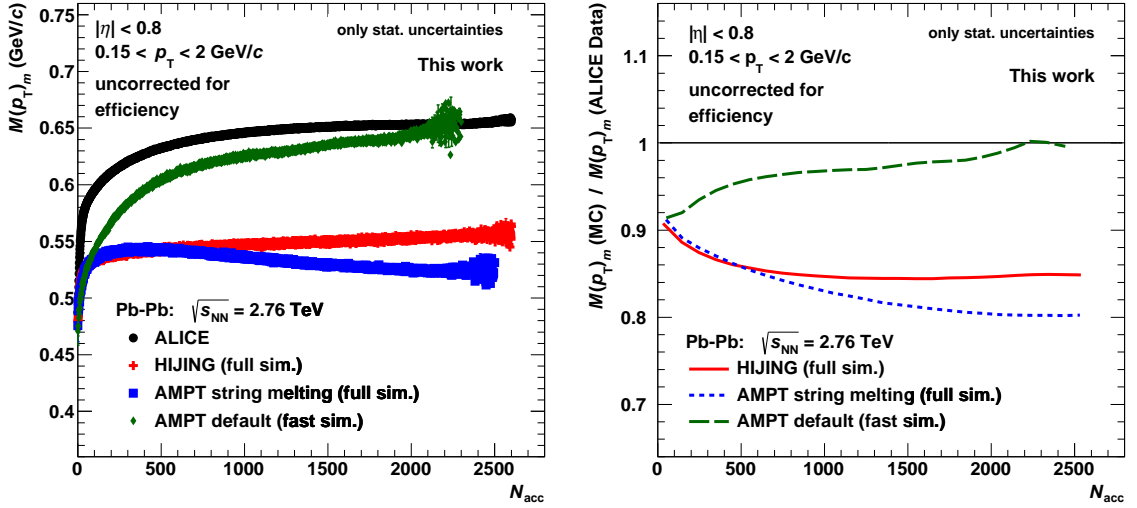
Figure 3.8.: Left: $M(p_\mathrm{T})_m$ as a function of N_acc in Pb–Pb collisions at $\sqrt{s_\mathrm{NN}}$ = 2.76 TeV for ALICE data and the MC simulations HIJING and AMPT (string melting and default). Right: Ratio of the model results to the ALICE data.

Figure 3.7 shows $M(p_\mathrm{T})_m$ as a function of N_acc for the same interval widths as in figure 3.6, but for the full simulation of the MC event generator HIJING. In the left panel of figure 3.7, the full multiplicity range is presented, while the right panel is zoomed in on the low multiplicity part up to $N_\mathrm{acc} \approx 200$. The overall trend is similar to that in data with a steep rise of $M(p_\mathrm{T})_m$ at low multiplicities. However, instead of a saturation around $N_\mathrm{acc} \approx 1000$, the behaviour changes to a weak and almost linear increase of $M(p_\mathrm{T})_m$ at significantly lower $N_\mathrm{acc} \approx 100$–200 reaching at high multiplicities at maximum $M(p_\mathrm{T})_m \approx 550\,\mathrm{MeV}/c$, about $100\,\mathrm{MeV}/c$ lower than in data.

As in data, a good agreement of the different interval widths is observed, although the narrow intervals with $\Delta N_\mathrm{acc} = 1$ show statistical fluctuations due to the significantly lower event statistics available in the MC simulation. In order to smooth these fluctuations, a power-law fit of the form $M(p_\mathrm{T})_m = a \cdot N_\mathrm{acc}^b + c \cdot N_\mathrm{acc}^d + e \cdot N_\mathrm{acc}^f$ is applied over the full N_acc range. The fit yields good agreement with the values of $M(p_\mathrm{T})_m$ with the exceptions of a small deviation at high multiplicities and a significant difference at very low N_acc. Therefore, the fit is used in the range $5 < N_\mathrm{acc} \leq 500$. For $N_\mathrm{acc} \leq 5$, the exact values obtained from the simulation are taken, for $N_\mathrm{acc} > 500$ large intervals with $\Delta N_\mathrm{acc} = 100$ or 5% centrality are used.

A comparison of the ALICE data for $M(p_\mathrm{T})_m$ as a function of N_acc in Pb–Pb collisions at $\sqrt{s_\mathrm{NN}}$ = 2.76 TeV to MC simulations is shown in figure 3.8 (left panel). The results both from HIJING and the version of AMPT with the string melting mechanism enabled are shown including the detector response. In the case of the default AMPT version, only the MC generator level is available. Therefore, the results modified by the efficiency filter are presented, as explained in pp collisions, see section 3.4.1. For
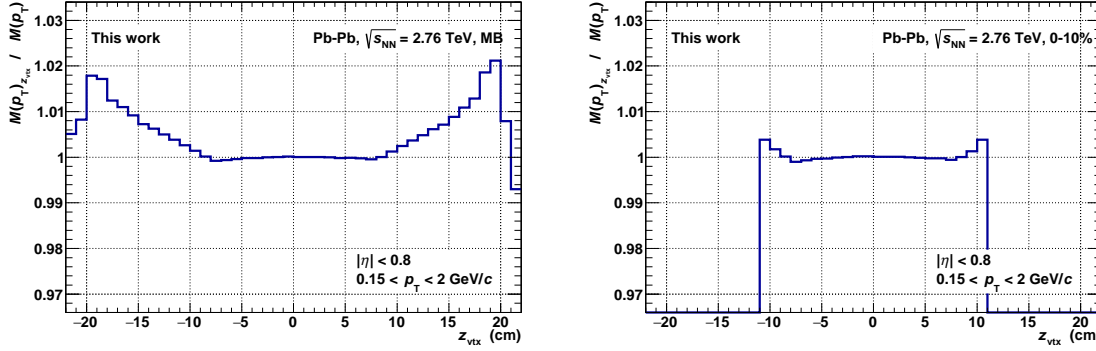
Figure 3.9.: $M(p_T)_{z_{vtx}}$ normalised to the inclusive $M(p_T)|_{|z_{vtx}| \leq 10\,cm}$ within $|z_{vtx}| \leq 10\,cm$ as a function of z_{vtx} in Pb–Pb collisions at $\sqrt{s_{NN}} = 2.76\,TeV$ for minimum-bias events (left) and for 0–10% most central collisions (right).

the data as well as for all MC simulations, intervals with $\Delta N_{acc} = 1$ are used. In the right panel of figure 3.8, the ratios of the model results to the data measured by ALICE are presented.

HIJING shows a qualitatively similar trend as the data, but quantitatively underpredicts the data by about 10–15%. At very low N_{acc}, both versions of AMPT reveal similar values of $M(p_T)_m$ like HIJING, but they show a different trend as a function of multiplicity. The default version of AMPT without string melting increases with N_{acc} even steeper as the data and reaches the data values at high N_{acc}, yielding the best quantitative description of the data. Enabling the string melting mechanism in AMPT results in a significant reduction of $M(p_T)_m$ compared to the default version. Exhibiting a similar trend as HIJING at low N_{acc}, $M(p_T)_m$ even slightly decreases with multiplicity for $N_{acc} \gtrsim 500$, opposite to the behaviour observed in data. This leads to a difference of AMPT with string melting to the measured data of up to 20% at high N_{acc}.

3.4.3. Differential mean transverse momentum

The mean transverse momentum increases clearly with the charged-particle multiplicity. This dependence has to be taken into account in the analysis of mean transverse-momentum fluctuations, which is achieved by calculating $M(p_T)_m$ within narrow intervals of N_{acc}. $M(p_T)$ may also depend on other observables, either due to the underlying physics or because of detector effects. In this section, the dependence of $M(p_T)$ on the position of the primary vertex along the beam direction z_{vtx}, the pseudorapidity η and the azimuthal angle φ is studied.

At first, the dependence of the mean transverse momentum on z_{vtx} is analysed. A shifted acceptance for large distances to the nominal interaction point at $z_{vtx} = 0$ could lead to modifications of the measured spectra and their corresponding $M(p_T)$. In figure 3.9, the mean transverse momentum $M(p_T)_{z_{vtx}}$ is presented as a function of z_{vtx} and normalised to the inclusive $M(p_T)|_{|z_{vtx}| \leq 10\,cm}$ measured within $|z_{vtx}| \leq 10\,cm$.
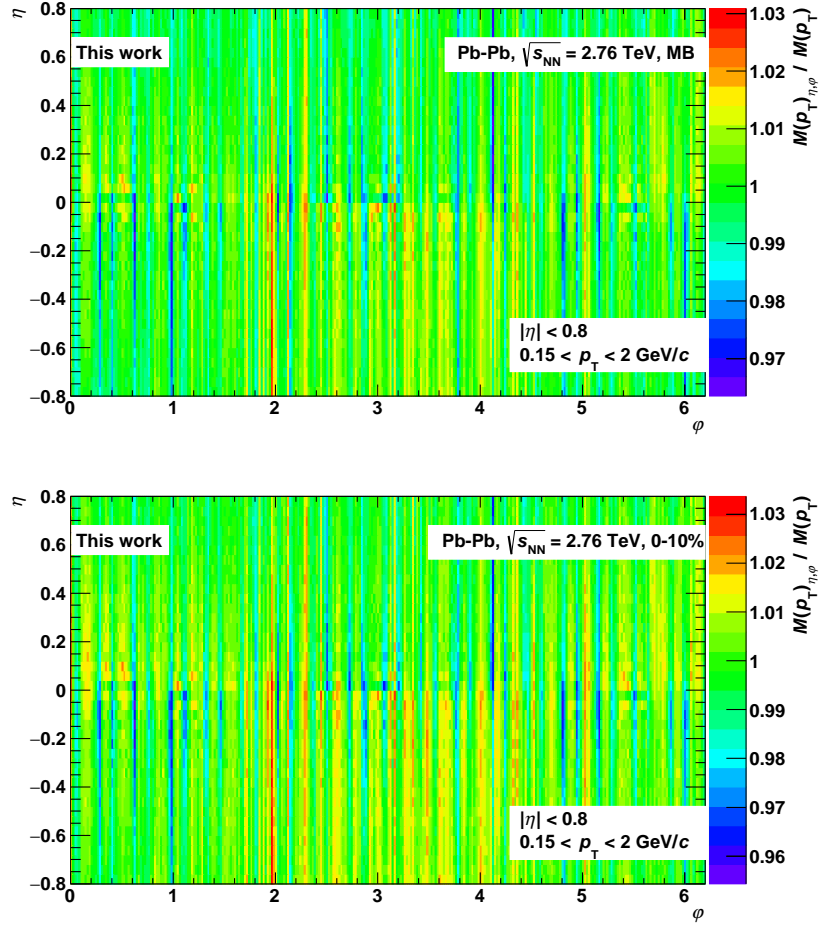
Figure 3.10.: $M(p_\mathrm{T})_{\eta,\varphi}$ normalised to the inclusive $M(p_\mathrm{T})$ as a function of the pseudo-rapidity η and azimuthal angle φ in Pb–Pb collisions at $\sqrt{s_\mathrm{NN}} = 2.76\,\mathrm{TeV}$ for minimum-bias events (upper panel) and 0–10% most central collisions (lower panel).

The left panel shows the result for minimum-bias triggered events in Pb–Pb collisions at $\sqrt{s_\mathrm{NN}} = 2.76\,\mathrm{TeV}$, in the right panel the event sample is reduced to the 0–10% most central collisions. One of the event selection criteria in this analysis is the restriction to events with a difference in z direction to the nominal interaction point of $|z_\mathrm{vtx}| \leq 10\,\mathrm{cm}$. Within this region, $M(p_\mathrm{T})_{z_\mathrm{vtx}}$ is very stable as a function of z_vtx, both for the minimum-bias and the central events, showing only a small increase at the edges of about 0.2%. Any possible bias on the results for C_m due to this small variation is restricted to low N_acc and covered by the systematic uncertainties, where the z-vertex event selection is varied by $\pm 2\,\mathrm{cm}$, see section 3.7. Note, that the selection of central collisions (right panel) does not yield any events with a primary vertex with $|z_\mathrm{vtx}| \geq 11\,\mathrm{cm}$. The reason for this may be the reduced acceptance on one side of
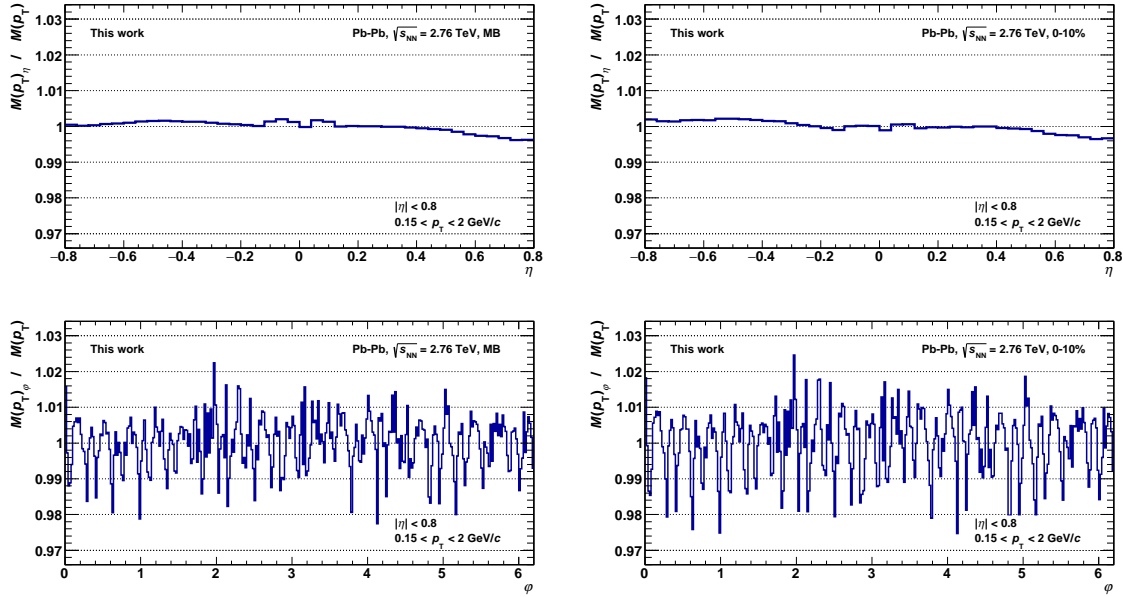
Figure 3.11.: Projections to the η (upper panels) and φ (lower panels) axes of figure 3.10 for minimum bias-events (left) and for 0–10% most central collisions (right).

the experiment for events further apart from the nominal centre leading to a lower maximum number of measured particles.

Figure 3.10 shows the dependence of $M(p_T)_{\eta,\varphi}$ on the pseudorapidity η and azimuthal angle φ in Pb–Pb collisions at $\sqrt{s_{NN}} = 2.76\,\text{TeV}$ for minimum-bias triggered events in the upper panel and for 0–10% most central collisions in the lower panel. In this representation, $M(p_T)_{\eta,\varphi}$ is normalised to the inclusive $M(p_T)$ of the two event samples, respectively. In general, $M(p_T)_{\eta,\varphi}$ is rather uniform in the η-φ plane. However, a periodic structure in the φ direction is observed, leading to deviations from the inclusive $M(p_T)$ of up to 3%. The behaviour is very similar in central collisions compared to the full minimum-bias sample, illustrating that the high track density in central events does not introduce an additional bias in the determination of $M(p_T)$.

Although the dependence on η and φ is clearly much less pronounced than that on the charged-particle multiplicity, it is analysed in more detail, to quantify whether or not it has to be taken into account in the determination of C_m. First, the dependence on η and φ is separated by projections of figure 3.10 on the axes, which is presented in figure 3.11 for the minimum-bias sample in the left panels and for 0–10% most central collisions in the right panels. In both cases, the upper and lower panels show the projection on η and on φ, respectively. No significant deviations of $M(p_T)$ are observed as a function of η, reaching at maximum about 0.4% difference to the inclusive $M(p_T)$ for large values of $|\eta|$, only slightly higher than those found as a function of z_{vtx}. However, a structure is observed for $M(p_T)$ as a function of φ, with an average deviation from the inclusive $M(p_T)$ of about 1% and maximum differences of about 2%
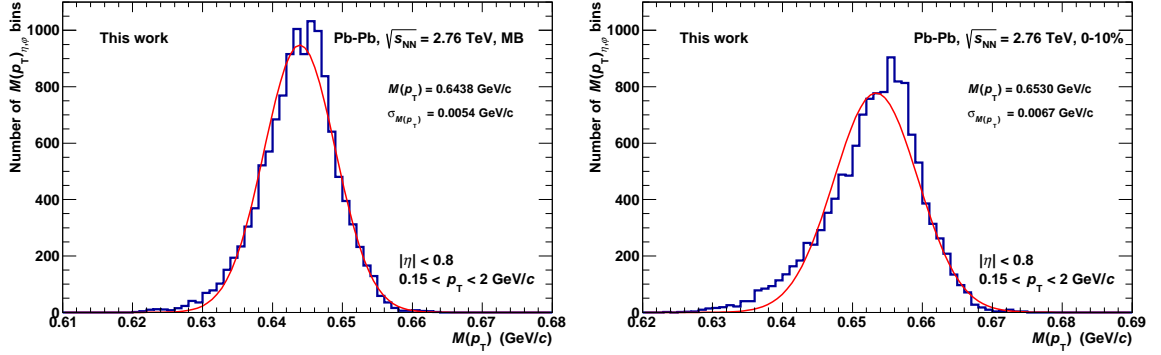
Figure 3.12.: Distributions of the $M(p_T)_{\eta,\varphi}$ values from figure 3.10 for minimum-bias events (left) and for 0–10% most central collisions (right). Also shown are Gaussian fits and the calculated mean and rms values.

for minimum-bias events and 2.5% in central collisions. This structure is potentially related to the separation of the TPC in sectors and especially to the sector boundaries, where the acceptance and efficiency are reduced.

Although the dependence on φ is small, it may have an influence on the calcuation of C_m. As next step, the distributions of the values of $M(p_T)_{\eta,\varphi}$ from the two-dimensional η-φ plane (figure 3.10) are presented in figure 3.12 together with Gaussian fits. In the case of the minimum-bias event sample (left panel), the fit gives a good description of the distribution and results in a mean $M(p_T) = 643.8\,\text{MeV}/c$ and a width $\sigma_{M(p_T)} = 5.4\,\text{MeV}/c$, i.e. about 0.8% of $M(p_T)$. The fit to the distribution of $M(p_T)_{\eta,\varphi}$ in central collisions (right panel) is slightly worse with some deviation from the Gaussian shape especially in the low-$M(p_T)$ part. Nevertheless, the fit yields reasonable estimates for $M(p_T) = 653.0\,\text{MeV}/c$ and $\sigma_{M(p_T)} = 6.7\,\text{MeV}/c$, the latter corresponding to about 1.0% of $M(p_T)$, which is a bit larger than in the minimum-bias case. As also the measured fluctuations in central Pb–Pb collisions are of the order of 1% of $M(p_T)$ (see results, chapter 5), this effect might have a significant influence on the final results and hence has to be investigated further. A toy Monte Carlo simulation is performed in order to address this issue, which is described in detail in section 3.9. It is concluded that the variations of $M(p_T)$ as a function of φ do not have a significant influence on the measurement of mean transverse-momentum fluctuations.

3.5. Two-particle transverse-momentum correlator

In this analysis, event-by-event fluctuations of the mean transverse momentum are quantified using the two-particle transverse-momentum correlator described in sec-

tion 1.5.3. This correlator is defined in equation 1.52 for a subsample m of events corresponding for example to an interval of the charged-particle multiplicity and yields

$$C_m = \frac{1}{\sum_{k=1}^{n_{\text{ev},m}} N_{\text{acc},k}^{\text{pairs}}} \sum_{k=1}^{n_{\text{ev},m}} \sum_{i=1}^{N_{\text{acc},k}} \sum_{j=i+1}^{N_{\text{acc},k}} (p_{\text{T},i} - M(p_\text{T})_m) \cdot (p_{\text{T},j} - M(p_\text{T})_m) \,. \qquad (3.3)$$

The final results are presented in the dimensionless quantity $\sqrt{C_m}/M(p_\text{T})_m$ representing the size of the mean p_T fluctuations relative to $M(p_\text{T})$.

3.5.1. The two-particle correlator as a function of multiplicity

The correlator C_m is calculated using those charged-particle tracks, which have been measured and accepted by the analysis criteria. The number of particle pairs is needed for each single event within this calculation. It is not possible to correct for the not measured particles on the level of a single event and, thus, the number of accepted charged-particle pairs $N_{\text{acc},k}^{\text{pairs}}$ has to be used. Therefore, C_m is at first determined as a function of the accepted multiplicity N_{acc}. In contrast to C_m, the measured multiplicity N_{acc} depends directly on the single-particle detection efficiency. Hence, a correction of the multiplicity is desirable for a comparison of the results to those of other experiments or MC simulations. This is achieved using an unfolding procedure described in section 3.6, where the corrected mean multiplicity $\langle N_{\text{ch}} \rangle$ is determined for each interval of N_{acc}. Finally, the results are presented as a function of the average charged-particle multiplicity density $\langle \mathrm{d}N_{\text{ch}}/\mathrm{d}\eta \rangle$.

Here, the determination of C_m as a function of N_{acc} is described for the experimental data. At first, the same procedure has also been applied to those MC productions, which are available as full simulations including the detector response. This procedure cannot be applied to those simulations, which are only available on the generator level. A simple efficiency filter – described in detail in section 3.8 – cannot solve this issue. Hence, all MC simulations are analysed at the pure generator level and the results for C_m are directly calculated as a function of N_{ch}.

In pp collisions, intervals of $\Delta N_{\text{acc}} = 1$ and $\Delta N_{\text{ch}} = 1$ are used for experimental data and MC generators, respectively. The available statistics are not large enough to employ the same narrow binning also in the case of Pb–Pb collisions. Instead, larger interval widths are used, starting from $\Delta N_{\text{acc}} = 10$ at low multiplicities and increasing with the multiplicity up to $\Delta N_{\text{acc}} = 100$. For MC generators, the binnings are applied in terms of N_{ch}. All interval widths and the corresponding multiplicity ranges used in Pb–Pb collision data and MC simulations are listed in table 3.6. Note, that events with less than 10 accepted tracks are not considered in the Pb–Pb analysis to remove possible contamination from non-hadronic interactions. In both AMPT simulations, a significantly lower number of events is available than in the experimental data or in HIJING. Furthermore, events have only been generated within the 0–80% centrality range for AMPT. Thus, the statistics are not sufficient in the low-multiplicity region and both AMPT simulations are only analysed for $N_{\text{ch}} \geq 25$ and applying interval widths of at least $\Delta N_{\text{ch}} = 25$.

Data/MC		$\Delta N = 10$	$\Delta N = 25$	$\Delta N = 100$
ALICE	Data	$10 \le N_{\mathrm{acc}} < 200$	$200 \le N_{\mathrm{acc}} < 1000$	$N_{\mathrm{acc}} \ge 1000$
HIJING	MC	$10 \le N_{\mathrm{ch}} < 200$	$200 \le N_{\mathrm{ch}} < 500$	$N_{\mathrm{ch}} \ge 500$
AMPT	MC	–	$25 \le N_{\mathrm{ch}} < 100$	$N_{\mathrm{ch}} \ge 100$

Table 3.6.: Interval widths (ΔN) and corresponding multiplicity ranges of ALICE data ($N \triangleq N_{\mathrm{acc}}$) and MC generators ($N \triangleq N_{\mathrm{ch}}$) in Pb–Pb collisions at $\sqrt{s_{\mathrm{NN}}} = 2.76\,\mathrm{TeV}$. The AMPT simulations have significantly lower statistics and are only generated in the 0–80% centrality range.

For interval widths larger than $\Delta N_{\mathrm{acc}} = 1$, the correctly weighted mean number of accepted tracks $\langle N_{\mathrm{acc}} \rangle$ has to be calculated. As C_m does not depend directly on N_{acc}, but on the number of particle pairs $N_{\mathrm{acc}}^{\mathrm{pairs}}$, $\langle N_{\mathrm{acc}} \rangle$ has to be weighted according to the mean number of pairs $\langle N_{\mathrm{acc}}^{\mathrm{pairs}} \rangle$. Rewriting equation 1.47 in terms of N_{acc} and as average of one interval m results in

$$
\begin{aligned}
\langle N_{\mathrm{acc}}^{\mathrm{pairs}} \rangle_m &= 0.5 \cdot \langle N_{\mathrm{acc}} \rangle_m \cdot (\langle N_{\mathrm{acc}} \rangle_m - 1) \\
&= 0.5 \cdot \langle N_{\mathrm{acc}} \rangle_m^2 - 0.5 \cdot \langle N_{\mathrm{acc}} \rangle_m .
\end{aligned}
\tag{3.4}
$$

One of the two mathematically possible solutions of this equation would yield negative $\langle N_{\mathrm{acc}} \rangle_m$, leaving one physically meaningful solution, which is

$$
\langle N_{\mathrm{acc}} \rangle_m = 0.5 + \sqrt{0.25 + 2 \cdot \langle N_{\mathrm{acc}}^{\mathrm{pairs}} \rangle_m} .
\tag{3.5}
$$

In each interval m, $\langle N_{\mathrm{acc}}^{\mathrm{pairs}} \rangle_m$ is calculated by summing up the $N_{\mathrm{acc},k}^{\mathrm{pairs}}$ of all events k in that interval and dividing by the corresponding number of events. With equation 3.5, the correctly weighted $\langle N_{\mathrm{acc}} \rangle_m$ is obtained.

3.5.2. The two-particle correlator as a function of centrality

In Pb–Pb collisions, C_m and $\sqrt{C_m}/M(p_{\mathrm{T}})_m$ are also calculated as a function of the collision centrality. In this analysis, interval widths of 5% are used ranging from 0–5% most central collisions up to 75–80%. The determination of the centrality is described in section 2.4.4. Here, the V0 amplitude, i.e. the sum of the multiplicities measured in the V0A and V0C arrays, is applied to obtain the centrality percentage for each event. With the help of a Glauber MC simulation, the average centrality percentile of each interval is translated into a mean number of participating nucleons $\langle N_{\mathrm{part}} \rangle$ [139, 149]. The mean number of participating nucleons $\langle N_{\mathrm{part}} \rangle$ is connected to the average charged-particle multiplicity density $\langle \mathrm{d}N_{\mathrm{ch}}/\mathrm{d}\eta \rangle$ via the relation

$$
\langle \mathrm{d}N_{\mathrm{ch}}/\mathrm{d}\eta \rangle = (1.33 \pm 0.08) \cdot \langle N_{\mathrm{part}} \rangle^{(1.19 \pm 0.01)} ,
\tag{3.6}
$$

which is described in [149]. Hence, $\langle \mathrm{d}N_{\mathrm{ch}}/\mathrm{d}\eta \rangle$ can be calculated using the centrality-based observable $\langle N_{\mathrm{part}} \rangle$ instead of the accepted multiplicity $\langle N_{\mathrm{acc}} \rangle$. These two alternatives can be compared at the level of the final results. Figure 3.13 shows the results
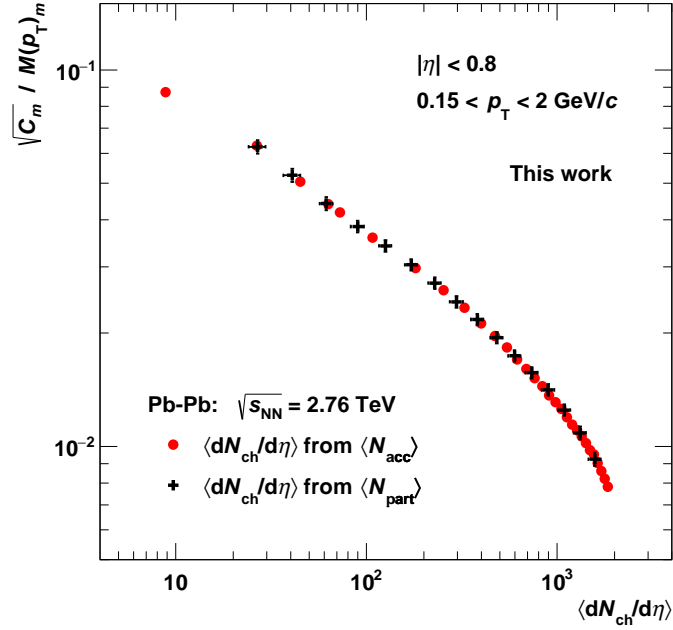
Figure 3.13.: Relative fluctuation $\sqrt{C_m}/M(p_T)_m$ as a function of $\langle \mathrm{d}N_{\mathrm{ch}}/\mathrm{d}\eta \rangle$ in Pb–Pb collisions at $\sqrt{s_{\mathrm{NN}}}$ = 2.76 TeV, calculated in intervals of $\langle N_{\mathrm{acc}} \rangle$ and $\langle N_{\mathrm{part}} \rangle$.

for $\sqrt{C_m}/M(p_T)_m$ as a function of $\langle \mathrm{d}N_{\mathrm{ch}}/\mathrm{d}\eta \rangle$ in Pb–Pb collisions at $\sqrt{s_{\mathrm{NN}}}$ = 2.76 TeV as obtained from $\langle N_{\mathrm{acc}} \rangle$ and from $\langle N_{\mathrm{part}} \rangle$. Both versions are in good agreement, which supports the perception that both are feasible and correctly implemented.

3.6. Multiplicity determination

The results for the two-particle correlator C_m and the relative dynamical fluctuation $\sqrt{C_m}/M(p_T)_m$ are presented as a function of the average charged-particle multiplicity density $\langle \mathrm{d}N_{\mathrm{ch}}/\mathrm{d}\eta \rangle$ and in Pb–Pb collisions in addition as a function of the collision centrality. Both $\langle \mathrm{d}N_{\mathrm{ch}}/\mathrm{d}\eta \rangle$ and centrality are corrected for detector effects and therefore well suited for comparisons of the results to other experiments or theoretical models. First, C_m has to be calculated as a function of the accepted multiplicity N_{acc}, as described in section 3.5.1. In this section, the procedures used to obtain $\langle \mathrm{d}N_{\mathrm{ch}}/\mathrm{d}\eta \rangle$ for each interval in N_{acc} are discussed.

3.6.1. Multiplicity unfolding in pp collisions

In pp collisions, the unfolding of the measured multiplicity N_{acc} to the true N_{ch} is performed using full simulations of the PYTHIA6 event generator with the default Perugia-0 tune including the detector response modelled with GEANT3. The unfold-

ing procedure described in the following is based on the approach outlined in [162]. It is applied for each collision energy, i.e. $\sqrt{s}$ = 0.9, 2.76 and 7 TeV, separately.

First, the detector response matrix relating the accepted N_{acc} to the true N_{ch} is created. For this purpose, the analysis of the MC events is executed simultaneously on the generator level and on the full simulation. For each event k, the number of accepted particles $N_{\mathrm{acc},k}$ in the full simulation is counted within the kinematic region used for the analysis of the experimental data, which is $|\eta| < 0.8$ and $0.15\,\mathrm{GeV}/c < p_{\mathrm{T}} < 2\,\mathrm{GeV}/c$. In addition, the number of true primary charged particles $N_{\mathrm{ch},k}$ within $|\eta| < 0.8$ is obtained from the generator level. Here, the selection on p_{T} is not applied to get the entire number of particles within this pseudorapidity range. One entry of $N_{\mathrm{acc},k}$ as a function of $N_{\mathrm{ch},k}$ is filled in the detector response matrix for each event.

The matrix obtained in this way is purely based on the MC simulation. While the modelling of the detector response with GEANT3 yields a good description of the behaviour of the real experimental setup, the physical processes within the collision events cannot be simulated precisely and, thus, the resulting multiplicity distribution does not have to agree with the experimentally measured one. Therefore, the response matrix has to be unfolded using the experimentally measured N_{acc} distribution. The unfolding method described in [162] is applied to obtain the unfolded matrix relating the experimentally measured N_{acc} to the corrected N_{ch}. This unfolded matrix is used to calculate the average corrected number of particles $\langle N_{\mathrm{ch}} \rangle$ for each value of N_{acc}.

This procedure has been verified in the analysis of $\langle p_{\mathrm{T}} \rangle$ as a function of N_{ch} in [76]. Here, the separate correction of $\langle p_{\mathrm{T}} \rangle$ together with a multiplicity unfolding as used in the present analysis is compared to a different approach using the weighted $\langle p_{\mathrm{T}} \rangle$ of different intervals in N_{acc} to build the corresponding $\langle p_{\mathrm{T}} \rangle$ of one interval in N_{ch}. The results of these two approaches are in good agreement supporting the procedure applied in the present work. In the case of C_m or $\sqrt{C_m}/M(p_{\mathrm{T}})_m$, a similar study is not feasible, as the multiplicity and accordingly the number of particle pairs is needed for the calculation of the quantity itself, which is not the case for $\langle p_{\mathrm{T}} \rangle$.

Both N_{acc} and N_{ch} are determined within $|\eta| < 0.8$, which is important to preserve a good multiplicity resolution within the response matrix. However, the final results are presented as a function of $\langle \mathrm{d}N_{\mathrm{ch}}/\mathrm{d}\eta \rangle$, i.e. the average charged-particle multiplicity density per unit of pseudorapidity corresponding to $|\eta| < 0.5$. As the distribution of charged particles is almost flat as a function of η around midrapidity, to first order $\langle N_{\mathrm{ch}} \rangle$ has to be divided by the factor $f_{\mathrm{mult}} = 0.8/0.5 = 1.6$ to obtain $\langle \mathrm{d}N_{\mathrm{ch}}/\mathrm{d}\eta \rangle$. In detail, a small dip is observed around $\eta \approx 0$, leading to slightly smaller values of $\langle \mathrm{d}N_{\mathrm{ch}}/\mathrm{d}\eta \rangle$. Hence, the exact factors are slightly higher than 1.6. They are determined separately for each collision energy and listed in table 3.7.

In this work, the experimental results for $\sqrt{C_m}/M(p_{\mathrm{T}})_m$ as a function of $\langle \mathrm{d}N_{\mathrm{ch}}/\mathrm{d}\eta \rangle$ are compared to several MC simulations in pp collisions at $\sqrt{s}$ = 7 TeV. The MC generator level is used for this comparison. Hence, no corrections for efficiency losses or other detector effects have to be applied in the determination of $\langle \mathrm{d}N_{\mathrm{ch}}/\mathrm{d}\eta \rangle$. Nevertheless, a correlation matrix is created for each MC generator, similar to those used for the multiplicity unfolding of the experimental data. However, both axes of this matrix contain true multiplicities corresponding to the true multiplicity N_{ch} within $|\eta| < 0.8$

$\sqrt{s}$	f_{mult}
0.9 TeV	1.6048
2.76 TeV	1.6003
7.0 TeV	1.6042

Table 3.7.: Factors f_{mult} for the conversion of $\langle N_{\text{ch}} \rangle$ (within $|\eta| < 0.8$) to $\langle \mathrm{d}N_{\text{ch}}/\mathrm{d}\eta \rangle$ (i.e. $|\eta| < 0.5$) in pp collisions at $\sqrt{s}$ = 0.9, 2.76 and 7 TeV.

and to the same quantity with the additional selection of $0.15\,\text{GeV}/c < p_{\text{T}} < 2\,\text{GeV}/c$, denoted by $N_{\text{ch}}^{p_{\text{T}}}$. As both multiplicities correspond to true generated multiplicities, no unfolding procedure has to be used. Instead, the average multiplicity $\langle N_{\text{ch}} \rangle$ can be calculated directly for each value of $N_{\text{ch}}^{p_{\text{T}}}$. Finally, $\langle N_{\text{ch}} \rangle$ has to be divided by the factor f_{mult} to obtain $\langle \mathrm{d}N_{\text{ch}}/\mathrm{d}\eta \rangle$. For the MC generators, these factors are listed in table 3.8.

Generator	Version	Tune	f_{mult}
PHOJET	1.12	–	1.6153
PYTHIA6	6.421	Perugia-0	1.6122
PYTHIA6	6.425	Perugia-11 default	1.6129
PYTHIA6	6.425	Perugia-11 NOCR	1.6141
PYTHIA8	8.150	4C	1.6138

Table 3.8.: Factors f_{mult} for the conversion of $\langle N_{\text{ch}} \rangle$ (within $|\eta| < 0.8$) to $\langle \mathrm{d}N_{\text{ch}}/\mathrm{d}\eta \rangle$ (i.e. $|\eta| < 0.5$) for MC event generators in pp collisions at $\sqrt{s}$ = 7 TeV.

3.6.2. Multiplicity determination in Pb–Pb collisions

The unfolding procedure described above in the case of pp collisions is not carried out explicitly for Pb–Pb collisions in this analysis. Instead, the published ALICE results for $\langle \mathrm{d}N_{\text{ch}}/\mathrm{d}\eta \rangle$ within intervals of the collision centrality are used from [139]. These values are related to the present measurement by calculating $\langle N_{\text{acc}} \rangle$ in the same centrality intervals, i.e. 0–5%, 5–10% and in 10% steps from 10–20% to 70–80% and within the kinematic acceptance of $|\eta| < 0.8$ and $0.15\,\text{GeV}/c < p_{\text{T}} < 2\,\text{GeV}/c$. Figure 3.14 (left panel) shows $\langle N_{\text{acc}} \rangle$ from this analysis as a function of $\langle \mathrm{d}N_{\text{ch}}/\mathrm{d}\eta \rangle$ from the published results in [139]. As expected, a linear relation is observed over the full centrality range under study, allowing interpolation to assign a value for $\langle \mathrm{d}N_{\text{ch}}/\mathrm{d}\eta \rangle$ to any value of $\langle N_{\text{acc}} \rangle$.

This procedure is applied to the MC event generators in Pb–Pb collisions in a similar way as in pp collisions. Here, $\langle N_{\text{ch}}^{p_{\text{T}}} \rangle$ is determined as the true mean number of charged particles within $|\eta| < 0.8$, $0.15\,\text{GeV}/c < p_{\text{T}} < 2\,\text{GeV}/c$ and a given centrality interval. $\langle \mathrm{d}N_{\text{ch}}/\mathrm{d}\eta \rangle$ represents the true average charged-particle multiplicity density per unit of pseudorapidity, i.e. within $|\eta| < 0.5$ and with no selection on p_{T}. Both values are obtained from the MC generator level. $\langle N_{\text{ch}}^{p_{\text{T}}} \rangle$ is plotted as a function of $\langle \mathrm{d}N_{\text{ch}}/\mathrm{d}\eta \rangle$ and
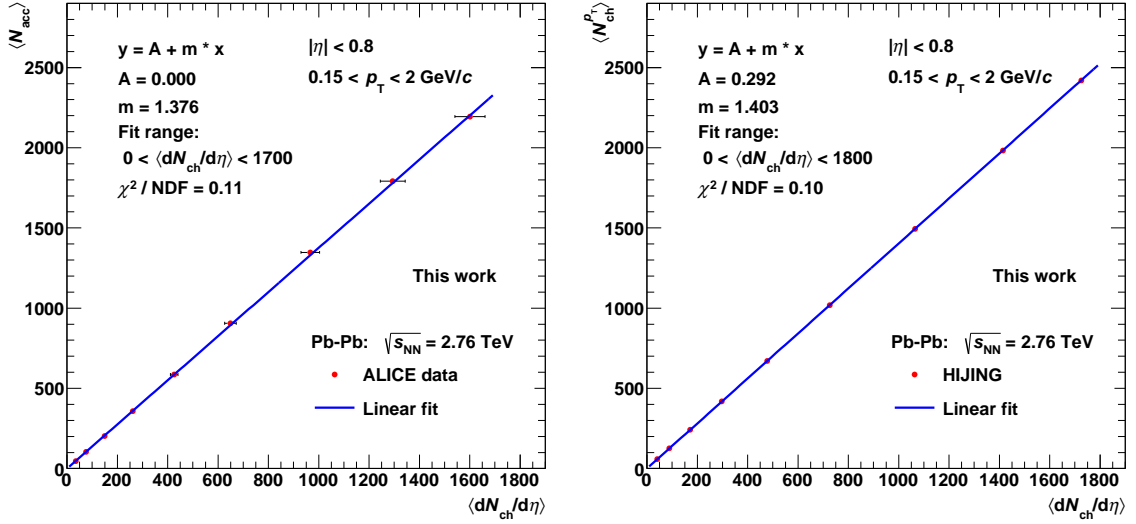
Figure 3.14.: Left: ALICE data for $\langle N_{\mathrm{acc}}\rangle$ as a function of $\langle \mathrm{d}N_{\mathrm{ch}}/\mathrm{d}\eta\rangle$ in Pb–Pb collisions at $\sqrt{s_{\mathrm{NN}}} = 2.76\,\mathrm{TeV}$ with $\langle \mathrm{d}N_{\mathrm{ch}}/\mathrm{d}\eta\rangle$ from [139]. Right: $\langle N_{\mathrm{ch}}^{p_{\mathrm{T}}}\rangle$ as a function of $\langle \mathrm{d}N_{\mathrm{ch}}/\mathrm{d}\eta\rangle$ in HIJING.

Data/MC		Version	Tune	A	m
ALICE	Data	–	–	0.000	1.376
HIJING	MC	1.36	no jet quenching	0.292	1.403
AMPT	MC	1.25	default	0.000	1.460
AMPT	MC	2.25	string melting	0.556	1.405

Table 3.9.: Linear fits of the form $y = A + m \cdot x$ for the transformation of $\langle N_{\mathrm{acc}}\rangle$ or $\langle N_{\mathrm{ch}}^{p_{\mathrm{T}}}\rangle$ (y) to $\langle \mathrm{d}N_{\mathrm{ch}}/\mathrm{d}\eta\rangle$ (x) in Pb–Pb collisions at $\sqrt{s_{\mathrm{NN}}} = 2.76\,\mathrm{TeV}$ for ALICE data and several MC event generators.

a linear fit is performed, which is presented in figure 3.14 (right panel) for HIJING. Table 3.9 summarises the fit parameters of the linear fits for the ALICE data and for the MC generators in Pb–Pb collisions.

3.7. Systematic uncertainties

The relative dynamical mean transverse-momentum fluctuation $\sqrt{C_m}/M(p_{\mathrm{T}})_m$ is robust against particle detection efficiency losses, as described in section 3.5. Nevertheless, it is affected by detector effects, like event-by-event variations of the detection efficiency, contamination with secondary particles and the p_{T} resolution. Event and track selection criteria are applied (see sections 3.2 and 3.3) to reduce the contamination by secondaries and low-quality tracks, while at the same time keeping the efficiency for primary particles as high as possible. These criteria themselves may
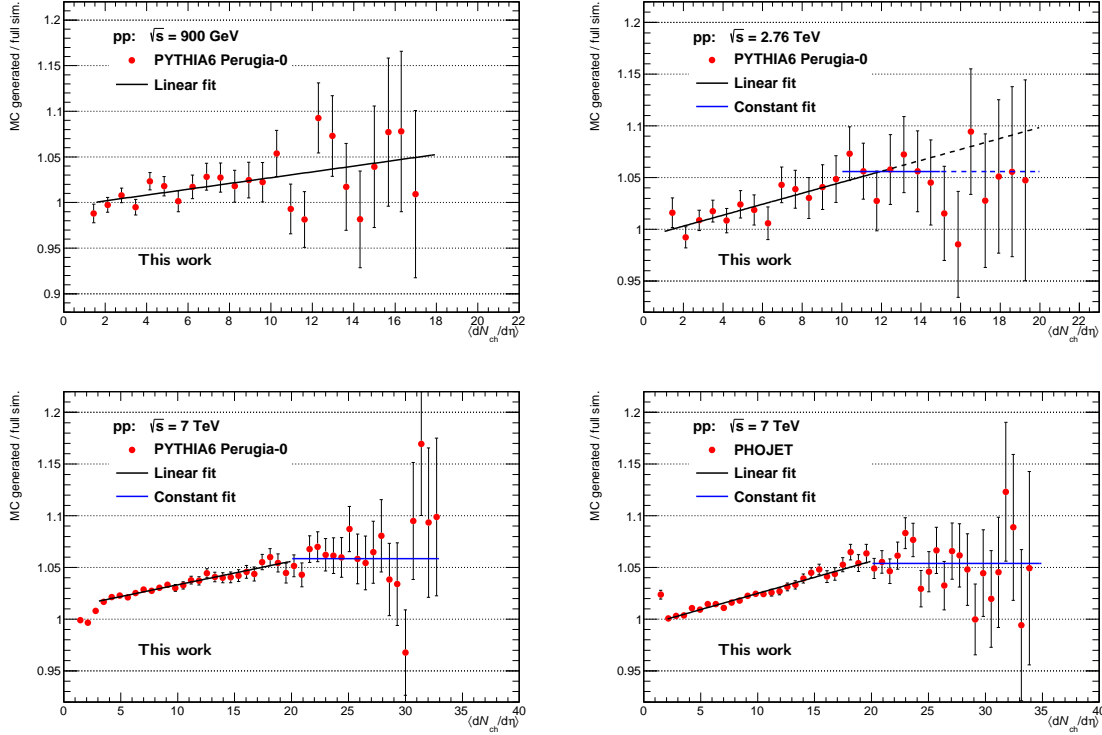
Figure 3.15.: Ratio of $\sqrt{C_m}/\langle p_T \rangle_m$ from the MC generator level to the full simulation using PYTHIA6 Perugia-0 in pp collisions at $\sqrt{s} = 0.9\,\text{TeV}$ (upper left), $\sqrt{s} = 2.76\,\text{TeV}$ (upper right) and $\sqrt{s} = 7\,\text{TeV}$ (lower left). For comparison, PHOJET is shown at $\sqrt{s} = 7\,\text{TeV}$ (lower right).

introduce some biases on the measurement of $\sqrt{C_m}/M(p_T)_m$. The influence of all of these detector- and analysis-related effects on the results has to be estimated.

An event-by-event analysis as in the present work cannot be corrected for the effects explained above in a straight-forward way. Comparisons of the results of MC event generators to their corresponding full simulations including the detector response could be used to correct the experimental data on the level of the final results. This procedure would in itself introduce a new source of uncertainty and hence it would not reduce significantly the overall uncertainties. Therefore, these differences are assigned to the experimental data as systematic uncertainties. In addition, variations of the selection criteria and the tracking scheme are studied. The influence of these variations on the final results is small and the corresponding differences are added to the systematic uncertainties. Adding the single contributions in quadrature results in total systematic uncertainties of about 4–8%. The systematic uncertainties are estimated separately for each collision energy in pp collisions, and for Pb–Pb collisions. The contributions to the uncertainties are explained in detail in the following and summarised in table 3.11 at the end of this section on page 85. In pp collisions, also the inclusive values for $\sqrt{C}/M(p_T)$ are calculated and the uncertainties are listed in table 3.12 on page 86.

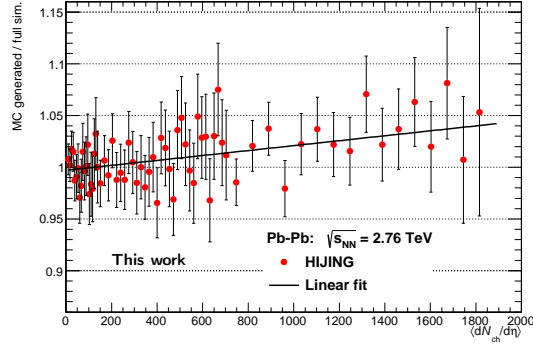## 3. Analysis of symmetric systems: pp and Pb–Pb

Figure 3.16.: Ratio of $\sqrt{C_m}/\langle p_T \rangle_m$ from the MC generator level to the full simulation using HIJING in Pb–Pb collisions at $\sqrt{s_{NN}} = 2.76\,\mathrm{TeV}$.

One of the most important contributions to the systematic uncertainties arises from the comparison of the MC generator level to the full simulations. For this study, the true results for $\sqrt{C_m}/\langle p_T \rangle_m$ as a function of $\langle \mathrm{d}N_{ch}/\mathrm{d}\eta \rangle$ are calculated from the generated MC events and compared to the the raw $\sqrt{C_m}/M(p_T)_m$ obtained from the full simulations. For the latter, the corresponding $\langle \mathrm{d}N_{ch}/\mathrm{d}\eta \rangle$ necessary for a direct comparison is obtained as described in section 3.6. In pp collisions, PYTHIA6 is used with the Perugia-0 tune. The results are presented in figure 3.15 as a ratio of generated over full simulations for all three collision energies, separately. In all cases, a similar behaviour is observed. At very low multiplicities, the differences between generated and fully simulated events are negligible. With increasing multiplicity, a linear increase of the deviations is found, which is saturating at a difference of about 6%. Up to that point, a linear fit is performed for each energy and the fit results are used as systematic uncertainty. Above, a constant uncertainty of 6% is assumed. In addition, results obtained with PHOJET are shown for $\sqrt{s} = 7\,\mathrm{TeV}$, confirming the behaviour observed with PYTHIA6. In Pb–Pb collisions, the comparison of MC generated events with the full simulation is performed with HIJING. The result is shown in figure 3.16, again as the ratio of the generated over the full simulation as a function of $\langle \mathrm{d}N_{ch}/\mathrm{d}\eta \rangle$. In peripheral collisions, i.e. at low multiplicities, the differences are negligible as in pp. A moderate linear increase is found with rising multiplicity over the full range, reaching at maximum about 4% in most central collisions. The result of a linear fit covering the complete multiplicity range is used as systematic uncertainty.

In section 3.3.1, several tracking schemes are described. As default, the TPC-stand-alone tracking is used in this analysis and a hybrid tracking scheme is applied for comparison. The differences of the two schemes are added as a contribution to the systematic uncertainties. In pp collisions, the size of this difference is about 4%, independent of the multiplicity. In Pb–Pb collisions, a multiplicity dependence is observed and the difference reaches at most 5%. A TPC-ITS tracking scheme always requiring the ITS information suffers from a non-uniform azimuthal (φ) distribution of
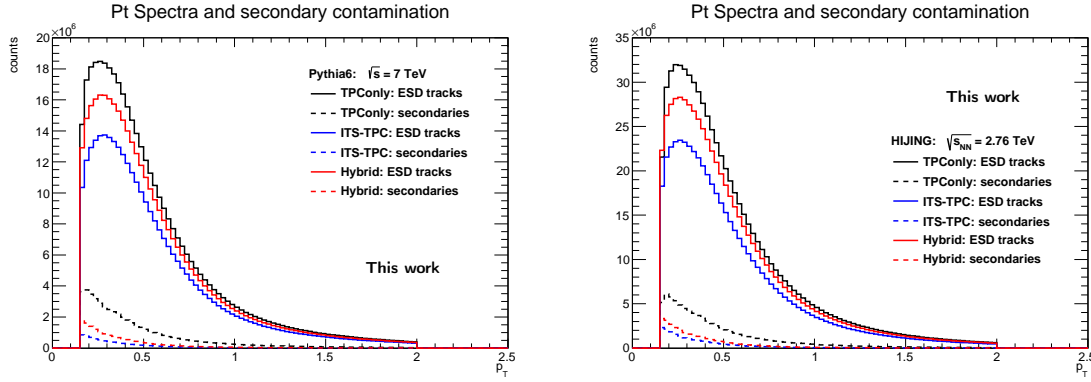
Figure 3.17.: Transverse-momentum spectra and secondary contamination for several tracking schemes studied with PYTHIA6 Perugia-0 for pp collisions at $\sqrt{s}$ = 7 TeV (left) and with HIJING for Pb–Pb collisions at $\sqrt{s_{\mathrm{NN}}}$ = 2.76 TeV (right).

the tracks, which can introduce large biases in any correlation or fluctuation analysis and is therefore not used for the evaluation of the uncertainties.

In the hybrid tracking scheme, the track distribution is also not as uniform in φ as in the TPC-standalone case. However, the hybrid tracking is expected to have a significantly lower contamination from secondary particles. The secondary contamination of the different tracking schemes is estimated using full MC simulations. In figure 3.17, the p_{T} spectra of all charged particles and explicitly of secondary particles are presented within the p_{T} range used in this analysis, which is $0.15\,\mathrm{GeV}/c < p_{\mathrm{T}} < 2\,\mathrm{GeV}/c$. The spectra are shown for the three different tracking schemes, using PYTHIA6 Perugia-0 for pp collisions at $\sqrt{s}$ = 7 TeV (left panel of figure 3.17) and HIJING for Pb–Pb collisions at $\sqrt{s_{\mathrm{NN}}}$ = 2.76 TeV (right panel). Taking the ratio of the secondary over all particles, the size of the secondary contamination can be determined. The lowest contamination is reached in the TPC-ITS tracking with about 2.5–4%. The hybrid tracking shows a slightly higher contamination of about 4–5%, whereas the TPC-standalone tracking exhibits significantly more secondary particles of about 12%. Thus, the comparison of the TPC-standalone and the hybrid tracking contains an estimate of the influence of the secondary contamination on the results for $\sqrt{C_m}/M(p_{\mathrm{T}})_m$. The difference of the MC generator level to the full simulation and the comparison of the TPC-standalone and hybrid tracking schemes constitute the two major contributions to the total systematic uncertainties in all data sets used in this analysis. In addition, the event and track selection criteria are varied within reasonable limits to estimate further uncertainties resulting from the analysis procedure. The variations are summarised in table 3.10.

At the event level, minor contributions to the systematic uncertainties arise from the determination of the primary collision vertex and the corresponding selection criteria. The cut on the maximum difference along the beam axis (i.e. in z direction) of the reconstructed vertex to the nominal interaction point has a default value of 10 cm

3. Analysis of symmetric systems: pp and Pb–Pb

Selection criterion	Default	Variations
Vertex-z-position cut	10 cm	8 cm, 12 cm
Vertex estimator	Global tracks	SPD tracklets, TPC tracks
Vertex-z-difference cut	10 cm	2 cm, no cut
Min. TPC space points	70	60, 80
TPC χ^2/d.o.f.	4.0	3.5, 5.0
DCA to vertex (xy)	2.4 cm	1.8 cm, 3.0 cm
DCA to vertex (z)	3.2 cm	2.4 cm, 4.0 cm
Magnetic field polarity	Both	pos. and neg. separately
Centrality intervals	5%	10%

Table 3.10.: Event and track selection criteria together with their default values in the TPC-standalone analysis and the variations used for the estimation of the systematic uncertainties.

and is varied by ± 2 cm. The effect of these variations on $\sqrt{C_m}/M(p_\mathrm{T})_m$ is small or even negligible in pp collisions and reaches 0.5–1% in Pb–Pb collisions. In the standard analysis, global TPC-ITS tracks are used for the determination of the vertex. As alternatives, vertex estimators using only SPD tracklets or only TPC tracks are applied. The choice of the vertex determination has no significant effect in Pb–Pb and only a small effect in pp collisions, where it reaches at maximum 2% for very low multiplicities. The default value for the maximum difference between the z positions of the TPC-standalone and the global vertex is set to 10 cm. As variations, the analysis is redone with a more stringent value of 2 cm and completely removing this criterion. A sizeable effect of about 2–3% is found only in low-multiplicity pp and peripheral Pb–Pb collisions.

At the track level, several of the track selection criteria are varied separately within the standard analysis using the TPC-standalone tracking. The minimum number of TPC space points per track (default: 70) is changed by ± 10. In pp collisions, this shows a variation in $\sqrt{C_m}/M(p_\mathrm{T})_m$ of 1–3%, increasing with multiplicity and with a slight dependence on the collision energy. In Pb–Pb collisions, only a weak dependence on multiplicity is found with values of 2–3%. The maximum TPC χ^2 per degree of freedom of the momentum fit is changed from the default 4.0 to 3.5 and 5.0, showing no significant effect in all collision systems and energies in the present study. The default values of the maximum distance of closest approach (DCA) of each track to the primary vertex are 3.2 cm along the beam (z) direction and 2.4 cm in the transverse (xy) plane. Both values are changed simultaneously by ± 25% resulting in variations of $\sqrt{C_m}/M(p_\mathrm{T})_m$ of about 0.5–1.5% with a small dependence on collision system and energy.

Most of the data presented in this work have been taken with a negative magnetic field polarity of the solenoid. An exception is the Pb–Pb data sample, where the field polarity is reversed (i.e. positive) for more than half of the events. After the physics selection procedure and all event and track selection criteria have been applied, $7.1 \cdot 10^6$

Collision system $\sqrt{s_{NN}}$	pp 0.9 TeV	pp 2.76 TeV	pp 7 TeV	Pb–Pb 2.76 TeV
Vertex-z-position cut	0–0.5%	<0.1%	<0.1%	0.5–1%
Vertex estimator	0–2%	0.5–2%	0.5–2%	<0.1%
Vertex-z-difference cut	0–1.5%	0–3%	0–2%	0–2%
Min. TPC space points	1.5–3%	1–2%	1–3%	2–3%
TPC χ^2/d.o.f.	<0.1%	<0.1%	<0.1%	<0.1%
DCA to vertex	1%	1–1.5%	0.5–1%	0.5–1%
Magnetic field polarity	0.5%	0.5%	0.5%	0.5%
Centrality intervals	–	–	–	1–3%
TPC-only vs. hybrid tracking	4%	4%	4%	1–5%
MC generator vs. full sim.	0–6%	0–6%	0–6%	0–4%
Total	**4.4–7.7%**	**4.4–7.6%**	**4.4–7.9%**	**4.2–7.4%**

Table 3.11.: Contributions to the systematic uncertainties on $\sqrt{C_m}/M(p_T)_m$ in pp collisions at $\sqrt{s}$ = 0.9, 2.76 and 7 TeV and Pb–Pb collisions at $\sqrt{s_{NN}}$ = 2.76 TeV. Ranges are given when the uncertainties depend on $\langle dN_{ch}/d\eta \rangle$ or centrality. The single contributions are added in quadrature to obtain the total uncertainties.

events with negative field and $9.5 \cdot 10^6$ events with positive field are available. The default analysis is performed on the full Pb–Pb data set combining the two field polarities, but they are also studied separately, exhibiting a small difference of about 0.5% in $\sqrt{C_m}/M(p_T)_m$, which is added to the systematic uncertainties. As in the pp data samples under study no subsets with positive field polarity exist, the value of 0.5% obtained in Pb–Pb collisions is used as an estimate.

Finally, the effect of finite centrality intervals in Pb–Pb collisions is studied by changing the interval width from 5% to 10%. The difference of about 1–3% depends on the centrality and is included in the systematic uncertainties. Different interval sizes are also studied in terms of the accepted multiplicity (see section 3.5.1), which is not added as a separate uncertainty. In pp collisions, intervals with ΔN_{acc} = 1 are used in all cases. Therefore, no uncertainty due to the interval width is expected.

For each data set, the individual contributions are added in quadrature to obtain the total systematic uncertainties on $\sqrt{C_m}/M(p_T)_m$. All contributions and the resulting total uncertainties are listed in table 3.11. In pp collisions, also the inclusive relative dynamical fluctuation $\sqrt{C}/M(p_T)$ is evaluated. The same systematic studies are performed as in the case of the multiplicity-dependent analyses. Table 3.12 summarises the contributions to the systematic uncertainties of $\sqrt{C}/M(p_T)$ in terms of absolute values rather than relative ones. The total systematic uncertainties are again calculated by adding the individual contributions in quadrature. Their size relative to $\sqrt{C}/M(p_T)$ of about 4–6% is comparable to the total uncertainties of $\sqrt{C_m}/M(p_T)_m$.

Collision system $\sqrt{s}$	pp 0.9 TeV	pp 2.76 TeV	pp 7 TeV
Vertex-z-position cut	0.0001	0.0000	0.0001
Vertex estimator	0.0006	0.0012	0.0009
Vertex-z-difference cut	0.0016	0.0028	0.0018
Min. TPC space points	0.0024	0.0016	0.0020
TPC χ^2/d.o.f.	0.0001	0.0000	0.0000
DCA to vertex	0.0008	0.0013	0.0009
Magnetic field polarity	0.0006	0.0006	0.0006
TPC-only vs. hybrid tracking	0.0017	0.0042	0.0027
MC generator vs. full sim.	0.0029	0.0043	0.0050
Total	**0.0046**	**0.0071**	**0.0064**

Table 3.12.: Contributions to the systematic uncertainties on the inclusive $\sqrt{C}/M(p_\mathrm{T})$ in pp collisions at $\sqrt{s}$ = 0.9, 2.76 and 7 TeV. The single contributions are added in quadrature to obtain the total uncertainties. They are presented in absolute values around $\sqrt{C}/M(p_\mathrm{T}) \approx 0.11$–0.12, i.e. the overall uncertainties have a relative size of about 4–6%.

3.8. Monte Carlo studies: full and fast simulations

In this work, several MC simulations are studied either on the MC generator level or as full simulations (see section 3.1.2). In general, the quantity $\sqrt{C_m}/M(p_\mathrm{T})_m$ is not sensitive to single-particle detection efficiency losses, which in principle enables a direct comparison of experimental results to the MC generator level. However, $\sqrt{C_m}/M(p_\mathrm{T})_m$ is influenced by other effects related to the measurement and analysis, like contamination by secondary particles and the momentum resolution of the detectors. Within the determination of the systematic uncertainties it is shown, that the differences between the MC generator level and the full simulations are small, but not negligible, reaching at maximum 6%.

It is not feasible to produce a full simulation for all MC generators and tunes studied in this work, due to their large processing time. Instead, an alternative faster method to obtain MC results is tested. In this approach, a full simulation is used to create an effective efficiency filter as a function of p_T. This method is tested in pp collisions at $\sqrt{s}$ = 7 TeV using PYTHIA6 Perugia-0 and in Pb–Pb collisions at $\sqrt{s_\mathrm{NN}}$ = 2.76 TeV using HIJING. The efficiency filter is obtained by taking the ratio of the accepted tracks of a full simulation to the corresponding MC generated primary particles. In the full simulation, the detector response is modelled and the standard TPC-standalone analysis criteria are applied to the reconstructed tracks. In this way, both the detection efficiency losses and the contamination by secondary particles enter the efficiency filter. It is important to note, that this filter is not identical to the primary charged-particle detection efficiency, which is presented in section 2.4.3 in figure 2.8.
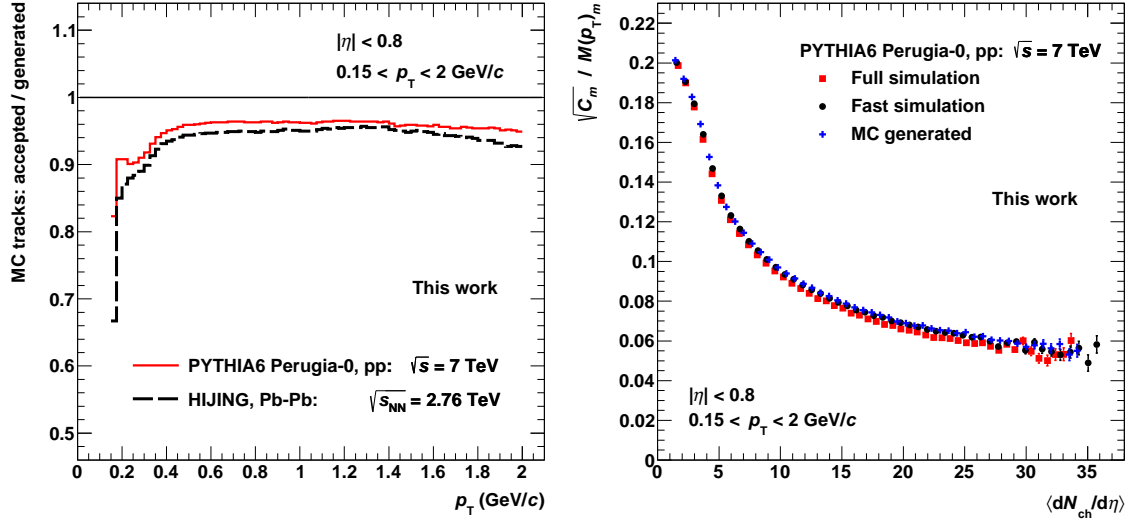
Figure 3.18.: Left: Ratio of accepted over generated MC tracks from PYTHIA6 Perugia-0 in pp collisions at $\sqrt{s}$ = 7 TeV and from HIJING in Pb–Pb collisions at $\sqrt{s_{\mathrm{NN}}}$ = 2.76 TeV. Right: $\sqrt{C_m}/M(p_{\mathrm{T}})_m$ as a function of $\langle \mathrm{d}N_{\mathrm{ch}}/\mathrm{d}\eta \rangle$ in pp collisions at $\sqrt{s}$ = 7 TeV from PYTHIA6 Perugia-0: the full simulation including the detector response, the corresponding fast simulation using the efficiency filter, and the MC generator level.

The left panel of figure 3.18 shows the efficiency filter as a function of p_{T} for pp collisions at $\sqrt{s}$ = 7 TeV and for Pb–Pb collisions at $\sqrt{s_{\mathrm{NN}}}$ = 2.76 TeV. In pp collisions, values above 95% are reached for $p_{\mathrm{T}} > 0.4\,\mathrm{GeV}/c$. A decreasing trend is found towards lower p_{T}, which is mitigated by a characteristic rising structure caused by secondary particles that are not rejected by the track selection criteria. At the lowest p_{T} of about $150\,\mathrm{MeV}/c$, the efficiency filter yields about 82%. The filter exhibits a similar behaviour in Pb–Pb collisions with values typically about 2–5% lower than in pp collisions. However, the effect of the secondary contamination at low p_{T} is much less pronounced, leading to smaller values of the filter. This may be attributed to – on average – a more precisely reconstructed primary interaction vertex, which is due to the larger number of primary particles in Pb–Pb collisions.

The effect of the efficiency filter on $\sqrt{C_m}/M(p_{\mathrm{T}})_m$ is studied focussing on pp collisions using PYTHIA6 Perugia-0. The filter is applied to the MC generator level by randomly rejecting tracks corresponding to the p_{T} dependence of the filter. This result is called "fast simulation", which is presented in figure 3.18 (right panel) together with the MC generator level and the full simulation results for $\sqrt{C_m}/M(p_{\mathrm{T}})_m$ as a function of the efficiency corrected $\langle \mathrm{d}N_{\mathrm{ch}}/\mathrm{d}\eta \rangle$. This representation shows, that all three approaches are qualitatively in good agreement. The small differences are quantified using ratios, which are presented in figure 3.19. The left panel shows the corresponding ratios of $\sqrt{C_m}/M(p_{\mathrm{T}})_m$ of the fast simulation and the generator level to the full simulation result as a function of $\langle \mathrm{d}N_{\mathrm{ch}}/\mathrm{d}\eta \rangle$. As discussed in section 3.7, the differences between
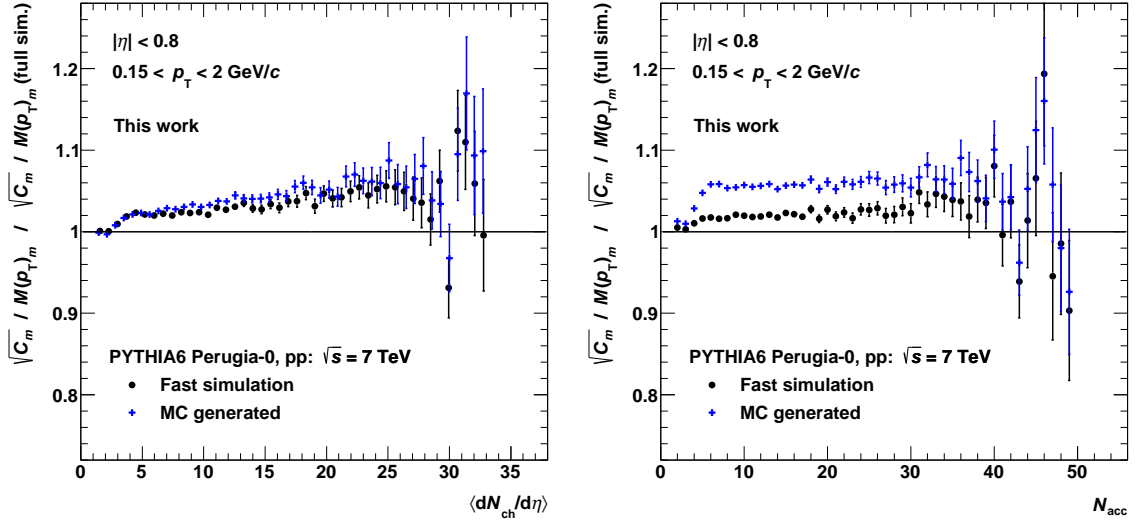
Figure 3.19.: Ratios of $\sqrt{C_m}/M(p_{\mathrm{T}})_m$ from PYTHIA6 Perugia-0, MC generator level and fast simulation, to the full simulation as a function of $\langle \mathrm{d}N_{\mathrm{ch}}/\mathrm{d}\eta \rangle$ (left) and as a function of N_{acc} (right) in pp collisions at $\sqrt{s} = 7\,\mathrm{TeV}$.

the generator level and the full simulation are negligible at the lowest multiplicities and increase linearly towards higher $\langle \mathrm{d}N_{\mathrm{ch}}/\mathrm{d}\eta \rangle$ with a maximum difference of about 6%. Interestingly, the fast simulation result is almost in perfect agreement with the generator level and not with the full simulation. This observation supports the robustness of $\sqrt{C_m}/M(p_{\mathrm{T}})_m$ against efficiency losses, even if those are depending on p_{T}. Other effects like secondary particles, which exhibit different correlations than primary particles, are responsible for the differences between generator level and full simulations. These differences cannot be reduced significantly by the simple efficiency filter, because it only includes the inclusive p_{T} distribution of the secondary particles but not their correlations.

Different observations are made when comparing the results as a function of N_{acc}, which is presented in the right panel of figure 3.19. The differences between the generator level and the full simulation increase steeply at low multiplicities and saturate already at $N_{\mathrm{acc}} = 6$ at the same maximum difference of 6% as in the representation as a function of $\langle \mathrm{d}N_{\mathrm{ch}}/\mathrm{d}\eta \rangle$. The fast simulation using the efficiency filter, on the other hand, shows a much better agreement with the full simulation. The differences yield 2–3% exhibiting only a moderate increase with multiplicity. Applying the correction of the multiplicity to obtain $\langle \mathrm{d}N_{\mathrm{ch}}/\mathrm{d}\eta \rangle$ in all three approaches changes this observation, as shown in the left panel of figure 3.19 and discussed above.

In conclusion, the differences of $\sqrt{C_m}/M(p_{\mathrm{T}})_m$ as a function of N_{acc} between the generator level and the full simulation result from an interplay of secondary particles and their correlations and the effect of efficiency losses on the multiplicity. The latter can be removed by correcting the multiplicity and presenting the results as a function of $\langle \mathrm{d}N_{\mathrm{ch}}/\mathrm{d}\eta \rangle$. In this representation, the MC generator level and the fast simulation
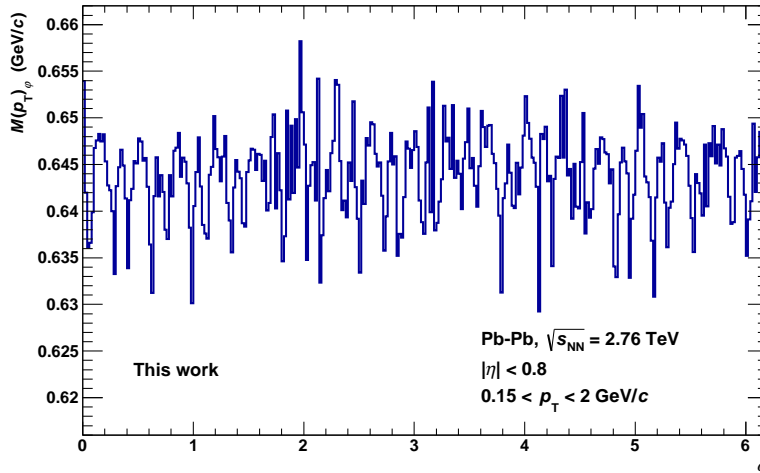
Figure 3.20.: $M(p_T)_\varphi$ as a function of φ in Pb–Pb collisions at $\sqrt{s_{NN}}$ = 2.76 TeV for minimum-bias events.

employing the efficiency filter are in agreement, showing that the effect of efficiency losses is almost completely removed while the contribution of secondary particles still has an influence on the results, which cannot be mitigated using the efficiency filter. Similar observations are made when using PHOJET in pp collisions at $\sqrt{s}$ = 7 TeV instead of PYTHIA6. As the efficiency filter has no significant effect in pp collisions, it is decided not to apply it to the MC simulations presented in this work. To be consistent throughout the collision systems, it is not applied to simulations in Pb–Pb collisions as well and a detailed study with HIJING is omitted. Instead, the MC generator level is used for all MC productions including those, where a full simulation is available. In this way, all MC simulations are directly comparable. The results of both the simulations and the experimental data are presented as a function of $\langle dN_{ch}/d\eta \rangle$. The remaining difference between the MC generator level and the full simulations is added as a systematic uncertainty to the experimental data, see also section 3.7. Within these systematic uncertainties, the MC simulations can be compared to the data.

3.9. Simple simulations

Simple "toy" Monte Carlo simulations are used to demonstrate, that the two-particle correlator vanishes in the case of purely statistical fluctuations, and to address the question, whether the dependence of $M(p_T)$ on φ has any significant influence on the results of $\sqrt{C_m}/M(p_T)_m$ (see section 3.4.3).

Within a first simulation, particle pairs are created by randomly choosing two values of the azimuthal angle φ, either by assuming a flat distribution, or according to the measured distribution of charged particles in φ. In the latter case, the detector effects on acceptance and efficiency, e.g. due to the TPC sector boundaries, are taken into

3. Analysis of symmetric systems: pp and Pb–Pb

N_{pairs}	flat in φ	measured φ	measured p_{T}
$5 \cdot 10^3$	$(-0.027 \pm 0.024)\,\%$	$(-0.049 \pm 0.019)\,\%$	$(0.934 \pm 1.655)\,\%$
$5 \cdot 10^5$	$(\ \ 0.004 \pm 0.009)\,\%$	$(\ \ 0.010 \pm 0.005)\,\%$	$(0.191 \pm 0.582)\,\%$
$5 \cdot 10^7$	$(\ \ 0.003 \pm 0.003)\,\%$	$(-0.001 \pm 0.002)\,\%$	$(0.077 \pm 0.187)\,\%$

Table 3.13.: Results for $\sqrt{C}/M(p_{\mathrm{T}})$ from simple simulations of particle pairs. In the first two versions, the transverse momenta are obtained from $M(p_{\mathrm{T}})_{\varphi}$ assuming a flat distribution in φ or taking the measured φ distribution. The last column corresponds to the raw measured p_{T} spectrum as input without any dependence on φ.

account. Next, the measured value of $M(p_{\mathrm{T}})_{\varphi}$ from figure 3.20 corresponding to the φ of each of the two particles is assigned to them as transverse momenta $p_{\mathrm{T},1}$ and $p_{\mathrm{T},2}$. For each particle pair, the quantity

$$c_{\mathrm{pair}} = (p_{\mathrm{T},1} - M(p_{\mathrm{T}})) \cdot (p_{\mathrm{T},2} - M(p_{\mathrm{T}})) \tag{3.7}$$

is calculated, which is equivalent to equation 1.46 for a single particle pair. The inclusive measured $M(p_{\mathrm{T}}) = 0.6437\,\mathrm{GeV}/c$ from minimum-bias Pb–Pb collisions at $\sqrt{s_{\mathrm{NN}}} = 2.76\,\mathrm{TeV}$ is applied. The average value of c_{pair} of all particle pairs is obtained for each cycle of the simulation. This average is used as the two-particle correlator C to determine the relative fluctuation $\sqrt{C}/M(p_{\mathrm{T}})$. The number of particle pairs N_{pairs} created within the simulation is varied and in each case the simulation is repeated ten times both for the flat and for the measured distribution in φ. The mean values and statistical uncertainties for $\sqrt{C}/M(p_{\mathrm{T}})$ from these ten cycles are summarised in table 3.13 in the columns "flat in φ" and "measured φ". Compared to the analysis of ALICE data, the number of particle pairs in these simple simulations is small. $5 \cdot 10^3$ pairs correspond approximately to a single event with 100 particles, $5 \cdot 10^5$ pairs match one event with 1000 particles and $5 \cdot 10^7$ pairs correspond to about 10^4 events with 100 particles or 100 events with 1000 particles.

These simulations yield $|\sqrt{C}/M(p_{\mathrm{T}})| < 0.1\,\%$ for the lowest number of particle pairs and $|\sqrt{C}/M(p_{\mathrm{T}})| \lesssim 0.01\,\%$ for the higher numbers of pairs and in most cases the results are in agreement with zero within the statistical uncertainties. In some cases, the mean value is even negative, which would imply an anti-correlation. For comparison, the ALICE results exhibit always positive values ranging from the smallest ones in central Pb–Pb collisions with $\sqrt{C_m}/M(p_{\mathrm{T}})_m \approx 1\%$ to the highest ones in low-multiplicity pp collisions with $\sqrt{C_m}/M(p_{\mathrm{T}})_m \approx 12\text{–}14\%$. A possible bias due to the fluctuating structure of $M(p_{\mathrm{T}})$ as a function of φ would be about two to three orders of magnitude smaller than the ALICE result in central Pb–Pb collisions. Therefore, it is concluded that the variations of $M(p_{\mathrm{T}})$ as a function of φ do not have any significant influence on the measurement of $\sqrt{C_m}/M(p_{\mathrm{T}})_m$. The small possible bias is very well covered by the systematic uncertainties and can be neglected. Using the measured φ distribution yields only slightly higher values than assuming a flat φ distribution, showing no significant influence of the small acceptance and efficiency modulation in φ.
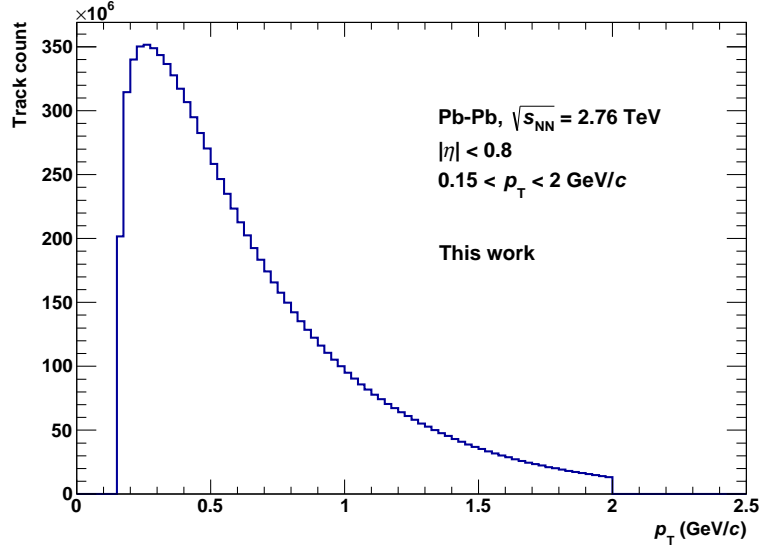
Figure 3.21.: Raw measured p_T spectrum in minimum-bias Pb–Pb collisions at $\sqrt{s_\mathrm{NN}} = 2.76\,\mathrm{TeV}$.

In addition, simulations of particle pairs are performed using the measured raw p_T spectrum within $0.15\,\mathrm{GeV}/c < p_\mathrm{T} < 2\,\mathrm{GeV}/c$, which is shown in figure 3.21. Here, no dependence on φ is taken into account. The transverse momenta $p_{\mathrm{T},1}$ and $p_{\mathrm{T},2}$ of each pair are randomly selected from the p_T spectrum. The subsequent procedure is identical to the one described above. The average values for $\sqrt{C}/M(p_\mathrm{T})$ from ten cycles for different numbers of pairs are listed in table 3.13 as well. The results are higher than in the other simulations, but always consistent with zero within the statistical uncertainties. They decrease with increasing number of particle pairs reaching $\sqrt{C}/M(p_\mathrm{T}) < 0.1\,\%$ for the hightest statistics, which is one order of magnitude smaller than in central Pb–Pb collisions.

These observations indicate, that $\sqrt{C}/M(p_\mathrm{T})$ vanishes for purely statistical fluctuations. However, the simple simulation of particle pairs might be not representative for the case of statistical fluctuations in real collision events, where the pairs are not completely random. Another simulation is developed to extent the investigation of the behaviour of $\sqrt{C}/M(p_\mathrm{T})$ for statistical fluctuations to a more realistic scenario. Instead of randomly generating particle pairs, full events are created. For each event, a number of particles N_ch is obtained either by randomly sampling N_ch times a flat or the measured φ distribution and applying as p_T the corresponding $M(p_\mathrm{T})_\varphi$ from figure 3.20 or by randomly selecting the p_T of the N_ch particles directly from the measured p_T spectrum in figure 3.21. Afterwards, the event is studied like in the analysis of real ALICE data, taking into account all possible pairs from the N_ch particles. Normalising to the number of particle pairs in the event N_k^pairs, the two-particle correlator of the event C_k from equation 1.48 is calculated. A sample of n_ev events is simulated and the average of the C_k is determined resulting in the relative event-by-event mean
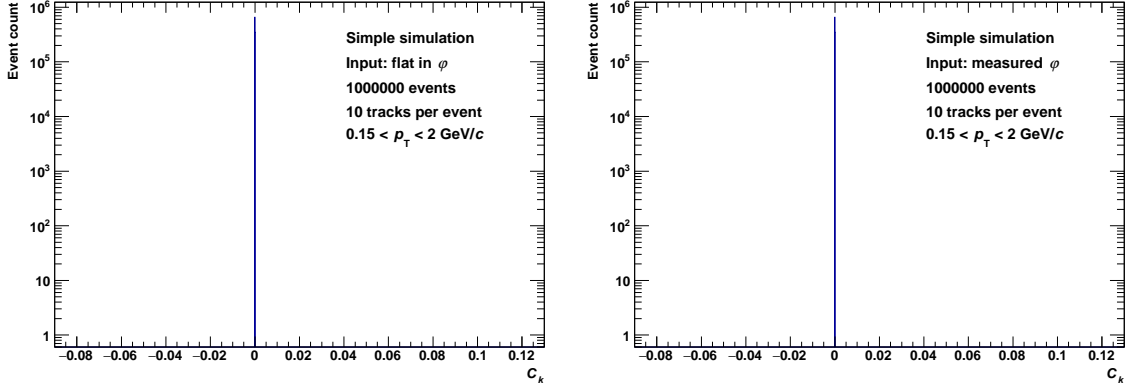
3. Analysis of symmetric systems: pp and Pb–Pb

Figure 3.22.: Distributions of C_k from simple simulations of 10^6 events with 10 particles assuming a flat distribution in φ (left) or taking the measured φ distribution (right). The scale of the x axis is identical to the one in figure 3.23.

p_T fluctuation measure $\sqrt{C_m}/M(p_T)_m$. Here, the subscript m denotes the number of particles N_{ch}.

The results for $\sqrt{C_m}/M(p_T)_m$ from the simulations of events are summarised in table 3.14 for the three different versions of the simulations and for several combinations of n_{ev} and N_{ch}. Those with 10^6 events with 10 particles, 10^4 events with 100 particles and 10^2 events with 1000 particles correspond to about the same total number of particle pairs like the highest number of $5 \cdot 10^7$ pairs in the first simple simulation. Using the flat or measured φ distribution yields comparable results of $|\sqrt{C}/M(p_T)| < 0.01\,\%$. This demonstrates, that the simple simulation of particle pairs is justified for the estimate of a possible bias due to the fluctuating $M(p_T)_\varphi$ and it supports the conclusion, that there is no significant bias. The other combinations of n_{ev} and N_{ch} yield similar results.

n_{ev}	N_{ch}	N_k^{pairs}	flat in φ	measured φ	measured p_T
10^4	10	45	$(0.009 \pm 0.006)\,\%$	$(-0.012 \pm 0.008)\,\%$	$(\;0.149 \pm 0.637)\,\%$
10^6	10	45	$(0.005 \pm 0.002)\,\%$	$(\;0.007 \pm 0.002)\,\%$	$(\;0.315 \pm 0.179)\,\%$
10^4	100	4 950	$(0.005 \pm 0.002)\,\%$	$(\;0.000 \pm 0.003)\,\%$	$(-0.238 \pm 0.175)\,\%$
10^6	100	4 950	$(0.006 \pm 0.001)\,\%$	$(\;0.003 \pm 0.001)\,\%$	$(-0.064 \pm 0.068)\,\%$
10^2	1000	499 500	$(0.004 \pm 0.002)\,\%$	$(\;0.003 \pm 0.001)\,\%$	$(\;0.299 \pm 0.167)\,\%$
10^4	1000	499 500	$(0.006 \pm 0.001)\,\%$	$(\;0.002 \pm 0.001)\,\%$	$(-0.088 \pm 0.049)\,\%$

Table 3.14.: Results for $\sqrt{C_m}/M(p_T)_m$ from simple simulations of events for different numbers of events n_{ev} and particles per event $m = N_{ch}$. The number of pairs per event is denoted by N_k^{pairs}. In the first two versions, the transverse momenta are obtained from $M(p_T)_\varphi$ assuming a flat distribution in φ or taking the measured φ distribution. The last column corresponds to the raw measured p_T spectrum as input without any dependence on φ.

Figure 3.22 shows the event-by-event distribution of C_k for the example of one simulation of 10^6 events with 10 particles assuming a flat distribution in φ (left panel) or taking the measured φ distribution (right panel). Both distributions are very narrow around $C_k = 0$, demonstrating that the influence of the φ modulation of $M(p_\mathrm{T})$ and efficiency does not even have any significant influence on the level of single events. The same observation also holds for all other combinations of n_ev and N_ch under study.

Considering the measured p_T spectrum as input for the event simulations leads to different findings, which are presented in figure 3.23. Three simulations of 10^4 events are compared, showing the results of the randomly sampled p_T spectra on the left panels and the event-by-event distributions of C_k on the right panels. The number of particles per event changes from 10 (top) to 100 (centre) and 1000 (bottom). All of the p_T spectra are comparable to the input spectrum from figure 3.21, although in the first example some deviations are observed due to the small total number of particles. The behaviour of the C_k distributions is significantly different from that observed in the other simulations presented in figure 3.22. In the first example with $N_\mathrm{ch} = 10$, the distribution is broad and asymmetric with a much larger tail of positive values. This asymmety is also observed when going to higher N_ch, but the distributions get significantly narrower. For the case of $N_\mathrm{ch} = 1000$, it is almost as narrow as for the simulations using the flat or measured φ distributions as input.

The different behaviour of the simulations using the measured p_T spectrum is also reflected in the average values of $\sqrt{C_m}/M(p_\mathrm{T})_m$ presented in table 3.14. In all cases, these averages yield $|\sqrt{C_m}/M(p_\mathrm{T})_m| \lesssim 0.5\,\%$. In contrast to the simple simulations of particle pairs, not all of the values are in agreement with zero within the statistical uncertainties, but those are still of the same order of magnitude as the mean values. Some of the averages are negative, indicating that the results are fluctuating around zero rather than showing a clear non-zero trend. For 100 and 1000 particles per event, the mean values decrease to $|\sqrt{C_m}/M(p_\mathrm{T})_m| < 0.1\,\%$ when going to higher event statistics.

In conclusion, the simple simulations of particle pairs and of events show, that for the case of purely statistical fluctuations the two-particle correlator $\sqrt{C_m}/M(p_\mathrm{T})_m$ is in agreement with or at least close to zero. The ALICE results of $\sqrt{C_m}/M(p_\mathrm{T})_m \approx 1$–$14\%$ are clearly orders of magnitude larger than any possible effect from statistical fluctuations. The modulations of $M(p_\mathrm{T})$ and efficiency as a function of φ have no significant influence on the measurement of mean p_T fluctuations.
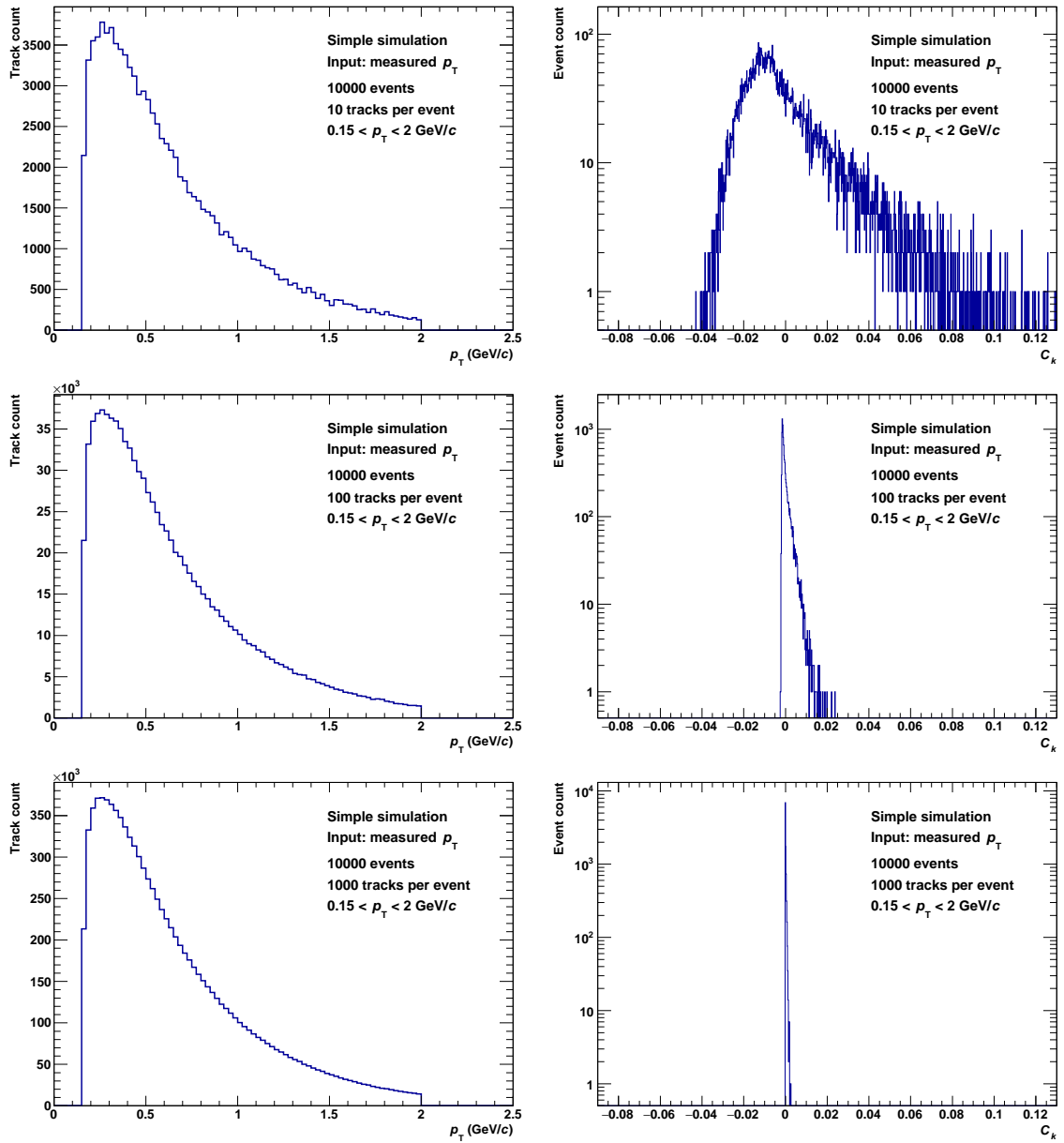
Figure 3.23.: Randomly generated p_T spectra (left panels) and resulting C_k distributions (right panels) for simulations using the measured p_T spectrum as input. 10^4 events are generated for different numbers of particles per event: 10 (top), 100 (centre) and 1000 (bottom).

4. Analysis of p–Pb collisions

The analysis of the mean transverse-momentum fluctuations as a function of multiplicity in symmetric collision systems has revealed an astonishing agreement of pp and Pb–Pb collisions in the overlapping region and for an extrapolation of pp also towards higher multiplicities, while central Pb–Pb collisions show a clear reduction of the fluctuations (see chapters 3 and 5.1 as well as [3]).

With p–Pb collisions, an intermediate-size and asymmetric system is studied within the new analysis presented in this chapter. Predictions of mean p_T fluctuation results in p–Pb collisions differ with respect to the question, whether or not the general trend is expected to be in agreement with the results of the symmetric systems [74, 163]. Furthermore, a similarity of high-multiplicity p–Pb results with the deviations from the pp baseline observed in Pb–Pb collisions could indicate a heavy-ion like behaviour in hadron–nucleus collisions not observed in hadron–hadron. This would add to the discussion about collectivity and a potential formation of QGP droplets in small collision systems, see e.g. [66].

As p–Pb collisions constitute an asymmetric system also with respect to the beam energy per nucleon, the centre-of-mass system of the collisions is shifted by about half a unit in rapidity [119, 164]. Therefore, midrapidity in the centre-of-mass and the laboratory system are no longer in coincidence, and, hence, the acceptance of the detectors is shifted. An investigation of the pseudorapidity range is described in detail in section 4.4 and a restricted acceptance is considered. The other two collision systems, pp and Pb–Pb, are re-analysed within a corresponding restricted pseudorapidity range. Performing the same new analyses in pp and Pb–Pb collisions within the pseudorapidity coverage of the first analysis, the agreement with the published results is verified.

4.1. Data sets

The new data set analysed in this second analysis consists of p–Pb collisions at a collision energy of $\sqrt{s_{NN}}$ = 5.02 TeV measured in 2013 at the end of LHC Run 1. In addition, pp collisions at $\sqrt{s}$ = 2.76 and 7 TeV and Pb–Pb collisions at $\sqrt{s_{NN}}$ = 2.76 TeV are re-analysed. In the case of the pp data, a new reconstruction is used with an increased performance of the charged-particle tracking. A summary of the data sets studied in this second analysis is presented in table 4.1. The considered periods and runs are listed in Appendix A.

The DPMJET Monte Carlo (MC) event generator [165, 166] is applied in p–Pb collisions to check the difference between the generator level and the full simulation, for

System	$\sqrt{s_{NN}}$	Year	Events
pp	2.76 TeV	2011	67.2 M
pp	7.0 TeV	2010	289.6 M
p–Pb	5.02 TeV	2013	111.6 M
Pb–Pb	2.76 TeV	2010	19.1 M

Table 4.1.: ALICE data sets studied in the new analysis. The number of events is quoted after the physics selection procedure and before any other selection criteria.

details on this procedure see sections 3.1.2 and 3.7. Furthermore, the mean p_T fluctuation results in p–Pb collision data are compared to those obtained with DPMJET. The analysed DPMJET event sample contains about 29.5 M events.

4.2. Event selection

Most of the event selection criteria applied in the new analysis are identical to the ones already used in the published analysis and described in section 3.2. However, some minor differences are present, which are described in this section. For example, an additional pile-up removal criterion is applied. Furthermore, some adjustments on the vertex selection are performed. The physics selection procedure corresponds to that summarised in section 3.2.1. Minimum-bias (MB) triggered data are used with the MBand condition, for details see section 2.4.2.

4.2.1. Selection criteria on the primary vertex

As in the previous analysis, the primary vertex calculated from global TPC-ITS tracks is used as the default one. If this vertex is not available, it can be replaced by the SPD-tracklets or the TPC-standalone vertex. Events without a reconstructed primary vertex are rejected. The vertex has to be located within 10 cm around the nominal interaction point along the beam (z) direction.

The z positions of the primary vertices obtained from the three different vertex estimators do not have to coincide, see section 3.2.2. In the new analysis, the z position of the SPD-tracklets vertex is used instead of the global TPC-ITS vertex for the comparison to the TPC-standalone one. The reason for this exchange is purely technical: the usage of AODs is implemented in the new analysis code to be able to profit from the faster analysis cycle on AODs[a]. In AODs, only the SPD-tracklets and TPC-standalone vertices are included explicitly together with a general primary vertex containing one of the three different implementations for each event. This general primary vertex is set to the global TPC-ITS vertex if availble and to the SPD-tracklets or TPC-standalone vertex otherwise. The global vertex parameters are not available explicitly

---

[a] The old analysis code used for the published analysis (chapter 3) is only running on ESDs. For a short introduction to ESDs and AODs and further references see section 2.4.5.
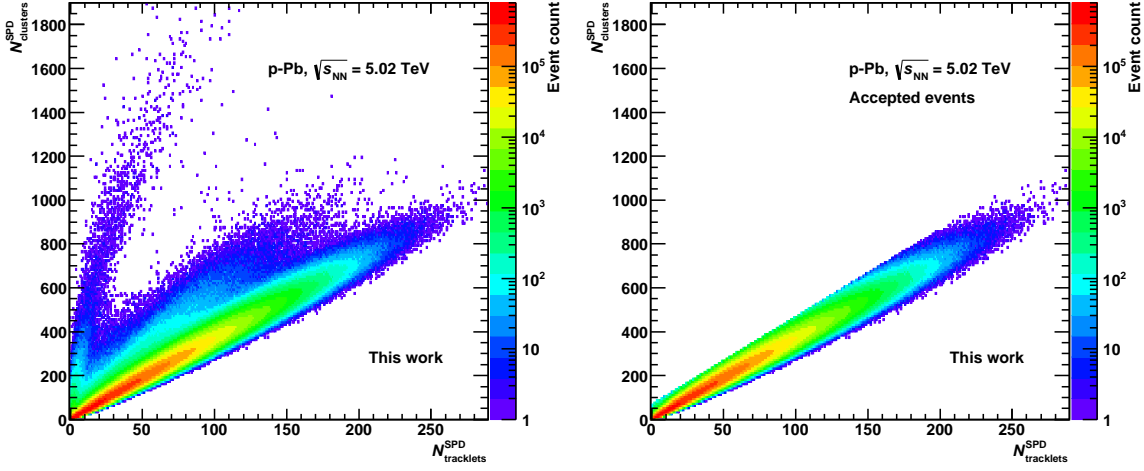
Figure 4.1.: Number of events as a function of the number of SPD clusters $N_{\text{clusters}}^{\text{SPD}}$ and the number of SPD tracklets $N_{\text{tracklets}}^{\text{SPD}}$ per event in p–Pb collisions at $\sqrt{s_{\text{NN}}}$ = 5.02 TeV. Left: With physics selection applied, but no other selection criteria. Right: Accepted events after all selection criteria are applied.

in AOD events and hence, the SPD-tracklets vertex is used for the vertex difference criterion. As the global TPC-ITS vertex is dominated by the contribution of the SPD, this change does not imply any significant differences. In addition, the selection criterion for the maximum absolute difference of the two vertex estimators is reduced to a stricter value of 4 cm. Overall, these changes have only small effects on the final results, which are studied in more detail together with variations of the other vertex selection criteria in section 4.7 about the systematic uncertainties of the new analysis.

4.2.2. Pile-up rejection

The main criterion to reduce pile-up in the new analysis is the SPD pile-up rejection explained in section 3.2.3. As in the published analysis, the minimum difference in z direction between the primary vertex and a pile-up vertex has to be 0.8 cm. However, the minimum multiplicity of the second vertex is not implemented as a fixed number, but depending on the number of SPD tracklets $N_{\text{tracklets}}^{\text{SPD}}$ of the primary vertex. For events, in which the primary vertex has $N_{\text{tracklets}}^{\text{SPD}} < 20$, the minimum number of tracklets of the pile-up vertex is set to three. This value is increased to four and five for primary vertices with $20 \leq N_{\text{tracklets}}^{\text{SPD}} < 50$ and $N_{\text{tracklets}}^{\text{SPD}} \geq 50$, respectively.

A new development with respect to pile-up rejection not implemented in the published analysis is the SPD cluster-versus-tracklets background rejection [112]. The number of events as a function of $N_{\text{tracklets}}^{\text{SPD}}$ and the total number of clusters per event in the SPD $N_{\text{clusters}}^{\text{SPD}}$ is presented in figure 4.1. The left panel shows this relation after the physics selection but before any other selection criteria are applied. For the majority of events, a clear correlation between $N_{\text{clusters}}^{\text{SPD}}$ and $N_{\text{tracklets}}^{\text{SPD}}$ is visible. Events originating

from pile-up or other background sources tend not to follow this trend, but are located in bands of outliers. With a selection criterion depending linearly on the number of SPD tracklets, most of these outliers can be removed without a significant loss of events containing only one collision. The right panel of figure 4.1 contains only those events, which are accepted by all of the selection criteria. Here, the outlier bands are removed. A further criterion used to reject pile-up is the maximum difference of the z components of the SPD-tracklets and TPC-standalone vertices as described above. Although pile-up events are expected to have a significant influence on correlation or fluctuation analyses as in the present work, this expectation cannot be confirmed. The effects on the final results, if the settings of the pile-up rejection conditions are modified or if they are even switched off completely, are rather small or even negligible. The details of this investigation are discussed within the systematic uncertainties, section 4.7.

4.2.3. Summary of the event selection

Event selection criterion	Value
Physics selection	active
Trigger condition	minimum bias
Number of vertex contributors	≥ 1
Vertex-z distance from nominal interaction point	$< 10\,\mathrm{cm}$
Vertex-z difference (TPC–SPD)	$< 4\,\mathrm{cm}$
SPD pile-up rejection: 2nd vertex min. multiplicity	3–5 (mult.dep.)
SPD pile-up rejection: distance of vertices	$> 0.8\,\mathrm{cm}$
SPD cluster-vs-tracklets background rejection	active

Table 4.2.: Summary of the event selection criteria applied in this analysis. In the SPD pile-up rejection, the minimum number of tracklets of the second vertex depends on the multiplicity of the primary vertex.

The event selection criteria in the new analysis resemble those of the previous analysis summarised in table 3.3 on page 61. The minor differences include the usage of the SPD-tracklets vertex estimator instead of the global one for the comparison of the z_{vtx} position to the TPC-standalone vertex, also using a stricter cut value. The SPD pile-up rejection is implemented in a multiplicity-dependent way and the additional requirement of the SPD cluster-versus-tracklets background rejection is applied. A summary of all event selection criteria used in the new analysis is presented in table 4.2. The number of events in p–Pb collisions at $\sqrt{s_{\mathrm{NN}}} = 5.02\,\mathrm{TeV}$ at the various stages of the analysis is shown in figure 4.2. The condition of a maximum difference of $10\,\mathrm{cm}$ of the z position of the primary vertex from the nominal interaction point is responsible for the largest reduction of the event count, followed by the physics selection procedure, the requirement of a maximum z_{vtx} difference of the TPC and SPD vertices and the
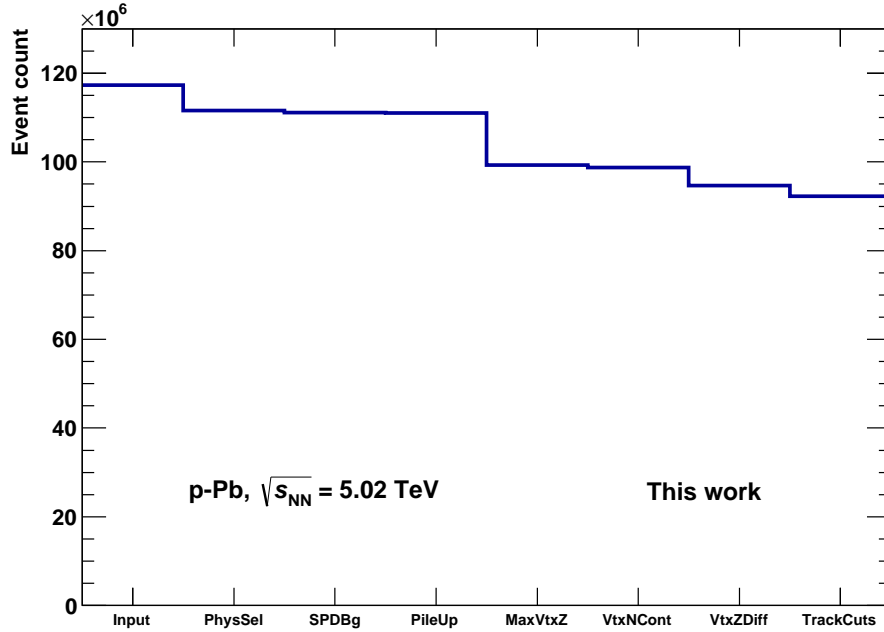
Figure 4.2.: Number of events in p–Pb collisions at $\sqrt{s_{NN}}$ = 5.02 TeV. From left to right: Number of events read in from the ESD files, after performing the physics selection, the SPD cluster-versus-tracklets background rejection, the SPD pile-up rejection and the cuts on the maximum z_{vtx} distance from the nominal interaction point, the number of contributors to the vertex and the difference of the TPC and SPD z_{vtx} positions and, finally, after application of the track selection criteria including the kinematic acceptance of $|\eta| < 0.8$ and $0.15\,\text{GeV}/c < p_{\text{T}} < 2\,\text{GeV}/c$.

track selection criteria[b]. The other conditions decrease the number of events only slightly.

4.3. Track selection

The same tracking schemes are applied as in the published analysis, using the TPC-standalone tracking as default and the hybrid tracking for comparison. For details about these tracking schemes see section 3.3. In both cases, track selection criteria almost identical to the first analysis are used as listed in table 3.4 on page 64. The main difference is the requirement of the TPC refit not only in the hybrid, but also in the TPC-standalone scheme. Improvements in the track reconstruction leading to a better efficiency for primary – but also for secondary – particles necessitate the usage of this additional criterion. These improvements have been implemented both in the

---

[b] An event is rejected, if less than two tracks within the kinematic range are accepted by the track selection criteria, because in this case the two-particle correlator cannot be calculated.
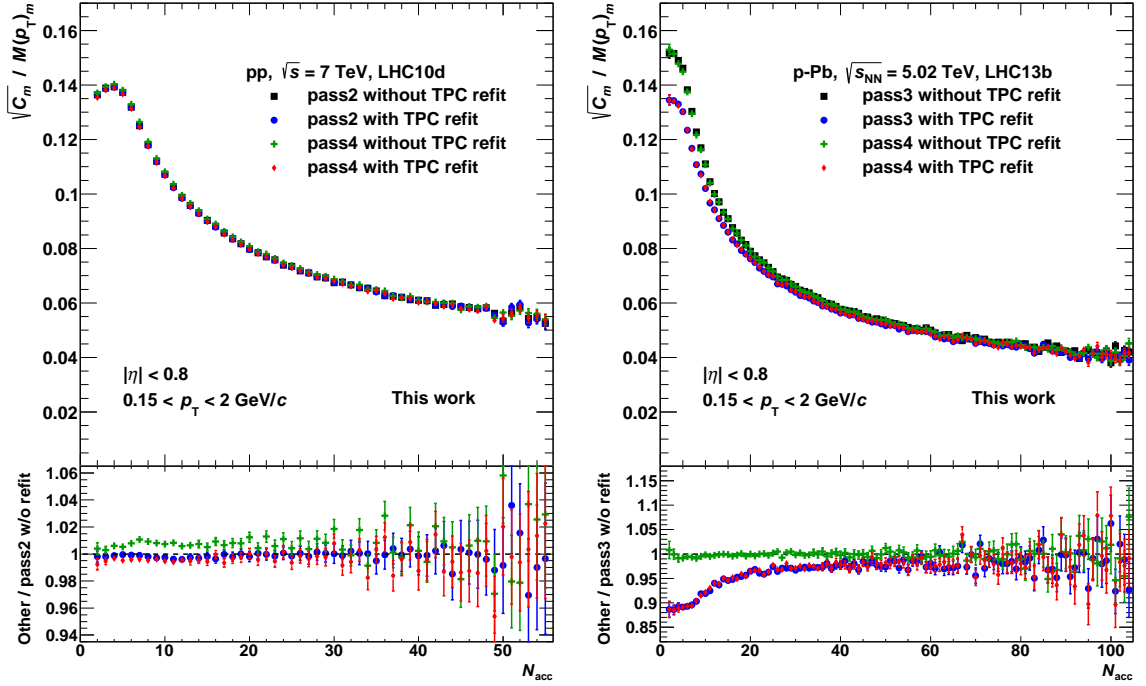
Figure 4.3.: Left: $\sqrt{C_m}/M(p_T)_m$ as a function of N_{acc} in pp collisions at $\sqrt{s}$ = 7 TeV. The old (pass2) and new (pass4) reconstructions are compared, both with and without TPC refit. The lower panel shows the ratio of the different versions to the pass2 without TPC refit. Right: The same in p–Pb collisions at $\sqrt{s_{NN}}$ = 5.02 TeV. Both pass3 and pass4 contain the reconstruction improvements. The lower panel shows the ratios to pass3 without TPC refit.

reconstruction (all passes) of the p–Pb data taken in 2013 and in the re-reconstruction (pass4) of the pp data from 2010, which are studied in this new analysis.

The effect of this new reconstruction and the TPC refit on the results is presented in figure 4.3 showing $\sqrt{C_m}/M(p_T)_m$ as a function of N_{acc} in pp collisions at $\sqrt{s}$ = 7 TeV (left panel) and in p–Pb collisions at $\sqrt{s_{NN}}$ = 5.02 TeV (right panel). In the case of pp collisions, the TPC refit has no significant influence for the old reconstruction (pass2). The new reconstruction (pass4) including the TPC refit is in agreement with pass2 as well, but pass4 without the TPC refit exhibits a difference of about 1%. The influence of the TPC refit is much larger in p–Pb collisions, where its application is necessary to reduce the contamination with secondary particles. At low multiplicities, the effect on $\sqrt{C_m}/M(p_T)_m$ reaches about 10% and it is decreasing for higher multiplicities. The right panel of figure 4.3 furthermore demonstrates the good agreement of the pass3 and pass4 reconstructions for the p–Pb data set.

There is no new reconstruction available for the 2010 Pb–Pb data and therefore the usage of the TPC refit would not be necessary, but it anyhow is applied to be consistent
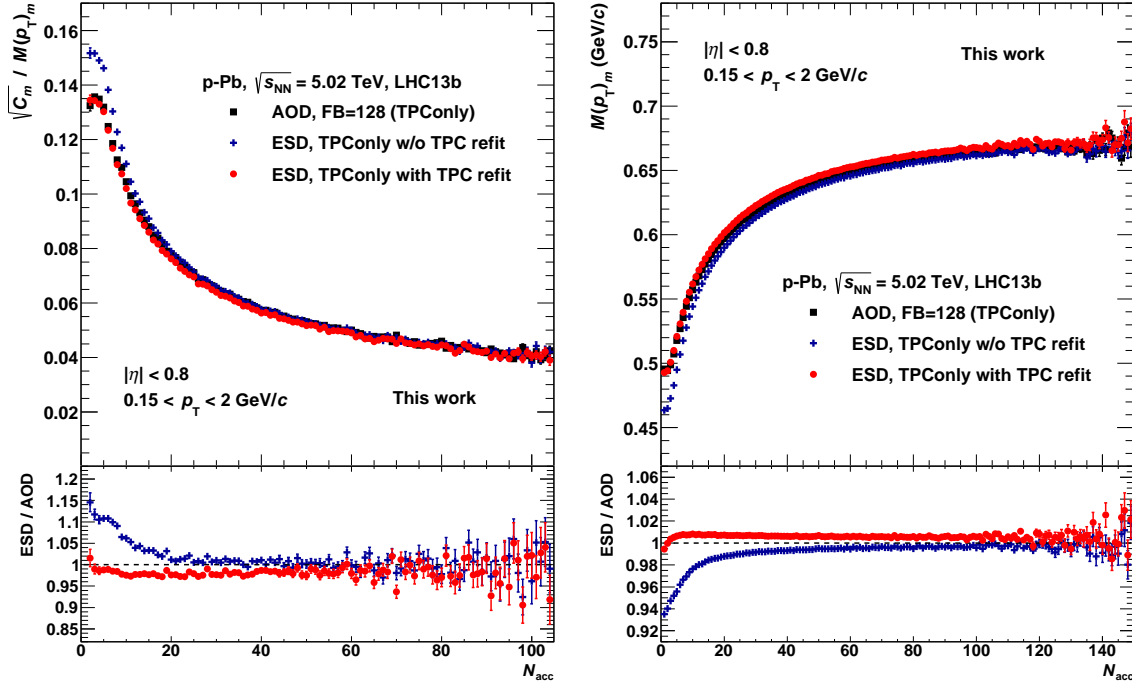
Figure 4.4.: Comparison of the analyses in p–Pb collisions at $\sqrt{s_{\mathrm{NN}}}$ = 5.02 TeV using AOD and ESD files. In both cases, a TPC-standalone tracking scheme is used. ESDs are studied with and without TPC refit, while this is enabled by default in AOD FB = 128. Left: $\sqrt{C_m}/M(p_{\mathrm{T}})_m$ as a function of N_{acc}. Right: $M(p_{\mathrm{T}})_m$ as a function of N_{acc}. The lower panels show the ratios of the ESD analyses to that using AODs.

throughout the data sets. Variations of the track selection criteria and their influence on the results are discussed in section 4.7 about the systematic uncertainties.

4.3.1. Comparison of AOD and ESD analyses

As described above, the new analysis code is able to use both ESD and AOD files as input. A comparison of the results in p–Pb collisions obtained with both data formats is presented in figure 4.4. In both the AOD and the ESD analyses a TPC-standalone tracking scheme is applied. In the case of AODs, the tracks are selected via pre-defined filter bits (FB) and here FB = 128 is used. For ESDs, the track selection criteria are applied explicitly and they correspond to those listed in table 3.4 on page 64, i.e. without the TPC refit. A second analysis of the ESDs is performed including the TPC refit, which is enabled in AOD FB = 128 as well. In the left panel of figure 4.4, the result for $\sqrt{C_m}/M(p_{\mathrm{T}})_m$ as a function of N_{acc} is shown for the three analyses. The ESD version without the TPC refit differs significantly from the result obtained on AODs, reaching a deviation of 10–15% at low multiplicities. This discrepancy is
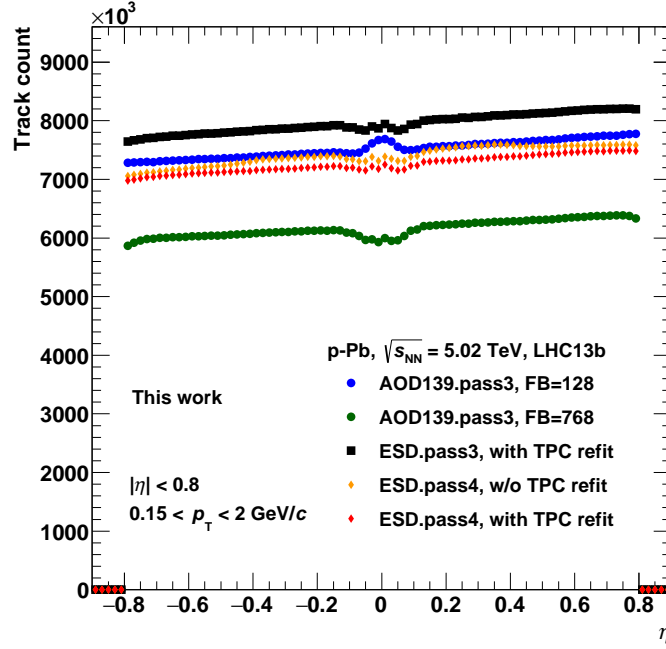
Figure 4.5.: Pseudorapidity distribution of tracks in p–Pb collisions at $\sqrt{s_{NN}}$ = 5.02 TeV in multiple analyses using AOD or ESD inputs and different track selection criteria. See text for details.

removed when including the TPC refit also in the ESD analysis with a small residual difference with opposite sign and a size of about 1–2%.

The right panel of figure 4.4 shows $M(p_T)_m$ as a function of N_{acc} for the same three analyses. Also here, the result using ESDs without TPC refit differs significantly from that employing AODs, reaching up to 6% at the lowest N_{acc}. Again, including the TPC refit removes this deviation, but exhibits a small difference < 1% in the opposite direction. This comparison shows, that the differences between AOD and ESD analyses are present not only in the fluctuations, but also in the average p_T, although here the effects are smaller. Additional variations of other track selection criteria are performed to investigate the residual differences of the AOD and ESD analyses, but the reason for this is not found. The number of events obtained from ESD and AOD files is slightly different, but figure 4.4 demonstrates, that the residual deviation – although small – is beyond the statistical uncertainties. As it is well covered by the systematic uncertainties related to the different tracking schemes (see section 4.7), it is not applied as a separate contribution to the systematic uncertainties.

4.3.2. Pseudorapidity distribution of tracks

Another part of the detailed investigation of the AOD–ESD difference is the study of underlying distributions. Here, the distribution of tracks as a function of the pseudorapidity η is analysed. For this study, AOD results with FB = 128 (TPC-standalone
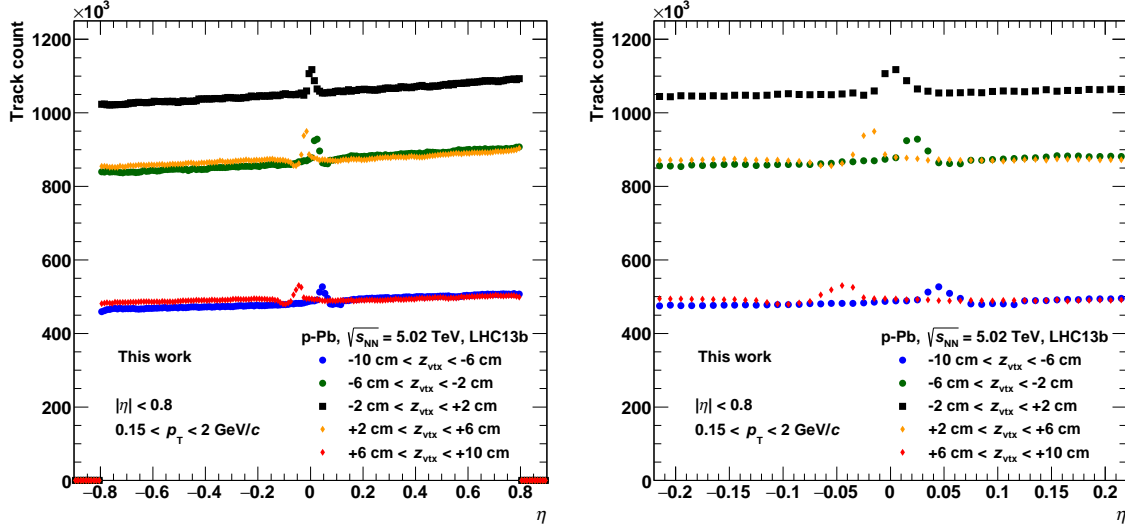
Figure 4.6.: Pseudorapidity distribution of tracks in p–Pb collisions at $\sqrt{s_{\mathrm{NN}}}$ = 5.02 TeV in the AOD analysis with FB = 128 and in different intervals of z_{vtx}. Left: Full distributions within $|\eta| < 0.8$. Right: Zoomed in on $|\eta| < 0.22$.

tracking) and with FB = 768 (hybrid tracking) are compared to ESD results from the pass3 reconstruction including the TPC refit and from pass4 with and without the TPC refit. These distributions are presented in figure 4.5. The overall trend is similar in all of these analyses with a moderate linear increase from negative to positive η values. This asymmetry in the particle production is related to the asymmetry of the p–Pb collision system with the proton beam going in the negative η direction, where less particles are produced.

Despite this common general trend, there are differences among the various analyses. The total number of accepted charged particles is significantly smaller when using the hybrid tracking (AOD FB = 768) instead of the TPC-standalone tracking (all other analyses). This is caused by the significantly stricter track selection criteria removing more secondary – but also more primary – particles. The discrepancies of the overall scale are smaller among the other analyses and mainly attributed to differences in the number of input events. The ESD reconstruction pass4 of the period LHC13b includes two runs less than the corresponding pass3 (see Appendix A.2) and hence contains a lower number of events and tracks.

Another distinct difference is observed around $\eta \approx 0$. Here, a small dip in the η distribution is expected, see for example [13, 20]. Using the hybrid tracking (AOD FB = 768), this dip is clearly visible. Considering a TPC-standalone tracking, the dip is still observed, but it is mitigated by an additional peak, which is a bit narrower and most pronounced in AOD FB = 128, where it exceeds the overal linearly rising trend of the distribution. Furthermore, a small increase (AOD FB = 128) or depletion (AOD FB = 768) is found at the edges of the considered η range and the ESD version without

4. Analysis of p–Pb collisions

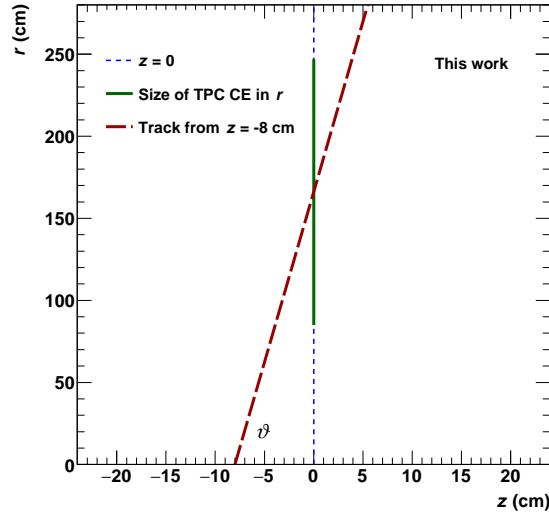Figure 4.7.: Sketch of a particle, which is emitted at an angle ϑ from a vertex at the position $z_{\mathrm{vtx}} = -8\,\mathrm{cm}$, such that it passes the Central Electrode (CE) of the TPC at its central value of the radius, $r = 166\,\mathrm{cm}$.

the TPC refit exhibits shoulders around the central η region, which are not expected and probably originate from secondary particles.

Overall, the details of the η distributions suggest the usage of the ESD analyses including the TPC refit as default for the results in p–Pb collisions. However, the unexpected peak at $\eta \approx 0$ is present in these analyses. Therefore, its origin and potential influences on the results are investigated further. As this peak is most distinct in AOD FB = 128, this analysis is used for the next step. It is repeated in intervals of the z position of the primary vertex z_{vtx}. The corresponding η distributions are shown in figure 4.6 within $|\eta| < 0.8$ (left panel) and zoomed in on $|\eta| < 0.22$ (right panel). The peak is visible in all intervals of z_{vtx}, but it is shifted for larger values of $|z_{\mathrm{vtx}}|$. While it is centred at $\eta = 0$ for the bin $-2\,\mathrm{cm} < z_{\mathrm{vtx}} < +2\,\mathrm{cm}$, the peaks for the other bins move away from $\eta = 0$ in the direction opposite to the z_{vtx} intervals.

These observations lead to a possible reason for the peaks. They may originate from particles crossing the Central Electrode (CE) of the TPC around its centre in the radial (r) direction, i.e. perpendicular to the beam (z) axis. The inner and the outer radius of the TPC are located at $r = 85\,\mathrm{cm}$ and $r = 247\,\mathrm{cm}$, respectively, see section 2.3.2 and [111]. Therefore, the radial centre of the CE lies at $r = 85\,\mathrm{cm} + 0.5 \cdot (247 - 85)\,\mathrm{cm} = 166\,\mathrm{cm}$. Those particles passing the CE around this radius could be reconstructed as two particle tracks in the TPC, one on each side of the CE. Particles originating from vertices farther away from the nominal interaction point have to be emitted at an angle $\vartheta \neq 90°$ and hence $|\eta| > 0$ to traverse the centre of the CE. This hypothesis is tested using the example illustrated in figure 4.7. Here, a particle originates from a vertex at the position $z_{\mathrm{vtx}} = -8\,\mathrm{cm}$ corresponding to the centre of the interval $-10\,\mathrm{cm} < z_{\mathrm{vtx}} < -6\,\mathrm{cm}$. It is emitted at an angle ϑ such that it crosses the CE at $r = 166\,\mathrm{cm}$. The angle can
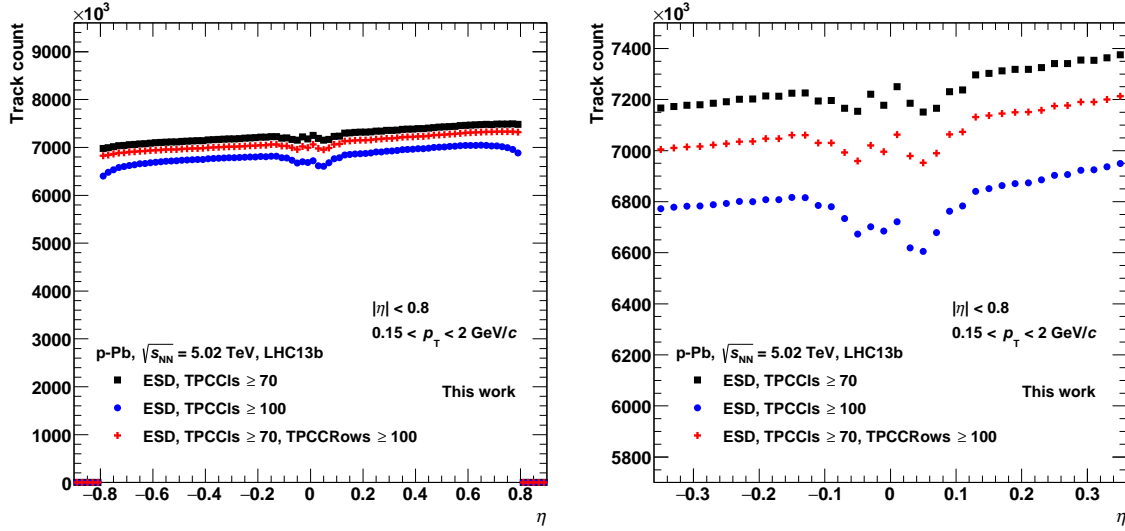
Figure 4.8.: Pseudorapidity distributions of tracks in p–Pb collisions at $\sqrt{s_{\mathrm{NN}}}$ = 5.02 TeV using different track selection criteria in the ESD analysis (pass4 with TPC refit). Left: Full range within $|\eta| < 0.8$. Right: Zoomed in on $|\eta| < 0.36$.

be obtained via the relation $\tan(\vartheta) = 166\,\mathrm{cm}\,/\,8\,\mathrm{cm}$ and with this, the pseudorapidity of the particle is calculated [13, 20]

$$\eta = -\ln\left[\tan\left(\frac{\vartheta}{2}\right)\right] = -\ln\left[\tan\left(\frac{1}{2}\cdot\arctan\left(\frac{166\,\mathrm{cm}}{8\,\mathrm{cm}}\right)\right)\right] \approx 0.048\,. \tag{4.1}$$

This value is in good agreement with the centre of the peak of the corresponding z_{vtx} interval, as can be seen in figure 4.6 (right panel). Thus, this example supports the hypothesis of two tracks being reconstructed out of one real particle trajectory passing the CE around its radial centre.

It should be noted, that the effect is only present for a small fraction of particles. If all particles traversing the CE around its centre would be reconstructed as two tracks, the η distribution would have to increase by about a factor of two around $\eta \approx 0$, but only a slight increase is observed. Nevertheless, using the standard track selection criteria introduced above, this track splitting is possible. For example the requirement of at least 70 out of a maximum of 159 clusters in the TPC [111] is low enough to allow for two tracks being reconstructed from one particle trajectory, furthermore as shared clusters are allowed, i.e. clusters belonging to more than one track. Therefore, it may be possible to remove this peak using stricter track selection criteria.

At first, the minimum number of TPC clusters (TPCCls) is increased to 100 and, as an alternative, additional TPC requirements are added to the minimum number of 70 TPC clusters. These include at least 100 crossed rows in the TPC[c], a minimum

---

[c] A pad row in the TPC is considered to be a "crossed row" of a particle track, if a TPC cluster is found in that row or in one of the two neighbouring rows on each side. Hence, for a given
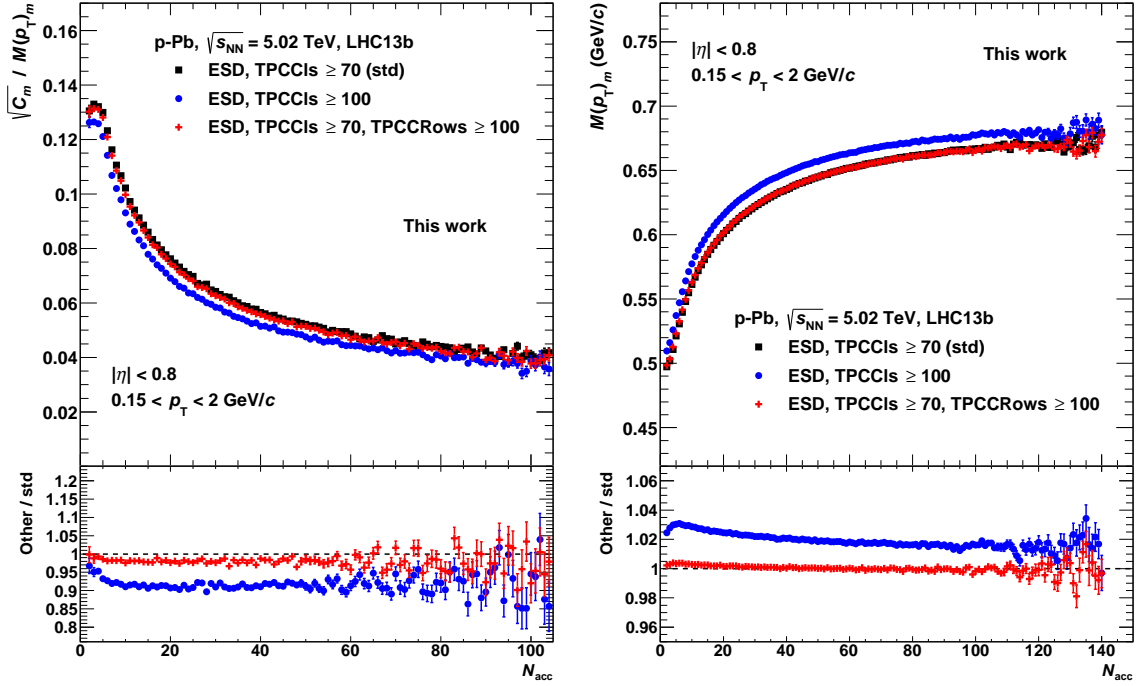
Figure 4.9.: Comparison of results in p–Pb collisions at $\sqrt{s_{NN}} = 5.02$ TeV using different track selection criteria in the ESD analysis (pass4 with TPC refit). Left: $\sqrt{C_m}/M(p_T)_m$ as a function of N_{acc}. Right: $M(p_T)_m$ as a function of N_{acc}. The lower panels show the ratios to the standard analysis (std).

fraction of 80% of the crossed rows with respect to the findable clusters along a track, excluding for example the chamber boundaries, and a maximum fraction of 40% of the clusters of a track being shared with different tracks. For this study, the ESD pass4 reconstruction is used. The corresponding η distributions are shown together with that of the standard analysis in figure 4.8 for the full range $|\eta| < 0.8$ (left panel) and zoomed in on $|\eta| < 0.36$ (right panel). Especially in the detailed view of the zoomed figure the peak turns out to be a double peak in contrast to the single and larger peak of the AOD FB = 128 analysis. Adding the additional conditions ("TPCCRows ≥ 100" in figure 4.8) reduces the overall number of accepted tracks, but the shape of the distribution including the double peak stays almost identical. Using the stricter criterion of at least 100 TPC clusters further reduces the number of accepted tracks and also the peak structure around $\eta \approx 0$, although some residual peaks remain within the clearly observed dip. In addition, more tracks are lost at the edges of the η distribution, similar to the effect observed in the hybrid analysis with AOD FB = 768, see figure 4.5.

In figure 4.9, the effects of the different track selection criteria on $\sqrt{C_m}/M(p_T)_m$ (left panel) and $M(p_T)_m$ (right panel) are presented. Using the additional conditions with

---

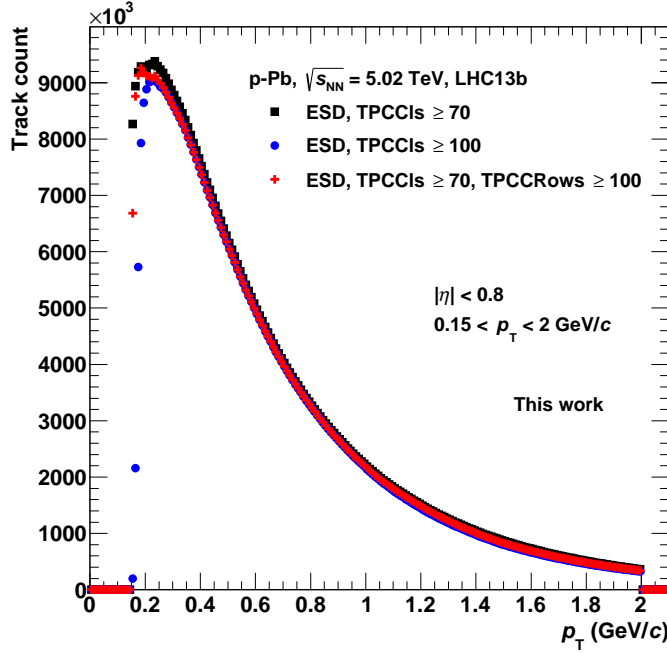track, the number of crossed rows in the TPC (TPCCRows) is typically higher than the number of clusters.

Figure 4.10.: Comparison of p_{T} distributions in p–Pb collisions at $\sqrt{s_{\mathrm{NN}}}$ = 5.02 TeV using different track selection criteria in the ESD analysis (pass4 with TPC refit).

the number of crossed rows and fraction of shared clusters does not alter the results for $M(p_{\mathrm{T}})_m$ significantly and only slightly decreases $\sqrt{C_m}/M(p_{\mathrm{T}})_m$ about 1–2%. The strict criterion of at least 100 clusters in the TPC, however, changes the results clearly increasing $M(p_{\mathrm{T}})_m$ about 2–3% and decreasing $\sqrt{C_m}/M(p_{\mathrm{T}})_m$ up to 10%. The significant increase of the mean transverse momentum hints to a loss of low-p_{T} tracks, which is verified by a comparison of the p_{T} spectra. These are shown in figure 4.10 for the ESD pass4 analyses and the three different sets of TPC track requirements. While the version using the crossed rows slightly differs from the standard analysis, the cut of at least 100 TPC clusters removes a significant fraction of low-p_{T} tracks and hence reduces the kinematic range of the analysis. This restriction is also responsible for at least some part of the decrease of $\sqrt{C_m}/M(p_{\mathrm{T}})_m$, as a restricted p_{T} range also reduces the fluctuations of the mean transverse momentum.

The behaviour of the different track selection criteria as a function of η and p_{T} is studied in more detail to avoid significant reductions of the kinematic ranges using stricter track selections. The corresponding figures are presented in Appendix B for the example of the standard ESD analysis using the pass4 reconstruction with a minimum number of 70 TPC clusters per track and including the TPC refit. In the distribution of the number of TPC clusters as a function of p_{T} (lower right panel of figure B.1), a sharp decrease is observed towards the lowest p_{T}. With a requirement of at least 100 TPC clusters, a large fraction of tracks is lost in this range. As a function of η (lower left panel of figure B.1), the number of TPC clusters exhibits a dip with a smaller

peak around $\eta \approx 0$ and decreases towards large values of $|\eta|$, which explains the loss of tracks in these parts using the strict condition. In the distribution of the number of crossed rows in the TPC a similar drop is observed as a function of p_T (lower right panel of figure B.2), but it is much less pronounced and a criterion of at least 100 crossed rows removes only a small fraction of the tracks. With the requirement of a minimum fraction of 80% crossed rows out of the findable clusters (figure B.3), the number of tracks is reduced with no dependence on η and only slightly depending on p_T.

In the distribution of the number of shared clusters in the TPC as a function of η a clear double-peak structure around $\eta \approx 0$ is observed (lower left panel of figure B.4) suggesting this criterion as a good candidate to remove the residual double-peak structure in η. Therefore, the analysis is redone using the ESD pass4 reconstruction with the standard track selection criteria including the TPC refit and the additional requirement of a maximum fraction of shared clusters in the TPC. This condition is varied in several steps down to a maximum fraction of 3%. With each step, the total number of tracks is reduced, but the double-peak structure does not vanish, even when applying the most strict condition. Obviously, the double-peak structure is also present in the tracks with only a very small number of shared clusters, although this is not visible on the scale of figure B.4. Furthermore, the TPC shared clusters requirement and its variations have no effect on the results for $M(p_T)_m$ and $\sqrt{C_m}/M(p_T)_m$. Therefore, this condition is not applied within the final set of track selection criteria.

The splitting of one trajectory into two tracks at the central electrode of the TPC could be related to issues in the calibration of the data, which may be observed in discontinuities in the distributions of the distance of closest approach (DCA) of the tracks to the primary vertex. If, for example, the calibration of the drift velocity would be wrong, a step in the distribution of the DCAs along the beam (z) direction is expected at $\eta = 0$. The DCA distributions are checked in detail in the transverse plane (figure B.6) and in z direction (figure B.7). All of these distributions, also as a function of η and p_T, look fine with no unexpected structures and no steps at $\eta = 0$. Furthermore, none of the features of the η distributions described in this section are observed in the DCAs, thus, stricter DCA conditions are not expected to have any influence within these studies.

In conclusion, the observed structures around $\eta \approx 0$ are most likely related to particle trajectories, which are reconstructed as two tracks, one on each side of the TPC. However, only a small fraction of the trajectories is affected and no severe issues concerning the calibration or tracking are found. The residual double-peak structure observed in the ESD analyses cannot be removed using stricter track selection criteria, unless the requirements are chosen in a way, which in addition restricts the kinematic acceptance. Overall, the effects of this track splitting for the results of $M(p_T)_m$ and $\sqrt{C_m}/M(p_T)_m$ are small. Those cases with larger deviations of the results go along with restrictions of the kinematic range and, hence, they cannot be considered as reasonable comparisons. Finally, the differences of the results obtained in the AOD analyses with FB = 128 (TPC-standalone tracking) and FB = 768 (hybrid tracking) are used in the determination of the systematic uncertainties, see section 4.7. As these two
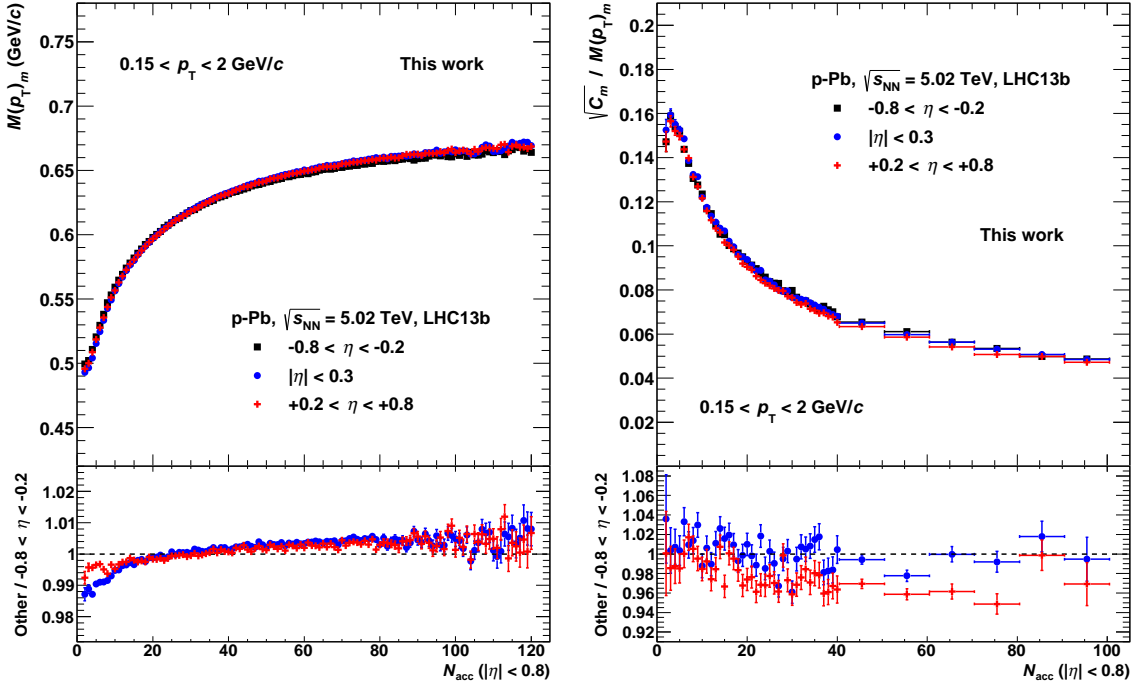
Figure 4.11.: Results in η intervals with $\Delta\eta = 0.6$ in p–Pb collisions at $\sqrt{s_{\mathrm{NN}}} = 5.02\,\mathrm{TeV}$. Left: $M(p_{\mathrm{T}})_m$ as a function of $N_{\mathrm{acc}}(|\eta| < 0.8)$. Right: $\sqrt{C_m}/M(p_{\mathrm{T}})_m$ as a function of $N_{\mathrm{acc}}(|\eta| < 0.8)$. The bottom panels show the ratios to the interval $-0.8 < \eta < -0.2$.

analyses also show pronounced differences in the η distribution, potential influences on the results are covered by these uncertainties.

Nevertheless, it should be noted that these track splitting effects around the centre of the experiment may significantly affect other correlation or fluctuation analyses, especially if narrow pseudorapidity intervals are compared, e.g. in forward-backward correlation studies. These effects should be investigated carefully in such analyses.

4.4. Acceptance in an asymmetric system

In the published analysis, symmetric collision systems have been analysed, where both particle beams in the LHC consist of the same particle species and are accelerated to the same beam energy. Hence, the centre-of-mass system of the collisions is in coincidence with the laboratory system leading to a symmetric acceptance in the central-barrel detectors of ALICE. Due to the magnetic coupling of the two LHC rings [33], the same beam energy and, thus, a symmetric acceptance in ALICE cannot be achieved for the collisions of different particle species with an unequal charge-to-mass ratio. In p–Pb collisions at $\sqrt{s_{\mathrm{NN}}} = 5.02\,\mathrm{TeV}$ the nucleon–nucleon centre-of-mass system is shifted in the direction of the proton beam by $\Delta y_{\mathrm{NN}} = 0.465$ [119, 164]. During the data-taking periods from the 2013 p–Pb run considered in this analysis,
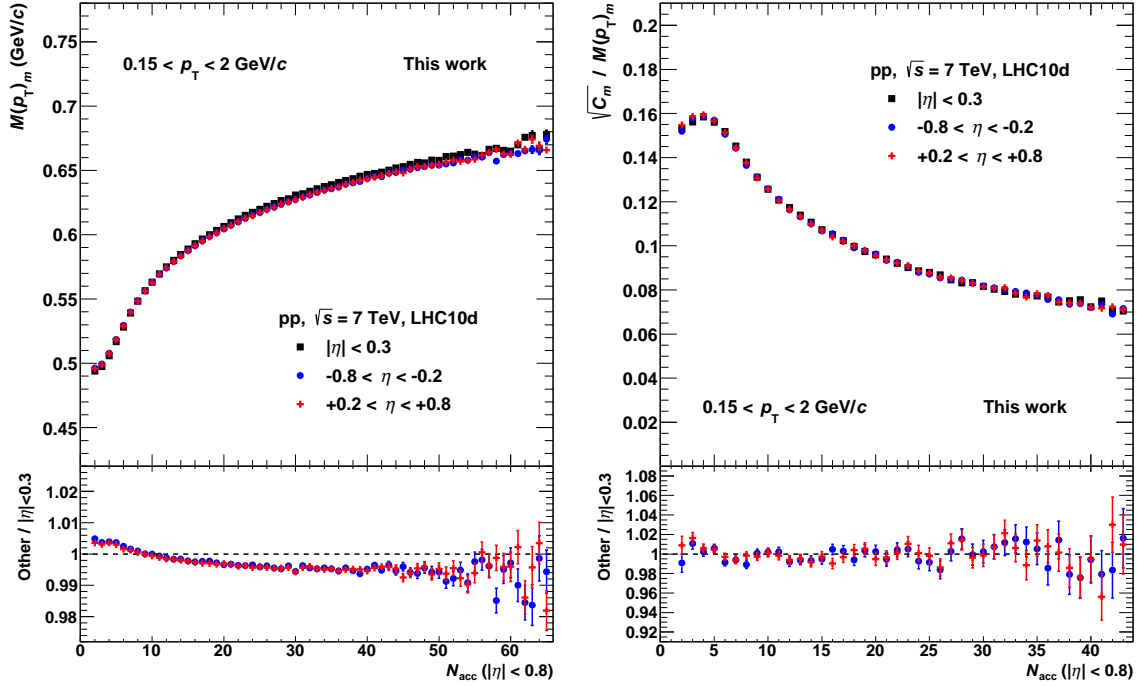
Figure 4.12.: Results in η intervals with $\Delta\eta = 0.6$ in pp collisions at $\sqrt{s} = 7\,\text{TeV}$. Left: $M(p_\text{T})_m$ as a function of $N_\text{acc}(|\eta| < 0.8)$. Right: $\sqrt{C_m}/M(p_\text{T})_m$ as a function of $N_\text{acc}(|\eta| < 0.8)$. The bottom panels show the ratios to the interval $|\eta| < 0.3$.

the proton beam was always going in the negative direction. As the rapidity and the pseudorapidity are in approximate agreement, the centre-of-mass is located in the laboratory system at $\eta \approx -0.465$.

Within the previous analysis, a detailed study of the dependence of the mean transverse momentum on z_vtx, p_T and η has been carried out, see section 3.4.3. No significant dependence on η is observed within $|\eta| < 0.8$ for symmetric collision systems, see figure 3.11, but a small decrease is found at the edges of the distributions especially on the positive η side. In an asymmetric collision system this effect may become more important if the full η range is analysed. Furthermore, also the particle production is asymmetric, which also may have an influence on mean p_T and its fluctuations.

To investigate these effects, both $M(p_\text{T})_m$ and $\sqrt{C_m}/M(p_\text{T})_m$ are analysed within a narrower η window approximately symmetric around the centre-of-mass of the collisions using $-0.8 < \eta < -0.2$. This interval is compared to intervals of the same size $\Delta\eta = 0.6$, but centred around midrapidity in the laboratory system ($|\eta| < 0.3$) and at positive pseudorapidity ($+0.2 < \eta < +0.8$) corresponding to forward rapidities in the centre-of-mass system. The results in p–Pb collisions at $\sqrt{s_\text{NN}} = 5.02\,\text{TeV}$ are presented in figure 4.11 showing $M(p_\text{T})_m$ (left panel) and $\sqrt{C_m}/M(p_\text{T})_m$ (right panel) as a function of the accepted multiplicity in the full η range, i.e. $N_\text{acc}(|\eta| < 0.8)$. At low multiplicities, $M(p_\text{T})_m$ is lower in the forward rapidities than at the centre-
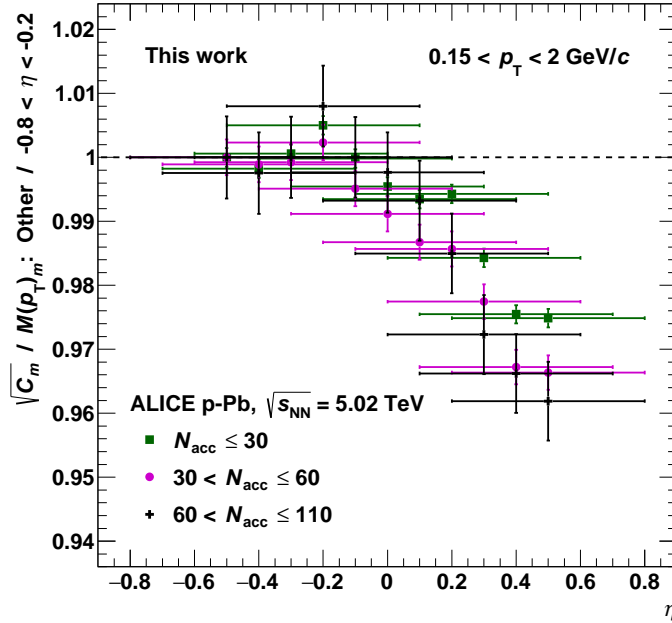
Figure 4.13.: Ratios of $\sqrt{C_m}/M(p_{\mathrm{T}})_m$ in different η windows with $\Delta\eta = 0.6$ to the result in $-0.8 < \eta < -0.2$ in p–Pb collisions at $\sqrt{s_{\mathrm{NN}}} = 5.02\,\mathrm{TeV}$ for three different multiplicity intervals.

of-mass midrapidity (i.e. $-0.8 < \eta < -0.2$), but it is rising and slightly higher for $N_{\mathrm{acc}}(|\eta| < 0.8) \gtrsim 30$. The effect at low N_{acc} is larger for the interval $|\eta| < 0.3$ although it is located closer to $-0.8 < \eta < -0.2$, but in general the deviations are small reaching at maximum about 1%. Concerning $\sqrt{C_m}/M(p_{\mathrm{T}})_m$ the results in the interval $|\eta| < 0.3$ are in agreement with those in $-0.8 < \eta < -0.2$ within the statistical uncertainties, but the results in the most forward rapidity $+0.2 < \eta < +0.8$ are significantly below the others with a difference of up to 4%. It is concluded, that the mean p_{T} fluctuations change with the rapidity, which may have to be taken into account when comparing the collision systems, but within the acceptance of the ALICE central-barrel detectors this effect is rather small.

A similar study is performed in pp collisions at $\sqrt{s} = 7\,\mathrm{TeV}$, which is presented in figure 4.12. Again, the left panel shows $M(p_{\mathrm{T}})_m$ and the right panel shows $\sqrt{C_m}/M(p_{\mathrm{T}})_m$ both as a function of $N_{\mathrm{acc}}(|\eta| < 0.8)$. In the ratio panels, the results in the forward intervals are divided by those within $|\eta| < 0.3$ corresponding to midrapidity both in the centre-of-mass and in the laboratory system. $M(p_{\mathrm{T}})_m$ is slightly higher in both forward intervals at small multiplicities, equal around $N_{\mathrm{acc}}(|\eta| < 0.8) \approx 10$ and slightly lower above, saturating at a maximum difference of about 0.5%. $\sqrt{C_m}/M(p_{\mathrm{T}})_m$ is in agreement in all three intervals within the statistical uncertainties. This demonstrates, that in the symmetric collision systems the physics of mean p_{T} fluctuations does not change significantly within the studied pseudorapidity range of $|\eta| < 0.8$.
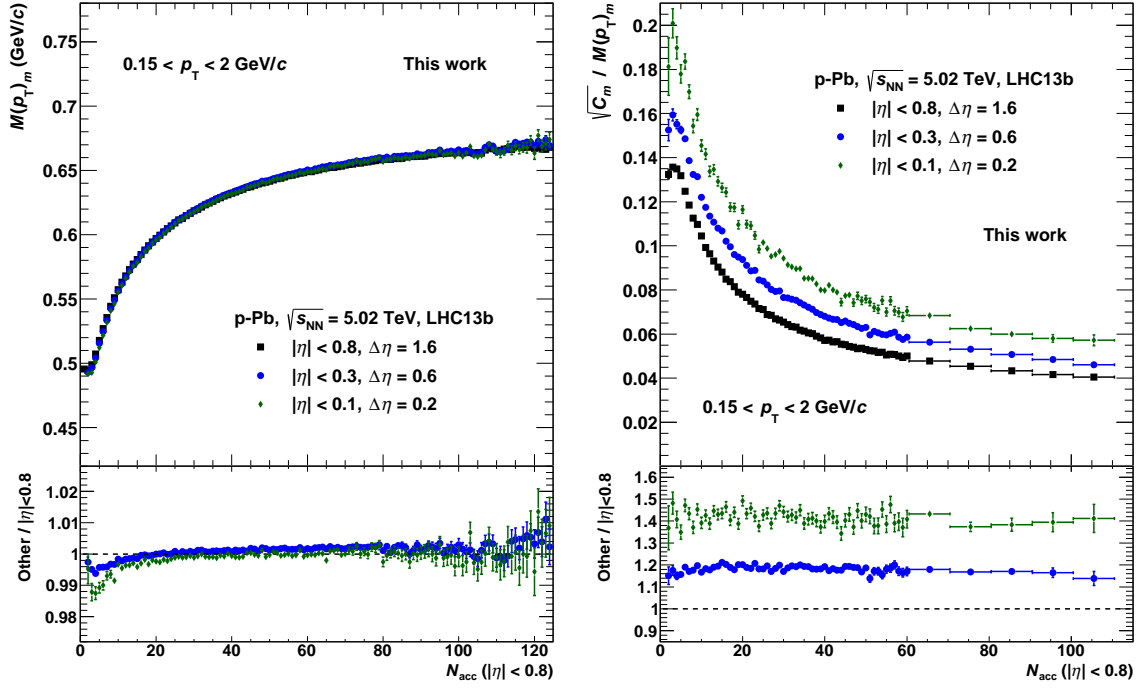
Figure 4.14.: Comparison of several $\Delta\eta$ widths in p–Pb collisions at $\sqrt{s_{NN}}$ = 5.02 TeV. Left: $M(p_T)_m$ as a function of $N_{acc}(|\eta| < 0.8)$. Right: $\sqrt{C_m}/M(p_T)_m$ as a function of $N_{acc}(|\eta| < 0.8)$. The bottom panels show the ratios to the full range $|\eta| < 0.8$.

The behaviour of $\sqrt{C_m}/M(p_T)_m$ as a function of η in p–Pb collisions is studied in more detail by performing a scan of the results along η using interval widths of $\Delta\eta$ = 0.6 and steps of $\delta\eta$ = 0.1. For this analysis, the data set is divided into three intervals of the accepted multiplicity. The results are shown in figure 4.13, for each multiplicity interval in terms of the ratio of all η intervals to $-0.8 < \eta < -0.2$. In the latter, the bin centre at $\eta = -0.5$ corresponds approximately to midrapidity in the centre-of-mass system. The results remain almost constant up to bin centres around $\eta = 0$ and start to decrease at positive values of η. For bin centres with $\eta > 0.2$ deviations of more than 2% are observed reaching at maximum 4%. No significant dependence on the multiplicity is found, although in the region of $\eta > 0$ a trend is observed, that the deviations get larger for higher multiplicities.

It is considered to restrict the analysis in p–Pb collisions to a pseudorapidity range of $-0.8 < \eta < +0.2$ corresponding to an interval width of $\Delta\eta$ = 1.0. Intervals completely located within this range exhibit deviations of $\sqrt{C_m}/M(p_T)_m$ of less than 1% and, hence, the results show no significant dependence on η. As the next step, it is checked, whether different interval sizes have an influence on the results. A comparison of three different interval widths is presented in figure 4.14 showing $M(p_T)_m$ (left panel) and $\sqrt{C_m}/M(p_T)_m$ (right panel) as a function of $N_{acc}(|\eta| < 0.8)$. $M(p_T)_m$ decreases slightly with decreasing $\Delta\eta$ width at low multiplicities and is almost independent

of the width for $N_{\text{acc}}(|\eta| < 0.8) \gtrsim 20$. However, the mean p_{T} fluctuations exhibit a distinct dependence on the interval width. They increase by about 20% when going from $\Delta\eta = 1.6$ to $\Delta\eta = 0.6$ and by about 40% in the case of $\Delta\eta = 0.2$. Therefore, in a comparison of different collision systems an identical $\Delta\eta$ width has to be used. This effect is much more important than the change of the results along η considering the same widths as demonstrated in figure 4.13.

In order to compare the results in p–Pb collisions to those obtained in pp and Pb–Pb collisions, both the full pseudorapidity acceptance of $|\eta| < 0.8$ and a restricted acceptance with $\Delta\eta = 1.0$ are employed. The results within the full acceptance can be compared directly to the published ones [3], see also chapters 3 and 5.1. For the second case, the analyses in pp and Pb–Pb collisions are repeated within $|\eta| < 0.5$, which is described in section 4.9.

4.5. Period and run comparisons

The periods and runs of the data sets used in this analysis are summarised in Appendix A. As part of the quality assurance of the data and selection of the runs, the results for $M(p_{\text{T}})_m$ and $\sqrt{C_m}/M(p_{\text{T}})_m$ are compared among the different periods used within one data set and among the runs of each period. As an example, such comparisons are presented here for p–Pb collisions at $\sqrt{s_{\text{NN}}} = 5.02\,\text{TeV}$ applying the kinematic acceptance of $|\eta| < 0.8$ and $0.15\,\text{GeV}/c < p_{\text{T}} < 2\,\text{GeV}/c$. Only those runs are used in the analysis, which are declared as good runs by the quality assurance of the experts of the ITS, TPC and V0 detectors.

In figure 4.15, comparisons of the runs of the period LHC13c using the ESD reconstruction pass4 with the TPC-standalone tracking are presented. In the top panels, $M(p_{\text{T}})_m$ is shown as a function of N_{acc} (left panel) and the corresponding ratios of $M(p_{\text{T}})_m$ of the single runs to the result of the complete period LHC13c (right panel). $M(p_{\text{T}})_m$ agrees well in all runs with only small deviations mainly at high multiplicities and always covered by the statistical uncertainties of the single runs. The bottom panels of figure 4.15 show $\sqrt{C_m}/M(p_{\text{T}})_m$ as a function of N_{acc} (left panel) and again the ratios of the single runs to the full sample (right panel). Also here, no run exhibits deviations from the full period beyond those expected from the statistical uncertainties. Therefore, all of these runs are kept in the analysis and used for the final results presented in chapter 5. The same comparisons are also carried out for the runs of the period LHC13b, which is also part of the 2013 p–Pb minimum-bias data set used in this study. Again, only those runs with a good detector quality assurance are included. Also in this period, the results of all of these runs agree with those of the full period within their statistical uncertainties and, thus, all of these runs are used as well for the final results.

In addition to the single runs within the periods, the results of the two periods LHC13b and LHC13c are compared. In figure 4.16, $M(p_{\text{T}})_m$ (left panel) and $\sqrt{C_m}/M(p_{\text{T}})_m$ (right panel) are presented as a function of N_{acc} for the two periods separately and for the merged data set of both periods. The results of both periods are in good
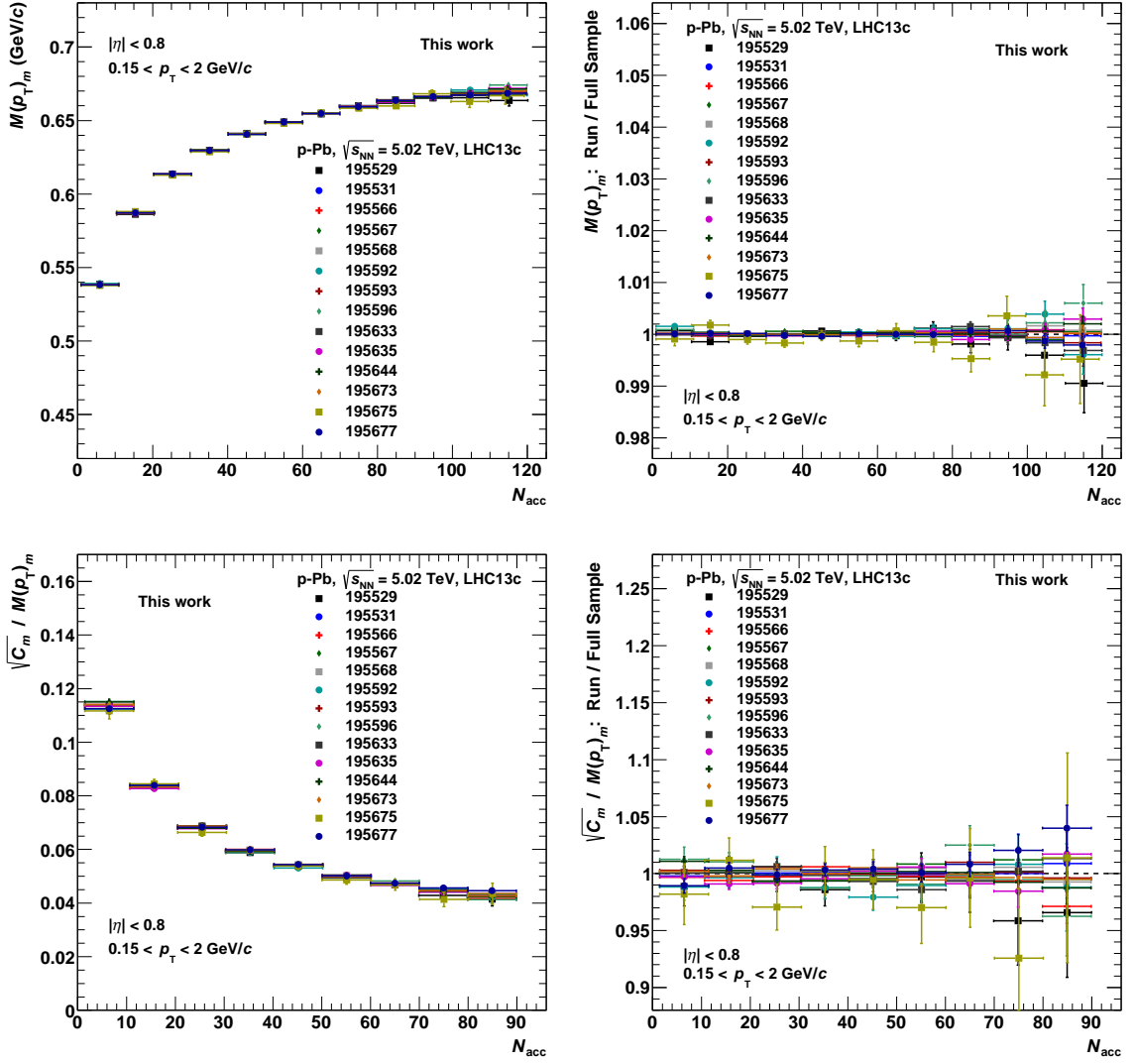
Figure 4.15.: Comparison of the results of single runs in the period LHC13c corresponding to p–Pb collisions at $\sqrt{s_{\mathrm{NN}}}$ = 5.02 TeV. Top panels: $M(p_{\mathrm{T}})_m$ as a function of N_{acc}. Bottom panels: $\sqrt{C_m}/M(p_{\mathrm{T}})_m$ as a function of N_{acc}. In both cases, the right panels show the ratio of the single-run results to that of the full period.

agreement. The period LHC13c contains about three times the event statistics of LHC13b and, hence, exhibits a better agreement with the merged sample and smaller statistical uncertainties.
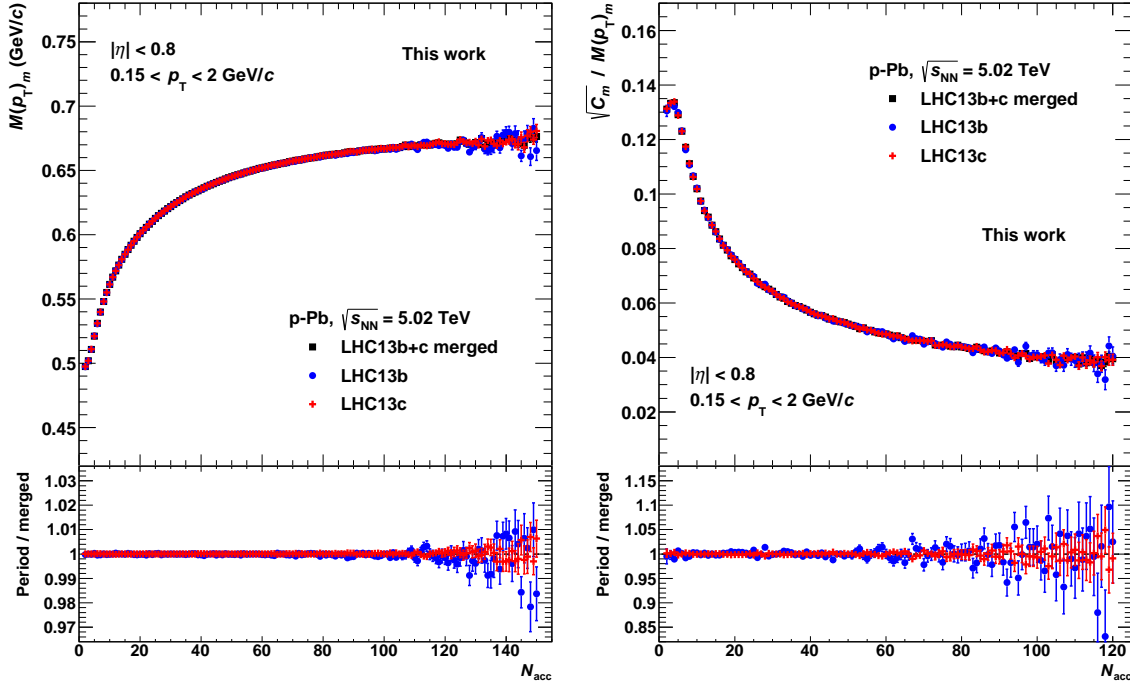
Figure 4.16.: Comparisons of the results of the periods LHC13b and LHC13c in p–Pb collisions at $\sqrt{s_{NN}} = 5.02\,\text{TeV}$. Left: $M(p_T)_m$ as a function of N_{acc}. Right: $\sqrt{C_m}/M(p_T)_m$ as a function of N_{acc}. The bottom panels show the ratios of the single periods to the merged sample of both periods.

4.6. Multiplicity determination

In the published analysis, most of the results are presented as a function of the average charged-particle multiplicity density $\langle dN_{\text{ch}}/d\eta \rangle$. This representation is also applied in the case of p–Pb collisions to be able to compare all three collision systems. Here, the same procedure is used as in Pb–Pb collisions, which is described in section 3.6.2.

The definition of multiplicity classes is not straightforward in p–Pb collisions and different estimators exhibit significant deviations [167]. For the transition from N_{acc} to $\langle dN_{\text{ch}}/d\eta \rangle$ these differences are not relevant as long as for a given estimator the average number of accepted particles $\langle N_{\text{acc}} \rangle$ within the intervals is related linearly to $\langle dN_{\text{ch}}/d\eta \rangle$ in the same intervals. In the symmetric collision systems, $\langle dN_{\text{ch}}/d\eta \rangle$ is typically quoted within $|\eta_{\text{lab}}| < 0.5$, where η_{lab} is the pseudorapidity in the laboratory system. This coincides with a symmetric acceptance around midrapidity. In p–Pb collisions, the centre-of-mass system is shifted and, furthermore, the particle production is not symmetric around midrapidity with more particles being created in the Pb-going direction. Nevertheless, $|\eta_{\text{lab}}| < 0.5$ is used for the comparison to the other collision systems and, to emphasize this aspect, the multiplicity density is explicitly denoted as "$\langle dN_{\text{ch}}/d\eta \rangle (|\eta_{\text{lab}}| < 0.5)$".

In the analysis of p–Pb collisions, V0A multiplicity classes are used as default estimator. The corresponding values of $\langle dN_{\text{ch}}/d\eta \rangle (|\eta_{\text{lab}}| < 0.5)$ are taken from [164]. In
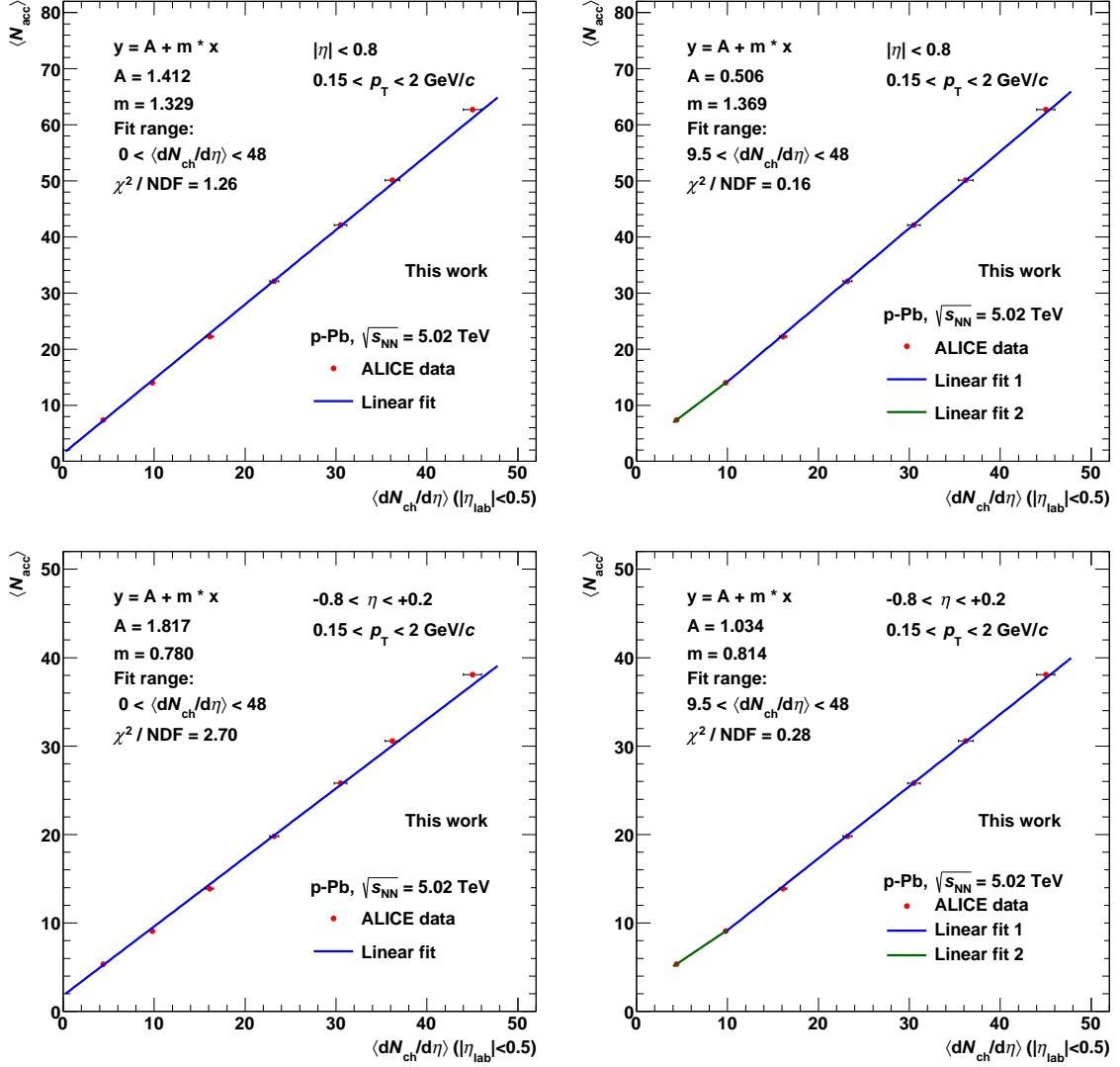
Figure 4.17.: $\langle N_{\mathrm{acc}} \rangle$ as a function of $\langle \mathrm{d}N_{\mathrm{ch}}/\mathrm{d}\eta \rangle (|\eta_{\mathrm{lab}}| < 0.5)$ obtained from V0A [164] in p–Pb collisions at $\sqrt{s_{\mathrm{NN}}} = 5.02\,\mathrm{TeV}$. $\langle N_{\mathrm{acc}} \rangle$ is shown for the pseudorapidity ranges $|\eta| < 0.8$ (upper panels) and $-0.8 < \eta < +0.2$ (lower panels). Left panels: Including one fit over the full $\langle \mathrm{d}N_{\mathrm{ch}}/\mathrm{d}\eta \rangle$ range. Right panels: With one fit excluding the first data point and an interpolation between the first two points.

figure 4.17, $\langle N_{\mathrm{acc}} \rangle$ is presented as a function of $\langle \mathrm{d}N_{\mathrm{ch}}/\mathrm{d}\eta \rangle (|\eta_{\mathrm{lab}}| < 0.5)$ using the V0A definition. In the upper panels, $\langle N_{\mathrm{acc}} \rangle$ is obtained within the full pseudorapidity range of $|\eta| < 0.8$, in the lower panels the acceptance is restricted to $-0.8 < \eta < +0.2$. In the left panels, the data points are fitted with one linear fit covering the full multiplicity range. The fit parameters are added on the figures and the fits exhibit a reasonable agreement with the data, although the correspondence is not as good as in the case of Pb–Pb collisions. At low multiplicities, a tendency of a flattening slope is observed,
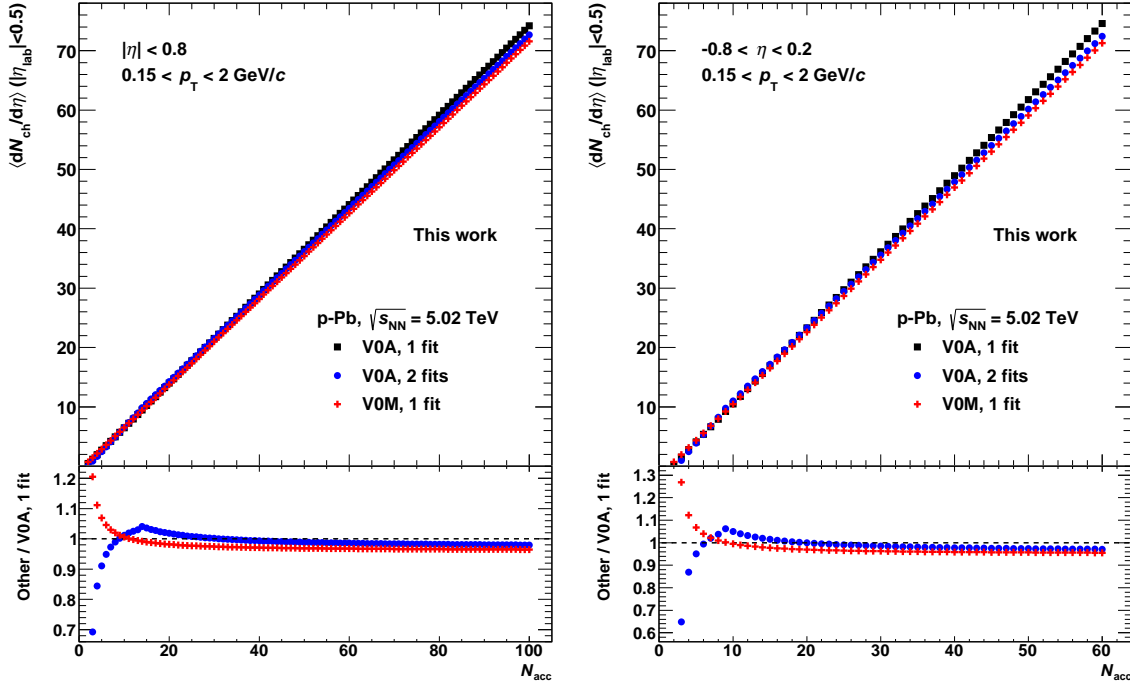
Figure 4.18.: $\langle dN_{ch}/d\eta \rangle (|\eta_{lab}| < 0.5)$ as a function of N_{acc} in p–Pb collisions at $\sqrt{s_{NN}} = 5.02\,\mathrm{TeV}$ for different fits: two versions using V0A [164] (see figure 4.17) and one with V0M [63]. Left: N_{acc} within $|\eta| < 0.8$. Right: N_{acc} within $-0.8 < \eta < +0.2$. The bottom panels show the ratios to one V0A fit over the full multiplicity range.

leading to slightly higher values of $\langle N_{acc} \rangle$. Therefore, as an alternative, the first point is removed from the fit and a linear interpolation between the first two points is used for multiplicities below the second point. The results are presented in the right panels of figure 4.17. Here, the parameters of the fits excluding the first point are displayed on the figures. They show a better agreement with the data than the fits covering the full range, which is indicated by a decreased χ^2/NDF.

As a second alternative, the procedure is repeated using V0M multiplicity classes from [63]. Here, only four intervals are available and the agreement of the linear fits with the data points is not as good as when using V0A multiplicity classes, but the fit parameters are similar to those obtained with V0A. Figure 4.18 presents a comparison of $\langle dN_{ch}/d\eta \rangle (|\eta_{lab}| < 0.5)$ as a function of N_{acc} obtained with the three different approaches. In the left panel, the results are shown for N_{acc} within $|\eta| < 0.8$ and in the right panels for $-0.8 < \eta < +0.2$. The ratios to the version with one fit over the full multiplicity range using V0A demonstrate a good agreement of the three approaches with deviations of the order of a few percent with the exception of multiplicities with $N_{acc} < 5$, where the differences exceed 10%. Please note, that in both ratio panels the data points for $N_{acc} = 2$ are exceeding the scale and are therefore not shown. It is concluded to use the V0A version with one fit for the results and
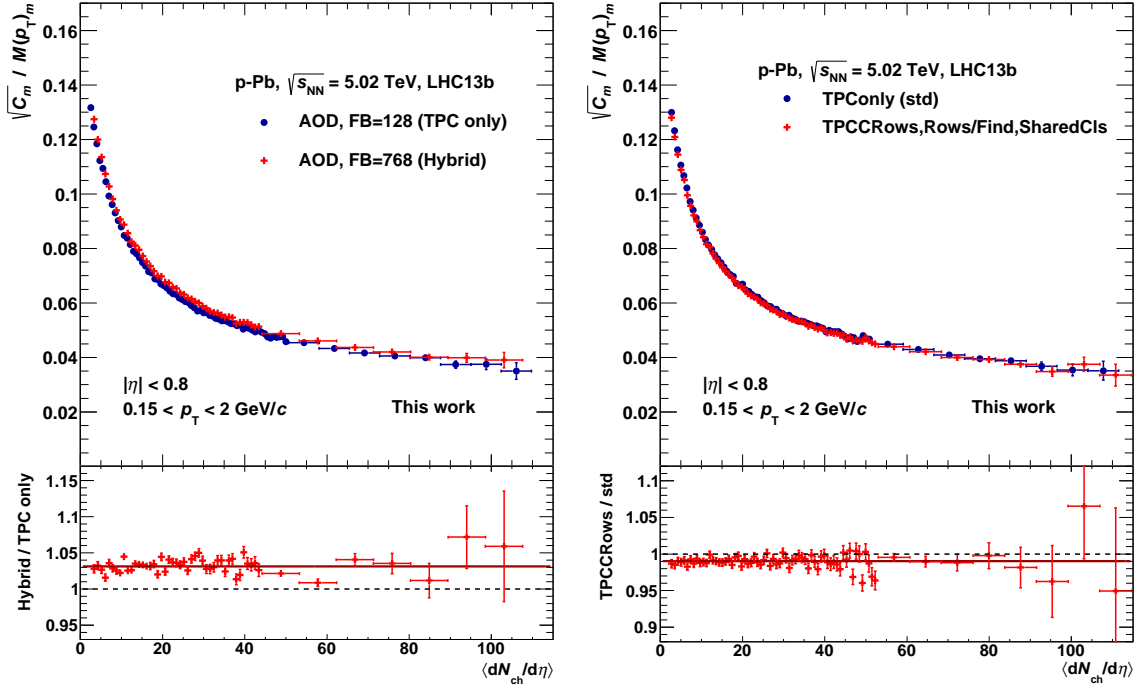
Figure 4.19.: $\sqrt{C_m}/M(p_{\mathrm{T}})_m$ as a function of $\langle \mathrm{d}N_{\mathrm{ch}}/\mathrm{d}\eta \rangle$ for different tracking schemes in p–Pb collisions at $\sqrt{s_{\mathrm{NN}}}$ = 5.02 TeV. Left: Comparison of TPC-standalone and hybrid tracking using AOD filter bits. Right: Two different TPC-standalone schemes applied on ESDs. The bottom panels show the ratios to the standard TPC-standalone tracking.

to exclude the results with N_{acc} < 5, as a reliable multiplicity determination is not possible in this range with the methods applied here.

4.7. Systematic uncertainties

The determination of the systematic uncertainties in the published analysis is described in section 3.7. In the new analysis, most of the contributions to the systematic uncertainties are evaluated according to the published analysis. Therefore, this section is focussed on the differences and some additional studies, whereas the details of the effects common to both analyses can be found in section 3.7.

The most important contributions to the systematic uncertainties in the previous analysis are composed of the tracking schemes and the differences of the MC simulations on the generator level to the full simulations. The deviations of the tracking schemes constitute the most important effect in this analysis of p–Pb collisions as well. In addition to the standard TPC-standalone and the hybrid tracking, an alternative TPC-standalone scheme is applied. Within this scheme, different track selection criteria are employed, which are described in section 4.3.2. Here, the following requirements are used: at least 100 crossed rows in the TPC, a minimum ratio of crossed
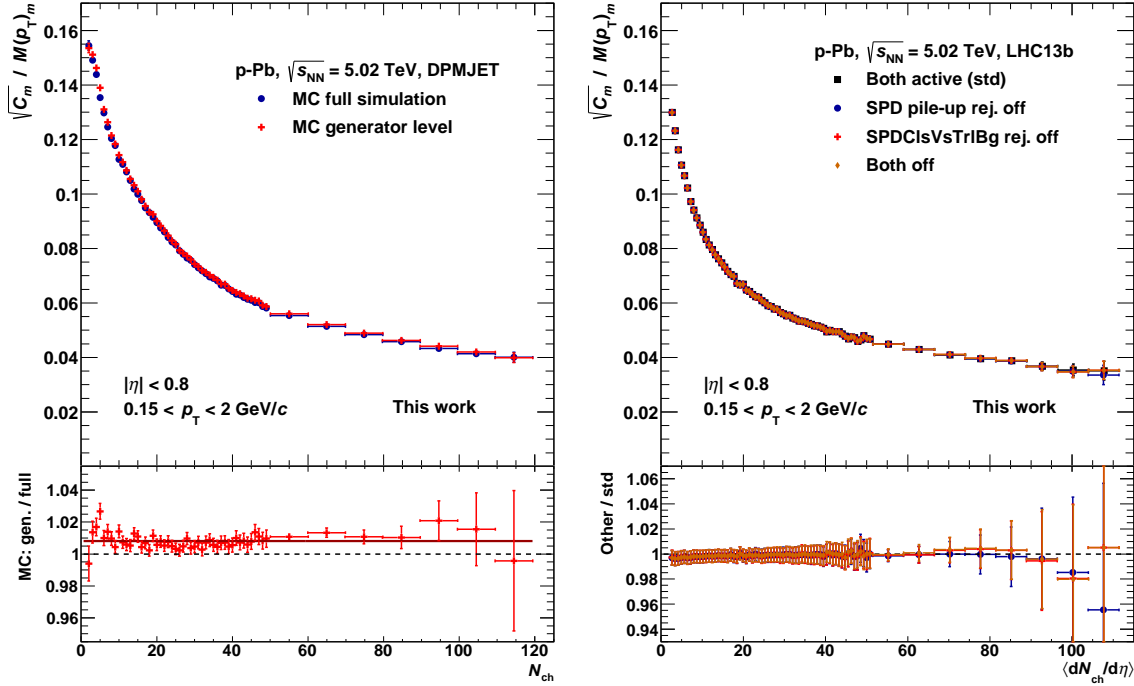
Figure 4.20.: Left: $\sqrt{C_m}/M(p_T)_m$ from the DPMJET MC generator and the corresponding full simulation in p–Pb collisions at $\sqrt{s_{NN}} = 5.02\,\text{TeV}$ as a function of N_{ch} from the generator level. The bottom panel shows the ratio of the generator level to the full simulation. Right: $\sqrt{C_m}/M(p_T)_m$ as a function of $\langle dN_{ch}/d\eta \rangle$ in data for different pile-up rejection settings. In the bottom panel, the ratios to the standard setting are presented.

rows to findable clusters of 80% and a maximum fraction of clusters shared with other tracks of 3%. No requirement on the minimum number of TPC clusters is applied. In figure 4.19, comparisons of the standard TPC-standalone tracking with the hybrid tracking (left panel) and with the alternative TPC-standalone scheme (right panel) are shown. In both cases, deviations from the standard scheme are observed, which exhibit no significant dependence on $\langle dN_{ch}/d\eta \rangle$. Constant fits are performed on the ratios to obtain the systematic uncertainty. Using the hybrid tracking increases $\sqrt{C_m}/M(p_T)_m$ by 3.1% while the second TPC-standalone tracking decreases the results by 1.0%. A symmetric and multiplicity-independent tracking uncertainty of 3.1% is applied.

In contrast to the previous analysis, the systematic uncertainty originating from the comparison of the MC generator level to the full simulation is significantly smaller than that from the tracking schemes and no clear dependence on the multiplicity is found. This comparison is presented for the DPMJET MC simulation in the left panel of figure 4.20, where $\sqrt{C_m}/M(p_T)_m$ is shown as a function of the charged-particle multiplicity N_{ch} from the generator level. The differences yield only 1–2%, whereas in pp and Pb–Pb collisions a linear rise with multiplicity is observed reaching up to 4–6%, see figures 3.15 and 3.16 in section 3.7. The reason for this deviation could

be related to the different generator used here, compared to PYTHIA and HIJING applied in the other collision systems. However, in all cases the full simulations are performed using GEANT3 for the propagation of the particle trajectories through the detector and, furthermore, an alternative study of the PHOJET generator in pp collisions at $\sqrt{s}$ = 7 TeV is in qualitative agreement with the corresponding observations in PYTHIA. In the p–Pb analysis using DPMJET, a constant fit to the ratio yields 0.8%, underestimating the differences at high and at very low multiplicities. Instead of small variations over $\langle \mathrm{d}N_{\mathrm{ch}}/\mathrm{d}\eta \rangle$, a rather conservative and multiplicity-independent uncertainty of 1.5% is assumed.

Most of the additional variations of the event and track selection criteria correspond to those summarised in table 3.10 on page 84. In the new analysis of p–Pb collisions, the lowest multiplicities with $N_{\mathrm{acc}} < 5$ are omitted, because a reliable determination of $\langle \mathrm{d}N_{\mathrm{ch}}/\mathrm{d}\eta \rangle$ is not possible in this range, see the preceding section. For multiplicities with $N_{\mathrm{acc}} \geq 5$, all variations related to the vertex estimation and vertex selection criteria do not exhibit any significant deviations with respect to the default analysis. At the event level, additional studies are performed concerning the pile-up rejection. At first, within the SPD pile-up rejection, the minimum number of SPD tracklets of the pile-up vertex is changed from the default multiplicity-dependent value (see section 4.2.2) to a constant value of three or five. These variations have no influence on the results for $\sqrt{C_m}/M(p_{\mathrm{T}})_m$. As a second step, the SPD pile-up rejection and the SPD cluster-versus-tracklets background rejection are switched off either separately, or simultaneously. The effect on $\sqrt{C_m}/M(p_{\mathrm{T}})_m$ as a function of $\langle \mathrm{d}N_{\mathrm{ch}}/\mathrm{d}\eta \rangle$ is presented in the right panel of figure 4.20. A small deviation is only observed at very high multiplicities, where it is covered by the statistical uncertainties. Hence, no systematic uncertainty is added due to the pile-up rejection.

At the track level, the variations of the maximum TPC χ^2 per degree of freedom of the momentum fit do not exhibit any significant influence on $\sqrt{C_m}/M(p_{\mathrm{T}})_m$ in the published analysis of pp and Pb–Pb collisions. Therefore, these studies are omitted in this analysis. The variations of the minimum number of TPC space points and the maximum distances of closest approach (DCAs) to the primary vertex are performed as listed in table 3.10. The average number of TPC space points per track decreases rapidly towards low p_{T} as can be seen in the appendix in figure B.1. Hence, changing this criterion corresponds to an estimate of the influence of the p_{T}-dependent particle-detection efficiency. However, setting a too strict value can lead to a reduction of the phase space, see also the discussion in section 4.3.2. Variations of the DCAs correspond to changes in the secondary contamination. The results for $\sqrt{C_m}/M(p_{\mathrm{T}})_m$ as a function of $\langle \mathrm{d}N_{\mathrm{ch}}/\mathrm{d}\eta \rangle$ are shown in figure 4.21. Constant fits to the ratios are used as systematic uncertainties, yielding 1.3% in the case of the minimum TPC space points and 1.0% for the DCAs.

Another check of the influence of secondary particles is carried out using the standard TPC-standalone tracking but switching off the rejection of tracks from reconstructed secondary weak-decay topologies (*kinks*). Switching off the rejection of tracks from kinks does not alter the results significantly.
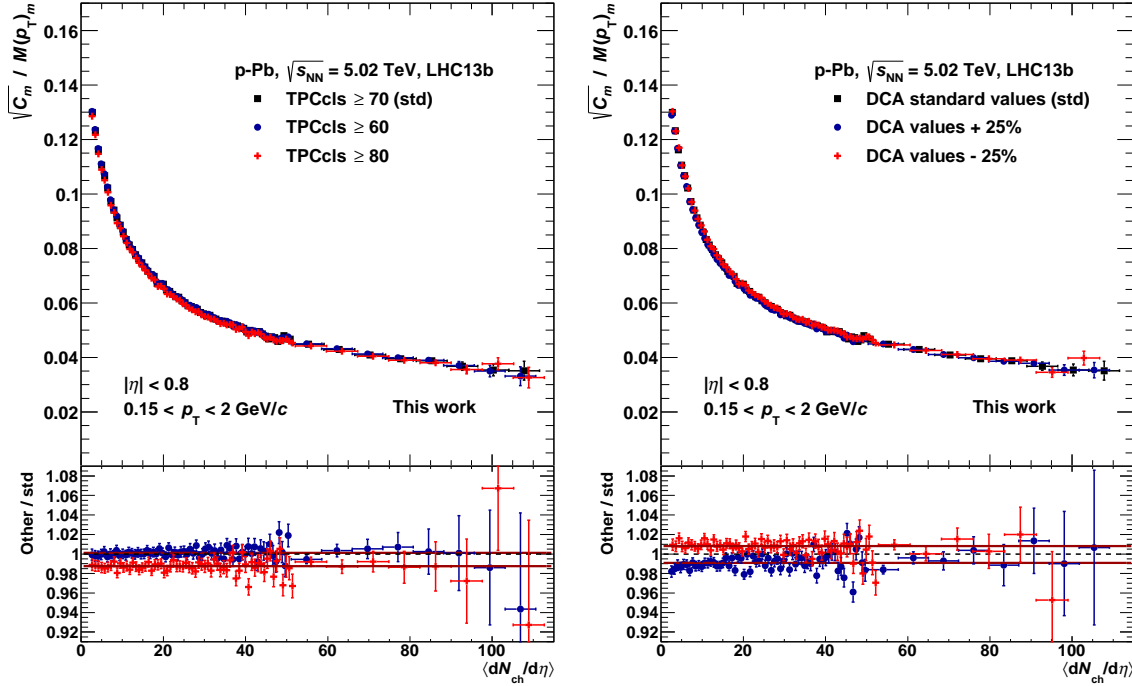
Figure 4.21.: $\sqrt{C_m}/M(p_{\mathrm{T}})_m$ as a function of $\langle \mathrm{d}N_{\mathrm{ch}}/\mathrm{d}\eta \rangle$ for variations of the minimum number of TPC space points (left) and of the maximum DCAs to the primary vertex (right) in p–Pb collisions at $\sqrt{s_{\mathrm{NN}}} = 5.02\,\mathrm{TeV}$. The bottom panels show the ratios to the standard analysis.

Within the two periods of p–Pb data taking studied in this work, no switch of the magnetic field polarity has been performed and all data have been taken with negative field polarity. As in pp collisions in the published analysis, the systematic uncertainty of 0.5% obtained in Pb–Pb collisions is used as an estimate.

Finally, the effects of the different approaches to determine the average charged-particle multiplicity density $\langle \mathrm{d}N_{\mathrm{ch}}/\mathrm{d}\eta \rangle$ on the results are investigated. The procedures and their influence on the values of $\langle \mathrm{d}N_{\mathrm{ch}}/\mathrm{d}\eta \rangle$ are described in section 4.6. Here, the uncertainties on the multiplicity axis are transformed to uncertainties on $\sqrt{C_m}/M(p_{\mathrm{T}})_m$, which facilitates the comparison to the other collision systems. The results for $\sqrt{C_m}/M(p_{\mathrm{T}})_m$ as a function of $\langle \mathrm{d}N_{\mathrm{ch}}/\mathrm{d}\eta \rangle$ obtained with the three approaches are presented in figure 4.22. The deviations of the different procedures exhibit some dependence on the multiplicity. However, no clear trend is observed and in the case of using two fits on the V0A selection a non-monotonic behaviour is found. Overall, these differences do not significantly exceed 1.5%, which is applied as constant systematic uncertainty. Please note, that the analysis is restricted to accepted multiplicities with $N_{\mathrm{acc}} \geq 5$.

The contributions to the systematic uncertainties on $\sqrt{C_m}/M(p_{\mathrm{T}})_m$ are summarised in table 4.3. The total systematic uncertainties are obtained by adding the individual contributions in quadrature. While the standard analysis is performed within the full
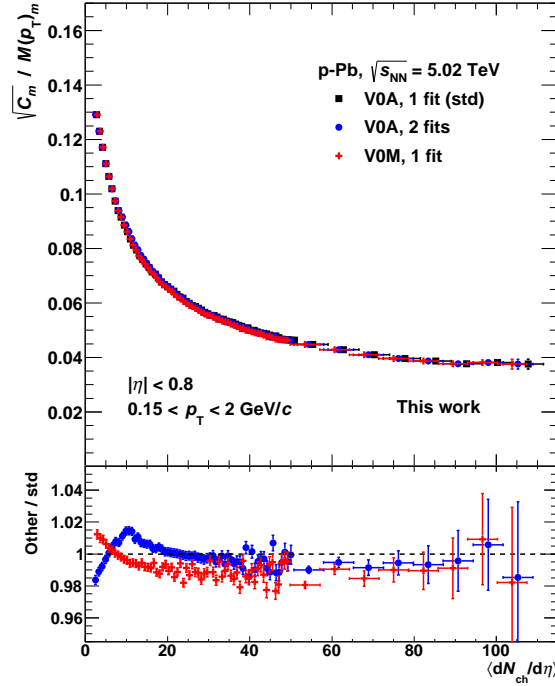
Figure 4.22.: $\sqrt{C_m}/M(p_T)_m$ as a function of $\langle dN_{ch}/d\eta \rangle$ for different approaches to determine $\langle dN_{ch}/d\eta \rangle$ in p–Pb collisions at $\sqrt{s_{NN}} = 5.02$ TeV. The bottom panel shows the ratios to the standard procedure using V0A and one fit.

pseudorapidity range of $|\eta| < 0.8$, also a restricted range of $-0.8 < \eta < +0.2$ is studied. The same contributions to the systematic uncertainties as in the standard analysis are investigated and the values are presented in table 4.3 as well. Most of the individual contributions yield identical or at least similar values in both analyses. The only exception is the uncertainty on the different tracking schemes, which is a bit larger for the restricted η range. The total systematic uncertainties of 4.1% ($|\eta| < 0.8$) and 4.6% ($-0.8 < \eta < +0.2$) are comparable.

Like in pp collisions, the inclusive $\sqrt{C}/M(p_T)$ of the complete event sample is also calculated in p–Pb collisions. The corresponding systematic uncertainties are presented in the last two columns of table 4.3, again for the two pseudorapidity ranges. Please note, that in this case no restriction of the multiplicity range is applied, which results in non-negligible uncertainties on the event selection criteria, although they still constitute minor contributions. This behaviour is in good agreement with that observed in pp collisions, where the variations of the vertex criteria show significant deviations only at the lowest multiplicities. The total systematic uncertainties of 4.0% and 4.5% are comparable to the total uncertainties on $\sqrt{C_m}/M(p_T)_m$. With central values of $\sqrt{C}/M(p_T) = 0.0704$ and $\sqrt{C}/M(p_T) = 0.0745$, the systematic uncertainties correspond to ± 0.0028 and ± 0.0033 for $|\eta| < 0.8$ and $-0.8 < \eta < +0.2$, respectively.

Quantity	$\sqrt{C_m}/M(p_{\mathrm{T}})_m$		$\sqrt{C}/M(p_{\mathrm{T}})$	
Pseudorapidity range	$\Delta\eta < 1.6$	$\Delta\eta < 1.0$	$\Delta\eta < 1.6$	$\Delta\eta < 1.0$
Vertex-z-position cut	<0.1%	<0.1%	<0.1%	<0.1%
Vertex estimator	<0.1%	<0.1%	0.3%	0.3%
Vertex-z-difference cut	<0.1%	<0.1%	0.6%	0.6%
Pile-up rejection	<0.1%	<0.1%	0.3%	0.3%
Tracking	3.1%	3.7%	3.6%	4.2%
Min. TPC space points	1.3%	1.3%	1.1%	1.1%
DCA to vertex	1.0%	0.8%	1.0%	0.8%
Magnetic field polarity	0.5%	0.5%	0.5%	0.5%
MC generator vs. full sim.	1.5%	1.5%	0.3%	0.1%
$\langle \mathrm{d}N_{\mathrm{ch}}/\mathrm{d}\eta\rangle$ determination	1.5%	1.5%	–	–
Total	**4.1%**	**4.6%**	**4.0%**	**4.5%**

Table 4.3.: Contributions to the systematic uncertainties on mean p_{T} fluctuations in p–Pb collisions at $\sqrt{s_{\mathrm{NN}}}$ = 5.02 TeV. In the first two columns, the relative uncertainties on $\sqrt{C_m}/M(p_{\mathrm{T}})_m$ are shown, both for accepted multiplicities $N_{\mathrm{acc}} \geq 5$. The two η ranges correspond to $|\eta| < 0.8$ and $-0.8 < \eta < +0.2$, respectively. The last two columns contain the uncertainties on the inclusive $\sqrt{C}/M(p_{\mathrm{T}})$ without restriction of the multiplicity range. The single contributions are added in quadrature to obtain the total uncertainties.

4.8. Dependence on charge combinations

Within the default analysis, the two-particle transverse-momentum correlator is calculated for all pairs of particles measured in one event, i.e. including all possible combinations of charges. These charge combinations consist of like-sign particle pairs with the charges (++) or (−−) and of unlike-sign particle pairs with the charges (+−). Some of the dynamical effects leading to transverse-momentum correlations are expected to have the same influence on all kinds of charge combinations of the particle pairs. Jets typically contain several positively and negatively charged particles with transverse momenta above $M(p_{\mathrm{T}})$ and, hence, the corresponding particle pairs contribute to a positive value of the transverse-momentum fluctuations independent of the charge combination. Another example is radial flow, which varies from event to event. In events with strong or weak radial flow, the particles tend to have a p_{T} above or below the average value, leading in both cases to a positive fluctuation signal, again independent of the charges of the particles. However, other effects do only have an influence on either the like-sign or the unlike-sign pairs. For example, Hanbury-Brown–Twiss (HBT) correlations occur among identical particles, which thus have to have the same charge sign. On the other hand, the decays of neutral resonances contribute only to the unlike-sign pairs.

In this section, mean p_{T} fluctuations are analysed separately for the different charge combinations and the results are compared to the default analysis including all combi-
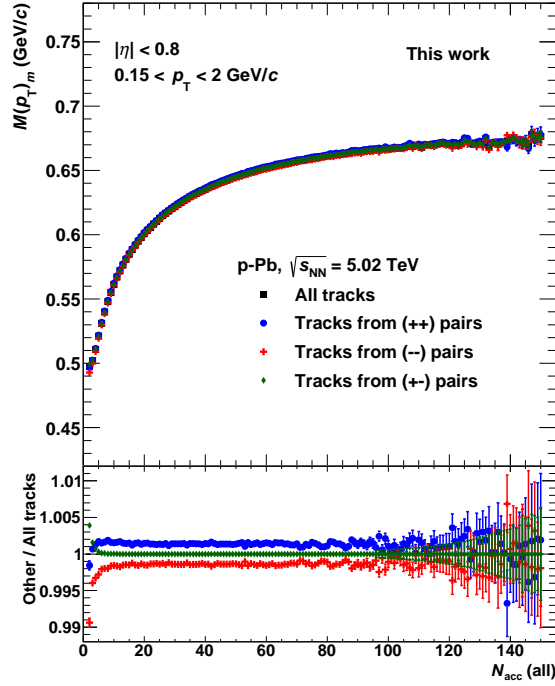
Figure 4.23.: Comparison of $M(p_{\mathrm{T}})_m$ of particles from different charge combinations to that from all charged particles as a function of the accepted multiplicity of all particles $N_{\mathrm{acc}}(\text{all})$ in p–Pb collisions at $\sqrt{s_{\mathrm{NN}}}$ = 5.02 TeV. The bottom panel shows the ratios of the results using specific charge combinations to those of all particles.

nations. At first, the mean transverse momentum of positively and negatively charged particles is compared to that of all particles. At LHC energies, approximately the same numbers of positive and negative particles are produced and their p_{T} spectra do not exhibit any significant differences [168]. Therefore, it is expected that the mean transverse momenta are comparable.

In figure 4.23, $M(p_{\mathrm{T}})_m$ is shown as a function of the accepted multiplicity of all particles $N_{\mathrm{acc}}(\text{all})$ in p–Pb collisions at $\sqrt{s_{\mathrm{NN}}}$ = 5.02 TeV. As supposed, the results for the single charges are in good agreement with the inclusive results. However, in the ratio a tiny difference is observed. Positive particles exhibit a slightly higher $M(p_{\mathrm{T}})_m$ than negative particles, but these deviations from the inclusive particle $M(p_{\mathrm{T}})_m$ are only of the order of 0.1–0.2% and, hence, are considered not problematic for the analysis. At the lowest multiplicities, the differences are slightly enhanced and both $M(p_{\mathrm{T}})_m$ of positive and of negative particles decrease with respect to the inclusive measurement. This effect can be explained taking into account that the positive and negative particles comprise only those from the corresponding like-sign pairs. A single positive particle contained in an event with otherwise only negative particles would thus be removed from the sample of positive particles shown here. Therefore, in addition to the positive, negative and inclusive particles, the $M(p_{\mathrm{T}})_m$ is presented for
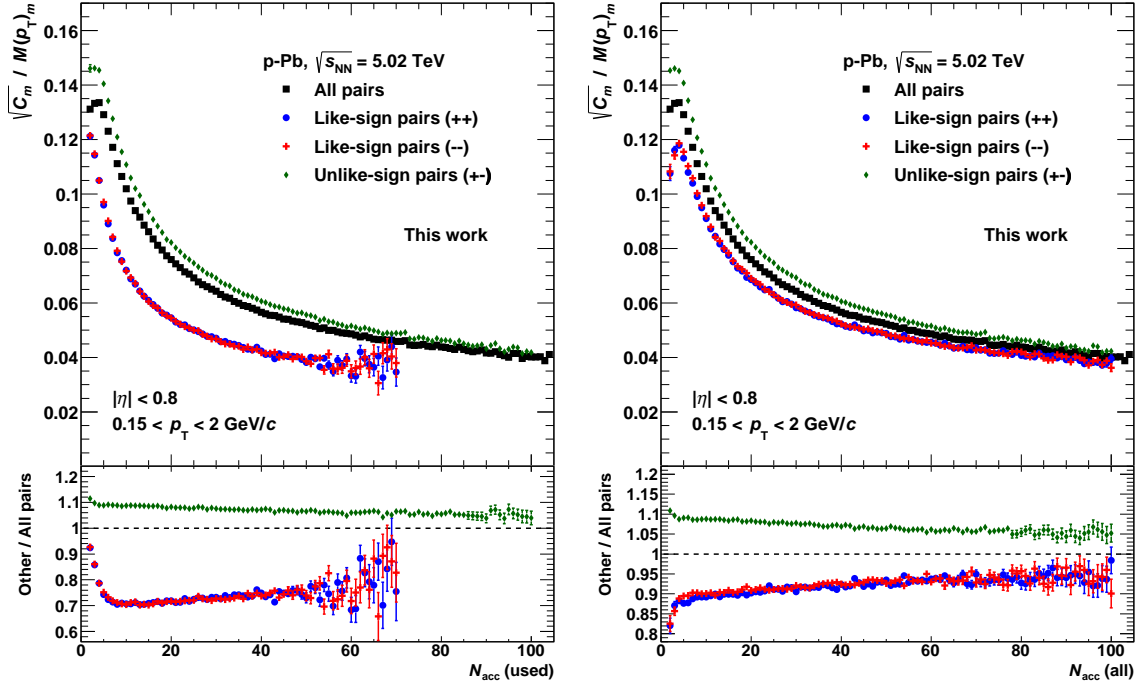
Figure 4.24.: Comparison of $\sqrt{C_m}/M(p_{\mathrm{T}})_m$ using only like-sign (++) or (−−) or only unlike-sign (+−) pairs to the inclusive results using all charge combinations in p–Pb collisions at $\sqrt{s_{\mathrm{NN}}} = 5.02\,\mathrm{TeV}$. Left: Results as a function of the accepted multiplicity of the particles used in the calculation of $\sqrt{C_m}/M(p_{\mathrm{T}})_m$, $N_{\mathrm{acc}}(\mathrm{used})$. Right: Results as a function of the accepted multiplicity of all particles $N_{\mathrm{acc}}(\mathrm{all})$. The bottom panels show the ratios of the results using specific charge combinations to those including all combinations.

those particles originating from unlike-sign pairs. The mean transverse momentum of these particles exhibits a trend opposite to the negative and positive particles at the lowest multiplicities and it is in exact agreement with that from inclusive particles for $N_{\mathrm{acc}}(\mathrm{all}) \gtrsim 5$.

The results of $\sqrt{C_m}/M(p_{\mathrm{T}})_m$ in p–Pb collisions at $\sqrt{s_{\mathrm{NN}}} = 5.02\,\mathrm{TeV}$ for the different charge combinations are presented in figure 4.24 as a function of accepted multiplicities. In the left panel, the multiplicity is determined from the accepted particles, which are used within the pairs of the specific charge combination, and, therefore, it is called $N_{\mathrm{acc}}(\mathrm{used})$. In this representation, the results of the like-sign charge combinations are below the inclusive results by about 30% for the largest part of the multiplicity range. The differences decrease slightly towards high multiplicities and strongly towards the lowest $N_{\mathrm{acc}}(\mathrm{used})$, where they reach values below 10%. The results of (++) and (−−) pairs are in agreement. Unlike-sign pairs exhibit $\sqrt{C_m}/M(p_{\mathrm{T}})_m$ values about 10% higher than the inclusive results at low multiplicities with a moderate decrease of the deviations for increasing multiplicities.
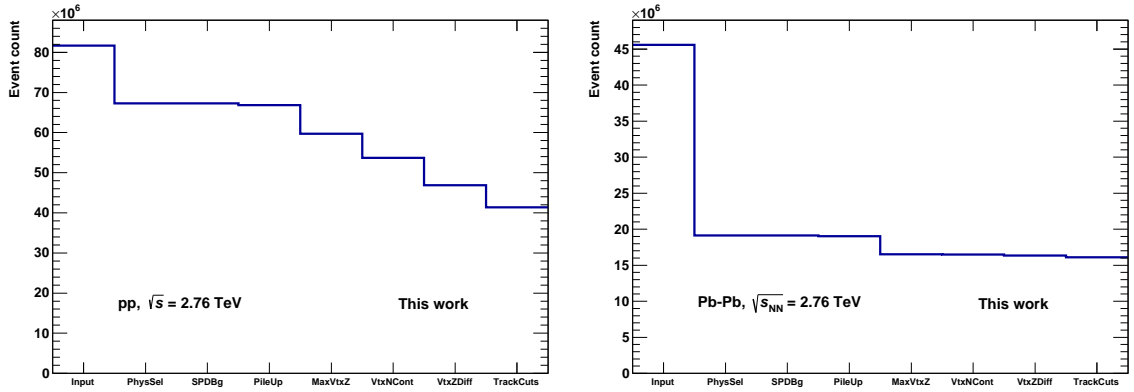
Figure 4.25.: Number of events in pp collisions (left) and Pb–Pb collisions (right) at $\sqrt{s_{NN}}$ = 2.76 TeV. From left to right: Number of events read in from the ESD files, after performing the physics selection, the SPD cluster-versus-tracklets background rejection (switched off here), the SPD pile-up rejection and the cuts on the maximum z_{vtx} distance from the nominal interaction point, the number of contributors to the vertex and the difference of the TPC and SPD z_{vtx} positions and, finally, after application of the track selection criteria including the kinematic acceptance of $|\eta| < 0.8$ and $0.15\,\text{GeV}/c < p_T < 2\,\text{GeV}/c$.

Another representation is shown in the right panel of figure 4.24. Here, the results of the different charge combinations are always presented as a function of the accepted multiplicity of all charged particles $N_{acc}(\text{all})$. As expected, the behaviour of the results of unlike-sign pairs does not change, because each event containing accepted particles of both charges has the same $N_{acc}(\text{used})$ considering only unlike-sign pairs or those of all charge combinations. However, the differences of the like-sign results to the inclusive ones are significantly reduced to about 10% at low multiplicities, although this trend is reversed towards the lowest $N_{acc}(\text{all})$, where the deviations are increasing instead of decreasing. For rising multiplicities, an almost linear weakening of the differences is found, reaching about 5% at the highest $N_{acc}(\text{all})$. The results for (++) and (−−) pairs are again in agreement. It is concluded that a large fraction of the differences observed in the left panel of figure 4.24 is related to the definition of the multiplicity. However, removing this dependence on $N_{acc}(\text{used})$ by comparing all results at the same multiplicities $N_{acc}(\text{all})$ does not remove the differences completely. The implications of these results are further discussed in the results chapter in section 5.2.

4.9. Re-analysis of pp and Pb–Pb collisions

The main intention of the new analysis of p–Pb collisions is the comparison to the other collision systems to investigate, whether the common trend of mean p_T fluctu-
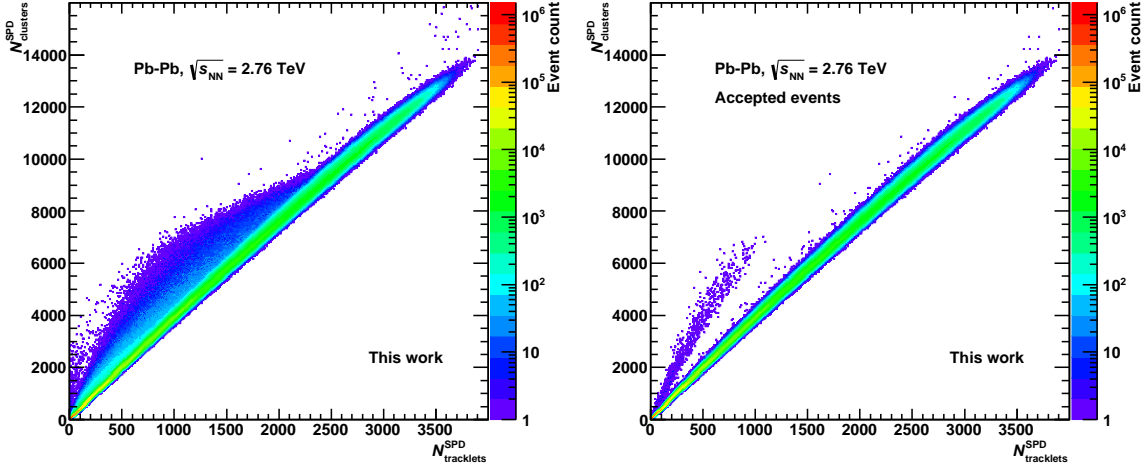
Figure 4.26.: Number of events as a function of the number of SPD clusters $N_{\text{clusters}}^{\text{SPD}}$ and the number of SPD tracklets $N_{\text{tracklets}}^{\text{SPD}}$ per event in Pb–Pb collisions at $\sqrt{s_{\text{NN}}}$ = 2.76 TeV. Left: With physics selection applied, but no other selection criteria. Right: Accepted events after performing all event and track selection criteria.

ations measured in the symmetric pp and Pb–Pb collisions is also oberserved in the asymmetric p–Pb collisions. As discussed in section 4.4, in addition to the standard analysis covering the full pseudorapidity acceptance of $|\eta| < 0.8$, the p–Pb analysis is also carried out in the restricted acceptance of $-0.8 < \eta < +0.2$ corresponding to a width of $\Delta\eta = 1.0$. As the size of the η interval has a significant influence on the final results, the analyses in pp and Pb–Pb collisions have to be repeated using a corresponding η window symmetric around the centre-of-mass system, i.e. $|\eta| < 0.5$.

At first, the analysis of pp and Pb–Pb collisions is repeated within the kinematic acceptance of the published results, i.e. $|\eta| < 0.8$ and $0.15\,\text{GeV}/c < p_{\text{T}} < 2\,\text{GeV}/c$. However, the new analysis code developed for the study of p–Pb collisions is used as well as the corresponding event and track selection criteria, which are similar to those of the published analysis, but differ in some details (see sections 4.2 and 4.3). In the case of pp collisions, the more recent reconstruction pass4 is used, whereas in Pb–Pb collisions no new reconstruction is available. This first step is performed to check the consistency with the published results.

The number of events at the different stages of the analysis is presented in figure 4.25 in pp collisions (left panel) and Pb–Pb collisions (right panel), both at $\sqrt{s_{\text{NN}}}$ = 2.76 TeV. The most prominent difference to p–Pb collisions (figure 4.2) is the physics selection in Pb–Pb collisions, which reduces the number of events by more than 50%.

In addition, the SPD cluster-versus-tracklets background rejection is switched off in the pp and Pb–Pb analysis. In the data sets from 2010 this criterion is not necessary, however, it cuts off a significant fraction of usable physics events without pile-up. This effect is especially pronounced in mid-central Pb–Pb collisions leading to a non-flat centrality distribution, and, therefore, this criterion is omitted. The distribution of
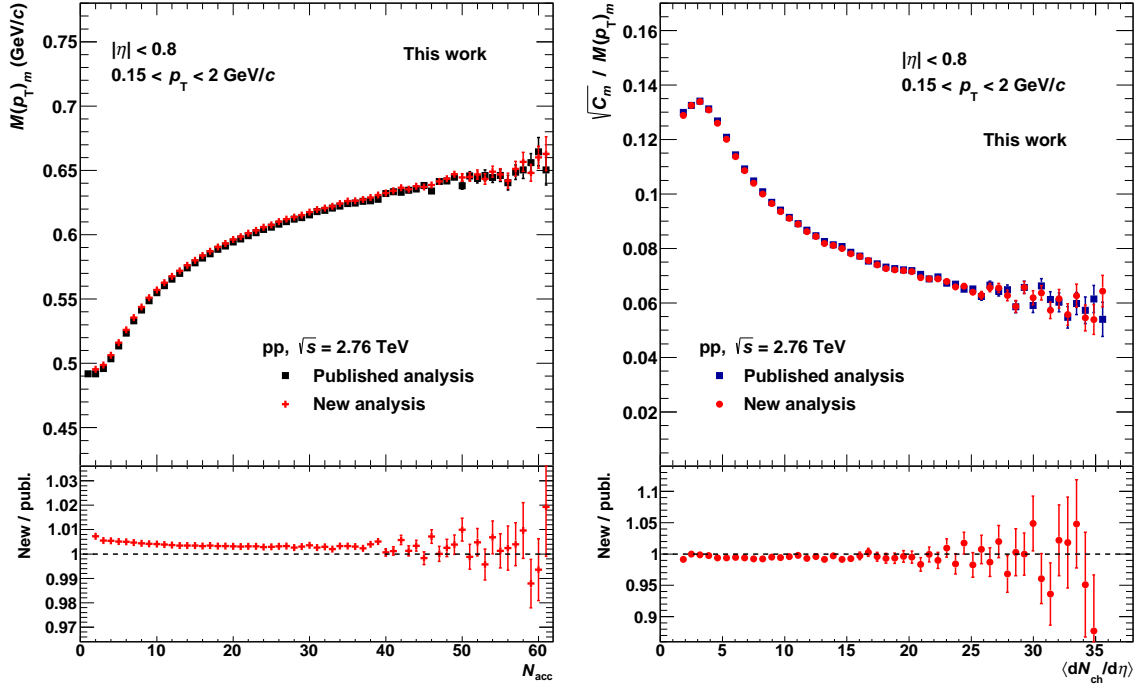
Figure 4.27.: Comparison of the new analysis to the published results from [3] in pp collisions at $\sqrt{s}$ = 2.76 TeV. Left: $M(p_{\mathrm{T}})_m$ as a function of N_{acc}. Right: $\sqrt{C_m}/M(p_{\mathrm{T}})_m$ as a function of $\langle \mathrm{d}N_{\mathrm{ch}}/\mathrm{d}\eta \rangle$. The bottom panels show the ratio of the new to the published results.

events versus SPD clusters $N_{\mathrm{clusters}}^{\mathrm{SPD}}$ and SPD tracklets $N_{\mathrm{tracklets}}^{\mathrm{SPD}}$ in Pb–Pb collisions at $\sqrt{s_{\mathrm{NN}}}$ = 2.76 TeV is shown in figure 4.26. In the left panel, only the physics selection is applied, while the distribution in the right panel contains all event and track selection criteria. The majority of events is located within a narrow diagonal band. The outliers visible above this band in the left panel are almost completely removed by the other selection criteria.

In figure 4.27, the results in pp collisions at $\sqrt{s}$ = 2.76 TeV of the new analysis are compared to the published ones [3]. The left panel shows $M(p_{\mathrm{T}})_m$ as a function of the accepted multiplicity N_{acc}, in the right panel $\sqrt{C_m}/M(p_{\mathrm{T}})_m$ is presented as a function of the average charged-particle pseudorapidity density $\langle \mathrm{d}N_{\mathrm{ch}}/\mathrm{d}\eta \rangle$. A good agreement of the two analyses is found in both observables. $M(p_{\mathrm{T}})_m$ is slightly higher in the new analysis by about 0.5% at low N_{acc}. This small deviation decreases further towards higher multiplicities. The results for $\sqrt{C_m}/M(p_{\mathrm{T}})_m$ in the new analysis are slightly below the published ones. A constant fit to the ratio yields a difference of about 0.5%, which is much smaller than the total systematic uncertainties of the published results of about 4–8%. Therefore, this weak effect is not considered as an issue for the new analysis.

The same comparison is performed in Pb–Pb collisions at $\sqrt{s_{\mathrm{NN}}}$ = 2.76 TeV and the results are presented in figure 4.28. Again, $M(p_{\mathrm{T}})_m$ as a function of N_{acc} (left panel)
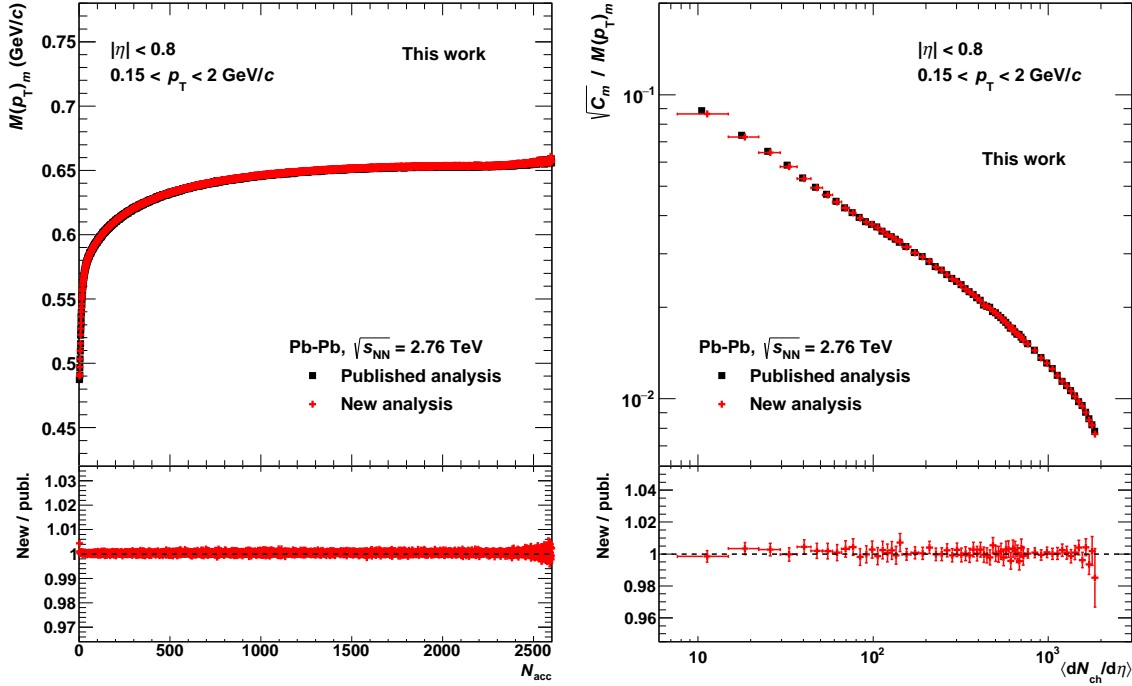
Figure 4.28.: Comparison of the new analysis to the published results from [3] in Pb–Pb collisions at $\sqrt{s_{NN}} = 2.76\,\text{TeV}$. Left: $M(p_T)_m$ as a function of N_{acc}. Right: $\sqrt{C_m}/M(p_T)_m$ as a function of $\langle \text{d}N_{\text{ch}}/\text{d}\eta \rangle$. The bottom panels show the ratio of the new to the published results.

and $\sqrt{C_m}/M(p_T)_m$ as a function of $\langle \text{d}N_{\text{ch}}/\text{d}\eta \rangle$ (right panel) are shown. In the case of Pb–Pb collisions, an excellent agreement of the new and the published results is found in both observables. No significant deviations are observed over the complete ranges of multiplicity.

After the verification of the agreement of the new analysis with the published results within an identical kinematic acceptance, the analyses in pp and Pb–Pb collisions are repeated within a restricted acceptance of $|\eta| < 0.5$ corresponding to the same width of $\Delta\eta = 1.0$ employed in p–Pb collisions. The other event and track selection criteria are not changed and the transverse-momentum range of $0.15\,\text{GeV}/c < p_T < 2\,\text{GeV}/c$ is kept. In p–Pb collisions, the systematic uncertainties are studied separately for the different pseudorapidity coverages of $\Delta\eta = 1.6$ and $\Delta\eta = 1.0$, see section 4.7. The total relative systematic uncertainties are comparable and, therefore, it is concluded not to repeat the full systematic studies in pp and Pb–Pb collisions within the restricted η range. Instead, the relative systematic uncertainties as a function of $\langle \text{d}N_{\text{ch}}/\text{d}\eta \rangle$ of the published analysis are used as an estimate of the relative uncertainties of the new analysis within $|\eta| < 0.5$. These uncertainties yield about 4–8% and the details of their evaluation can be found in section 3.7.

Finally, the results within the two different pseudorapidity intervals are compared. As expected from the study of the mean transverse momentum as a function of η described
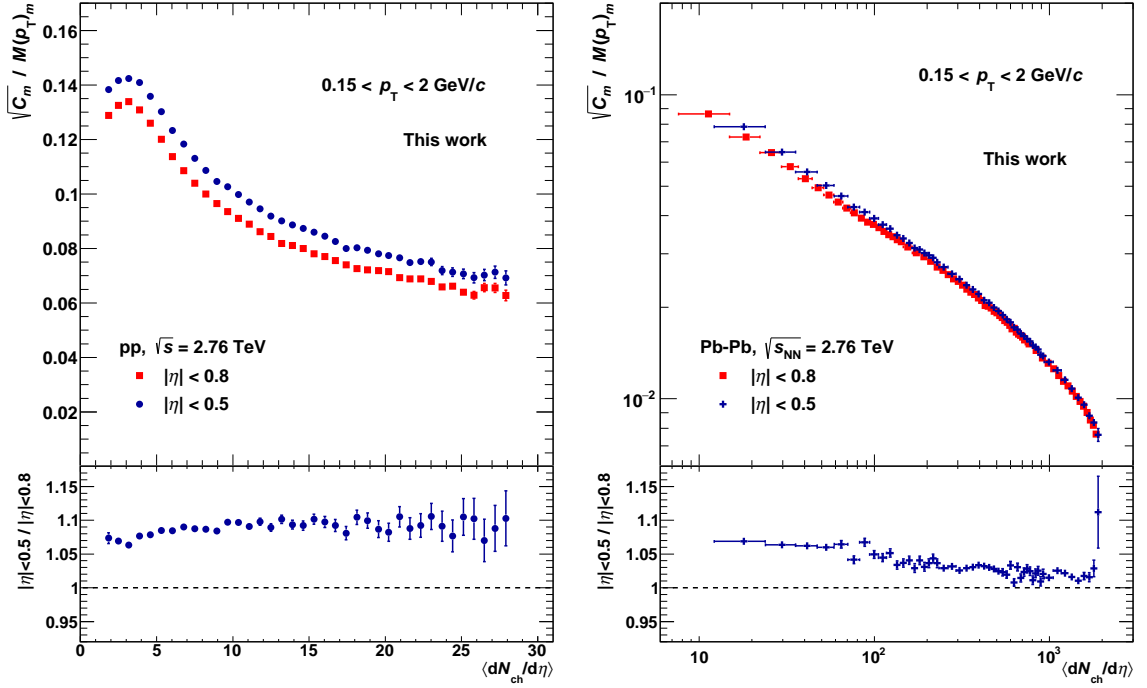
Figure 4.29.: Comparison of $\sqrt{C_m}/M(p_T)_m$ as a function of $\langle \mathrm{d}N_{\mathrm{ch}}/\mathrm{d}\eta \rangle$ within different η ranges in pp collisions (left) and in Pb–Pb collisions (right), both at $\sqrt{s_{\mathrm{NN}}} = 2.76\,\mathrm{TeV}$. The bottom panels show the ratio of the results within $|\eta| < 0.5$ to those within $|\eta| < 0.8$.

in section 3.4.3, no significant differences are found for $M(p_T)_m$ in case it is considered in the analyses of both η intervals as a function of the accepted multiplicity within the full coverage of $|\eta| < 0.8$. The results for $\sqrt{C_m}/M(p_T)_m$ as a function of $\langle \mathrm{d}N_{\mathrm{ch}}/\mathrm{d}\eta \rangle$ are presented in figure 4.29 in pp collisions (left panel) and in Pb–Pb collisions (right panel) at $\sqrt{s_{\mathrm{NN}}} = 2.76\,\mathrm{TeV}$. In both systems, the results within the narrower η window are higher than those within the full coverage, which is in agreement with the findings in p–Pb collisions, see section 4.4. However, while this difference does not show any significant dependence on the multiplicity in pp and p–Pb collisions, it is decreasing with increasing multiplicity in Pb–Pb collisions and almost reaches the values of the full acceptance for the highest multiplicities.

The final results of the pp and Pb–Pb data within $|\eta| < 0.5$ are compared to those obtained in p–Pb collisions within $-0.8 < \eta < +0.2$ in the results chapter in section 5.2. In order to check any possible detector effects, e.g. of a different acceptance or efficiency as a function of η, the analysis in Pb–Pb collisions is repeated within the exact interval used in p–Pb, i.e. $-0.8 < \eta < +0.2$. No significant differences are found, supporting the reliability of the comparison of the different collision systems. A similar study is performed in pp collisions at $\sqrt{s} = 7\,\mathrm{TeV}$ within the investigation of the acceptance in an asymmetric collision system, see section 4.4 and especially figure 4.12. Also in pp collisions, no significant variations are observed as a function of η.

5. Results

Within the last two chapters, the analyses of mean transverse-momentum fluctuations in symmetric and asymmetric collision systems are described. This chapter is devoted to the presentation of the results. Throughout the chapter, the dimensionless quantity $\sqrt{C_m}/M(p_T)_m$, describing the dynamical fluctuations relative to the mean transverse momentum, is employed. If not explicitly stated otherwise, the statistical uncertainties of the measurements are depicted by error bars while the systematic uncertainties are illustrated as boxes.

In the first section, the measurements in pp and Pb–Pb collisions are shown and compared to previous experiments and to Monte Carlo (MC) simulations. In addition, PYTHIA MC studies of multi-parton interactions and colour reconnections in pp collisions are presented. Section 5.2 is dedicated to the results in p–Pb collisions including comparisons to the DPMJET MC generator and to the symmetric collision systems. Further theoretical calculations of mean transverse-momentum fluctuations at LHC energies are compared to the data in section 5.3.

5.1. Results of symmetric systems: pp and Pb–Pb

5.1.1. Results in pp collisions

Many of the results presented within this first part about the symmetric collision systems are published by the ALICE Collaboration in [3]. Prior to these ALICE measurements, results in pp collisions were only available as inclusive measurements of full event samples [94]. The first differential measurements in pp collisions are shown in figure 5.1, depicting the relative dynamical mean transverse-momentum fluctuations $\sqrt{C_m}/M(p_T)_m$ as a function of the average charged-particle multiplicity density $\langle \mathrm{d}N_{\mathrm{ch}}/\mathrm{d}\eta \rangle$. Significant dynamical fluctuations are observed over the complete multiplicity range under study. At low multiplicities, the size of the fluctuations is saturated around 12–14% and exhibits a monotonic decrease for increasing multiplicity and $\langle \mathrm{d}N_{\mathrm{ch}}/\mathrm{d}\eta \rangle \gtrsim 5$, reaching about 5% at the highest multiplicities. The results are compared at $\sqrt{s} = 0.9$, 2.76 and 7 TeV showing no significant dependence on the collision energy.

In addition to the multiplicity-dependent measurements, inclusive results are obtained in pp collisions at all three collision energies. The inclusive dynamical fluctuation $\sqrt{C}/M(p_T)$ is presented in figure 5.2 as a function of the collision energy. It is compared to the measurements of the Split Field Magnet (SFM) detector at the Intersection Storage Rings (ISR) at much lower collision energies of $\sqrt{s} = 30.8$, 45, 52,
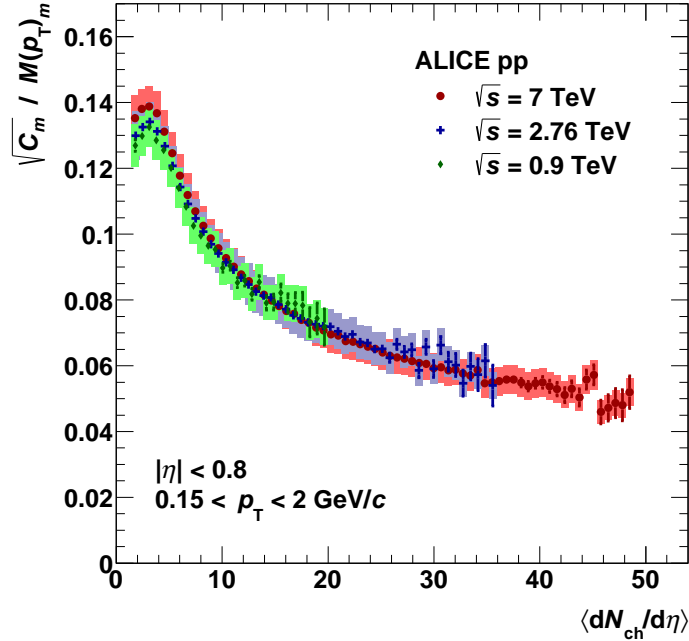
5. Results

Figure 5.1.: $\sqrt{C_m}/M(p_T)_m$ as a function of $\langle \mathrm{d}N_{\mathrm{ch}}/\mathrm{d}\eta \rangle$ in pp collisions at $\sqrt{s}$ = 0.9, 2.76 and 7 TeV [3].

and 63 GeV [94]. At ISR, the measure R is employed for the analysis of relative dynamical mean p_T fluctuations, which is discussed in section 1.5.4. The comparability of $\sqrt{C}/M(p_T)$ and R has been checked using a PYTHIA8 MC simulation, showing an agreement of the two quantities within 10–15%. The inclusive relative dynamical mean p_T fluctuations do not exhibit any significant dependence on the collision energy in the range from ISR to LHC energies.

The results for $\sqrt{C_m}/M(p_T)_m$ as a function of $\langle \mathrm{d}N_{\mathrm{ch}}/\mathrm{d}\eta \rangle$ in pp collisions at $\sqrt{s}$ = 7 TeV are compared to several MC event generators, see also section 3.1.2. This comparison is shown in figure 5.3 (left panel) together with the ratio of the MC generators to the ALICE data (right panel). The general decreasing trend of the fluctuations with increasing multiplicity is described by all of the models. The PYTHIA tunes are in qualitative agreement with a saturation at low multiplicities and a monotonic decrease with no further structures above. PHOJET, however, exhibits additional changes of the slope not observed in data and is quantitatively furthest away from the data above $\langle \mathrm{d}N_{\mathrm{ch}}/\mathrm{d}\eta \rangle \approx 5$. In this range, all PYTHIA6 tunes show quantitative agreement with the data within the uncertainties while PYTHIA8 (tune 4C) is about 10–15% too high. On the other hand, PYTHIA8 yields the best description in the low-multiplicity part. For $\langle \mathrm{d}N_{\mathrm{ch}}/\mathrm{d}\eta \rangle \gtrsim 5$, the results can be described well by power-law fits of $\sqrt{C_m}/M(p_T)_m \propto \langle \mathrm{d}N_{\mathrm{ch}}/\mathrm{d}\eta \rangle^b$ both for the data and all studied MC generators except PHOJET. A fit to pp data at $\sqrt{s}$ = 7 TeV in the interval $5 < \langle \mathrm{d}N_{\mathrm{ch}}/\mathrm{d}\eta \rangle < 30$ yields $b = -0.431 \pm 0.001$ (stat.) ± 0.021 (syst.). Such a decreasing trend is expected in heavy-ion collisions within a simple scenario of the superposition of independent particle-emitting
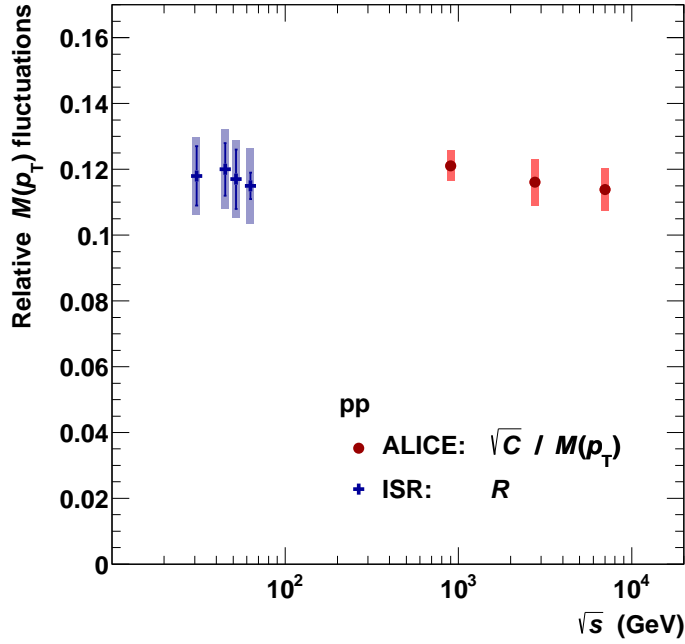
Figure 5.2.: Relative dynamical mean p_T fluctuations in pp collisions as a function of the collision energy [3]. The ALICE results for $\sqrt{C}/M(p_T)$ are compared to the quantity R measured at the ISR [94].
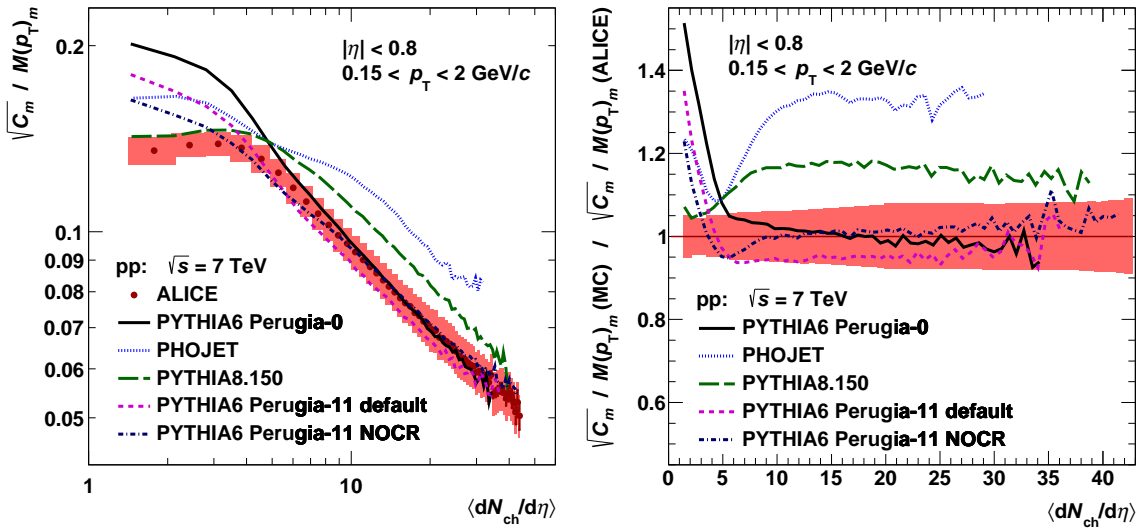

Figure 5.3.: Left: $\sqrt{C_m}/M(p_T)_m$ as a function of $\langle \mathrm{d}N_{\mathrm{ch}}/\mathrm{d}\eta \rangle$ for ALICE data and different MC event generators in pp collisions at $\sqrt{s} = 7\,\mathrm{TeV}$ [3]. Right: Ratio of the MC generators to the ALICE data [3]. The red error band indicates the statistical and systematic data uncertainties added in quadrature.
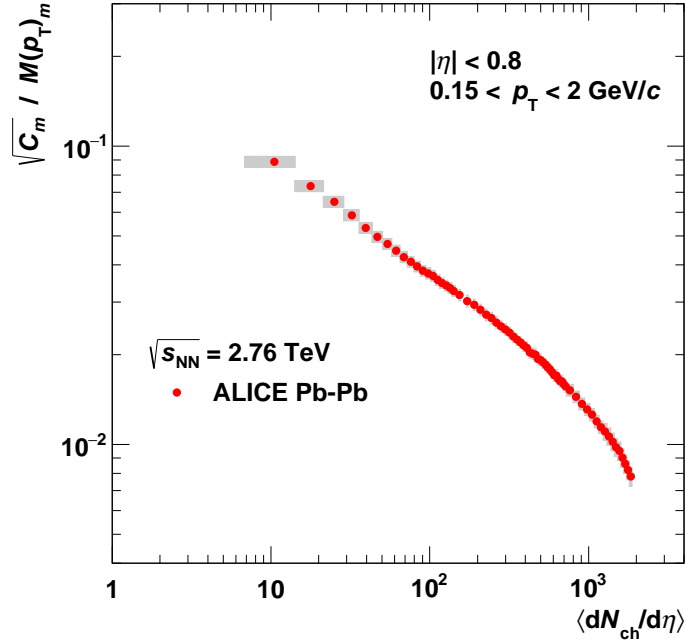
Figure 5.4.: $\sqrt{C_m}/M(p_T)_m$ as a function of $\langle dN_{ch}/d\eta \rangle$ in Pb–Pb collisions at $\sqrt{s_{NN}} = 2.76\,\text{TeV}$. The data points are taken from [3].

sources, albeit with a different power-law index of $b = -0.5$ [69, 88]. The implications of these findings are discussed in detail in section 5.1.3. In summary, pp collisions can be considered as collisions of partonic states, allowing for multiple parton–parton interactions.

5.1.2. Results in Pb–Pb collisions

Dynamical mean p_T fluctuations are also observed in Pb–Pb collisions at $\sqrt{s_{NN}} = 2.76\,\text{TeV}$. In figure 5.4, the results for $\sqrt{C_m}/M(p_T)_m$ are presented as a function of $\langle dN_{ch}/d\eta \rangle$. As in pp collisions, a decreasing trend with increasing multiplicity is found. The size of the relative fluctuations is ranging from about 10% at the lowest multiplicities corresponding to peripheral collisions to less than 1% for the most central events at $\langle dN_{ch}/d\eta \rangle$ of almost 2000. While the evolution from peripheral to mid-central events follows a power-law shape, the fluctuations exhibit a significant additional decrease towards central collisions.

In figure 5.5, the measurement in Pb–Pb collisions is compared to that in pp collisions and to a HIJING simulation at the same collision energy of $\sqrt{s_{NN}} = 2.76\,\text{TeV}$. The HIJING results are very well described by a power-law fit with the exception of low multiplicities. Employing a fit range of $30 < \langle dN_{ch}/d\eta \rangle < 1500$, the exponent yields $b = -0.499 \pm 0.003\,\text{(stat.)} \pm 0.005\,\text{(syst.)}$, which is in accordance with the simple superposition expectation of $b = -0.5$ introduced above. HIJING simulates heavy-ion collisions via the independent superposition of nucleon–nucleon collisions obtained
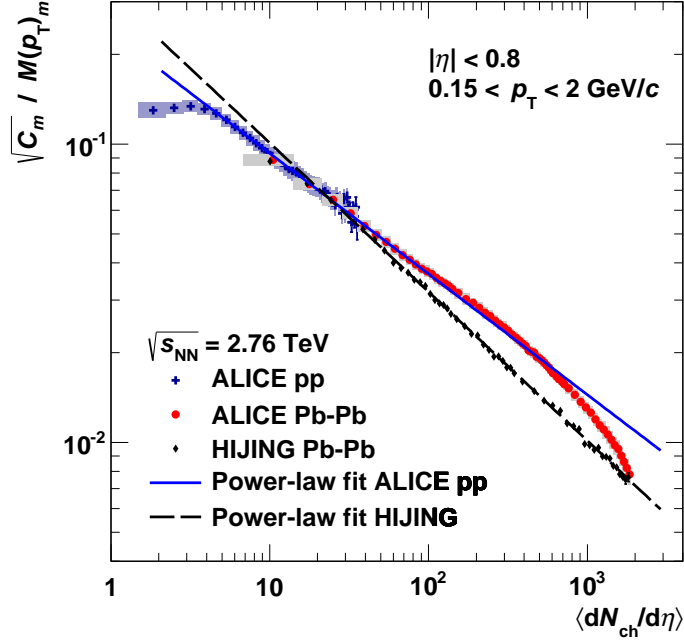
Figure 5.5.: $\sqrt{C_m}/M(p_T)_m$ as a function of $\langle dN_{ch}/d\eta\rangle$ in pp and Pb–Pb collisions at $\sqrt{s_{NN}}$ = 2.76 TeV [3]. In addition, results from a HIJING simulation as well as power-law fits to pp data (solid line) and HIJING (dashed line) are shown.

from PYTHIA calculations, which is supporting this expectation. This multiplicity dependence is significantly different from that observed in data.

A power-law fit to the pp results at $\sqrt{s}$ = 2.76 TeV in the interval $5 < \langle dN_{ch}/d\eta\rangle < 25$ is also shown in figure 5.5 including an extrapolation to higher multiplicities. The fit results in an exponent of $b = -0.405 \pm 0.002\,(\text{stat.}) \pm 0.036\,(\text{syst.})$. Within the uncertainties, this result is in agreement with that obtained in pp collisions at $\sqrt{s}$ = 7 TeV and differs clearly from HIJING. However, the peripheral Pb–Pb data are in very good agreement with the pp data in the overlapping region and up to $\langle dN_{ch}/d\eta\rangle \approx 100$ with the extrapolation of the pp data. This is a remarkable observation, especially when taking the significant differences in the mean transverse momentum into account, which are found between pp and Pb–Pb results, see the right panel of figure 1.7 in the first chapter and [76]. In the intermediate multiplicity part of about $100 < \langle dN_{ch}/d\eta\rangle < 500$, a slight enhancement over the pp extrapolation is observed, which is followed by a pronounced decrease of the fluctuations clearly below the pp fit line. This strong reduction of the fluctuations corresponds to centralities < 40%.

In the 0–5% most central Pb–Pb collisions, the ALICE measurement of the relative dynamical fluctuations yields $\sqrt{C_m}/M(p_T)_m = (0.925 \pm 0.002\,(\text{stat.}) \pm 0.068\,(\text{syst.}))\%$. This value is compared to results in central heavy-ion collisions at lower collision energies obtained by CERES at the SPS [93] and by STAR at RHIC [92]. Together with ALICE, these experiments span a range of collision energies of more than two
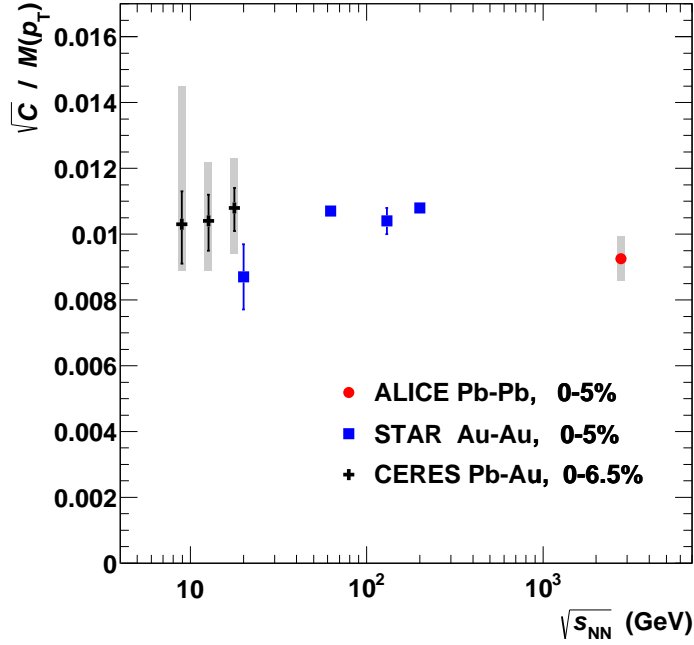
Figure 5.6.: Relative dynamical mean p_{T} fluctuations in central heavy-ion collisions as a function of the collision energy [3]. The ALICE data point is compared to results from the STAR [92] and CERES [93] experiments. The uncertainties of the STAR results are statistical only.

orders of magnitude. As shown in figure 5.6, no significant dependence of dynamical mean p_{T} fluctuations over this large range of $\sqrt{s_{\text{NN}}}$ is observed in central heavy-ion collisions.

The STAR Collaboration has also published differential results for $\sqrt{C_m}/M(p_{\text{T}})_m$ in Au–Au collisions in [92]. In the top left panel of figure 5.7, the STAR measurements at $\sqrt{s_{\text{NN}}} = 200\,\text{GeV}$ are compared to the ALICE data as a function of $\langle \text{d}N_{\text{ch}}/\text{d}\eta \rangle$. The monotonically decreasing trend with multiplicity is similar for both data sets, but the value of the relative mean p_{T} fluctuations at a given multiplicity is significantly lower in STAR. The power-law extrapolation from ALICE pp data is also shown and a similar fit is performed on the peripheral part of the STAR data, fixing the exponent to $b = -0.405$ as obtained from ALICE pp and fitting the STAR data points for $\langle \text{d}N_{\text{ch}}/\text{d}\eta \rangle < 200$. The slope of the ALICE pp data describes the trend of the peripheral STAR Au–Au data very well, which is illustrated in the lower panel showing the ratios of the ALICE and STAR heavy-ion data to the corresponding fits. In contrast to ALICE, no significant enhancement is found in semi-central Au–Au collisions in STAR, but the decrease of the fluctuations below the fits in central collisions is observed in STAR as well, although it is not as pronounced as in ALICE.

The average charged-particle multiplicity density $\langle \text{d}N_{\text{ch}}/\text{d}\eta \rangle$ may not be the best scale to compare the two experiments with collision energies differing by more than one order of magnitude, as the overall multiplicity reach at the LHC energy is about a factor of
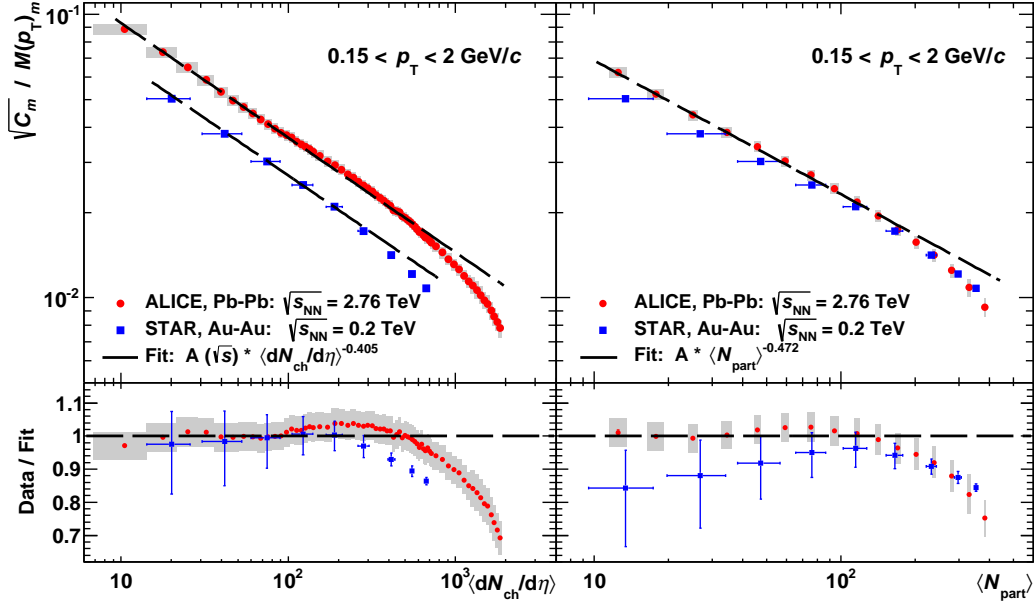
Figure 5.7.: Left: $\sqrt{C_m}/M(p_T)_m$ as a function of $\langle \mathrm{d}N_{\mathrm{ch}}/\mathrm{d}\eta \rangle$ in Pb–Pb collisions at $\sqrt{s_{\mathrm{NN}}} = 2.76$ TeV from ALICE compared to results from STAR in Au–Au collisions at $\sqrt{s_{\mathrm{NN}}} = 200$ GeV [3]. The STAR measurements are taken from [92]. The dashed lines depict power-law fits (see text for details). Right: $\sqrt{C_m}/M(p_T)_m$ as a function of $\langle N_{\mathrm{part}} \rangle$ for the same data [3].

two higher. Instead, the same results of $\sqrt{C_m}/M(p_T)_m$ can also be shown as a function of the mean number of participating nucleons $\langle N_{\mathrm{part}} \rangle$, which is presented in the top right panel of figure 5.7. $\langle N_{\mathrm{part}} \rangle$ is closely related to the geometry of the collisions and in this geometrical picture, the fluctuation results of ALICE and STAR agree within the rather large uncertainties on $\langle N_{\mathrm{part}} \rangle$ in STAR. The peripheral part of the ALICE data ($10 < \langle N_{\mathrm{part}} \rangle < 40$) is fitted with a power law $\sqrt{C_m}/M(p_T)_m \propto \langle N_{\mathrm{part}} \rangle^b$. The result $b = -0.472 \pm 0.007\,(\mathrm{stat.}) \pm 0.037\,(\mathrm{syst.})$ is in agreement with an exponent of $b = -0.5$. Ratios of ALICE and STAR data to this fit are presented in the lower panel, illustrating that the decrease below the fit occurs at the same centrality.

So far, the scenario of an independent superposition of particle-emitting sources has been discussed and from the comparison with HIJING in figure 5.5 it is clear, that this scenario is not able to describe the multiplicity trend of the mean p_T fluctuations observed in data. The decrease with increasing multiplicity is weaker in the data, indicating correlations between the emitted particles, which enhance the fluctuations. In heavy-ion collisions, collective effects like flow have to be taken into account, which may have an influence on mean p_T and thus on the mean p_T fluctuations. The effect of event-averaged radial flow and azimuthal asymmetries is expected to be small [93, 101]. However, initial-state fluctuations leading to event-by-event flow fluctuations may change the mean p_T fluctuations significantly. The AMPT model incorporates
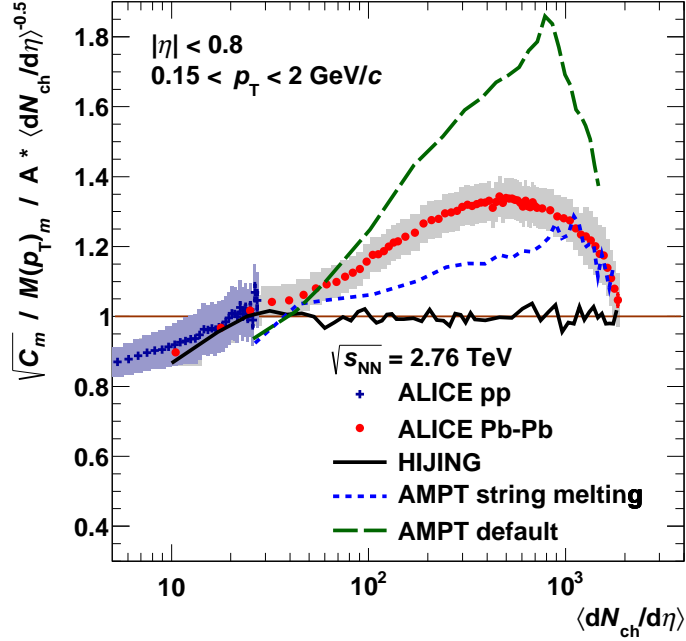
5. Results

Figure 5.8.: $\sqrt{C_m}/M(p_T)_m$ normalised to $\langle dN_{ch}/d\eta \rangle^{-0.5}$ as a function of $\langle dN_{ch}/d\eta \rangle$ in pp and Pb–Pb collisions at $\sqrt{s_{NN}}$ = 2.76 TeV [3]. The ALICE results are compared to the MC event generators HIJING and AMPT, the latter in the default version and with the string-melting mechanism enabled.

such collective effects and it gives a reasonable description of event-averaged properties like the flow coefficients v_n in Pb–Pb collisions at the LHC [169].

The ALICE data on mean p_T fluctuations in pp and Pb–Pb collisions are compared to two versions of AMPT and to HIJING in figure 5.8. In addition to a default AMPT calculation, another version including string melting is employed. In AMPT, the string-melting mechanism recombines particles after the rescattering stage using a hadronic coalescence scheme. In figure 5.8, $\sqrt{C_m}/M(p_T)_m$ is normalised to a fit $\propto \langle dN_{ch}/d\eta \rangle^{-0.5}$ to the HIJING results using the fit range $30 < \langle dN_{ch}/d\eta \rangle < 1500$. For multiplicities below the fit interval, HIJING agrees well with the ALICE data, but fails to describe the data for $\langle dN_{ch}/d\eta \rangle \gtrsim 30$. Both AMPT simulations show qualitatively a better agreement with the data than HIJING. They exhibit an increase over the simple superposition expectation illustrated by HIJING and a steep decrease towards the highest multiplicities corresponding to the most central collisions. However, none of the models is able to describe the data quantitatively. The default AMPT calculation overshoots the data significantly, while the fluctuations in the version including string melting are not large enough.

5.1.3. Multiplicity dependence in pp: Monte Carlo studies

In Pb–Pb collisions, the decrease of the mean p_T fluctuations with increasing multiplicity can be understood as a consequence of the superposition of many nucleon–nucleon interactions. This is also reflected in the representation of the fluctuations as a function of $\langle N_{\mathrm{part}} \rangle$, shown in the right panel of figure 5.7, which exhibits a power-law behaviour with an exponent being in agreement with $b = -0.5$. However, each pp collision constitutes only one single nucleon–nucleon collision and, hence, the number of participating nucleons is always two. Nevertheless, the behaviour of the fluctuations as a function of the multiplicity density $\langle \mathrm{d}N_{\mathrm{ch}}/\mathrm{d}\eta \rangle$ is the same in pp collisions as in peripheral to mid-central Pb–Pb collisions. Although the decrease with $\langle \mathrm{d}N_{\mathrm{ch}}/\mathrm{d}\eta \rangle$ is weaker than the simple superposition expectation, the general fact of a falling trend suggests a superposition of particle-emitting sources, which may be correlated to some extent, also in pp collisions.

These effects have been studied within the scope of a Bachelor's Thesis [5] under the assistance of the author of the present work. For this purpose, simulations of pp collisions using the MC event generator PYTHIA8 [159] have been performed. In PYTHIA, a collision of two protons is treated as a collision of two parton configurations. The most probable case for the initial state of such a collision in PYTHIA is the occurence of a single hard process corresponding to a parton–parton collision with significant momentum transfer. However, it is also possible that multiple parton–parton interactions (or "multi-parton interactions", MPIs) take place within one pp collision [170]. Hereby, the number of participating partons per proton is not restricted to the number of valence quarks, because the sea quarks and gluons are also able to contribute to these processes.

In the first place, the multiple parton–parton interactions constitute separate, uncorrelated sources of particle production. However, via a mechanism called "colour reconnections", partons originating from different parton–parton collisions can be (re-)combined [170–172]. Within this approach, it is assumed that the colour strings produced by the different parton–parton interactions overlap, which can lead to a rearrangement of the colour charges going along with a favoured reduction of the string lengths. This results in a lower number of partons, hadronising to a correspondingly lower number of final-state hadrons, which in turn have on average a higher momentum. This effect is necessary for PYTHIA simulations to be able to describe the observed increase of the mean transverse momentum as a function of N_{ch} [76].

In [5], the effects of multi-parton interactions and colour reconnections on mean p_T fluctuations are investigated using PYTHIA8 in the version 8.175 corresponding to the tune 4Cx [173, 174]. Two simulations on the generator level are performed, each containing $100\,\mathrm{M}$ pp collisions at $\sqrt{s} = 7\,\mathrm{TeV}$. In the first simulation, the default options of tune 4Cx are used, which include the mechanism of colour reconnections. This simulation is therefore called "WITHCR" in the following. The second simulation differs from the first one only by switching off the colour reconnections, keeping all other parameters identical. It is referred to as "NOCR". The number of parton–parton interactions N_{MPI} per event does not depend on the type of the simulation (WITHCR
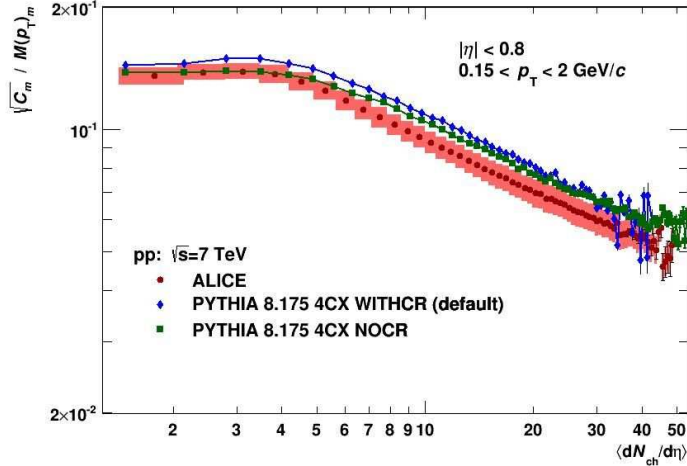
5. Results

Figure 5.9.: $\sqrt{C_m}/M(p_\mathrm{T})_m$ as a function of $\langle \mathrm{d}N_\mathrm{ch}/\mathrm{d}\eta \rangle$ from the PYTHIA8 MC generator (tune 4Cx) with (WITHCR) and without (NOCR) colour reconnections in pp collisions at $\sqrt{s}$ = 7 TeV and comparison to the ALICE data from [3]. Figure from [5].

or NOCR). In these PYTHIA8 calculations, about 35% of the events contain exactly one parton–parton interaction. The distribution of events as a function of N_MPI is falling, reaching up to $N_\mathrm{MPI} \approx 30$.

The results of the two simulations for $\sqrt{C_m}/M(p_\mathrm{T})_m$ as a function of $\langle \mathrm{d}N_\mathrm{ch}/\mathrm{d}\eta \rangle$ are presented in figure 5.9 and compared to the ALICE data in pp collisions at $\sqrt{s}$ = 7 TeV from [3]. Like the other PYTHIA tunes shown in figure 5.3, both curves agree qualitatively with the behaviour observed in data. Quantitatively, they lie slightly above the data, with the NOCR version exhibiting a somewhat better agreement with the data, although the differences between the two simulations are small. This comparison demonstrates that the colour reconnections, despite their large influence on $\langle p_\mathrm{T} \rangle$ versus N_ch, do not have a significant influence on the mean p_T fluctuations. The same observation holds in the case of PYTHIA6 Perugia-11, where tunes with and without colour reconnections are in agreement as well, see figure 5.3.

In the MC simulations, it is possible to investigate the mean p_T fluctuations for specific numbers of parton–parton interactions, i.e. considering only events with a single parton–parton interaction, with exactly two such interactions, with N_MPI = 3 and so on. This study is performed within both simulations and the corresponding results for $\sqrt{C_m}/M(p_\mathrm{T})_m$ as a function of $\langle \mathrm{d}N_\mathrm{ch}/\mathrm{d}\eta \rangle$ are shown in figure 5.10. In the left panel, the version without colour reconnections (NOCR) is shown. In this case, the parton–parton interactions represent completely independent sources of particle production. Taking into account only a specific number of parton–parton interactions, the results for $\sqrt{C_m}/M(p_\mathrm{T})_m$ are constant as a function of multiplicity instead of the decreasing trend observed considering the full event ensembles. The size of the fluctuations decreases with increasing N_MPI, but not with $\langle \mathrm{d}N_\mathrm{ch}/\mathrm{d}\eta \rangle$. Small deviations of this behaviour are observed for N_MPI = 1 with a moderate increase at the lowest
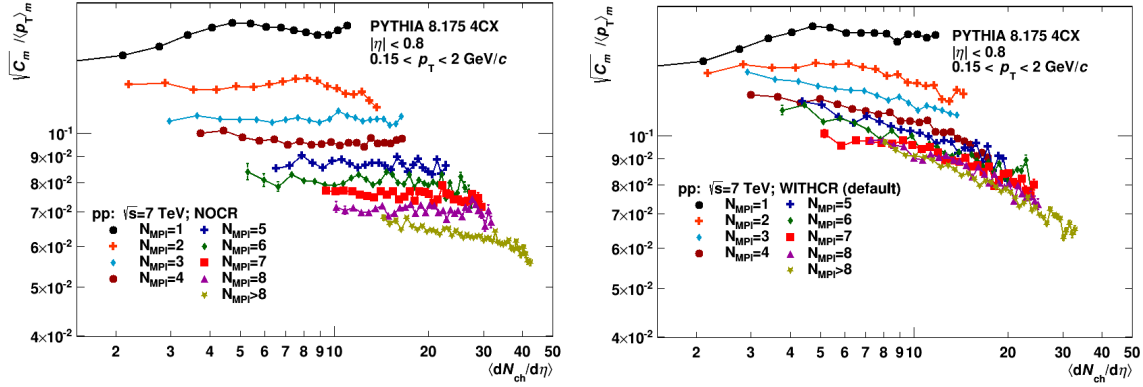
Figure 5.10.: $\sqrt{C_m}/M(p_T)_m$ as a function of $\langle dN_{ch}/d\eta \rangle$ from the PYTHIA8 MC generator (tune 4Cx) in pp collisions at $\sqrt{s}$ = 7 TeV for separate numbers of parton–parton interactions N_{MPI}. Left: Without colour reconnections (NOCR). Right: With colour reconnections enabled (WITHCR). Figures from [5].

multiplicities, and for $N_{MPI} > 8$, where a decrease with $\langle dN_{ch}/d\eta \rangle$ ist found. In the latter case, this can be explained by the fact, that this class of events, due to statistical reasons, combines various N_{MPI} from 8 up to 30.

The right panel of figure 5.10 shows the results obtained with the default tune including the colour reconnections (WITHCR). The combination of partons from different initial colour strings leads to correlations among the parton–parton interactions, which cannot be considered independent sources of particle production anymore. As expected, the case with N_{MPI} = 1 resembles that of the NOCR simulation, because here, only one colour string is present. For N_{MPI} = 2, $\sqrt{C_m}/M(p_T)_m$ decreases slightly with $\langle dN_{ch}/d\eta \rangle$ and for higher N_{MPI} this trend gets stronger. Having a closer look at the quantitative results, the values of the two simulations agree rather at high than at low multiplicities. Thus, the reconnection of the sources via their colour charges leads to correlations among them, enhancing the fluctuations at low multiplicities, but with a decreasing trend as a function of multiplicity. The ordering of absolut values of the separate curves is preserved, but it is weaker than in the NOCR case. These effects cancel to a large extent in the full event samples, leading to the approximate agreement of the WITHCR and NOCR simulations shown in figure 5.9.

In conclusion, these observations suggest that the most relevant scale for mean p_T fluctuations in pp collisions is the number of initial-state sources. Within this picture, the sources of particle production are multiple parton–parton interactions, which may be recombined via the colour reconnection mechanism. These findings can explain the qualitative similarity of the results in pp collisions when compared to Pb–Pb collisions, where the number of sources can be trivially explained by the number of nucleon–nucleon interactions.
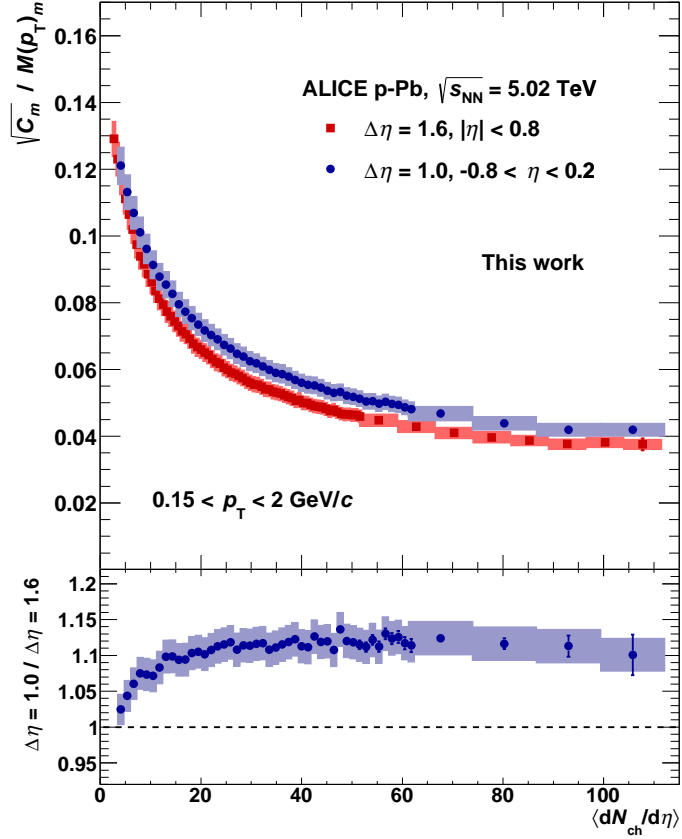
Figure 5.11.: $\sqrt{C_m}/M(p_\mathrm{T})_m$ as a function of $\langle \mathrm{d}N_\mathrm{ch}/\mathrm{d}\eta \rangle$ within the two pseudorapidity ranges $|\eta| < 0.8$ and $-0.8 < \eta < +0.2$ in p–Pb collisions at $\sqrt{s_\mathrm{NN}} = 5.02\,\mathrm{TeV}$. The bottom panel shows the ratio of the narrower ($-0.8 < \eta < +0.2$) to the wider ($|\eta| < 0.8$) range.

5.2. Results in p–Pb collisions

In this section, the results of the new analysis of the asymmetric p–Pb collision system are presented and compared to those of the symmetric pp and Pb–Pb collisions. At first, $\sqrt{C_m}/M(p_\mathrm{T})_m$ is shown as a function of $\langle \mathrm{d}N_\mathrm{ch}/\mathrm{d}\eta \rangle$ in p–Pb collisions at $\sqrt{s_\mathrm{NN}} = 5.02\,\mathrm{TeV}$ in figure 5.11. As in the other systems, significant non-statistical mean transverse-momentum fluctuations are observed in p–Pb collisions, exhibiting a decreasing trend with increasing multiplicity.

In order to enable a quantitative comparison among all collision systems, the influence of the acceptance in an asymmetric system has to be taken into account, which is discussed in more detail in section 4.4. Therefore, the results in p–Pb collisions are determined both within the full pseudorapidity acceptance of $|\eta| < 0.8$ corresponding to an interval width of $\Delta\eta = 1.6$ as well as within a restricted range of $-0.8 < \eta < +0.2$ corresponding to a width of $\Delta\eta = 1.0$. In figure 5.11, the results within both η windows are presented. Considering the narrower interval of $\Delta\eta = 1.0$ yields higher mean p_T

Figure 5.12.: Relative dynamical mean p_{T} fluctuations in small collision systems as a function of the collision energy. The ALICE results for $\sqrt{C}/M(p_{\mathrm{T}})$ are compared to the quantity R measured at the ISR [94]. The ALICE data points in pp collisions are obtained within $|\eta| < 0.8$ and taken from [3], the p–Pb results are shown for both ranges $|\eta| < 0.8$ and $-0.8 < \eta < +0.2$.

fluctuations of about 10% for most part of the multiplicity range. This difference is decreasing towards the lowest multiplicities. Please note, that the systematic uncertainties of the two samples are to a large extent correlated, see section 4.7. Hence, in the ratio shown in the lower panel of figure 5.11, the systematic uncertainties are reduced. As an estimate of the remaining uncorrelated uncertainties, the quadratic difference of the uncertainties is used, yielding $\Delta \mathrm{syst} = \sqrt{(4.6\%)^2 - (4.1\%)^2} \approx 2.1\%$.

Like in pp collisions, the inclusive relative mean p_{T} fluctuation $\sqrt{C}/M(p_{\mathrm{T}})$ of the full event ensemble is calculated as well in p–Pb collisions, again for both η ranges under study. The results are presented together with those obtained in pp collisions as a function of the collision energy $\sqrt{s_{\mathrm{NN}}}$ in figure 5.12. In p–Pb collisions at $\sqrt{s_{\mathrm{NN}}}$ = 5.02 TeV, $\sqrt{C}/M(p_{\mathrm{T}})$ = 0.0704 ± 0.0001 (stat.) ± 0.0028 (syst.) and $\sqrt{C}/M(p_{\mathrm{T}})$ = 0.0745±0.0001 (stat.) ± 0.0033 (syst.) within $|\eta| < 0.8$ and $-0.8 < \eta < +0.2$, respectively. These results are in agreement within their uncertainties, but taking into consideration that the systematic uncertainties are largely correlated, the trend of higher fluctuations within the narrower η interval observed in the multiplicity-dependent study is also found in the case of the inclusive results. Compared to the results in pp collisions of $\sqrt{C}/M(p_{\mathrm{T}}) \approx 0.11$–0.12, the values in p–Pb collisions are about 40% lower.

5. Results

The ALICE results for $\sqrt{C}/M(p_T)$ in figure 5.12 are compared to those of the observable R measured at the ISR [94], for details see the corresponding discussion of figure 5.2 in section 5.1.1. In addition to pp collisions, these results include measurements in p–α and α–α collisions. Within the uncertainties, the ALICE results in p–Pb collisions at $\sqrt{s_{NN}}$ = 5.02 TeV agree with the ISR results in p–α collisions at a collision energy about two orders of magnitude lower and despite the difference in the colliding nucleus. Hence, the influence on inclusive relative mean p_T fluctuations of the shift from a hadron–hadron collision to a hadron–nucleus collision is already described when using a small α nucleus consisting of only four nucleons. Exchanging the α with a large Pb nucleus composed of 208 nucleons does not significantly alter the result. In addition, the results from ISR in α–α collisions are in agreement with the p–α measurement.

In [94] it is assumed, that the relevant scale for the inclusive relative mean p_T fluctuations is the number of nucleon–nucleon collisions N_{coll}. This is tested by constructing "double events" from two independent pp collisions and calculating R for this sample. The result is in agreement with those in α–α collisions corresponding on average to $\langle N_{coll} \rangle \approx 1.8$ [175]. Within this picture, it is expected that the result in p–α collisions should fall in between those in pp and α–α collisions, which cannot be excluded within the uncertainties. However, in p–Pb collisions at $\sqrt{s_{NN}}$ = 5.02 TeV, ALICE has measured $\langle N_{coll} \rangle$ = 6.87 ± 0.55 (syst.) [167] and, hence, a significantly lower value of the fluctuations would be expected. Given the agreement of the ALICE and ISR results in pp collisions, a significant energy dependence is not expected also for the other systems. Therefore, the number of nucleon–nucleon collisions can be excluded as the only relevant scale of inclusive mean p_T fluctuations.

The ALICE results for $\sqrt{C_m}/M(p_T)_m$ as a function of $\langle dN_{ch}/d\eta \rangle$ in p–Pb collisions at $\sqrt{s_{NN}}$ = 5.02 TeV are compared to those obtained by the DPMJET MC generator in figure 5.13. Both in data and in MC, the full pseudorapidity acceptance of $|\eta| < 0.8$ is employed. The results of DPMJET are shown on the generator level, as it is also performed in the MC comparisons to data in the symmetric collision systems. DPMJET is able to describe the general trend of non-statistical fluctuations, which are monotonically decreasing with increasing multiplicity. Quantitatively, the DPMJET results are too high by about 10% at the lowest multiplicities. With increasing $\langle dN_{ch}/d\eta \rangle$, this difference rises up to 20% at $\langle dN_{ch}/d\eta \rangle \approx 10$–15, where the slope of the MC results changes to a steeper one. This effect, which is not observed in data, leads to a decrease of the deviations and an approximate agreement with the data at the highest multiplicities.

In figure 5.14, the comparison of the results in all three collision systems is presented. The upper panels show the results within the full pseudorapidity acceptance of $|\eta| < 0.8$ corresponding to an interval width of $\Delta\eta$ = 1.6, the lower panels contain the results within the restricted width of $\Delta\eta$ = 1.0. This corresponds to an η window of $-0.8 < \eta <$ +0.2 in p–Pb collisions and to $|\eta| < 0.5$ in pp and Pb–Pb collisions. In the left panels, $\sqrt{C_m}/M(p_T)_m$ is shown as a function of $\langle dN_{ch}/d\eta \rangle$. In both cases, a power-law fit is performed on the pp data and the fit result is drawn as a line including an extrapolation
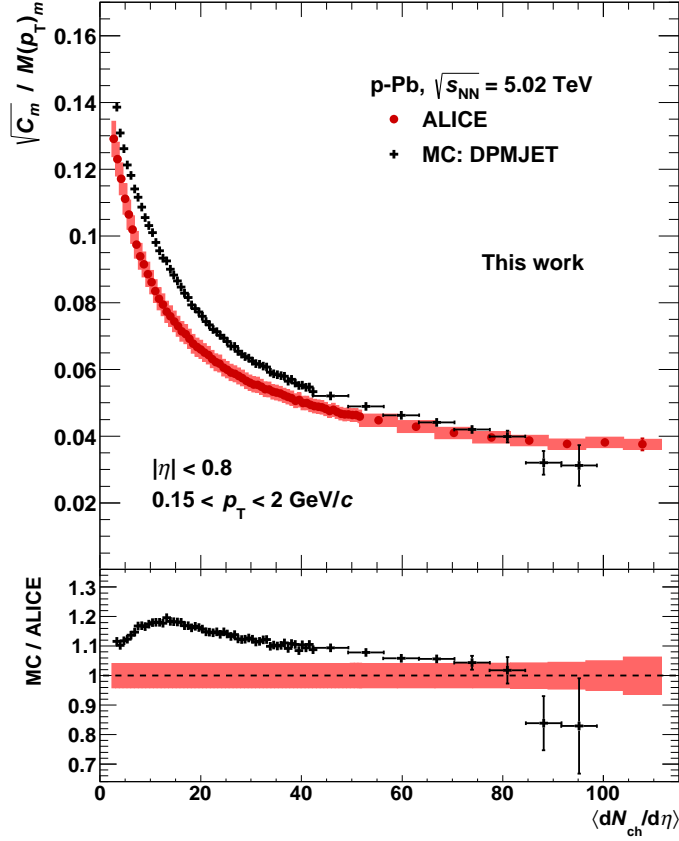
Figure 5.13.: Comparison of the ALICE data on $\sqrt{C_m}/M(p_T)_m$ as a function of $\langle dN_{ch}/d\eta \rangle$ with the DPMJET MC event generator in p–Pb collisions at $\sqrt{s_{NN}} = 5.02$ TeV. The bottom panel shows the ratio of DPMJET to the ALICE data. The red error band indicates the statistical and systematic data uncertainties added in quadrature.

to higher multiplicities. The right panels present the ratios of $\sqrt{C_m}/M(p_T)_m$ in the three collision systems to the pp power-law fits obtained in the left panels.

Qualitatively, the p–Pb data exhibit a very similar behaviour to that found in pp and Pb–Pb collisions. $\sqrt{C_m}/M(p_T)_m$ is decreasing as a function of $\langle dN_{ch}/d\eta \rangle$ following a power-law trend with a similar slope. Quantitatively, however, the p–Pb results fall below those in the other systems. Taking into account that the systematic uncertainties of the various data sets are at least to some extent correlated, these differences have to be regarded as being significant. Considering the full acceptance (upper panels in figure 5.14), the difference to the pp fit amounts to 8–10% at low multiplicities with $\langle dN_{ch}/d\eta \rangle \lesssim 10$. The decrease of the fluctuations with multiplicity is slightly weaker in p–Pb compared to pp collisions and, hence, the deviations get smaller reaching about 5–6% at $\langle dN_{ch}/d\eta \rangle \approx 50$. For even higher multiplicities, the slope of the p–Pb results weakens further and the pp fit is reached at $\langle dN_{ch}/d\eta \rangle \approx 100$. This behaviour resembles that of Pb–Pb collisions at slightly higher multiplicities, where an increase above

5. Results
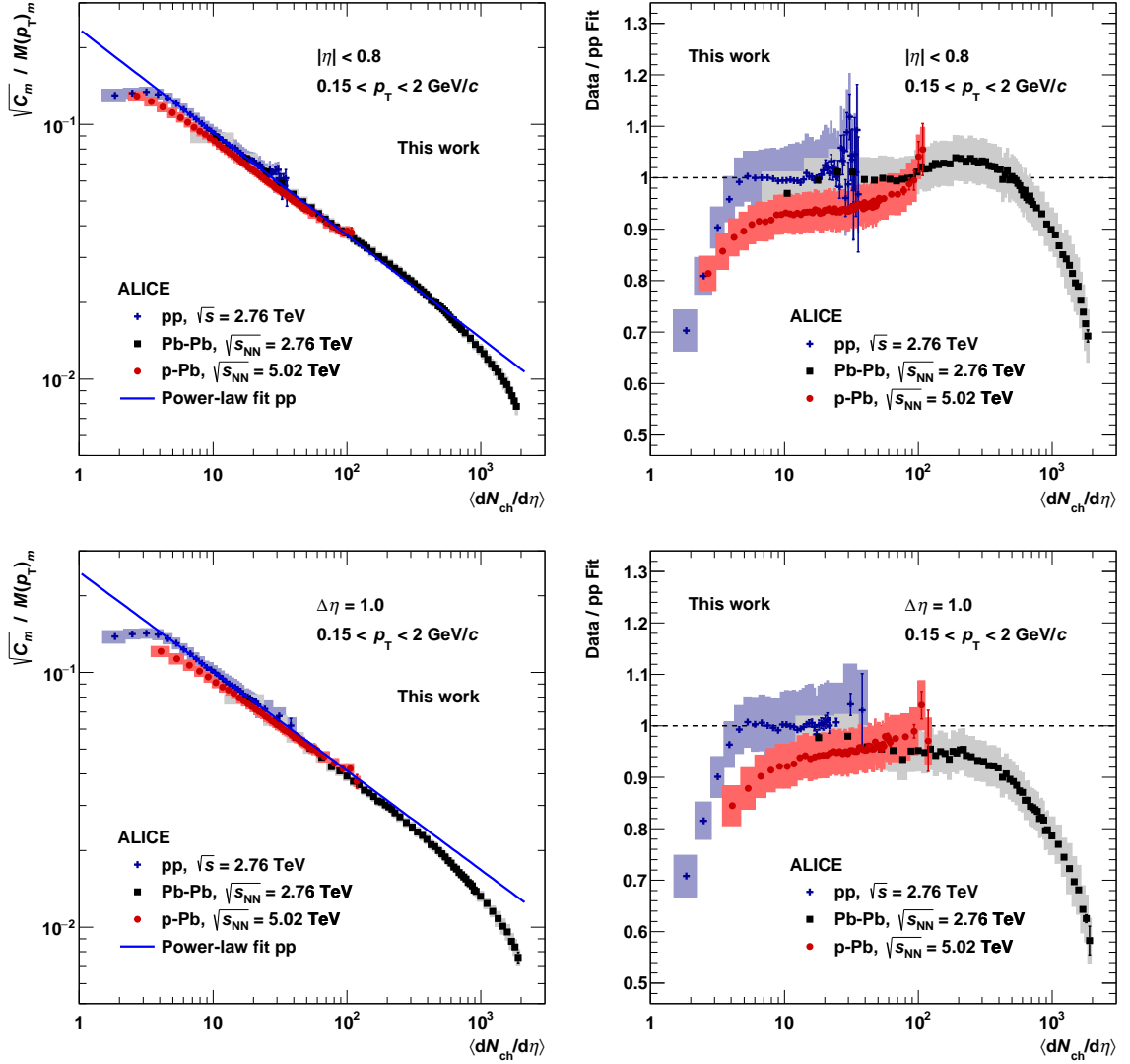
Figure 5.14.: Comparison of the results in pp, p–Pb and Pb–Pb collisions. Left panels: $\sqrt{C_m}/M(p_T)_m$ as a function of $\langle dN_{ch}/d\eta \rangle$ including a power-law fit to the pp data. Right panels: Ratio of the data in all collision systems to the pp fits from the left panels. In the upper panels, the results within the full pseudorapidity acceptance of $|\eta| < 0.8$ are shown. In the lower panels, restricted ranges of the width $\Delta\eta = 1.0$ are employed.

the pp extrapolation is observed. However, while this multiplicity range corresponds to peripheral to mid-central collisions in Pb–Pb, it constitutes the high-multiplicity tail in p–Pb collisions.

It is possible, that this increase found in p–Pb collisions is only an edge effect due to the selection of events with especially high multiplicity within the acceptance of $|\eta| < 0.8$, without any further significant change of the physics involved and hence of the fluctuation signal. This hypothesis is tested using the DPMJET MC simulation.
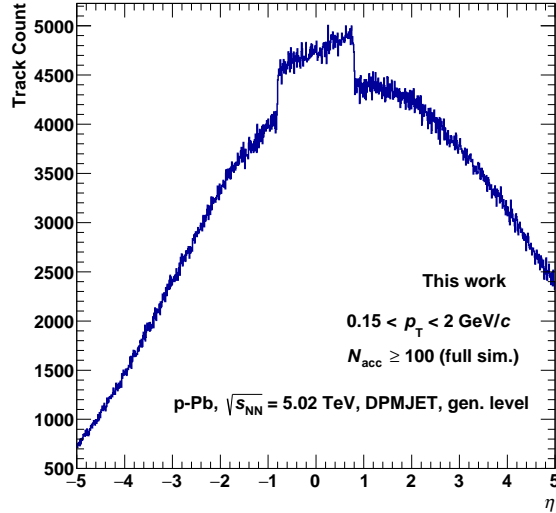
Figure 5.15.: Distribution of generated particles as a function of η in p–Pb collisions at $\sqrt{s_{\mathrm{NN}}}$ = 5.02 TeV from the DPMJET MC event generator for events with an accepted multiplicity of $N_{\mathrm{acc}} \geq 100$ within $|\eta| < 0.8$ in the corresponding full simulation.

The analysis is performed simultaneously on the generator level and employing the full simulation including the detector response. Only events with at least 100 accepted tracks in the full simulation within $|\eta| < 0.8$ are selected. For these events, the true η distribution from the generator level is obtained, which is presented in figure 5.15. The typical double-peak structure observed in high-multiplicity p–Pb collisions with a more pronounced peak on the Pb-going side [176] is not observed anymore. It is covered by the prominent increase of particles within $|\eta| < 0.8$, which is mainly due to the corresponding event selection. Therefore, it is concluded that the additional increase of the high-multiplicity p–Pb results with respect to the pp fit may be explained by a selection bias and does not necessarily have to correspond to the physics observed in peripheral to mid-central Pb–Pb collisions.

Restricting the acceptance to $\Delta\eta$ = 1.0, as shown in the lower panels of figure 5.14, reduces the deviations of the p–Pb results from the pp fit only slightly. The overall picture in the comparison of the two small systems persists, although in detail some differences are found. In contrast to the results within $|\eta| < 0.8$, the p–Pb data do not exhibit any significant changes of the slope for $\langle \mathrm{d}N_{\mathrm{ch}}/\mathrm{d}\eta \rangle \gtrsim 10$. In particular, no weakening of the slope in high-multiplicity events corresponding to an additional increase with respect to the pp baseline is observed. However, the behaviour of the Pb–Pb results compared to the other two systems is modified. The power-law slope of the Pb–Pb data as a function of $\langle \mathrm{d}N_{\mathrm{ch}}/\mathrm{d}\eta \rangle$ is slightly steeper and the agreement with the pp fit is only preserved at the lowest multiplicities. For $\langle \mathrm{d}N_{\mathrm{ch}}/\mathrm{d}\eta \rangle \gtrsim 40$, the Pb–Pb data points fall clearly below the pp fit and no enhancement above the fit is observed for mid-central events. The pronounced decrease of the fluctuations towards central

5. Results

System	Sample	$\sqrt{s_{\mathrm{NN}}}$	Scale	Exponent b
pp	Data	2.76 TeV	$\langle \mathrm{d}N_{\mathrm{ch}}/\mathrm{d}\eta \rangle$	-0.405 ± 0.002 (stat.) ± 0.036 (syst.)
pp	Data	7.0 TeV	$\langle \mathrm{d}N_{\mathrm{ch}}/\mathrm{d}\eta \rangle$	-0.431 ± 0.001 (stat.) ± 0.021 (syst.)
p–Pb	Data	5.02 TeV	$\langle \mathrm{d}N_{\mathrm{ch}}/\mathrm{d}\eta \rangle$	-0.393 ± 0.001 (stat.) ± 0.013 (syst.)
Pb–Pb	HIJING	2.76 TeV	$\langle \mathrm{d}N_{\mathrm{ch}}/\mathrm{d}\eta \rangle$	-0.499 ± 0.003 (stat.) ± 0.005 (syst.)
Pb–Pb	Data	2.76 TeV	$\langle N_{\mathrm{part}} \rangle$	-0.472 ± 0.007 (stat.) ± 0.037 (syst.)

Table 5.1.: Results for the exponent b of power-law fits to $\sqrt{C_m}/M(p_{\mathrm{T}})_m$ as a function of the scale $\langle \mathrm{d}N_{\mathrm{ch}}/\mathrm{d}\eta \rangle$ or $\langle N_{\mathrm{part}} \rangle$ in multiple collision systems and energies. In all cases, the full pseudorapidity range of $|\eta| < 0.8$ is used.

collisions is more pronounced, reaching a ratio to the pp fit of about 0.6 for the most central collisions, compared to about 0.7 within the full η acceptance. The differences between pp and p–Pb on the one hand and pp and Pb–Pb on the other hand have a similar size. Thus, the results in p–Pb and Pb–Pb collisions are quantitatively in agreement, at least around $\langle \mathrm{d}N_{\mathrm{ch}}/\mathrm{d}\eta \rangle = 40$–50. Due to the different slopes some small deviations are found at lower and higher multiplicities. The implications of these findings are not conclusive, yet. One possiblity is an issue within the determination of $\langle \mathrm{d}N_{\mathrm{ch}}/\mathrm{d}\eta \rangle$ in pp collisions using the results within $|\eta| < 0.5$. In this case, the overall picture could change to a better agreement of all data sets within the restricted acceptance. However, the different slopes of the p–Pb and Pb–Pb results also suggest further effects relevant for the comparison.

Despite the differences observed in the details of the comparison of the three collision systems, the overall trend of the results in the asymmetric p–Pb collisions is in accord with those in the symmetric pp and Pb–Pb collisions. The decrease of the mean p_{T} fluctuations with $\langle \mathrm{d}N_{\mathrm{ch}}/\mathrm{d}\eta \rangle$ follows a power-law behaviour and is also quantitatively comparable, as the observed deviations yield only a few percent. The level of agreement of the multiplicity dependence is further studied by a comparison of the exponents b of the power-law fits. The results for b considering the full acceptance $|\eta| < 0.8$ are summarised in table 5.1. In the case of the fit exponents, the systematic uncertainties are to a larger extent uncorrelated than the uncertainties of the data points themselves. They are obtained by variations of the fit range and by moving the data points to the upper and lower bound of their systematic uncertainties and re-performing the fits. The second step is not applicable in p–Pb collisions, as the corresponding systematic uncertainties are independent of the multiplicity. However, in p–Pb collisions several methods to determine $\langle \mathrm{d}N_{\mathrm{ch}}/\mathrm{d}\eta \rangle$ are employed, see section 4.6. The power-law fits are performed for each of these methods and the resulting changes in b are used as an additional systematic uncertainty.

Within their uncertainties, the results for b of the two pp data sets at $\sqrt{s} = 2.76$ and 7 TeV are in agreement as well as the pp result at $\sqrt{s} = 2.76$ TeV and the p–Pb value at $\sqrt{s_{\mathrm{NN}}} = 5.02$ TeV. However, the pp result at $\sqrt{s} = 7$ TeV is higher than at $\sqrt{s} = 2.76$, while the p–Pb value is lower. The corresponding difference of the results in pp at $\sqrt{s} = 7$ TeV and in p–Pb is not covered by the uncertainties. In summary,
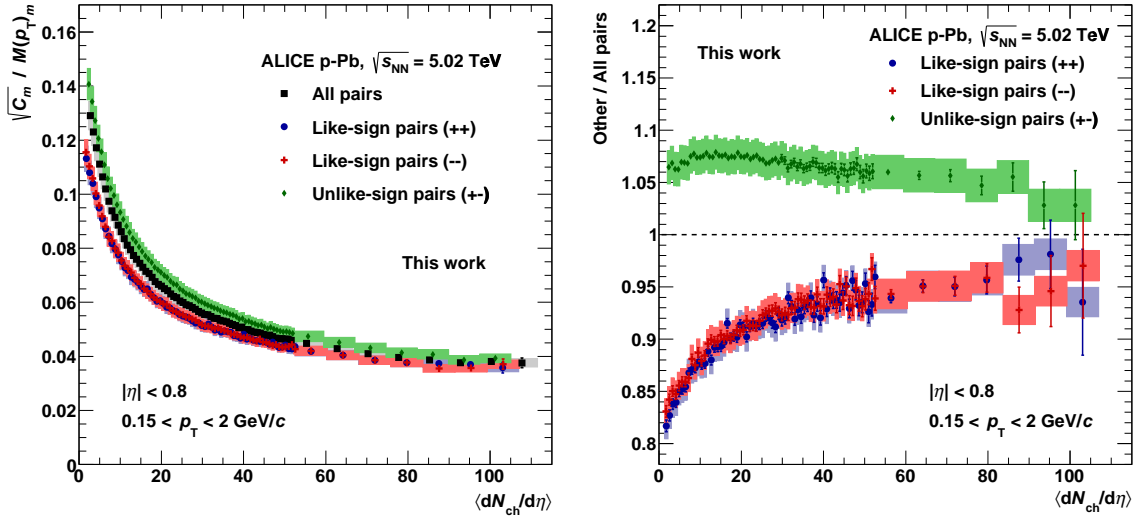
Figure 5.16.: Comparison of $\sqrt{C_m}/M(p_T)_m$ using only like-sign (++) or (−−) or only unlike-sign (+−) pairs to the inclusive results using all charge combinations in p–Pb collisions at $\sqrt{s_{NN}}$ = 5.02 TeV. Left: Results as a function of $\langle dN_{ch}/d\eta \rangle$. Right: Ratios of the results using specific charge combinations to those including all combinations. It is assumed that most of the systematic uncertainties are correlated and cancel in the ratios, with the exception of the uncertainty on the $\langle dN_{ch}/d\eta \rangle$ determination.

there is a tendency observed that the decrease of the fluctuations as a function of multiplicity is weaker in p–Pb as compared to pp collisions. In all of these cases, though, the exponents are clearly different from the simple superposition expectation $b = -0.5$ discussed in section 5.1. In contrast, the fit to the HIJING event generator in Pb–Pb collisions at $\sqrt{s_{NN}}$ = 2.76 TeV does almost perfectly reflect this $1/\sqrt{\langle dN_{ch}/d\eta \rangle}$ behaviour. Changing the scale from $\langle dN_{ch}/d\eta \rangle$ to $\langle N_{part} \rangle$, also the peripheral Pb–Pb data agree with $b = -0.5$ within the uncertainties.

Finally, the results for the different charge combinations in p–Pb collisions at $\sqrt{s_{NN}}$ = 5.02 TeV are presented in figure 5.16. For this study, the full acceptance of $|\eta| < 0.8$ is employed. In the left panel, $\sqrt{C_m}/M(p_T)_m$ is shown as a function of $\langle dN_{ch}/d\eta \rangle$, separately for like-sign pairs (++) and (−−) as well as for unlike-sign pairs (+−). These results are compared to the default ones considering all charge combinations. The corresponding ratios of the results of separate to all charge combinations are shown in the right panel of figure 5.16. It is assumed that the systematic uncertainties are correlated except of those related to the determination of $\langle dN_{ch}/d\eta \rangle$, which yield 1.5%. Therefore, the systematic uncertainties cancel to a large extent in the ratios.

The results using only unlike-sign pairs are above those including all pairs by 6–7% at the lowest multiplicities, followed by a small increase to a maximum deviation of 8% at $\langle dN_{ch}/d\eta \rangle = 10$–15 and an almost linear decrease to about 5% at the highest multiplicities. The results of the like-sign pairs exhibit lower values than those of all

pairs, with (++) and (−−) pairs being in agreement within their statistical uncertainties. At the lowest multiplicities, the deviations from the results using all combinations exceed 15%, decreasing to about 10% at $\langle \mathrm{d}N_{\mathrm{ch}}/\mathrm{d}\eta \rangle \approx 20$ and further to about 5% at $\langle \mathrm{d}N_{\mathrm{ch}}/\mathrm{d}\eta \rangle \approx 80$. For even higher multiplicities, the statistical uncertainties get large, and within these uncertainties also an agreement of the results of all different charge combinations cannot be excluded.

Despite the observed differences, the overall magnitude of mean p_{T} fluctuations for pairs of specific charge combinations is similar to those using all pairs. This demonstrates that the main effects responsible for the fluctuations have a similar influence on all particles and do not separate between like-sign and unlike-sign pairs. Examples for such effects are radial and higher-order flow and their event-by-event fluctuations as well as jets, typically containing several correlated particles of both charges. Effects unique to unlike-sign pairs, like the decays of neutral resonances, further increase the fluctuations. This can be understood, as many resonances decay into particles of similar or identical mass, and, hence, the probability is high, that both decay particles will obtain a similar fraction of the overall momentum. Particles close together in momentum space are typically either both below or above the average p_{T} and lead to a positive fluctuation signal. Those effects with an influence only on the like-sign pairs have to reduce the fluctuations with respect to the baseline of all pairs. Possible such effects are Coulumb interactions or Hanbury-Brown–Twiss (HBT) correlations. The influence of the effects specific to either like-sign or unlike-sign pairs decreases with increasing multiplicity. Thus, the dominance of the effects on all particles and combinations, like flow and jets, gets even stronger in events with many particles.

5.3. Comparison to theory

The publication [3] has triggered multiple theoretical calculations of dynamical mean transverse-momentum fluctuations at LHC energies [74, 163, 177–179]. Comparisons of the data obtained in this work to two of these models are presented in this section. Within one of these models, the Boltzmann equation is used to describe a locally thermalised system in heavy-ion collisions [163]. Within an earlier version of this model [180], the system was assumed to be fully thermalised independent of event quantities like the impact parameter. This version of the model is shown as dotted lines in the left panel of figure 5.17. A comparison of this earlier version to the ALICE data from [3][a] and to the STAR data from [92] shows good agreement in the mid-central to central part of heavy-ion collisions, but fails to describe peripheral collisions. It is interesting to note, that the agreement starts from the point onwards, where the ALICE Pb–Pb data begin to decrease significantly below the pp extrapolation, see figure 5.5.

The more recent version of the model includes dynamic fluctuations from a Langevin noise and furthermore assumes only partial thermalisation in the peripheral to mid-

---

[a] In the original publication [180], the model was compared to the preliminary ALICE data from [2], but the data did not change significantly in [3] and the statements are still valid.
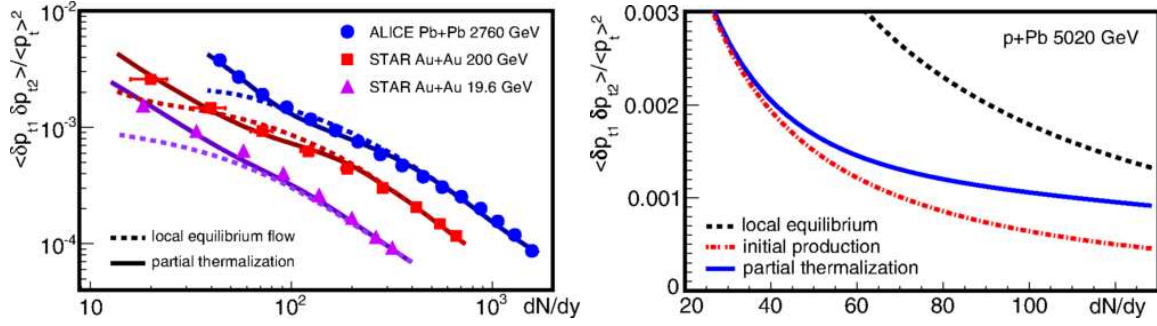
Figure 5.17.: $\left(\sqrt{C_m}/M(p_\mathrm{T})_m\right)^2$ as a function of $\mathrm{d}N_\mathrm{ch}/\mathrm{d}y$ from a model using a Boltzmann-Langevin approach [163]. Left: Results of the model with local equilibrium flow or alternatively with a partial thermalisation and comparison to experimental data from [3, 92]. Right: Predictions for p–Pb collisions at $\sqrt{s_\mathrm{NN}}$ = 5.02 TeV from the same versions of the model and a third one assuming purely inital-state production. Figures from [163].

central region of heavy-ion collisions [163]. At lowest multiplicities corresponding to the most peripheral collisions, the particle production is purely driven by initial-state interactions. At $\mathrm{d}N_\mathrm{ch}/\mathrm{d}y \lesssim 100$ a transition starts assuming a partial thermalisation with an increasing fraction of thermalisation. Around $\mathrm{d}N_\mathrm{ch}/\mathrm{d}y$ = 400 the complete local equilibrium is approached and the results agree with those from the older version of the model [180]. The multiplicity range of this transition corresponds to the range in the ALICE measurements (figure 5.5 and the left panels of figure 5.7), where a slight enhancement of the Pb–Pb data over the pp extrapolation is observed, and might explain this small deviation. The new approach corresponds to the solid lines in figure 5.17. The agreement with the data in peripheral heavy-ion collisions is significantly improved and, in this new version, this model is able to describe the mean p_T fluctuations data over the complete range of multiplicities under study.

In the right panel of figure 5.17, predictions for p–Pb collisions at $\sqrt{s_\mathrm{NN}}$ = 5.02 TeV are presented. In addition to the calculations assuming local equilibrium or partial thermalisation, a third version is shown containing purely initial-state particle production. The authors of [163] state, that the p–Pb prediction for partial thermalisation uses some extrapolations from their heavy-ion results, which might affect the results in p–Pb collisions. However, their results in p–Pb show a similar trend and also comparable values as their Pb–Pb results. This similarity is confirmed by the measurements in this work, see figure 5.14.

The results of a different model [74] starting from wounded nucleons or wounded quarks in the inital state followed by an evolution using viscous hydrodynamics are presented in figure 5.18. While the version assuming wounded nucleons only roughly describes the qualitative trend of the Pb–Pb data at $\sqrt{s_\mathrm{NN}}$ = 2.76 TeV, the other version employing wounded quarks agrees not only qualitatively, but also quantitatively with the experimental results. This demonstrates, that also in heavy-ion collisions, partonic
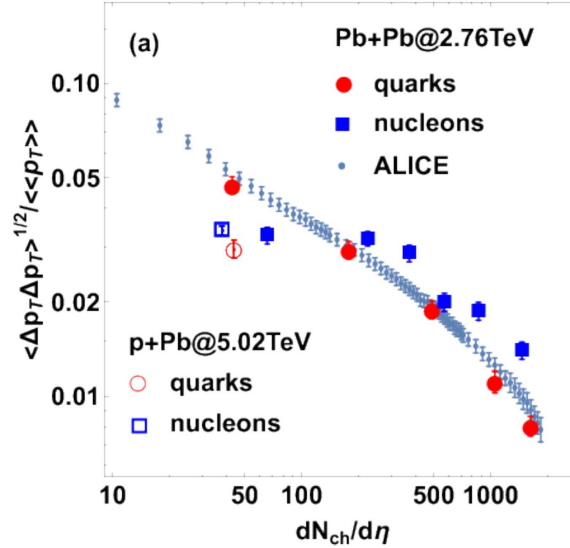
Figure 5.18.: $\sqrt{C_m}/M(p_T)_m$ as a function of $dN_{ch}/d\eta$ from a model using an initial state of wounded nucleons or wounded quarks and viscous hydrodynamics [74]. The calculations are compared to ALICE Pb–Pb data from [3] and predictions for p–Pb collisions at $\sqrt{s_{NN}}$ = 5.02 TeV are included. Figure from [74].

degrees of freedom have to be assumed in the initial state of the collisions. In addition to the heavy-ion calculations, predictions for p–Pb collisions at $\sqrt{s_{NN}}$ = 5.02 TeV are shown in figure 5.18. In contrast to the predictions presented in figure 5.17, only one point per version of the model is calculated corresponding to the 0–3% most central collisions in p–Pb [74]. Both predictions assuming wounded nucleons and wounded quarks yield values significantly below those measured in Pb–Pb collisions at $\sqrt{s_{NN}}$ = 2.76 TeV. These predictions are not supported by the measurements in this work presented in figure 5.14. However, it should be noted, that some part of this discrepancy might be related to the evaluation of the multiplicity density in p–Pb collisions within the model.

5.4. Discussion

Taking all the measurements, Monte Carlo simulations and model calculations presented in this chapter into account, a common picture of non-statistical mean transverse-momentum fluctuations in high-energy nuclear and heavy-ion collisions emerges. The results of the two-particle transverse-momentum correlator relative to the mean transverse momentum are observed to decrease as a function of the charged-particle multiplicity density in all analysed collision systems, i.e. from pp to p–Pb and Pb–Pb collisions. This decrease in itself is a strong evidence, that in all systems multiple particle-production sources have to be present. In pp collisions, this can only be achieved, if the relevant degrees of freedom in the initial state are of partonic nature

and multiple parton–parton collisions are allowed within a single pp event. PYTHIA simulations including only a single parton–parton collision do not exhibit this decrease, but show a flat behaviour as a function of multiplicity.

In p–Pb and Pb–Pb collisions, the behaviour of the fluctuations is in agreement or at least comparable to that found in pp collisions up to multiplicity densities around $\langle \mathrm{d}N_{\mathrm{ch}}/\mathrm{d}\eta \rangle = 500$ in Pb–Pb. In these systems, multiple sources of particle production are trivially present on the hadronic scale with multiple nucleon–nucleon collisions. However, model calculations show a significantly better agreement with the Pb–Pb data, if also in heavy-ion collisions partonic degrees of freedom are assumed in the initial state. Another model employing a thermodynamic description of heavy-ion collisions shows good agreement with the data, if in the peripheral part the particle production is dominated by initial-state interactions, followed by an increasing fraction of thermalisation with increasing multiplicity. The transition region in this model corresponds to multiplicities, at which a slight enhancement of the Pb–Pb results with respect to the pp baseline is observed. For $\langle \mathrm{d}N_{\mathrm{ch}}/\mathrm{d}\eta \rangle \gtrsim 500$, the fluctuations in Pb–Pb collisions are increasingly suppressed compared to the pp extrapolation. Such a behaviour may be explained with the creation of a Quark-Gluon Plasma, which would destroy a large fraction of the transverse-momentum correlations among the particles produced in the initial stages of the collisions and, hence, lead to a reduction of the fluctuations as well.

Towards the highest multiplicities in p–Pb collisions, a slight weakening of the slope corresponding to an increase with respect to the pp baseline is found, which resembles the behaviour at somewhat higher multiplicities in the Pb–Pb data. It is tempting to associate this observation with a possible creation of a Quark-Gluon-Plasma droplet in high-multiplicity p–Pb collisions, as it may be the case in Pb–Pb collisions within the transition region from peripheral to mid-central events. However, the effect in p–Pb collisions is also in accordance with a simple high-multiplicity selection bias. In pp collisions, the uncertainties of the current measurements do not allow any conclusive statement about a possible similar behaviour in high-multiplicity collisions.

In summary, the description of mean transverse-momentum fluctuations as a function of multiplicity requires the consideration of partonic degrees of freedom in the initial state. In pp collisions, the observations can be explained with multi-parton interactions. In heavy-ion collisions, the creation of a QGP may set in already at rather low multiplicities, where the results can be described assuming a partial thermalisation of the system. When a large fraction of the system is thermalised, the fluctuations are clearly reduced and the creation of a Quark-Gluon Plasma is very likely. Although the data presented here can be described without the creation of a QGP in small collision systems, it cannot be excluded, that the common decreasing slope with increasing multiplicities is related to such effects. Thus, this scenario, although disfavoured, cannot be excluded.

6. Summary and outlook

Within this thesis, data of ultra-relativistic hadron–hadron and heavy-ion collisions measured with ALICE in the first running period of the Large Hadron Collider (LHC) at CERN are analysed. Event-by-event mean transverse-momentum fluctuations are studied in proton–proton (pp), proton–lead (p–Pb) and lead–lead (Pb–Pb) collisions. The pp data have been taken in the years 2010 and 2011, covering three different centre-of-mass collision energies of $\sqrt{s}$ = 0.9, 2.76 and 7 TeV. The Pb–Pb data at a nucleon–nucleon collision energy of $\sqrt{s_{\mathrm{NN}}}$ = 2.76 TeV have been measured in 2010 and the considered p–Pb data-taking period at $\sqrt{s_{\mathrm{NN}}}$ = 5.02 TeV has concluded the first LHC running period in early 2013.

Measurements of event-by-event fluctuations of thermodynamic quantities are used to investigate the structure of the phase diagram of strongly interacting matter. Within this diagram, elementary particles are confined into hadrons at low temperature (T) and baryo-chemical potential (μ_{B}). At very high energy densities corresponding to a strong increase in T and/or μ_{B}, a deconfined state, i.e. a Quark-Gluon Plasma (QGP), may be reached. Examples for the thermodynamic quantities being studied are the temperature and the conserved quantum numbers like the baryon number, the electric charge and the strangeness. Fluctuations of the mean transverse momentum are related to fluctuations of these thermodynamic quantities, but also to other dynamical processes in the collisions like collective behaviour, resonance decays and jets. At the very high collision energies reached at the LHC, corresponding to a vanishing μ_{B}, the transition to a QGP is expected to be a crossover. Here, no large variations of the observed fluctuations are expected due to a phase transition, but mean transverse-momentum (p_{T}) fluctuations can be employed to investigate the relevant degrees of freedom in the initial state of the collisions.

In order to quantify the non-statistical mean p_{T} fluctuations, the two-particle transverse-momentum correlator is studied. It is constructed such, that it vanishes in the case of purely statistical fluctuations. Any non-zero signal indicates correlations of the particles in momentum space leading to dynamical mean p_{T} fluctuations. The analysis is performed selecting soft particles within a transverse-momentum range of $0.15\,\mathrm{GeV}/c < p_{\mathrm{T}} < 2\,\mathrm{GeV}/c$. A pseudorapidity acceptance of $|\eta| < 0.8$ is covered, which is mainly determined by the requirement of a uniform acceptance and efficiency in the most important ALICE detector system for this analysis, which is the Time Projection Chamber.

The data analysis in this work is divided into two parts. In the first part, the symmetric systems of pp and Pb–Pb collisions are studied, while the second part is dedicated to the analysis of the asymmetric p–Pb collisions. In addition to the corresponding chronological order of the data taking, the most important reason for this choice is

6. Summary and outlook

the fact, that the analysis in an asymmetric system is more complex. In symmetric systems, the centre-of-mass system of the collisions and the laboratory system coincide, facilitating the analysis procedure. This advantage is used to establish the analysis in the symmetric systems and to extend it afterwards to p–Pb collisions, where effects of the asymmetric acceptance have to be taken into account.

The results are presented taking the square root of the two-particle correlator divided by the mean transverse momentum. In this way, a dimensionless observable is obtained, which quantifies the size of the fluctuations relative to mean p_{T}. Most of the results are shown as a function of the charged-particle multiplicity density ($\langle \mathrm{d}N_{\mathrm{ch}}/\mathrm{d}\eta \rangle$). In pp and p–Pb collisions, also the inclusive values considering the full event samples are determined. In all cases, significant non-statistical mean p_{T} fluctuations are found. In pp collisions, the fluctuations do not exhibit any significant dependence on the collision energy. This invariance is also preserved in comparison to measurements by other experiments at much lower collision energies.

The mean p_{T} fluctuations decrease with increasing multiplicity density in all three collision systems following a power-law behaviour. Furthermore, the results are in quantitative agreement or at least comparable in the overlapping region in multiplicity. The Pb–Pb data are in agreement with an extrapolation of the pp results to higher multiplicities, exhibiting a slight enhancement above this pp baseline in the region $100 \lesssim \langle \mathrm{d}N_{\mathrm{ch}}/\mathrm{d}\eta \rangle \lesssim 500$ and a significant reduction of the fluctuations above. Model calculations suggest, that the behaviour in Pb–Pb may be related to a partial thermalisation of the created system with an increasing thermalised fraction with increasing multiplicity. High-multiplicity p–Pb data show a slight increase above the pp trend as well, but this is in accordance with a high-multiplicity selection bias and not necessarily related to the creation of a QGP droplet. In pp collisions, the results can be explained by a superposition of multiple parton–parton collisions. The statistics within the pp data sets under study are not sufficient for any conclusive investigation of the high-multiplicity part. Finally, in p–Pb collisions the fluctuations are studied separately for like-sign and unlike-sign charged-particle pairs. Some differences are found, which decrease with increasing multiplicity.

For future analyses, it would be interesting to continue the studies of multi-parton interactions in pp collisions, which have been started in Monte Carlo (MC) simulations. Especially relevant would be the developement of quantities enabling the classification of the experimentally measured pp events corresponding to their number of parton–parton interactions in the initial state. This would allow for a direct test of the observation in MC simulations, that the magnitude of mean p_{T} fluctuations is independent of the multiplicity for an identical number of sources of particle production.

In addition, the behaviour of the high-multiplicity tail of the data in small collision systems could be investigated further by analysing the data sets of the second LHC running period. Large data sets in pp collisions, mainly at an energy of $\sqrt{s} = 13\,\mathrm{TeV}$, are available, which may be sufficient to resolve any effects similar to those observed in Pb–Pb and high-multiplicity p–Pb collisions. There are also significantly more events

available in p–Pb collisions, increasing the statistics of the minimum-bias data set at $\sqrt{s_{\mathrm{NN}}} = 5.02\,\mathrm{TeV}$ by about a factor of five. Finally, the charge-dependent studies performed in p–Pb collisions could be extended to the other collision systems. Especially in Pb–Pb collisions it would be interesting to clarify, whether the contributions from like-sign and unlike-sign pairs converge at some range in multiplicity or whether they stay different up to the highest multiplicities.

Appendix A.

Data periods and runs

In this appendix, the data taking periods and reconstruction passes used in the present work are specified. For each combination of period and pass the run numbers are listed of those runs, which are selected for the analyses.

A.1. Analysis of symmetric systems: pp and Pb–Pb

The following data sets are used in the first analysis, which is described in chapter 3.

pp collisions at $\sqrt{s} = 0.9\,\text{TeV}$

LHC10c pass3

118506, 118507, 118512, 118518, 118556, 118558, 118560, 118561, 121039, 121040

pp collisions at $\sqrt{s} = 2.76\,\text{TeV}$

LHC11a without_SDD.pass2

146746, 146747, 146748, 146801, 146802, 146803, 146804, 146805, 146806, 146807, 146817, 146824, 146856, 146858, 146859, 146860

pp collisions at $\sqrt{s} = 7\,\text{TeV}$

LHC10d pass2

122374, 122375, 124751, 125023, 125085, 125097, 125100, 125101, 125134, 125296, 125628, 125630, 125632, 125633, 125842, 125843, 125844, 125847, 125848, 125849, 125850, 125851, 125855, 126004, 126007, 126008, 126073, 126078, 126081, 126082, 126088, 126090, 126097, 126158, 126160, 126168, 126283, 126284, 126285, 126351, 126352, 126359, 126403, 126404, 126405, 126406, 126407, 126408, 126409, 126422, 126424, 126425, 126432, 126437

LHC10e pass2

127712, 127714, 127718, 127822, 127933, 127935, 127936, 127937, 127940, 127941,
127942, 128185, 128186, 128189, 128191, 128192, 128260, 128366, 128452, 128483,
128486, 128494, 128495, 128503, 128504, 128507, 128582, 128605, 128609, 128611,
128615, 128677, 128678, 128777, 128778, 128820, 128823, 128824, 128835, 128836,
128843, 128850, 128853, 128855, 128913, 129512, 129513, 129514, 129520, 129523,
129527, 129528, 129540, 129586, 129587, 129599, 129639, 129641, 129647, 129650,
129652, 129653, 129654, 129659, 129666, 129667, 129723, 129725, 129726, 129729,
129735, 129736, 129738, 129742, 129744, 129959, 129960, 129961, 129983, 130149,
130157, 130158, 130172, 130178, 130179, 130342, 130343, 130354, 130356, 130375,
130480, 130517, 130519, 130696, 130704, 130793, 130795, 130798, 130799, 130834,
130840, 130844, 130847, 130848

Pb–Pb collisions at $\sqrt{s_{\mathrm{NN}}} = 2.76\,\mathrm{TeV}$

LHC10h pass2

137161, 137162, 137231, 137232, 137235, 137236, 137243, 137366, 137431, 137432,
137434, 137439, 137440, 137441, 137443, 137530, 137531, 137539, 137541, 137544,
137546, 137549, 137595, 137608, 137638, 137639, 137685, 137686, 137691, 137692,
137693, 137704, 137718, 137722, 137724, 137751, 137752, 137844, 137848, 138190,
138192, 138197, 138201, 138225, 138275, 138364, 138396, 138438, 138439, 138442,
138469, 138534, 138578, 138579, 138582, 138583, 138621, 138624, 138638, 138652,
138653, 138662, 138666, 138730, 138732, 138837, 138870, 138871, 138872, 139028,
139029, 139036, 139037, 139038, 139105, 139107, 139173, 139309, 139310, 139314,
139328, 139329, 139360, 139437, 139438, 139465, 139503, 139505, 139507, 139510

A.2. New analysis including p–Pb collisions

These data sets are employed in the second analysis, see chapter 4.

p–Pb collisions at $\sqrt{s_{\mathrm{NN}}} = 5.02\,\mathrm{TeV}$

LHC13b pass3

195344, 195351, 195389, 195391, 195478, 195479, 195480, 195481, 195482, 195483

LHC13b pass4

195344, 195351, 195389, 195391, 195479, 195480, 195482, 195483

LHC13c pass4

195529, 195531, 195566, 195567, 195568, 195592, 195593, 195596, 195633, 195635,
195644, 195673, 195675, 195677

pp collisions at $\sqrt{s} = 2.76$ TeV

LHC11a without_SDD.pass4
Runs: see above, Appendix A.1

pp collisions at $\sqrt{s} = 7$ TeV

LHC10d pass4
Runs: see above, Appendix A.1

Pb–Pb collisions at $\sqrt{s_{\mathrm{NN}}} = 2.76$ TeV

LHC10h pass2
Runs: see above (Appendix A.1), but without run 138579, because it was identified as bad calibrated in the TPC when the TPC qualitiy assurance was re-analysed for the full LHC10h pass2 data set.

Appendix B.

Detailed distributions of track selection criteria

Selection criteria are applied to each reconstructed track and only those tracks passing all criteria are accepted within the analysis. More information about the track selection procedures in the present work can be found in sections 3.3 and 4.3. Here, detailed distributions of some of these criteria are presented. As an example, the distributions are shown in p–Pb collisions at $\sqrt{s_{\mathrm{NN}}}$ = 5.02 TeV using the standard ESD analysis of the pass4 reconstruction with the TPC-standalone tracking and including the TPC refit. These distributions are also studied in the other ESD analyses as well as in the other (pp and Pb–Pb) collision systems. Most of these distributions cannot be obtained in the AOD analyses, as the corresponding values are not stored in AOD files.

The criteria presented here are summarised in table B.1. For those, which are used in the track selection of the standard ESD analysis, the value of the cut is also given in the table. The other criteria are not used in the standard analysis, but they are for example applied during the investigation of the pseudorapidity distributions, see section 4.3.2. In table B.1, also the figure numbers and the respective page numbers of the figures are listed.

Track selection criterion	Abbreviation	Cut value	Figure	Page
Number of TPC clusters	TPCCls	≥ 70	B.1	164
Number of TPC crossed rows	TPCCRows	–	B.2	165
Fraction of TPC c.rows/find.cls.	TPCCRowsFind	–	B.3	166
Fraction of TPC shared clusters	TPCSharedCls	–	B.4	167
TPC χ^2/d.o.f.	TPCChi2	≤ 4.0	B.5	168
DCA to vertex (xy)	DCAxy	≤ 2.4 cm	B.6	169
DCA to vertex (z)	DCAz	≤ 3.2 cm	B.7	170

Table B.1.: Track selection criteria of which detailed distributions are presented. The cut values are listed for the standard ESD analysis using the TPC-standalone tracking. The other criteria are not used in the standard analysis but for further studies. The numbers of the figures and their corresponding pages are listed as well.
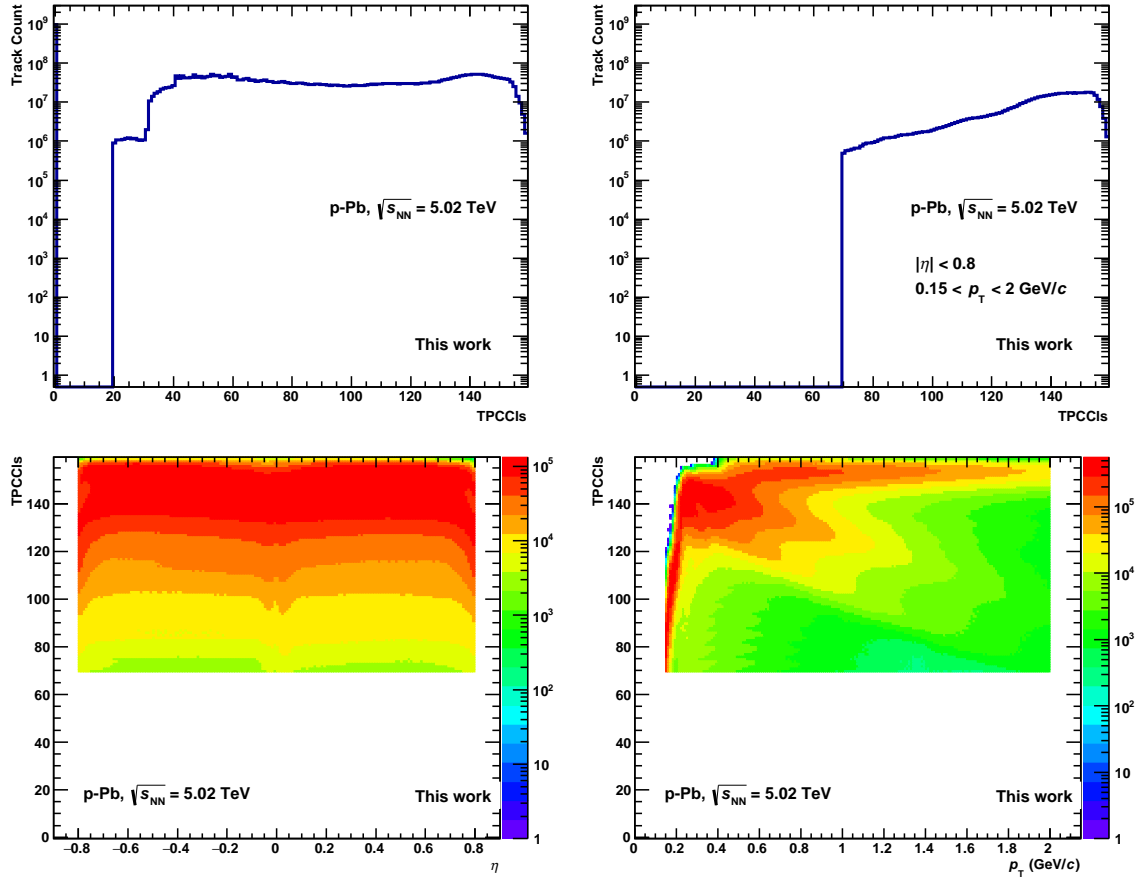
Figure B.1.: Distributions of the number of TPC clusters (TPCCls) per track in p–Pb collisions at $\sqrt{s_{NN}}$ = 5.02 TeV using the standard ESD analysis (pass4 with TPC refit). Top left: Before any track selections. Top right: All selection criteria applied including the kinematic acceptance and TPCCls ≥ 70. Bottom panels: Two-dimensional distributions – including all selection criteria – of the TPCCls as a function of η (left) and as a function of p_T (right).
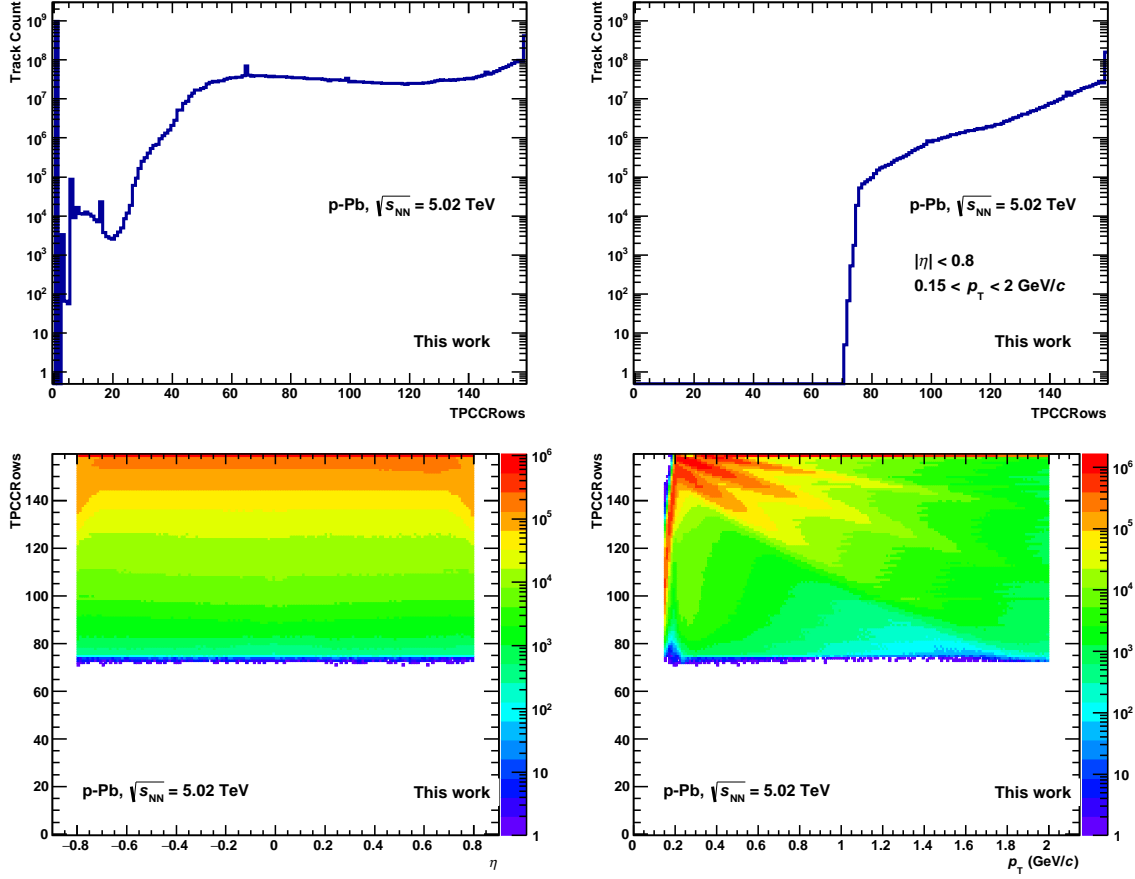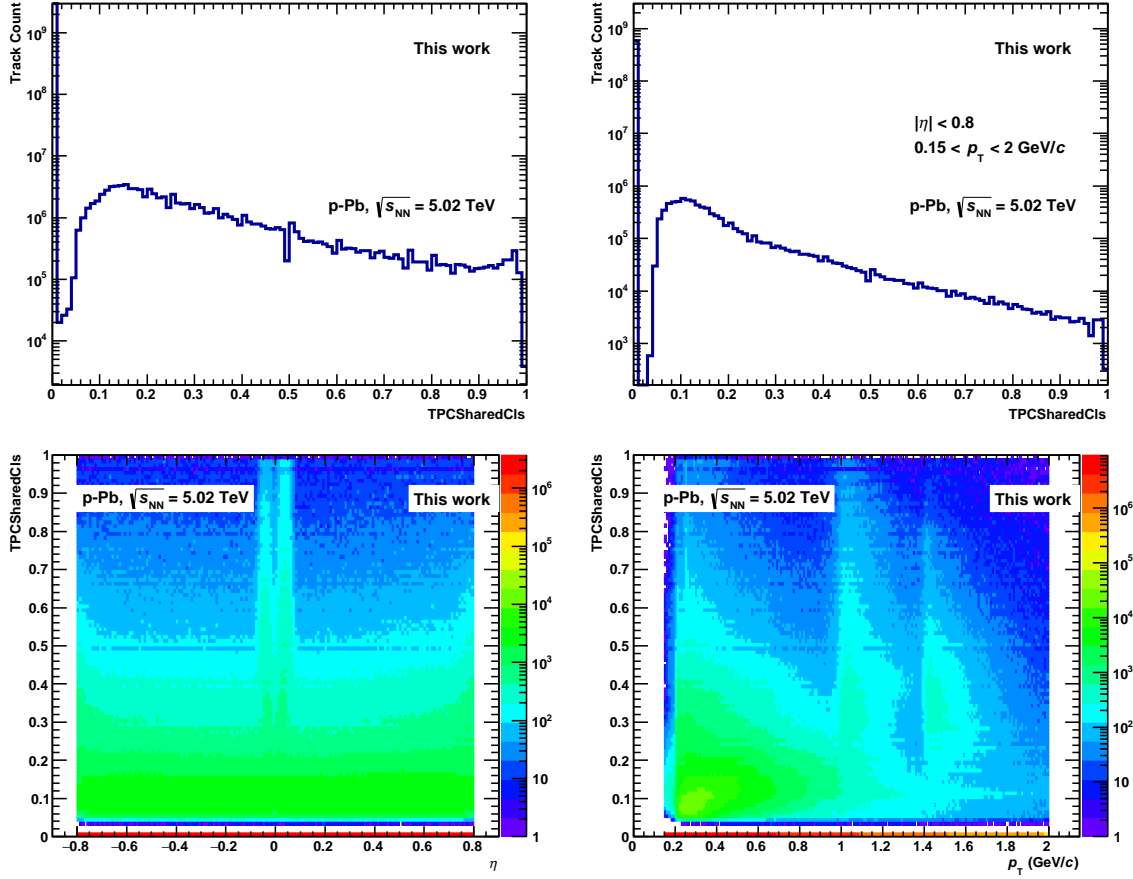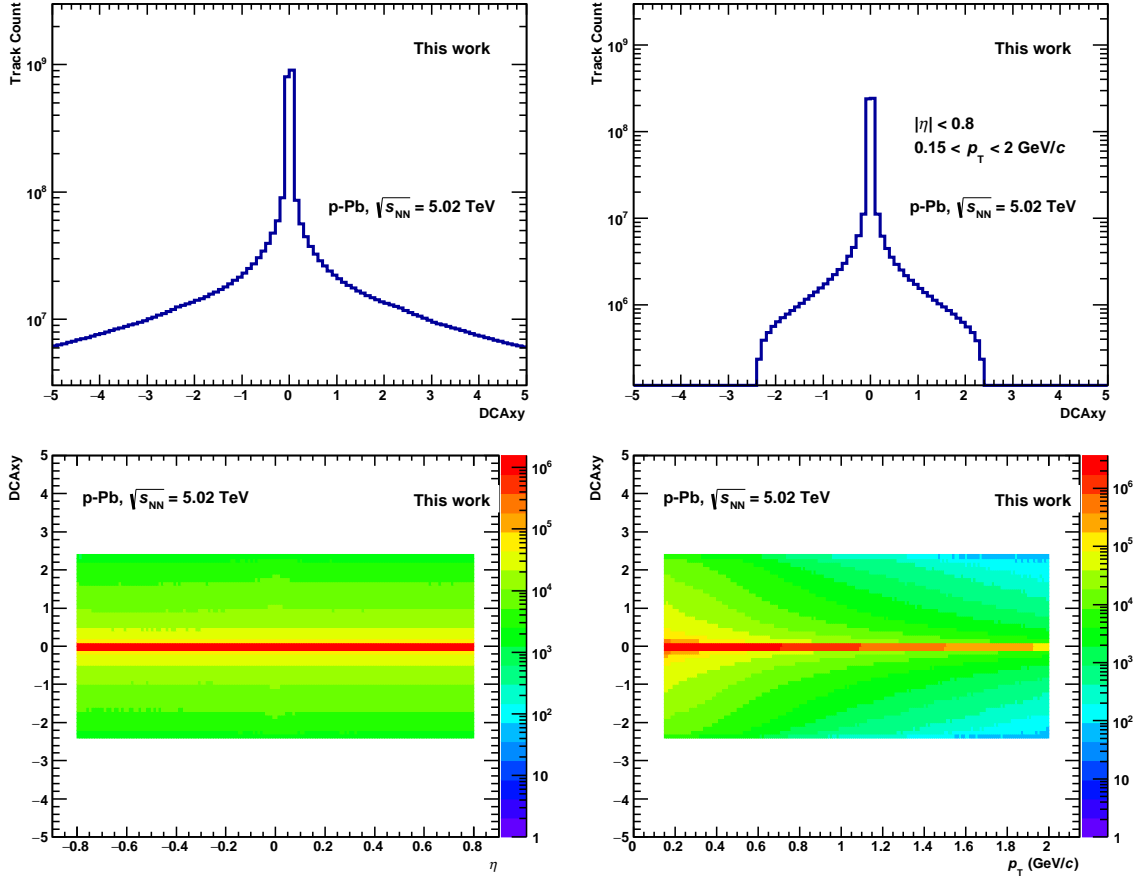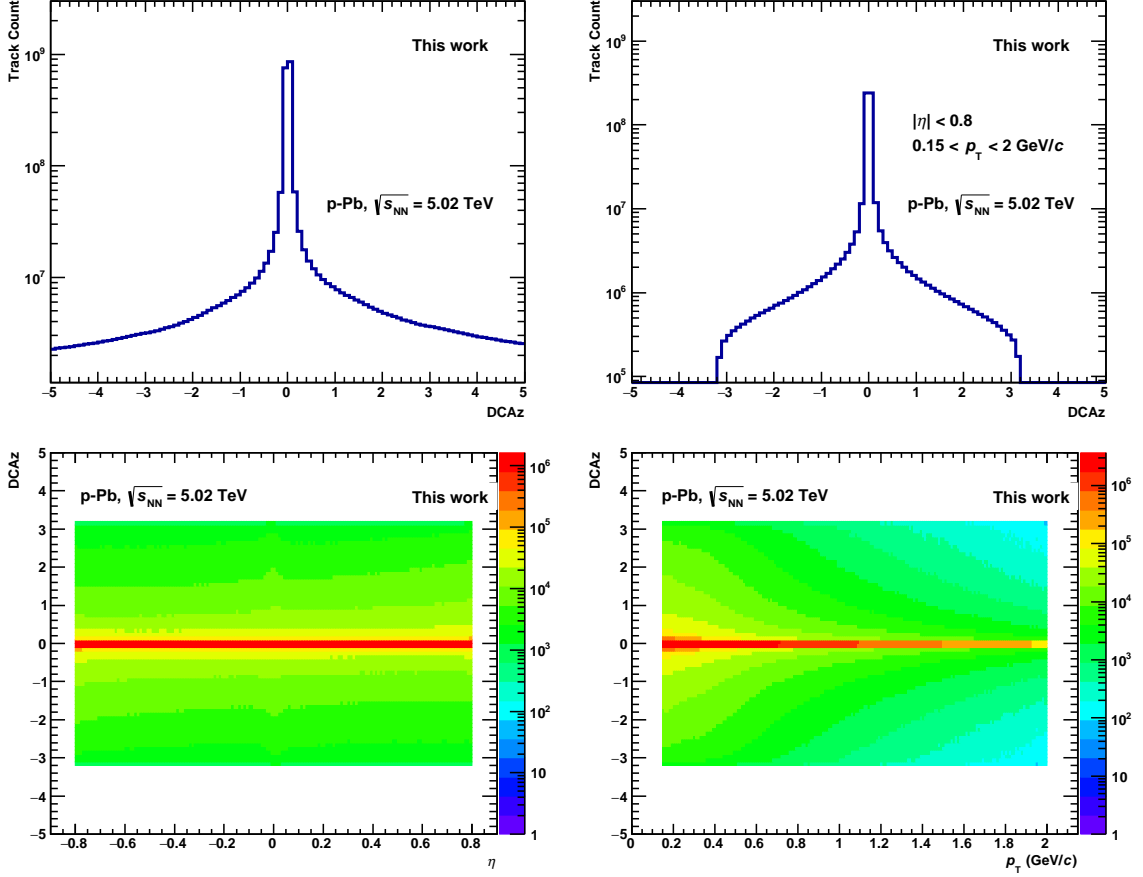
Figure B.2.: Distributions of the number of crossed rows in the TPC (TPCCRows) per track in p–Pb collisions at $\sqrt{s_{\mathrm{NN}}}$ = 5.02 TeV using the standard ESD analysis (pass4 with TPC refit). Top left: Before any track selections. Top right: All selection criteria applied including the kinematic acceptance. No condition on TPCCRows is applied, but TPCCls $\geq$ 70 is also the lower limit for the TPCCRows. Bottom panels: Two-dimensional distributions – including all selection criteria – of the TPCCRows as a function of η (left) and as a function of p_{T} (right).
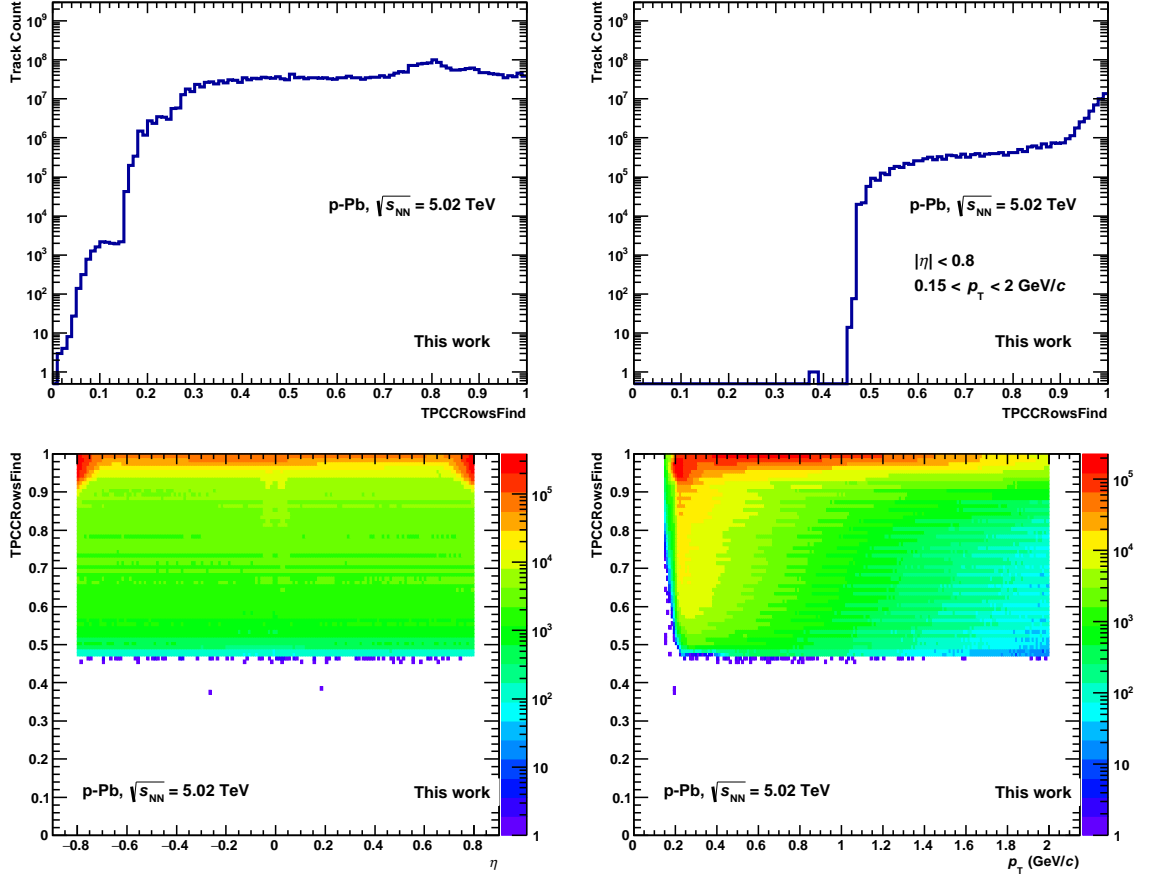
Figure B.3.: Distributions of the fraction of crossed rows over findable clusters in the TPC (TPCCRowsFind) per track in p–Pb collisions at $\sqrt{s_{NN}} = 5.02$ TeV using the standard ESD analysis (pass4 with TPC refit). Top left: Before any track selections. Top right: All selection criteria applied including the kinematic acceptance. No condition on TPCCRowsFind is applied. Bottom panels: Two-dimensional distributions – including all selection criteria – of the TPCCRowsFind as a function of η (left) and as a function of p_T (right).

Figure B.4.: Distributions of the fraction of shared clusters in the TPC (TPCShared-Cls) per track in p–Pb collisions at $\sqrt{s_{\mathrm{NN}}} = 5.02$ TeV using the standard ESD analysis (pass4 with TPC refit). Top left: Before any track selections. Top right: All selection criteria applied including the kinematic acceptance. No condition on TPCSharedCls is applied. Bottom panels: Two-dimensional distributions – including all selection criteria – of the TPCSharedCls as a function of η (left) and as a function of p_{T} (right).
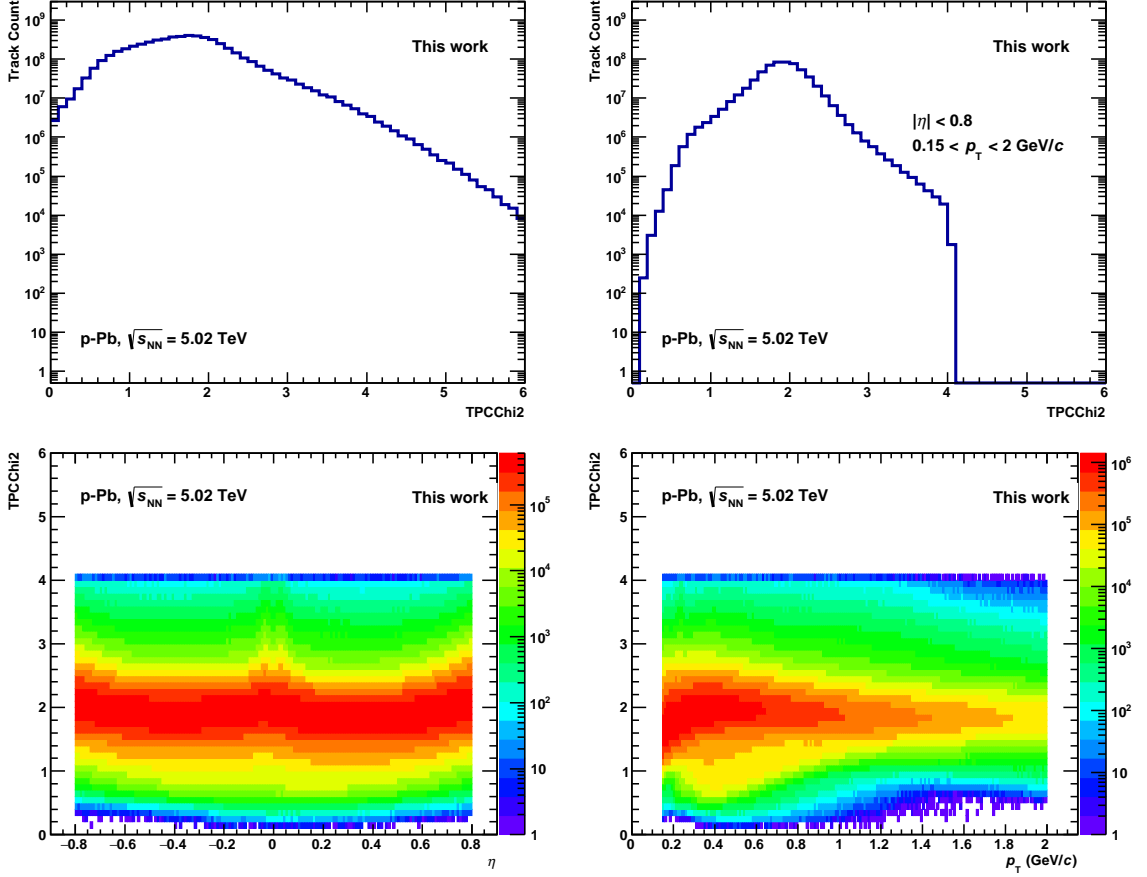
Figure B.5.: Distributions of the χ^2 of the momentum fit in the TPC per degree of freedom (TPCChi2) per track in p–Pb collisions at $\sqrt{s_{\mathrm{NN}}} = 5.02\,\mathrm{TeV}$ using the standard ESD analysis (pass4 with TPC refit). Top left: Before any track selections. Top right: All selection criteria applied including the kinematic acceptance and TPCChi2 $\leq$ 4.0. Bottom panels: Two-dimensional distributions – including all selection criteria – of the TPC-Chi2 as a function of η (left) and as a function of p_{T} (right).

Figure B.6.: Distributions of the distance of closest approach to the primary vertex in the transverse plane (DCAxy) per track in p–Pb collisions at $\sqrt{s_{\mathrm{NN}}} = 5.02\,\mathrm{TeV}$ using the standard ESD analysis (pass4 with TPC refit). Top left: Before any track selections. Top right: All selection criteria applied including the kinematic acceptance and DCAxy $\leq 2.4\,\mathrm{cm}$. Note, that a two-dimensional DCA criterion is enabled, see section 3.3.2. This criterion is responsible for the reduction of the DCAxy close to the cut values. Bottom panels: Two-dimensional distributions – including all selection criteria – of the DCAxy as a function of η (left) and as a function of p_{T} (right).

Figure B.7.: Distributions of the distance of closest approach to the primary vertex along the beam direction (DCAz) per track in p–Pb collisions at $\sqrt{s_{\mathrm{NN}}} = 5.02\,\mathrm{TeV}$ using the standard ESD analysis (pass4 with TPC refit). Top left: Before any track selections. Top right: All selection criteria applied including the kinematic acceptance and DCAz $\leq 3.2\,\mathrm{cm}$. Note, that a two-dimensional DCA criterion is enabled, see section 3.3.2. This criterion is responsible for the reduction of the DCAz close to the cut values. Bottom panels: Two-dimensional distributions – including all selection criteria – of the DCAz as a function of η (left) and as a function of p_{T} (right).

Bibliography

[1] S. T. Heckel, "Event-by-event Fluktuationen des mittleren Transversalimpulses in pp- und Pb–Pb-Kollisionen gemessen mit dem ALICE Experiment am LHC," Master's thesis, *Goethe-Universität, Frankfurt am Main*, 2011. In German.

[2] **ALICE** Collaboration, S. T. Heckel, "Event-by-event mean p_T fluctuations in pp and Pb–Pb collisions measured by the ALICE experiment at the LHC," *J. Phys.* **G38** (2011) 124095, `arXiv:1107.4327 [nucl-ex]`.

[3] **ALICE** Collaboration, B. B. Abelev *et al.*, "Event-by-event mean p_T fluctuations in pp and Pb–Pb collisions at the LHC," *Eur. Phys. J.* **C74** (2014) 3077, `arXiv:1407.5530 [nucl-ex]`.

[4] **ALICE** Collaboration, S. T. Heckel, "Event-by-event mean p_T fluctuations in pp and Pb–Pb collisions at the LHC," *EPJ Web Conf.* **90** (2015) 08006, `arXiv:1502.00537 [nucl-ex]`.

[5] B. Schütz, "Monte-Carlo-Studien zum Einfluss von Multi-Parton-Interaktionen auf die Fluktuationen des mittleren Transversalimpulses in pp-Kollisionen," Bachelor's thesis, *Goethe-Universität, Frankfurt am Main*, 2014. In German.

[6] S. Weinberg, *The First Three Minutes: A Modern View of the Origin of the Universe*. Basic Books (New York, USA), 1977.

[7] D. S. Gorbunov and V. A. Rubakov, *Introduction to the Theory of the Early Universe: Hot Big Bang Theory*. World Scientific (Singapore, Singapore), 2011.

[8] H. Karttunen, P. Kröger, H. Oja, M. Poutanen, and K. J. Donner, *Fundamental Astronomy*. Springer (Berlin Heidelberg, Germany), 6th ed., 2017.

[9] I. Morison, *Introduction to Astronomy and Cosmology*. Wiley (Chichester, UK), 2008.

[10] B. Povh, K. Rith, C. Scholz, F. Zetsche, and W. Rodejohann, *Teilchen und Kerne: Eine Einführung in die physikalischen Konzepte*. Springer (Berlin Heidelberg, Germany), 9th ed., 2014. In German.

[11] W. N. Cottingham and D. A. Greenwood, *An Introduction to the Standard Model of Particle Physics*. Cambridge University Press (Cambridge, UK), 2nd ed., 2007.

Bibliography

[12] T. Morii, C. S. Lim, and S. N. Mukherjee, *The Physics of the Standard Model and Beyond*. World Scientific (Singapore, Singapore), 2004.

[13] C. Y. Wong, *Introduction to High-Energy Heavy-Ion Collisions*. World Scientific (Singapore, Singapore), 1994.

[14] H. Satz, *Extreme States of Matter in Strong Interaction Physics*, vol. 945 of *Lect. Notes Phys.* Springer International Publishing (Cham, Switzerland), 2nd ed., 2018.

[15] **ATLAS** Collaboration, G. Aad *et al.*, "Observation of a new particle in the search for the Standard Model Higgs boson with the ATLAS detector at the LHC," *Phys. Lett.* **B716** (2012) 1, `arXiv:1207.7214 [hep-ex]`.

[16] **CMS** Collaboration, S. Chatrchyan *et al.*, "Observation of a new boson at a mass of 125 GeV with the CMS experiment at the LHC," *Phys. Lett.* **B716** (2012) 30, `arXiv:1207.7235 [hep-ex]`.

[17] **Particle Data Group** Collaboration, M. Tanabashi *et al.*, "Review of Particle Physics," *Phys. Rev.* **D98** (2018) 030001.

[18] **ATLAS** Collaboration, M. Aaboud *et al.*, "Evidence for light-by-light scattering in heavy-ion collisions with the ATLAS detector at the LHC," *Nature Phys.* **13** (2017) 852, `arXiv:1702.01625 [hep-ex]`.

[19] J. Bartke, *Introduction to Relativistic Heavy Ion Physics*. World Scientific (Singapore, Singapore), 2009.

[20] W. Florkowski, *Phenomenology of Ultra-Relativistic Heavy-Ion Collisions*. World Scientific (Singapore, Singapore), 2010.

[21] H. Satz, "The Thermodynamics of Quarks and Gluons," in *The Physics of the Quark-Gluon Plasma: Introductory Lectures*, S. Sarkar, H. Satz, and B. Sinha, eds., vol. 785 of *Lect. Notes Phys.*, p. 1. Springer (Berlin Heidelberg, Germany), 2010.

[22] M. Kliemant, R. Sahoo, T. Schuster, and R. Stock, "Global Properties of Nucleus–Nucleus Collisions," in *The Physics of the Quark-Gluon Plasma: Introductory Lectures*, S. Sarkar, H. Satz, and B. Sinha, eds., vol. 785 of *Lect. Notes Phys.*, p. 23. Springer (Berlin Heidelberg, Germany), 2010.

[23] Y. Aoki, G. Endrödi, Z. Fodor, S. D. Katz, and K. K. Szabo, "The Order of the quantum chromodynamics transition predicted by the standard model of particle physics," *Nature* **443** (2006) 675, `arXiv:hep-lat/0611014 [hep-lat]`.

[24] C. Ratti, "Lattice QCD and heavy ion collisions: a review of recent progress," *Rept. Prog. Phys.* **81** (2018) 084301, `arXiv:1804.07810 [hep-lat]`.

[25] M. A. Stephanov, K. Rajagopal, and E. V. Shuryak, "Signatures of the tricritical point in QCD," *Phys. Rev. Lett.* **81** (1998) 4816, `arXiv:hep-ph/9806219 [hep-ph]`.

[26] M. A. Stephanov, K. Rajagopal, and E. V. Shuryak, "Event-by-event fluctuations in heavy ion collisions and the QCD critical point," *Phys. Rev.* **D60** (1999) 114028, `arXiv:hep-ph/9903292 [hep-ph]`.

[27] M. G. Alford, A. Schmitt, K. Rajagopal, and T. Schäfer, "Color superconductivity in dense quark matter," *Rev. Mod. Phys.* **80** (2008) 1455, `arXiv:0709.4635 [hep-ph]`.

[28] H. Meyer-Ortmanns and T. Reisz, *Principles of Phase Structures in Particle Physics.* World Scientific (Singapore, Singapore), 2007.

[29] G. F. Burgio, A. Drago, G. Pagliara, H. J. Schulze, and J. B. Wei, "Has deconfined quark matter been detected during GW170817/AT2017gfo?," `arXiv:1803.09696 [astro-ph.HE]`.

[30] **Virgo, LIGO Scientific** Collaboration, B. P. Abbott *et al.*, "Observation of Gravitational Waves from a Binary Black Hole Merger," *Phys. Rev. Lett.* **116** (2016) 061102, `arXiv:1602.03837 [gr-qc]`.

[31] **Virgo, LIGO Scientific** Collaboration, B. Abbott *et al.*, "GW170817: Observation of Gravitational Waves from a Binary Neutron Star Inspiral," *Phys. Rev. Lett.* **119** (2017) 161101, `arXiv:1710.05832 [gr-qc]`.

[32] B. Sinha, "The Mini Bang and the Big Bang: From Collider to Cosmology," in *Exciting Interdisciplinary Physics: Quarks and Gluons / Atomic Nuclei / Relativity and Cosmology / Biological Systems*, W. Greiner, ed., p. 261. Springer International Publishing (Cham, Switzerland), 2013.

[33] L. Evans and P. Bryant, "LHC Machine," *JINST* **3** (2008) S08001.

[34] **ALICE** Collaboration, L. Y. Abramova *et al.*, *ALICE: Technical proposal for A Large Ion Collider Experiment at the CERN LHC.* LHC Tech. Proposal. CERN, Geneva, 1995. `http://cds.cern.ch/record/293391`.

[35] **ALICE** Collaboration, K. Aamodt *et al.*, "The ALICE experiment at the CERN LHC," *JINST* **3** (2008) S08002.

[36] H. Petersen, J. Steinheimer, G. Burau, M. Bleicher, and H. Stöcker, "Fully integrated transport approach to heavy ion reactions with an intermediate hydrodynamic stage," *Phys. Rev.* **C78** (2008) 044901, `arXiv:0806.1695 [nucl-th]`.

Bibliography

[37] H. Petersen and madai.us, "Models and Data Analysis Initiative."
https://madai.phy.duke.edu/indexaae2.html?page_id=503. Accessed on
2019-07-10.

[38] A. Andronic, P. Braun-Munzinger, K. Redlich, and J. Stachel, "Decoding the
phase structure of QCD via particle production at high energy,"
Nature **561** (2018) 321, arXiv:1710.09425 [nucl-th].

[39] J. C. Collins and M. J. Perry, "Superdense Matter: Neutrons or
Asymptotically Free Quarks?," *Phys. Rev. Lett.* **34** (1975) 1353.

[40] N. Cabibbo and G. Parisi, "Exponential Hadronic Spectrum and Quark
Liberation," *Phys. Lett.* **59B** (1975) 67.

[41] E. V. Shuryak, "Quark-Gluon Plasma and Hadronic Production of Leptons,
Photons and Psions," *Phys. Lett.* **78B** (1978) 150. [Yad. Fiz. 28 (1978) 796].

[42] CERN, "New State of Matter created at CERN," Feb, 2000.
https://home.cern/news/press-release/cern/new-state-matter-created-cern.
Accessed on 2019-02-25.

[43] **STAR** Collaboration, J. Adams *et al.*, "Experimental and theoretical
challenges in the search for the quark gluon plasma: The STAR
Collaboration's critical assessment of the evidence from RHIC collisions,"
Nucl. Phys. **A757** (2005) 102, arXiv:nucl-ex/0501009 [nucl-ex].

[44] **PHENIX** Collaboration, K. Adcox *et al.*, "Formation of dense partonic matter
in relativistic nucleus-nucleus collisions at RHIC: Experimental evaluation by
the PHENIX collaboration," *Nucl. Phys.* **A757** (2005) 184,
arXiv:nucl-ex/0410003 [nucl-ex].

[45] S. Sarkar, H. Satz, and B. Sinha,
The Physics of the Quark-Gluon Plasma: Introductory Lectures, vol. 785 of
Lect. Notes Phys. Springer (Berlin Heidelberg, Germany), 2010.

[46] T. Matsui and H. Satz, "J/ψ Suppression by Quark-Gluon Plasma Formation,"
Phys. Lett. **B178** (1986) 416.

[47] F. Karsch and H. Satz, "The Spectral analysis of strongly interacting matter,"
Z. Phys. **C51** (1991) 209.

[48] J. D. Björken, "Energy Loss of Energetic Partons in Quark-Gluon Plasma:
Possible Extinction of High p_T Jets in Hadron–Hadron Collisions."
Fermilab-Pub-82-059-THY, 1982.

[49] M. Gyulassy and M. Plumer, "Jet Quenching in Dense Matter,"
Phys. Lett. **B243** (1990) 432.

174

[50] J. Alam, S. Raha, and B. Sinha, "Electromagnetic probes of quark gluon plasma," *Phys. Rept.* **273** (1996) 243.

[51] J. Rafelski and B. Müller, "Strangeness Production in the Quark-Gluon Plasma," *Phys. Rev. Lett.* **48** (1982) 1066. [Erratum: Phys. Rev. Lett. 56 (1986) 2334].

[52] **ALICE** Collaboration, B. B. Abelev *et al.*, "Centrality, rapidity and transverse momentum dependence of J/ψ suppression in Pb–Pb collisions at $\sqrt{s_{\mathrm{NN}}}$ = 2.76 TeV," *Phys. Lett.* **B734** (2014) 314, `arXiv:1311.0214 [nucl-ex]`.

[53] **ALICE** Collaboration, B. B. Abelev *et al.*, "Centrality dependence of charged particle production at large transverse momentum in Pb–Pb collisions at $\sqrt{s_{\mathrm{NN}}}$ = 2.76 TeV," *Phys. Lett.* **B720** (2013) 52, `arXiv:1208.2711 [hep-ex]`.

[54] **ALICE** Collaboration, S. Acharya *et al.*, "Measurement of dielectron production in central Pb–Pb collisions at $\sqrt{s_{\mathrm{NN}}}$ = 2.76 TeV," `arXiv:1807.00923 [nucl-ex]`.

[55] **ALICE** Collaboration, B. B. Abelev *et al.*, "Multi-strange baryon production at mid-rapidity in Pb–Pb collisions at $\sqrt{s_{\mathrm{NN}}}$ = 2.76 TeV," *Phys. Lett.* **B728** (2014) 216, `arXiv:1307.5543 [nucl-ex]`. [Erratum: Phys. Lett. B734 (2014) 409].

[56] R. C. Hwa and X.-N. Wang, eds., *Quark-Gluon Plasma 3.* World Scientific (Singapore, Singapore), 2004.

[57] R. C. Hwa and X.-N. Wang, eds., *Quark-Gluon Plasma 4.* World Scientific (Singapore, Singapore), 2010.

[58] X.-N. Wang, ed., *Quark-Gluon Plasma 5.* World Scientific (Singapore, Singapore), 2016.

[59] T. Schörner-Sadenius, ed., *The Large Hadron Collider: Harvest of Run 1.* Springer International Publishing (Cham, Switzerland), 2015.

[60] R. Averbeck, J. W. Harris, and B. Schenke, "Heavy-Ion Physics at the LHC," in *The Large Hadron Collider: Harvest of Run 1*, T. Schörner-Sadenius, ed., p. 355. Springer International Publishing (Cham, Switzerland), 2015.

[61] N. Armesto and E. Scomparin, "Heavy-ion collisions at the Large Hadron Collider: A review of the results from Run 1," *Eur. Phys. J. Plus* **131** (2016) 52, `arXiv:1511.02151 [nucl-ex]`.

[62] E. L. Bratkovskaya, W. Cassing, P. Moreau, and T. Song, "Review of the theoretical heavy-ion physics," *KnE Energ. Phys.* **3** (2018) 234, `arXiv:1711.01976 [nucl-th]`.

[63] **ALICE** Collaboration, B. B. Abelev *et al.*, "Long-range angular correlations on the near and away side in p–Pb collisions at $\sqrt{s_{NN}}$ = 5.02 TeV," *Phys. Lett.* **B719** (2013) 29, `arXiv:1212.2001 [nucl-ex]`.

[64] **ALICE** Collaboration, J. Adam *et al.*, "Enhanced production of multi-strange hadrons in high-multiplicity proton-proton collisions," *Nature Phys.* **13** (2017) 535, `arXiv:1606.07424 [nucl-ex]`.

[65] J. L. Nagle and W. A. Zajc, "Small System Collectivity in Relativistic Hadronic and Nuclear Collisions," *Ann. Rev. Nucl. Part. Sci.* **68** (2018) 211, `arXiv:1801.03477 [nucl-ex]`.

[66] M. Strickland, "Small system studies: A theory overview," *Nucl. Phys.* **A982** (2019) 92, `arXiv:1807.07191 [nucl-th]`.

[67] **PHENIX** Collaboration, C. Aidala *et al.*, "Creating small circular, elliptical, and triangular droplets of quark-gluon plasma," *Nature Phys.* **15** (2019) 214, `arXiv:1805.02973 [nucl-ex]`.

[68] U. W. Heinz, "Concepts of heavy-ion physics," in *2002 European School of high-energy physics, Pylos, Greece, 25 Aug-7 Sep 2002: Proceedings*, p. 165. 2004. `arXiv:hep-ph/0407360 [hep-ph]`.

[69] C. A. Pruneau, *Data Analysis Techniques for Physical Scientists*. Cambridge University Press (Cambridge, UK), 2017.

[70] S. Jeon and V. Koch, "Event by event fluctuations," in *Quark-Gluon Plasma 3*, R. C. Hwa and X.-N. Wang, eds., p. 430. World Scientific (Singapore, Singapore), 2004. `arXiv:hep-ph/0304012 [hep-ph]`.

[71] V. Koch, "Hadronic Fluctuations and Correlations," in *Relativistic Heavy Ion Physics*, R. Stock, ed., vol. 23 of *Landolt-Börnstein New Series I*, p. 626. Springer (Berlin Heidelberg, Germany), 2010. `arXiv:0810.2520 [nucl-th]`.

[72] P. Braun-Munzinger, K. Redlich, and J. Stachel, "Particle production in heavy ion collisions," in *Quark-Gluon Plasma 3*, R. C. Hwa and X.-N. Wang, eds., p. 491. World Scientific (Singapore, Singapore), 2004. `arXiv:nucl-th/0304013 [nucl-th]`.

[73] W. Broniowski, B. Hiller, W. Florkowski, and P. Bożek, "Event-by-event p_T fluctuations and multiparticle clusters in relativistic heavy-ion collisions," *Phys. Lett.* **B635** (2006) 290, `arXiv:nucl-th/0510033 [nucl-th]`.

[74] P. Bożek and W. Broniowski, "Transverse momentum fluctuations in ultrarelativistic Pb+Pb and p+Pb collisions with wounded quarks," *Phys. Rev.* **C96** (2017) 014904, `arXiv:1701.09105 [nucl-th]`.

[75] R. J. Barlow, *Statistics: A Guide to the Use of Statistical Methods in the Physical Sciences.* The Manchester Physics Series. Wiley (Chichester, UK), 1989.

[76] **ALICE** Collaboration, B. B. Abelev *et al.*, "Multiplicity dependence of the average transverse momentum in pp, p–Pb, and Pb–Pb collisions at the LHC," *Phys. Lett.* **B727** (2013) 371, `arXiv:1307.1094 [nucl-ex]`.

[77] F. Karsch and K. Redlich, "Probing freeze-out conditions in heavy ion collisions with moments of charge fluctuations," *Phys. Lett.* **B695** (2011) 136, `arXiv:1007.2581 [hep-ph]`.

[78] P. Braun-Munzinger, A. Kalweit, K. Redlich, and J. Stachel, "Confronting fluctuations of conserved charges in central nuclear collisions at the LHC with predictions from Lattice QCD," *Phys. Lett.* **B747** (2015) 292, `arXiv:1412.8614 [hep-ph]`.

[79] **STAR** Collaboration, B. I. Abelev *et al.*, "Beam-energy and system-size dependence of dynamical net charge fluctuations," *Phys. Rev.* **C79** (2009) 024906, `arXiv:0807.3269 [nucl-ex]`.

[80] **STAR** Collaboration, L. Adamczyk *et al.*, "Energy Dependence of Moments of Net-proton Multiplicity Distributions at RHIC," *Phys. Rev. Lett.* **112** (2014) 032302, `arXiv:1309.5681 [nucl-ex]`.

[81] **STAR** Collaboration, L. Adamczyk *et al.*, "Beam Energy Dependence of Moments of the Net-Charge Multiplicity Distributions in Au+Au Collisions at RHIC," *Phys. Rev. Lett.* **113** (2014) 092301, `arXiv:1402.1558 [nucl-ex]`.

[82] **STAR** Collaboration, X. Luo, "Energy Dependence of Moments of Net-Proton and Net-Charge Multiplicity Distributions at STAR," *PoS* **CPOD2014** (2015) 019, `arXiv:1503.02558 [nucl-ex]`.

[83] **ALICE** Collaboration, S. Acharya *et al.*, "Relative particle yield fluctuations in Pb–Pb collisions at $\sqrt{s_{\mathrm{NN}}}$ = 2.76 TeV," *Submitted to: Eur. Phys. J.* (2017) , `arXiv:1712.07929 [nucl-ex]`.

[84] **STAR** Collaboration, N. M. Abdelwahab *et al.*, "Energy Dependence of K/π, p/π, and K/p Fluctuations in Au+Au Collisions from $\sqrt{s_{\mathrm{NN}}}$ = 7.7 to 200 GeV," *Phys. Rev.* **C92** (2015) 021901, `arXiv:1410.5375 [nucl-ex]`.

[85] **ALICE** Collaboration, B. B. Abelev *et al.*, "Net-Charge Fluctuations in Pb–Pb collisions at $\sqrt{s_{\mathrm{NN}}}$ = 2.76 TeV," *Phys. Rev. Lett.* **110** (2013) 152301, `arXiv:1207.6068 [nucl-ex]`.

[86] **ALICE** Collaboration, A. Rustamov, "Net-baryon fluctuations measured with ALICE at the CERN LHC," *Nucl. Phys.* **A967** (2017) 453, `arXiv:1704.05329 [nucl-ex]`.

[87] Z. Citron *et al.*, "Future physics opportunities for high-density QCD at the LHC with heavy-ion and proton beams," `arXiv:1812.06772 [hep-ph]`.

[88] S. Voloshin, V. Koch, and H. Ritter, "Event-by-event fluctuations in collective quantities," *Phys. Rev.* **C60** (1999) 024901, `arXiv:nucl-th/9903060 [nucl-th]`.

[89] S. Gavin, "Traces of thermalization from transverse momentum fluctuations in nuclear collisions," *Phys. Rev. Lett.* **92** (2004) 162301, `arXiv:nucl-th/0308067 [nucl-th]`.

[90] **NA49** Collaboration, H. Appelshäuser *et al.*, "Event-by-event fluctuations of average transverse momentum in central Pb+Pb collisions at 158 GeV per nucleon," *Phys. Lett.* **B459** (1999) 679, `arXiv:hep-ex/9904014 [hep-ex]`.

[91] M. J. Tannenbaum, "The distribution function of the event-by-event average p_T for statistically independent emission," *Phys. Lett.* **B498** (2001) 29.

[92] **STAR** Collaboration, J. Adams *et al.*, "Incident energy dependence of p_T correlations at RHIC," *Phys. Rev.* **C72** (2005) 044902, `arXiv:nucl-ex/0504031 [nucl-ex]`.

[93] **CERES** Collaboration, D. Adamová *et al.*, "Scale-dependence of transverse momentum correlations in Pb–Au collisions at 158 A GeV/c," *Nucl. Phys.* **A811** (2008) 179, `arXiv:0803.2407 [nucl-ex]`.

[94] **CERN-Dortmund-Heidelberg-Warsaw-Ames-Bologna** and **CERN-Heidelberg-Lund** Collaboration, K. Braune *et al.*, "Fluctuations in the Hadronic Temperature in pp, pα and $\alpha\alpha$ Collisions at ISR Energies," *Phys. Lett.* **123B** (1983) 467.

[95] **NA49** Collaboration, T. Anticic *et al.*, "Transverse momentum fluctuations in nuclear collisions at 158 A GeV," *Phys. Rev.* **C70** (2004) 034902, `arXiv:hep-ex/0311009 [hep-ex]`.

[96] **NA49** Collaboration, K. Grebieszkow *et al.*, "Event-by-event transverse momentum fluctuations in nuclear collisions at CERN SPS," *PoS* **CPOD07** (2007) 022, `arXiv:0707.4608 [nucl-ex]`.

[97] **CERES** Collaboration, D. Adamová *et al.*, "Event-by-event fluctuations of the mean transverse momentum in 40, 80 and 158 A GeV/c Pb–Au collisions," *Nucl. Phys.* **A727** (2003) 97, `arXiv:nucl-ex/0305002 [nucl-ex]`.

[98] **CERES** Collaboration, H. Sako, H. Appelshäuser, *et al.*, "Event-by-event fluctuations at 40, 80 and 158 A GeV/c in Pb+Au collisions," *J. Phys.* **G30** (2004) S1371, `arXiv:nucl-ex/0403037 [nucl-ex]`.

[99] **CERES** Collaboration, H. Appelshäuser, H. Sako, *et al.*, "Event-by-event fluctuations at SPS," *Nucl. Phys.* **A752** (2005) 394, `arXiv:nucl-ex/0409022 [nucl-ex]`.

[100] **PHENIX** Collaboration, K. Adcox *et al.*, "Event-by-event fluctuations in mean p_T and mean e_T in $\sqrt{s_{NN}}$ = 130 GeV Au+Au collisions," *Phys. Rev.* **C66** (2002) 024901, `arXiv:nucl-ex/0203015 [nucl-ex]`.

[101] **PHENIX** Collaboration, S. S. Adler *et al.*, "Measurement of Nonrandom Event-by-Event Fluctuations of Average Transverse Momentum in $\sqrt{s_{NN}}$ = 200 GeV Au+Au and p+p Collisions," *Phys. Rev. Lett.* **93** (2004) 092301, `arXiv:nucl-ex/0310005 [nucl-ex]`.

[102] **STAR** Collaboration, J. Adams *et al.*, "Event-wise $\langle p_T \rangle$ fluctuations in Au–Au collisions at $\sqrt{s_{NN}}$ = 130 GeV," *Phys. Rev.* **C71** (2005) 064906, `arXiv:nucl-ex/0308033 [nucl-ex]`.

[103] **STAR** Collaboration, L. Adamczyk *et al.*, "System-size dependence of transverse momentum correlations at $\sqrt{s_{NN}}$ = 62.4 and 200 GeV at the BNL Relativistic Heavy Ion Collider," *Phys. Rev.* **C87** (2013) 064902, `arXiv:1301.6633 [nucl-ex]`.

[104] **NA61/SHINE** Collaboration, A. Aduszkiewicz *et al.*, "Multiplicity and transverse momentum fluctuations in inelastic proton–proton interactions at the CERN Super Proton Synchrotron," *Eur. Phys. J.* **C76** (2016) 635, `arXiv:1510.00163 [hep-ex]`.

[105] **NA61/SHINE** Collaboration, E. Andronov, "Transverse momentum and multiplicity fluctuations in Ar+Sc collisions at the CERN SPS from NA61/SHINE," *Acta Phys. Polon. Supp.* **10** (2017) 449, `arXiv:1710.06197 [nucl-ex]`.

[106] **NA61/SHINE** Collaboration, M. Gazdzicki, "Fluctuations and correlations from NA61/SHINE," *PoS* **CPOD2017** (2018) 012, `arXiv:1801.00178 [nucl-ex]`.

[107] **CDF** Collaboration, D. Acosta *et al.*, "Soft and hard interactions in $p\bar{p}$ collisions at $\sqrt{s}$ = 1800 GeV and 630 GeV," *Phys. Rev.* **D65** (2002) 072005.

[108] W. Broniowski, P. Bożek, W. Florkowski, and B. Hiller, "p_T-fluctuations and multiparticle clusters in heavy-ion collisions," *PoS* **CFRNC2006** (2006) 020, `arXiv:nucl-th/0611069 [nucl-th]`.

[109] **ALICE** Collaboration, J. Adam *et al.*, "Flow dominance and factorization of transverse momentum correlations in Pb–Pb collisions at the LHC," *Phys. Rev. Lett.* **118** (2017) 162302, `arXiv:1702.02665 [nucl-ex]`.

Bibliography

[110] **ALICE** Collaboration, S. Acharya *et al.*, "Two particle differential transverse momentum and number density correlations in p–Pb and Pb–Pb at the LHC," arXiv:1805.04422 [nucl-ex].

[111] J. Alme *et al.*, "The ALICE TPC, a large 3-dimensional tracking device with fast readout for ultra-high multiplicity events,"
Nucl. Instrum. Meth. **A622** (2010) 316,
arXiv:1001.1950 [physics.ins-det].

[112] **ALICE** Collaboration, B. B. Abelev *et al.*, "Performance of the ALICE Experiment at the CERN LHC," *Int. J. Mod. Phys.* **A29** (2014) 1430044,
arXiv:1402.4476 [nucl-ex].

[113] CERN, "About CERN." https://home.cern/about. Accessed on 2019-02-25.

[114] E. Mobs, "The CERN accelerator complex. Complexe des accélérateurs du CERN," 2017. http://cds.cern.ch/record/2197559. General Photo.

[115] CERN, "LHC Guide." CERN-Brochure-2017-002-Eng, 2017.
http://cds.cern.ch/record/2255762.

[116] J. Wenninger, "Approaching the Nominal Performance at the LHC," in *Proceedings, 8th International Particle Accelerator Conference (IPAC 2017): Copenhagen, Denmark, May 14-19, 2017*, p. MOYAA1. 2017.

[117] J. Jowett *et al.*, "The 2015 Heavy-Ion Run of the LHC," in *Proceedings, 7th International Particle Accelerator Conference (IPAC 2016): Busan, Korea, May 8-13, 2016*, p. TUPMW027. 2016.

[118] C. A. Salgado *et al.*, "Proton–Nucleus Collisions at the LHC: Scientific Opportunities and Requirements," *J. Phys.* **G39** (2012) 015010,
arXiv:1105.3919 [hep-ph].

[119] **ALICE** Collaboration, B. B. Abelev *et al.*, "Pseudorapidity density of charged particles in p–Pb collisions at $\sqrt{s_{NN}}$ = 5.02 TeV,"
Phys. Rev. Lett. **110** (2013) 032301, arXiv:1210.3615 [nucl-ex].

[120] J. Jowett *et al.*, "Proton–nucleus Collisions in the LHC," in *Proceedings, 4th International Particle Accelerator Conference (IPAC 2013): Shanghai, China, May 12-17, 2013*, p. MOODB201. 2013.

[121] J. Jowett *et al.*, "The 2016 Proton–Nucleus Run of the LHC," in *Proceedings, 8th International Particle Accelerator Conference (IPAC 2017): Copenhagen, Denmark, May 14-19, 2017*, p. TUPVA014. 2017.

[122] **ALICE** Collaboration, S. Acharya *et al.*, "Anisotropic flow in Xe–Xe collisions at $\sqrt{s_{NN}}$ = 5.44 TeV," *Phys. Lett.* **B784** (2018) 82,
arXiv:1805.01832 [nucl-ex].

180

[123] **ATLAS** Collaboration, G. Aad *et al.*, "The ATLAS Experiment at the CERN Large Hadron Collider," *JINST* **3** (2008) S08003.

[124] **CMS** Collaboration, S. Chatrchyan *et al.*, "The CMS Experiment at the CERN LHC," *JINST* **3** (2008) S08004.

[125] **LHCb** Collaboration, A. A. Alves, Jr. *et al.*, "The LHCb Detector at the LHC," *JINST* **3** (2008) S08005.

[126] **ATLAS, CMS** Collaboration, G. Aad *et al.*, "Measurements of the Higgs boson production and decay rates and constraints on its couplings from a combined ATLAS and CMS analysis of the LHC pp collision data at $\sqrt{s}$ = 7 and 8 TeV," *JHEP* **08** (2016) 045, `arXiv:1606.02266 [hep-ex]`.

[127] **LHC Higgs Cross Section Working Group** Collaboration, D. de Florian *et al.*, "Handbook of LHC Higgs Cross Sections: 4. Deciphering the Nature of the Higgs Sector," `arXiv:1610.07922 [hep-ph]`.

[128] **ATLAS** Collaboration, G. Aad *et al.*, "Search for new phenomena in final states with an energetic jet and large missing transverse momentum in pp collisions at $\sqrt{s}$ = 8 TeV with the ATLAS detector," *Eur. Phys. J.* **C75** (2015) 299, `arXiv:1502.01518 [hep-ex]`. [Erratum: Eur. Phys. J. C75 (2015) 408].

[129] **CMS** Collaboration, V. Khachatryan *et al.*, "Search for physics beyond the standard model in dilepton mass spectra in proton–proton collisions at $\sqrt{s}$ = 8 TeV," *JHEP* **04** (2015) 025, `arXiv:1412.6302 [hep-ex]`.

[130] **LHCb** Collaboration, R. Aaij *et al.*, "Implications of LHCb measurements and future prospects," *Eur. Phys. J.* **C73** (2013) 2373, `arXiv:1208.3355 [hep-ex]`.

[131] **LHCf** Collaboration, O. Adriani *et al.*, "The LHCf detector at the CERN Large Hadron Collider," *JINST* **3** (2008) S08006.

[132] **TOTEM** Collaboration, G. Anelli *et al.*, "The TOTEM experiment at the CERN Large Hadron Collider," *JINST* **3** (2008) S08007.

[133] **MoEDAL** Collaboration, J. Pinfold *et al.*, "Technical Design Report of the MoEDAL Experiment." CERN-LHCC-2009-006, MoEDAL-TDR-001, 2009. `https://cds.cern.ch/record/1181486`.

[134] CERN, "Experiments." `https://home.cern/science/experiments`. Accessed on 2019-02-25.

[135] **L3** Collaboration, B. Adeva *et al.*, "The Construction of the L3 Experiment," *Nucl. Instrum. Meth.* **A289** (1990) 35.

[136] **ALICE** Collaboration, "The ALICE Collaboration."
`http://alice-collaboration.web.cern.ch/general/index.html`. Accessed on 2019-02-25.

[137] **ALICE** Collaboration, S. Acharya *et al.*, "The ALICE Transition Radiation Detector: construction, operation, and performance,"
Nucl. Instrum. Meth. **A881** (2018) 88,
`arXiv:1709.02743 [physics.ins-det]`.

[138] **ALICE** Collaboration, K. Aamodt *et al.*, "Alignment of the ALICE Inner Tracking System with cosmic-ray tracks," *JINST* **5** (2010) P03003,
`arXiv:1001.0502 [physics.ins-det]`.

[139] **ALICE** Collaboration, K. Aamodt *et al.*, "Centrality dependence of the charged-particle multiplicity density at mid-rapidity in Pb–Pb collisions at $\sqrt{s_{\mathrm{NN}}}$ = 2.76 TeV," *Phys. Rev. Lett.* **106** (2011) 032301,
`arXiv:1012.1657 [nucl-ex]`.

[140] **ALICE** Collaboration, J. Adam *et al.*, "First results of the ALICE detector performance at 13 TeV." ALICE-PUBLIC-2015-004, 2015.
`http://cds.cern.ch/record/2047855`.

[141] H. Bethe, "Zur Theorie des Durchgangs schneller Korpuskularstrahlen durch Materie," *Annalen der Physik* **397** (1930) 325. In German.

[142] F. Bloch, "Zur Bremsung rasch bewegter Teilchen beim Durchgang durch Materie," *Annalen der Physik* **408** (1933) 285. In German.

[143] W. Blum, W. Riegler, and L. Rolandi, *Particle Detection with Drift Chambers.* Springer (Berlin Heidelberg, Germany), 2nd ed., 2008.

[144] **ALICE** Collaboration, E. Abbas *et al.*, "Performance of the ALICE VZERO system," *JINST* **8** (2013) P10016, `arXiv:1306.3130 [nucl-ex]`.

[145] **ALICE** Collaboration, J. Adam *et al.*, "Study of cosmic ray events with high muon multiplicity using the ALICE detector at the CERN Large Hadron Collider," *JCAP* **1601** (2016) 032, `arXiv:1507.07577 [astro-ph.HE]`.

[146] M. Ivanov, I. Belikov, P. Hristov, and K. Safarik, "Track reconstruction in high density environment," *Nucl. Instrum. Meth.* **A566** (2006) 70.

[147] R. Frühwirth, "Application of Kalman filtering to track and vertex fitting," *Nucl. Instrum. Meth.* **A262** (1987) 444.

[148] **ALICE** Collaboration, S. Acharya *et al.*, "The ALICE definition of primary particles." ALICE-PUBLIC-2017-005, 2017.
`https://cds.cern.ch/record/2270008`.

[149] **ALICE** Collaboration, B. B. Abelev *et al.*, "Centrality determination of Pb–Pb collisions at $\sqrt{s_{\mathrm{NN}}}$ = 2.76 TeV with ALICE," *Phys. Rev.* **C88** (2013) 044909, `arXiv:1301.4361 [nucl-ex]`.

[150] M. L. Miller, K. Reygers, S. J. Sanders, and P. Steinberg, "Glauber modeling in high energy nuclear collisions," *Ann. Rev. Nucl. Part. Sci.* **57** (2007) 205, `arXiv:nucl-ex/0701025 [nucl-ex]`.

[151] R. Brun, P. Buncic, F. Carminati, A. Morsch, F. Rademakers, and K. Safarik, "Computing in ALICE," *Nucl. Instrum. Meth.* **A502** (2003) 339.

[152] **ALICE** Collaboration, P. Cortese *et al.*, *ALICE Technical Design Report of the Computing.* CERN, Geneva, 2005. `http://cds.cern.ch/record/832753`.

[153] R. Brun and F. Rademakers, "ROOT: An object oriented data analysis framework," *Nucl. Instrum. Meth.* **A389** (1997) 81.

[154] CERN, "ROOT Data Analyis Framework." `https://root.cern.ch/`. Accessed on 2019-02-25.

[155] R. Brun, F. Carminati, and S. Giani, "GEANT Detector Description and Simulation Tool." CERN-W5013, 1994.

[156] T. Sjöstrand, S. Mrenna, and P. Z. Skands, "PYTHIA 6.4 Physics and Manual," *JHEP* **05** (2006) 026, `arXiv:hep-ph/0603175 [hep-ph]`.

[157] P. Z. Skands, "Tuning Monte Carlo Generators: The Perugia Tunes," *Phys. Rev.* **D82** (2010) 074018, `arXiv:1005.3457 [hep-ph]`.

[158] W.-T. Deng, X.-N. Wang, and R. Xu, "Gluon shadowing and hadron production in heavy-ion collisions at LHC," *Phys. Lett.* **B701** (2011) 133, `arXiv:1011.5907 [nucl-th]`.

[159] T. Sjöstrand, S. Mrenna, and P. Z. Skands, "A Brief Introduction to PYTHIA 8.1," *Comput. Phys. Commun.* **178** (2008) 852, `arXiv:0710.3820 [hep-ph]`.

[160] R. Engel, J. Ranft, and S. Roesler, "Hard diffraction in hadron hadron interactions and in photoproduction," *Phys. Rev.* **D52** (1995) 1459, `arXiv:hep-ph/9502319 [hep-ph]`.

[161] Z.-W. Lin, C. M. Ko, B.-A. Li, B. Zhang, and S. Pal, "A Multi-phase transport model for relativistic heavy ion collisions," *Phys. Rev.* **C72** (2005) 064901, `arXiv:nucl-th/0411110 [nucl-th]`.

[162] **ALICE** Collaboration, K. Aamodt *et al.*, "Charged-particle multiplicity measurement in proton–proton collisions at $\sqrt{s}$ = 0.9 and 2.36 TeV with ALICE at LHC," *Eur. Phys. J.* **C68** (2010) 89, `arXiv:1004.3034 [hep-ex]`.

[163] S. Gavin, G. Moschelli, and C. Zin, "Boltzmann-Langevin Approach to Pre-equilibrium Correlations in Nuclear Collisions," *Phys. Rev.* **C95** (2017) 064901, `arXiv:1612.07856 [nucl-th]`.

[164] **ALICE** Collaboration, B. B. Abelev *et al.*, "Multiplicity dependence of pion, kaon, proton and lambda production in p–Pb collisions at $\sqrt{s_{NN}}$ = 5.02 TeV," *Phys. Lett.* **B728** (2014) 25, `arXiv:1307.6796 [nucl-ex]`.

[165] J. Ranft, "DPMJET version II.5: Sampling of hadron–hadron, hadron–nucleus and nucleus–nucleus interactions at accelerator and cosmic ray energies according to the two-component dual parton model: Code manual," `arXiv:hep-ph/9911232 [hep-ph]`.

[166] S. Roesler, R. Engel, and J. Ranft, "The Monte Carlo event generator DPMJET-III," in *Advanced Monte Carlo for radiation physics, particle transport simulation and applications. Proceedings, Conference, MC2000, Lisbon, Portugal, October 23-26, 2000*, p. 1033. 2000. `arXiv:hep-ph/0012252 [hep-ph]`.

[167] **ALICE** Collaboration, J. Adam *et al.*, "Centrality dependence of particle production in p–Pb collisions at $\sqrt{s_{NN}}$ = 5.02 TeV," *Phys. Rev.* **C91** (2015) 064905, `arXiv:1412.6828 [nucl-ex]`.

[168] **ALICE** Collaboration, B. B. Abelev *et al.*, "Centrality dependence of π, K, and p production in Pb–Pb collisions at $\sqrt{s_{NN}}$ = 2.76 TeV," *Phys. Rev.* **C88** (2013) 044910, `arXiv:1303.0737 [hep-ex]`.

[169] J. Xu and C. M. Ko, "Higher-order anisotropic flows and dihadron correlations in Pb–Pb collisions at $\sqrt{s_{NN}}$ = 2.76 TeV in a multiphase transport model," *Phys. Rev.* **C84** (2011) 044907, `arXiv:1108.0717 [nucl-th]`.

[170] T. Sjöstrand, "The Development of MPI Modeling in PYTHIA," *Adv. Ser. Direct. High Energy Phys.* **29** (2018) 191, `arXiv:1706.02166 [hep-ph]`.

[171] A. Ortiz Velasquez, P. Christiansen, E. Cuautle Flores, I. Maldonado Cervantes, and G. Paić, "Color Reconnection and Flowlike Patterns in *pp* Collisions," *Phys. Rev. Lett.* **111** (2013) 042001, `arXiv:1303.6326 [hep-ph]`.

[172] T. Sjöstrand, "Colour reconnection and its effects on precise measurements at the LHC," `arXiv:1310.8073 [hep-ph]`.

[173] R. Corke and T. Sjöstrand, "Multiparton Interactions with an x-dependent Proton Size," *JHEP* **05** (2011) 009, `arXiv:1101.5953 [hep-ph]`.

[174] T. Sjöstrand, "PYTHIA 8.1 Tunes."
`http://home.thep.lu.se/~torbjorn/pythia81html/Tunes.html`. Accessed on 2019-03-06.

[175] **CERN-Heidelberg-Lund** Collaboration, W. Bell *et al.*, "Study of inelatstic $\alpha\alpha$ and αp collisions in the CERN ISR," in *Proceedings, 5th High-Energy Heavy Ion Study: Berkeley, California, May 18-22, 1981*, p. 540. 1981.

[176] **ALICE** Collaboration, C. H. Christensen, "System-size dependence of the charged-particle pseudorapidity density at $\sqrt{s_{\mathrm{NN}}}$ = 5.02 TeV with ALICE," *Nucl. Phys.* **A967** (2017) 301.

[177] T. A. Trainor, "Eventwise mean-p_{T} fluctuations versus minimum-bias jets (minijets) at energies available at the CERN Large Hadron Collider," *Phys. Rev.* **C92** (2015) 024915, `arXiv:1503.02197 [hep-ph]`.

[178] Q. Liu and W.-Q. Zhao, "Color reconnection and event-by-event fluctuations of mean transverse momentum in proton-proton collisions at $\sqrt{s}$ = 7 TeV in PYTHIA6.4," `arXiv:1611.02532 [hep-ph]`.

[179] T. Osada and M. Ishihara, "Event-by-event mean p_{T} fluctuations and transverse size of color flux tube generated in p-p collisions at $\sqrt{s}$ = 0.90 TeV," *J. Phys.* **G45** (2018) 015104, `arXiv:1702.07440 [hep-ph]`.

[180] S. Gavin and G. Moschelli, "Fluctuation Probes of Early-Time Correlations in Nuclear Collisions," *Phys. Rev.* **C85** (2012) 014905, `arXiv:1107.3317 [nucl-th]`.

Danksagung